J/ψ Production in Heavy Ion Collisions at the STAR Detector at RHIC

by

Christopher Beresford Powell

Thesis presented for the Degree of

Doctor of Philosophy in Physics

Faculty of Science
University of Cape Town
Cape Town, Western Cape
South Africa

Supported by the
Nuclear Science Division
Lawrence Berkeley National Laboratory
Berkeley, California
United States of America

November 2012

Dedication

To my mom, for your unconditional support and selfless generosity. You have been a friend, a role model, and an inspiration.

Acknowledgements

I thank the Lawrence Berkeley National Laboratory for their full-time support throughout my graduate research. They provided me with the opportunity to live in California and supported my travel to meetings and conferences around America and Europe. Interacting with the international physics community and the excellent scientists at LBNL has been a great adventure. I owe enormous gratitude for the support of Grazyna Odyniec, who has encouraged me to be thoughtful, critical, and actively involved. This has been complemented by the tremendous amount of advice and help provided by Daniel Kikoła, who endured endless questions and confusion during my formative months at LBNL. The University of Cape Town has been a great support, and I thank Prof. Jean Cleymans and Prof. Andre Peshier for their efforts.

There are many members of the Relativistic Nuclear Collisions group at LBNL whose support has been essential, including the past and present group heads Hans-Georg Ritter, Ernst Sichtermann, and Peter Jacobs, and the STAR spokesperson Nu Xu. Useful discussions and lunch breaks with Xin Dong, Hiroshi Masui, Len Eun, Evan Sangaline, Patrick Huck, Alex Schmah, Sevil Salur, Art Poskanzer, Vi Nham Tram, Andrew Rose, and the rest of the RNC group made LBNL a great place to work. Thanks to the colleagues and friends like Mateusz Ploskon, Bo Fenton-Olsen, Rosi Reed, and Manuel Calderon de la Barca Sanchez, that made the physics world such a fun environment. Thanks to Jerome Lauret for his endless computing support and encouragement, and Leo Greiner and Michal Szelezniak for the entertaining conversations and recreational activities.

I could not have done this without the support and patience of my family, friends, and loved ones, who have endured my frustration and complaints, and have provided distractions when I needed them, and when I didn't.

ABSTRACT

J/ψ Production in Heavy Ion Collisions at the STAR Detector at RHIC

Christopher Beresford Powell

November 2012

The success of the Standard Model of particle physics in describing a large variety of experimental results has been supported by the prediction and subsequent discovery of the charm, bottom, and top quarks, and the Z, $W^{\pm}$, and Higgs bosons. The theory of *Quantum Chromodynamics* (QCD), which describes the strong interaction between quarks and gluons in the Standard Model, predicts a phase transition from hadronic matter to a deconfined *Quark Gluon Plasma* (QGP) at high temperature and energy density. The *Relativistic Heavy Ion Collider* (RHIC) was built to achieve these conditions to test the predictions of QCD and understand the properties of a deconfined medium. Charm (c) quarks have been suggested as ideal probes of the medium created in heavy ion collisions, as they are created primarily in the initial hard scattering of the collision because of their large mass.

The suppression of the charm anti-charm bound state $J/\psi(1S)$ has been proposed as a signature of the formation of a quark gluon plasma, and is expected to arise from the color screening of the charm quark potential in a deconfined medium. There are, however, other modifications to J/ψ production in heavy ion collisions that need to be investigated in order for a suppression from color screening to be determined. *Cold Nuclear Matter* (CNM) effects, which arise due to the presence of ordinary nuclear matter in the collision, must be determined using d+Au collisions where nuclear matter is present but the formation of a QGP is not possible.

The production of J/ψ via the dielectron decay channel $J/\psi \rightarrow e^+ + e^-$ at the STAR detector is presented in this thesis. The p_T spectrum and nuclear modification factor are calculated for J/ψ with $p_T < 5$ GeV/c and $|y| < 1$ in d+Au and Au+Au at a collision energy of $\sqrt{s_{_{NN}}} = 200$ GeV. The results in d+Au are used to determine the cold nuclear matter effects, and the J/ψ nuclear absorption cross section is calculated. These effects are subtracted from the J/ψ nuclear modification factor in Au+Au collisions. A suppression in excess of the expectations from cold nuclear matter effects consistent with the formation of a QGP is observed. The results are also compared to model predictions involving a suppression from color screening, regeneration of J/ψ from charm quarks in the QGP sea, feed-down from excited states and B decays, and cold nuclear matter effects. The models agree with the data well and exhibit a suppression of J/ψ increasing with collision centrality due to color screening.

Author's Contribution

I have been employed by the Nuclear Science Division at the Lawrence Berkeley National Laboratory since July 2008 where I have been an active member of the Relativistic Nuclear Collisions group. I have also been a member of the STAR collaboration at the Relativistic Heavy Ion Collider since July 2008, where I have made a number of contributions to the running of the experiment, analysis of new data, and presenting new results to the international community. These contributions are described below, and a list of attended conferences and publications is also provided.

Analysis

I have studied the production of low-p_T ($p_T < 5$ GeV/c) J/ψ in d+Au and Au+Au collisions at STAR. The analysis of J/ψ in d+Au at STAR has not been performed before, and this thesis provides a detailed description of the analysis procedures I used and developed. A high-statistics Au+Au dataset was recorded in 2010, and this was the first Au+Au data with the new Time of Flight detector installed. In both the d+Au and Au+Au collision system, I have contributed to ensuring a high quality of data by investigating the dependence of observables with collision kinematics, beam luminosity, and time. I have also been involved in determining the collision centrality selection in the d+Au collisions system, and these contributions have been used by a number of analyses. I have provided a detailed explanation of how electron identification is performed at STAR. This includes studies of the kinematic and centrality dependence of the detector response to electrons, calculations for the efficiencies of the identification techniques, and a description of uncertainties within these methods.

I have presented the J/ψ yield in d+Au and Au+Au collisions, and have determined the modification to J/ψ production compared to p+p collisions, and these results have been shown regularly at weekly meetings to members of the RNC group and STAR experiment. In addition, I have attended and presented results at the bi-annual STAR collaboration meetings and STAR analysis meetings.

A description of the analysis methods I have developed and implemented on data from d+Au and Au+Au collisions is given in Chapter 4, and the results I have calculated using these methods are provided in Chapter 5.

Service Work

In addition to the contributions to data analysis previously described, I have also participated in taking shifts to assist the running of the STAR experiment for two weeks each year. After completing the training for quality analysis of the recorded data (shift crew) and operating the detectors, I accepted the role of shift leader where I supervised and coordinated the data recording, and trained new members of the shift team.

I participated in understanding various aspects of the d+Au data, and worked with a group to determine the centrality selection in d+Au collisions. This required understanding and correcting for the trigger inefficiencies in d+Au collisions. There were also some hardware errors during data taking, and I was involved with the software and computing team at STAR in developing a method to identify and remove events where the event rates were incorrectly recorded.

Throughout 2011 and 2012, I was a member of the software and computing team for the STAR collaboration. I was responsible for the role of embedding deputy, which manages the running of complex Monte Carlo simulations which are embedded into real data events. These simulations are used to understand the detector response and efficiency, and are essential for many analyses.

Conferences and Seminars

The results presented in this thesis have been presented in the talks listed below.

Invited Talks

- Quarkonium production at STAR,
  European Physical Society High Energy Physics (2011).
- J/ψ measurements at STAR,
  RHIC and AGS Users' Meeting (2011).

Accepted talks

- J/ψ production in minimum bias d+Au collisions at $\sqrt{s_{NN}}$ =200 GeV in STAR,
  American Physical Society Division of Nuclear Physics and the Physical Society of Japan (2009).

Seminars

- Particle identification and J/ψ production at STAR
  University of Cape Town (2012).
- J/ψ production in heavy ion collisions at RHIC
  University of Cape Town (2010).

Posters

- J/ψ production in minimum bias d+Au collisions at $\sqrt{s_{NN}}$ =200 GeV in STAR,
  Quark Matter (2009).

Publication List

Publications of the results I have calculated which are presented in this thesis are provided below.

1. C. B. Powell [STAR Collaboration], *Quarkonium Production at STAR*, PoS (EPS-HEP2011) (2011) 485, ArXiv:1111.6944 [nucl-ex]

2. C. B. Powell, D. Kikola, and G. Odyniec [STAR Collaboration], *Low-p_T J/ψ production in Au+Au and Cu+Cu collisions at* $\sqrt{s_{_{NN}}} = 200$ GeV/c
   (in progress, awaiting GPC)

3. C. B. Powell, L. Kosarzewski, and G. Odyniec [STAR Collaboration], *Low-p_T J/ψ production in p+p and d+Au collisions at* $\sqrt{s_{_{NN}}} = 200$ GeV/c
   (in progress, awaiting GPC)

Papers published by the STAR collaboration while I have been an active participant and part of the author list are provided below.

1. B. Abelev et al. [STAR Collaboration], *Single Spin Asymmetry A_N in Polarized Proton-Proton Elastic Scattering at* $\sqrt{s} = 200$ *GeV*, ArXiv: 1206.1928

2. B. Abelev et al. [STAR Collaboration], *Transverse Single-Spin Asymmetry and Cross-Section for π^0 and η Mesons at Large Feynman-x in Polarized p+p Collisions at* $\sqrt{s} = 200$ *GeV*, ArXiv: 1205.6826

3. B. Abelev et al. [STAR Collaboration], *Measurements of D^0 and D^* Production in p + p Collisions at* $\sqrt{s} = 200$ *GeV*, ArXiv: 1204.4244

4. B. Abelev et al. [STAR Collaboration], *Di-electron spectrum at mid-rapidity in* $p + p$ *collisions at* $\sqrt{s} = 200$ *GeV*, ArXiv: 1204.1890

5. B. Abelev et al. [STAR Collaboration], *Hadronic Trigger using electromagnetic calorimeter and particle identification at high-pT with STAR Detector*, ArXiv: 1112.2946

6. B. Abelev et al. [STAR Collaboration], *Directed Flow of Identified Particles in Au + Au Collisions at* $\sqrt{s_{NN}} = 200$ *GeV at RHIC*, Phys. Rev. Lett. **108** (2012) 202301

7. B. Abelev et al. [STAR Collaboration], *Measurement of the* $W \to e\nu$ *and* $Z/\gamma^* \to e^+e^-$ *Production Cross Sections at Mid-rapidity in Proton-Proton Collisions at* $\sqrt{s}$ *= 500 GeV*, Phys. Rev. D **85** (2012) 92010

8. B. Abelev et al. [STAR Collaboration], *Energy and system-size dependence of two- and four-particle* v_2 *measurements in heavy-ion collisions at RHIC and their implications on flow fluctuations and nonflow*, ArXiv: arXiv:1111.5637v1

9. B. Abelev et al. [STAR Collaboration], *System size and energy dependence of near-side di-hadron correlation*, Phys. Rev. C **85** (2012) 14903

10. B. Abelev et al. [STAR Collaboration], *Identified hadron compositions in p+p and Au+Au collisions at high transverse momenta at* $\sqrt{s_{_{NN}}} = 200$ *GeV*, Phys. Rev. Lett. **108** (2012) 72302

11. B. Abelev et al. [STAR Collaboration], *Directed and elliptic flow of charged particles in Cu+Cu collisions at* $\sqrt{s_{NN}}$ *= 22.4 GeV*, Phys. Rev. C **85** (2012) 14901

12. B. Abelev et al. [STAR Collaboration], *Anomalous centrality evolution of two-particle angular correlations from Au-Au collisions at* $\sqrt{s_{\rm NN}}$ *= 62 and 200 GeV*, ArXiv: 1109.4380

13. B. Abelev et al. [STAR Collaboration], rho^0 *Photoproduction in AuAu Collisions at* $\sqrt{s_{NN}}$*=62.4 GeV with STAR*, Phys. Rev. C **85** (2012) 14910

14. B. Abelev et al. [STAR Collaboration], *Strangeness Enhancement in Cu+Cu and Au+Au* $\sqrt{s_{NN}}$ *200 GeV Collisions*, Phys. Rev. Lett. **108** (2012) 72301

15. B. Abelev et al. [STAR Collaboration], *Evolution of the differential transverse momentum correlation function with centrality in Au+Au collisions at* $\sqrt{s_{NN}} =$ 200 *GeV*, Phys. Lett. B **704** (2011) 467

16. B. Abelev et al. [STAR Collaboration], *Observation of the antimatter helium-4 nucleus*, Nature **473** (2011) 353

17. B. Abelev et al. [STAR Collaboration], *Experimental studies of di-jet survival and surface emission bias in Au+Au collisions via angular correlations with respect to back-to-back leading hadrons*, Phys. Rev. C **83** (2011) 061901

18. B. Abelev et al. [STAR Collaboration], *High p_T non-photonic electron production in p+p collisions at $\sqrt{s}$ = 200 GeV*, Phys. Rev. D **83** (2011) 52006

19. B. Abelev et al. [STAR Collaboration], *Measurements of Dihadron Correlations Relative to the Event Plane in Au+Au Collisions at s NN = 200 GeV*, ArXiv: 1010.0690

20. B. Abelev et al. [STAR Collaboration], *Strange and Multi-strange Particle Production in Au+Au Collisions at $\sqrt{s_{NN}}$ = 62.4 GeV*, Phys. Rev. C **83** (2011) 24901

21. B. Abelev et al. [STAR Collaboration], *Measurement of the parity-violating longitudinal single-spin asymmetry for $W^{\pm}$ boson production in polarized proton-proton collisions at $\sqrt{s} = 500$ GeV*, Phys. Rev. Lett. **106** (2011) 62002

22. B. Abelev et al. [STAR Collaboration], *Scaling properties at freeze-out in relativistic heavy ion collisions* , Phys. Rev. C **83** (2011) 34910

23. B. Abelev et al. [STAR Collaboration], *An Experimental Exploration of the QCD Phase Diagram: The Search for the Critical Point and the Onset of Deconfinement*, ArXiv: 1007.2613

24. B. Abelev et al. [STAR Collaboration], *Measurement of the Bottom contribution to non-photonic electron production in p+p collisions at sqrts=200 GeV*, Phys. Rev. Lett. **105** (2010) 202301

25. B. Abelev et al. [STAR Collaboration], *K*0 production in Cu+Cu and Au+Au collisions at $\sqrt{s_N N}$ = 62.4 GeV and 200 GeV*, Phys. Rev. C **84** (2011) 34909

26. B. Abelev et al. [STAR Collaboration], *Balance Functions from Au+Au, d+Au, and p+p Collisions at* $\sqrt{s_{NN}}$ *= 200 GeV*, Phys. Rev. C **82** (2010) 24905

27. B. Abelev et al. [STAR Collaboration], *Higher Moments of Net-proton Multiplicity Distributions at RHIC*, Phys. Rev. Lett. **105** (2010) 22302

28. B. Abelev et al. [STAR Collaboration], *Azimuthal di-hadron correlations in d+Au and Au+Au collisions at* $\sqrt{s_{NN}}$ = 200 *GeV from STAR*, Phys. Rev. C **82** (2010) 24912

29. B. Abelev et al. [STAR Collaboration], *Pion femtoscopy in p+p collisions at sqrt(s)=200 GeV*, Phys. Rev. C **83** (2011) 64905

30. B. Abelev et al. [STAR Collaboration], *Longitudinal scaling property of the charge balance function in Au + Au collisions at 200 GeV*, Phys. Lett. B **690** (2010) 239

31. B. Abelev et al. [STAR Collaboration], *Charged and strange hadron elliptic flow in Cu+Cu collisions at* $\sqrt{s_{NN}}$ *= 62.4 and 200 GeV*, Phys. Rev. C **81** (2010) 44902

32. B. Abelev et al. [STAR Collaboration], *Upsilon cross section in p+p collisions at sqrt(s) = 200 GeV*, Phys. Rev. D **82** (2010) 12004

33. B. Abelev et al. [STAR Collaboration], *Three-particle coincidence of the long range pseudorapidity correlation in high energy nucleus-nucleus collisions*, Phys. Rev. Lett. **105** (2010) 22301

34. B. Abelev et al. [STAR Collaboration], *Inclusive* π^0*, eta, and direct photon production in p+p and d+Au collisions at sqrt(sNN) = 200 GeV*, Phys. Rev. C **81** (2010) 64904

35. B. Abelev et al. [STAR Collaboration], *Studying Parton Energy Loss in Heavy-Ion Collisions via Direct-Photon and Charged-Particle Azimuthal Correlations*, Phys. Rev. C **82** (2010) 34909

36. B. Abelev et al. [STAR Collaboration], *Observation of $\pi^+\pi^-\pi^+\pi^-$ photoproduction in ultraperipheral heavy-ion collisions at sqrt(sNN) = 200 GeV at the STAR detector*, Phys. Rev. C **81** (2010) 44901

37. B. Abelev et al. [STAR Collaboration], *Identified high-p_T spectra in Cu+Cu collisions at $\sqrt{s_{NN}}$=200 GeV*, Phys. Rev. C **81** (2010) 54907

38. B. Abelev et al. [STAR Collaboration], *Longitudinal double-spin asymmetry and cross section for inclusive neutral pion production at midrapidity in polarized proton collisions at sqrt(s) = 200 GeV*, Phys. Rev. D **80** (2009) 111108

39. B. Abelev et al. [STAR Collaboration], *Observation of an Antimatter Hypernucleus*, Science **328** (2010) 58

Contents

Chapter 1

Introduction

The understanding of nature and the properties of matter is one of the most important questions of physics. The most fundamental aspect of this study is determining the building blocks which comprise all matter, the elementary particles that make up the universe, and elucidating their properties.

1.1 The History of Particle Theory

The idea that matter is made up of discrete and finite components has been present for thousands of years, originating from the philosophies of ancient Greece and India [1]. These notions were later used by John Dalton who proposed that chemical elements were made up of atoms in the early 19^{th} century. Atoms were believed to be the smallest constituent of matter until the end of the 19^{th} century, when Joseph Thompson discovered the electron in 1897 in his work with cathode rays. The nucleus was later discovered in 1909 by Ernest Rutherford, who proposed the planetary model of the atom, where negatively charged electrons orbited a positively charged nucleus. This, along with the work from Max Planck and Albert Einstein on the quantization of radiation and light, provided Niels Bohr with the tools to develop the first atomic model based on quantum theory in 1913. This introduced the concept of discrete energy levels of electron orbitals, and predicted the observed spectral lines

of hydrogen. The understanding of the nucleus was improved again by Rutherford, who found evidence for the proton in 1919, and inferred the existence of the neutron, which was later discovered by James Chadwick in 1932. However, the Bohr model fell short of explaining more complex atoms, and required the developments of the exclusion principle formulated by Wolfgang Pauli in 1925 (and his later work in understanding particle spin), and the uncertainty principle developed by Werner Heisenberg in 1927. This, combined with the work of Louis de Broglie and Erwin Schrödinger on the wave-like nature of particles in 1924 and 1926, respectively, led to the description of the electron formulated by Paul Dirac in 1928, which combined special relativity and quantum mechanics, and predicted the existence of anti-matter. This was confirmed with the discovery of the positron by Carl Anderson in 1932, and the observation of the anti-proton by Emilio Segré and Owen Chamberlain in 1955.

The alpha, beta, and gamma radiation from atoms had been observed by this time, and the neutrino had been postulated by Pauli in 1930 to explain the continuous beta decay spectrum. Enrico Fermi then introduced the weak interaction for the theory of beta decay in 1933, which was the first theory to use the neutrino. Hideki Yukawa proposed a theory in 1935 to describe strong nuclear interactions, which provided an understanding for the binding of nuclei despite the electromagnetic repulsion of protons, as well as the limited range of the strong force compared to the electromagnetic force.

Following the discovery of the pion in 1947, there was a dramatic increase in the discovery of new particles with the invention of the bubble chamber in 1952 by Donald Glaser, and the development of particle accelerators. A particle classification system was developed by Murray Gell-Mann in 1961, in which *hadrons* (bound-states of quarks) were organized using a group theory formalism of the flavor symmetry under SU(3). This allowed for the prediction of unobserved particles, such as the Ω^-, which was later discovered in 1964. The necessity for an additional quantum number arose from the observation of the Ω^- baryon, which is composed of three strange quarks with parallel spins, and the Δ^{++} baryon, which is composed of three up quarks

with parallel spins. Since quarks are fermions, these baryons were forbidden by the Pauli exclusion principle. In order to resolve this problem, in 1965 Moo-Young Han, Yoichiro Nambu, and Oscar W. Greenberg proposed that quarks possess color charge, an additional SU(3) gauge degree of freedom.

From this theory came the quark model, proposed by Gell-Mann and George Zweig in 1964, which hypothesized that these particles were not elementary, but rather were composed of constituent particles named *quarks*. Their model involved three flavors of quark, namely *up*, *down*, and *strange*, and these were given intrinsic properties such as spin and electric charge. In order to better describe the weak interaction and the known meson masses [2], a fourth quark, *charm*, was included. Then in 1973, in order to explain the charge-parity (CP) violation observed in the weak interaction [3], the existence of another pair of quarks was suggested, and these were named *top* and *bottom* in 1975 [4].

There was much contention over the physical existence of quarks, until the discovery of the up and down quark, and the indirect observation of the strange quark in 1968 from deep inelastic scattering (DIS) experiments of leptons on hadrons [5, 6]. The validity of the quark model was further demonstrated in 1974, with the discovery of the charm quark through the observation of the charm anti-charm bound state, J/ψ. The bottom quark was observed several years later in 1977 [7], followed by the top quark in 1995 [8].

In order to describe the interaction of leptons and quarks that make up the large variety of observed particles, the *Standard Model of Particle Physics* was developed throughout the later part of the 20^{th} century. The first developments were made by Abdus Salam, Steven Weinberg, and Sheldon Glashow [9], who made significant contributions to the unified description of the electromagnetic and weak, or *electroweak* interaction. The Higgs [10] mechanism was incorporated into the model in 1967 by Weinberg [11], and is responsible for the masses of quarks and leptons, and of the W and Z bosons which mediate the weak interaction. This was supported by the

recent discovery of a boson compatible with the Higgs, which was announced on July 2012 [12]. The neutral weak current was observed in 1973, followed by the discovery of the W and Z bosons in 1981 whose masses agreed with the predictions made by the Standard Model. The strong force was later incorporated into the Standard Model after the experimental verification of the existence of quarks. A brief overview of the Standard Model is given below, and a comprehensive description can be found in [13].

1.2 The Standard Model

The Standard Model (SM) of particle physics is a quantum field theory that successfully describes the electromagnetic, weak, and strong interactions, and the elementary particles that experience these interactions. It has been able to explain and calculate a large variety of particles and their interactions, and has been experimentally verified with the prediction and subsequent discovery of the charm, bottom, and top quark, and of the W and Z bosons and their precise masses.

The Standard Model Lagrangian is derived from the global Poincarè symmetry and is defined by the local gauge symmetry SU(3)⊗SU(2)⊗U(1), where SU(3) describes the symmetries of the strong interaction between the color charges, SU(2) describes the weak symmetries, and U(1) describes the electromagnetic symmetries. The Standard Model is not a complete theory of fundamental interactions, as it does not incorporate gravity. It is also in conflict with observations from cosmology, as the Standard Model does not include dark matter. Despite this, the Standard Model has been incredibly successful in explaining and predicting a large variety of observed particles.

The idea behind the Standard Model is that there are a small number of elementary particles and the abundant variety of composite particles that we observe can be explained by the interactions between these fundamental particles. The elementary particles in the SM are separated into two groups; spin particles, known as *Fermions*,

and the force mediators of the fundamental interactions, *gauge Bosons*, which have integral spin.

Fermions are classified by how they interact, and are separated into six leptons and six quarks. They are further separated into three generations of increasing mass, each with similar properties. The charge -1 leptons, the *electron* (e^-), *muon* (μ^-), and *tau* (τ^-), form the three lepton generations, along with their chargeless neutrino pairs, ν_e, ν_μ, and ν_τ. The quarks carry fractional electric charge of $+2/3e$ or $-1/3e$ and are grouped as such, with *up* (u) and *down* (d), *charm* (c) and *strange* (s), and *top* (t) and *bottom* (b) forming the three generations. This is illustrated in Table 1.1, and the mass of each particle is given [13]. The SM predicts that neutrinos are massless. However, non-zero masses are required to explain the observed neutrino oscillations, implying that neutrinos must have a mass. For each particle shown in Table 1.1, there exists an anti-particle with opposite quantum numbers (e.g. charge, lepton number, etc.). The first generation are the lightest particles that do not decay and make up the atoms we observe in nature. The more massive higher generation particles are short-lived (except for neutrinos) and only exist in high-energy environments. Fermions follow the Pauli exclusion principle because of their half-integer spin, giving rise to the electron orbital structure in atoms. The defining property of quarks is that they carry a color charge and experience the strong interaction. In addition, they also carry an electric charge and weak isospin, and as a result also interact through the electromagnetic and weak interaction.

The gauge bosons are the force carriers that mediate the electromagnetic, weak, and strong interactions in the Standard Model. These spin 1 particles can be separated according to the interaction types, and the number of gauge bosons in each interaction is determined by the dimension of their gauge group. The electromagnetic mediator is the *photon* (γ), which is a massless and chargeless particle that couples to electric charge and is well described by *Quantum Electrodynamics* (QED). The mediators of the weak interaction are the neutral Z^0 boson, and the $W^\pm$ bosons, which carry a charge of $\pm 1e$. The strong force mediators are the *gluons*, which are massless

and interact with the color charge of quarks. There are eight types of gauge gluons for each non-vanishing color-anticolor charge combination, and the non-zero color charge of the gluons means that they are also self-interacting. The fundamental interactions are summarized in Table 1.2 along with their gauge boson charge and mass [13].

The strong force between the color charge of quarks and gluons is responsible for the binding of nucleons into a nucleus, and also for the binding of quarks into hadrons. The theory of *Quantum Chromodynamics* is used to describe the strong interaction between quarks and gluons, and this is discussed in the following section.

Table 1.1: The Fermions in the Standard Model [13].

Charge	1st Generation		2nd Generation		3rd Generation	
(e)	Flavor	Mass (GeV/c^2)	Flavor	Mass (GeV/c^2)	Flavor	Mass (GeV/c^2)
			Quarks			
$+2/3$	u	$2.3^{+0.7}_{-0.5} \times 10^{-3}$	c	1.275 ± 0.025	t	$173.5 \pm 0.6 \pm 0.8$
$-1/3$	d	$4.8^{+0.7}_{-0.3} \times 10^{-3}$	s	0.095 ± 0.005	b	4.18 ± 0.03
			Leptons			
-1	e^-	0.51×10^{-3}	μ^-	0.11	τ^-	1.78
0	ν_e	$< 0.46 \times 10^{-6}$	ν_μ	$< 0.19 \times 10^{-3}$	ν_τ	$< 18.2 \times 10^{-3}$

Table 1.2: The gauge Bosons of the fundamental interactions in the Standard Model.

Interaction	Electroweak			Strong
	Electromagnetic	Weak		
Gauge Boson	γ	$W^{\pm}$	Z^0	gluons
Charge	0	± 1	0	0
Mass (GeV/c^2)	0	80.399 ± 0.023	91.1876 ± 0.0021	0

1.3 Quantum Chromodynamics

Quantum Chromodynamics (QCD) is the non-Abelian SU(3) Yang-Mills gauge theory of the strong interaction, and describes the fundamental force experienced by color-charged fermions (quarks) and mediated by gluon exchange in the Standard Model. The gauge invariant QCD Lagrangian, which describes the dynamics of the quarks and gluons, is:

$$\mathcal{L}_{QCD} = -\frac{1}{4}G^a_{\mu\nu}G^{\mu\nu}_a + \bar{\psi}^i_q\left(i\gamma^\mu\left(D_\mu\right)_{ij} - m\delta_{ij}\right)\psi^j_q, \tag{1.1}$$

$$\left(D_\mu\right)_{ij} = \delta_{ij}\partial_\mu + \frac{i}{2}g_s\lambda^a_{ij}\left(G_\mu\right)_a, \tag{1.2}$$

where ψ^i_q are the 4-component Dirac spinor quark fields in SU(3), i and j are the quark color, q is the quark flavor, m is the quark mass, and γ^μ are the Dirac matrices. The tensor $G^a_{\mu\nu}$ represents the gauge invariant gluon field strength:

$$G^a_{\mu\nu} = \partial_\mu G^a_\nu - \partial_\nu G^a_\mu - g_s f^{abc} G_{b\mu} G_{c\nu} \tag{1.3}$$

where G^a_μ are the Yang-Mills gluon fields, g_s is the QCD coupling constant, and f^{abc} are the structure constants of SU(3). The fields in the first two terms are similar to those in Quantum Electrodynamics, except that there are 8 gluons rather than 1 photon which mediate the interaction. However, unlike QED, the gluons possess a non-vanishing color charge which is described by the third term in the gluon field strength.

Quantum Chromodynamics provides a description of the strong interaction and the quarks and gluons experiencing this force. Several interesting properties and features of QCD that can be used to test the validity of the Standard Model are described next.

1.3.1 Quarks and Gluons

Quarks possess color charge unlike leptons, and as a result they interact through the strong force. Gluons are the massless gauge bosons of the strong interaction, and interact with the color charge of quarks. However, since gluons also carry color charge, they are able to self-interact as well. This feature of a non-abelian gauge theory greatly complicates the possible interactions in contrast to QED, where the photon carries no electric charge.

There are three color charges a quark can possess, *red* (r), *green* (g), and *blue* (b), and three corresponding anti-colors ($\bar{r}$, $\bar{g}$, and $\bar{b}$) for the anti-quarks. Quarks bind together through the strong interaction to form color-neutral bound-states, known as *hadrons*, through the combination of a quark and anti-quark, known as a *meson*, or through the combination of three quarks or anti-quarks each with different color, known as a *baryon*. Hadrons only exist in color-neutral states because of a property of QCD called *color confinement*, and this is discussed in the following section. This means that the color charge of the constituent quarks in a hadron must combine to a net color charge of zero. Mesons are formed from quark pairs with color and anti-color, such as red and anti-red ($r\bar{r}$), to form a color neutral state. Similarly, baryons are formed from quarks with all three colors (r, g, b) or anti-colors ($\bar{r}\bar{g}\bar{b}$), to form a net color charge of zero. Because hadrons only exist in color neutral states, free quarks and gluons cannot be observed and their properties cannot be directly measured. There are however some features of QCD that make it possible to to study the behavior of quarks and the strong interaction, and test the predictions made by QCD.

1.3.2 The QCD Running Coupling Constant

The QCD interaction strength is parameterized by the renormalized *strong coupling constant* ($\alpha_s \equiv g_s^2/4\pi$). The magnitude of α_s depends on the energy scale or momentum transfer (Q), which is determined by the mass (m) of the gauge boson exchanged in the interaction. The Heisenberg uncertainty principle allows short-lived (*virtual*)

gauge bosons to acquire a mass that may differ from the nominal value, allowing virtual gluons and photons to acquire a non-zero mass. While the value of α_s at a given energy scale cannot be predicted by QCD and relies on experiment, the energy dependence of α_s can be calculated. If the value of α_s is known at a specific energy scale Q, then the energy dependence can be obtained using the QCD renormalization group β-function [14]. To first order, the interaction strength can be written as

$$\alpha_s\left(Q^2\right) \approx \frac{1}{\beta_0 \ln\left(Q^2/\Lambda^2_{\mathrm{QCD}}\right)}, \tag{1.4}$$

where Λ_{QCD} is the QCD scale, $\beta_0 = (33 - 2N_f)/12\pi$ is a positive-definite coefficient, and N_f are the number of active quark flavors, which depends on the energy scale. Higher-order approximations for α_s can be found in [15]. At mass scales approaching the QCD scale, $Q \to \Lambda_{\mathrm{QCD}}$, QCD is strongly coupled. However, as the energy scale increases, $\alpha_s \to 0$ and QCD can be calculated using perturbation theory. The distance of the interaction is inversely proportional to the energy scale, and large-Q^2 interactions signify short distances.

Values for α_s have been obtained from experiment, and recent calculations have used τ-decays, global fits of electroweak data, and measurements of the proton structure function to determine α_s using pQCD calculations up to $O(\alpha_s^4)$ [15]. Measurements of α_s are shown in Fig. 1.1 for a range of energy scales from $Q = 1.78$ GeV to $Q = 209$ GeV. The world average value of the strong coupling constant is evaluated at the mass of the Z boson, and is calculated as $\alpha_s(M_{Z^0}) = 0.1184 \pm 0.0007$ [15]. The measured values of α_s are compared to the QCD predictions using the world average of $\alpha_s\left(M_{Z^0}\right)$ (lines), and the predictions are able to reproduce the experimental data with high precision.

The strength of α_s increases at low energy scales or over long ranges, unlike the electromagnetic force which decreases with increasing separation. As a result, an infinite amount of energy is needed to separate quarks and overcome the strong force. At large enough distances, less energy is required to produce another quark anti-quark pair than to increase the separation distance and additional quark anti-quark pairs

are created (*fragmentation*). This means that quarks can never be isolated and are confined to color neutral bound states. This property of QCD, known as *color confinement*, has so far not been mathematically proven. However it does explains the failure in the search for free quarks, and can be verified using *lattice QCD* (lQCD) which is briefly described in the following section.

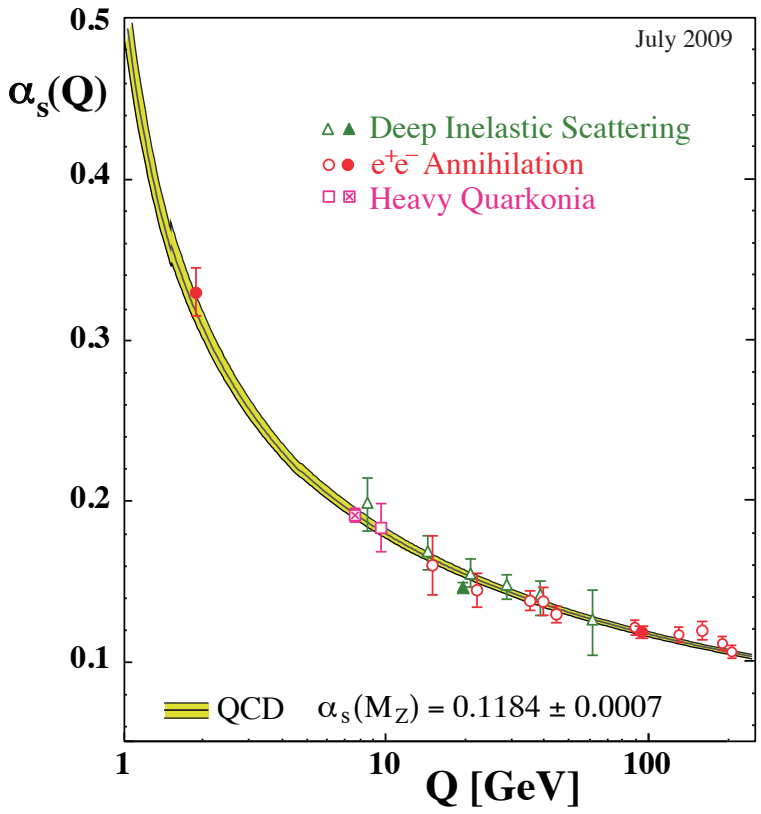

Figure 1.1: The strong coupling constant α_s as a function of the energy scale Q, from various experiments and QCD predictions. Figure taken from [15].

1.3.3 Asymptotic Freedom

The color confinement of quarks inside bound state hadrons means that quarks and gluons cannot be studied in isolation under ordinary conditions, which provides challenges to testing the theory of QCD. However, the strong coupling constant decreases for large energy scales and short distances, as illustrated in Fig. 1.1. Under extreme conditions, $\alpha_s \to 0$ and *Asymptotic Freedom* is achieved, whereby quarks and gluons behave like quasi-free particles.

At sufficiently large energy scales where $\alpha_s \ll 1$, QCD can be calculated perturbatively using *perturbative QCD* (pQCD) [16] by computing a truncated expansion of physical quantities in powers of α_s. Perturbative QCD can only be used where $\alpha_s \ll 1$, and is not valid for $Q < 1$ GeV.

Non-perturbative techniques have been developed to describe low energy scale interactions, such as the fragmentation of quarks and gluons into colorless hadrons (*hadronization*), however the mechanism behind hadronization is still not well understood. The most developed non-perturbative QCD method is that of *Lattice Gauge Theory* (lQCD) [17, 18], which applies field operators to a discrete 4-dimensional space-time lattice of hypercubes. This approach utilizes Monte Carlo methods and numerical simulations, and lattice spacings are varied to understand the sensitivity of the calculations to the lattice size in attempts to approach a continuum limit. This method has been very successful, and has provided accurate predictions for the mass of various hadrons [19] and the value of α_s with a precision of 1% [20]. There are, however, limitations to lQCD, as calculations can only be performed at zero net baryon density, $\mu_B = 0$. Several techniques have been developed to try solve this [21], however none have been successful so far.

Perturbative and lattice QCD provides different tools to calculate physical quantities that can be measured experimentally, which is essential in verifying the validity and success of the Standard Model. There are some limitations to these calculations,

as pQCD can only be used for $Q > 1$ GeV, and lQCD calculations can only be performed for $\mu_B = 0$. Calculations outside of these limits rely on extrapolating from regions where these conditions are met, and the validity of these approximations also requires experimental verification.

1.3.4 QCD Phase Transition

QCD predicts that, under conditions of extremely high temperatures and densities, hadronic matter will undergo a phase transition or crossover to a new form of matter known as *Quark Gluon Plasma* (QGP) [22, 23, 24, 25, 26, 27]. In this new phase, quarks and gluons are *deconfined* from bound states of hadrons and become the relevant color degrees of freedom (`dof`). A phase transition from the ordinary hadronic matter observed in nature to a new phase populated by quarks and gluons is one of the most striking predictions of QCD. Observing this new state of matter would provide strong evidence for the success of QCD and the Standard Model.

Deconfinement results from the screening of the color charge between quarks and gluons in the high density environment, analogous to the Debye screening of electric charge. When the screening radius becomes smaller than the hadron radius, the interaction strength between the quarks is no longer enough to keep them bound. At this point, deconfinement sets in and hadronic matter transitions to a soup of quarks and gluons. Quark Gluon Plasma has never been directly observed, and was expected to exist in the early universe microseconds after the Big Bang [26] when the energy density was sufficiently large.

Lattice QCD predicts a phase transition from hadronic matter to a QGP to occur at a critical temperature T_c, where $T_c \sim 150 - 180$ MeV [28] depending on the methods used for the lattice calculation and temperature extraction. The phase transition is illustrated in Fig. 1.2, where the temperature dependence of the pressure p/T^4 is shown for several flavor configurations (left panel). A sharp increase in the pressure

can be observed around T_c regardless of the number of flavors, and this results from the appearance of the color `dof` of the quarks. The energy density ε/T^4 is shown versus T/T_c (right panel), and the transition can be observed for $T/T_c \sim 1$ where the energy density sharply increases. The arrows indicate the Stefan-Boltzmann limits for massless, non-interacting quarks and gluons.

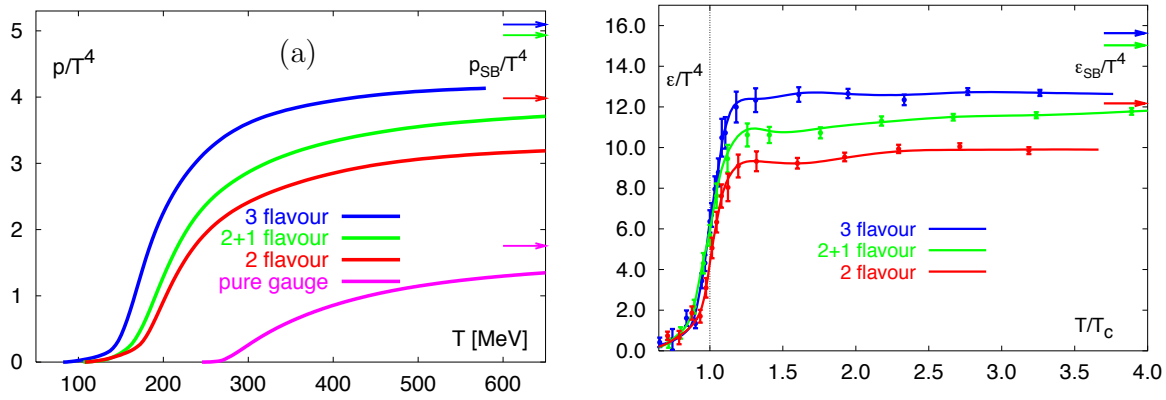

Figure 1.2: The evolution of pressure (left) and energy density (right) for three different flavor configurations. The arrows indicate the SB limits. Figure taken from [28].

The QCD phase diagram is schematically depicted in Fig. 1.3, and is described using the temperature and baryon chemical potential. Ordinary matter exists at low temperature and chemical potential as a hadron gas, and at high temperatures the hadrons melt and a phase transition to a QGP is expected. The results from lattice calculations indicate that at zero net baryon chemical potential, $\mu_B = 0$, the transition from hadronic matter to a quark gluon plasma for $T > T_c$ is a smooth *crossover* (dashed line). At higher μ_B, a *first-order* phase transition is expected [29, 30] (solid line), resulting in the existence of a critical point (circle) in the QCD phase diagram where the transition to a deconfined phase changes from a crossover to a first-order. Calculations indicate that the critical point is expected to exist in the range $250 < \mu_B < 450$ MeV [31, 32].

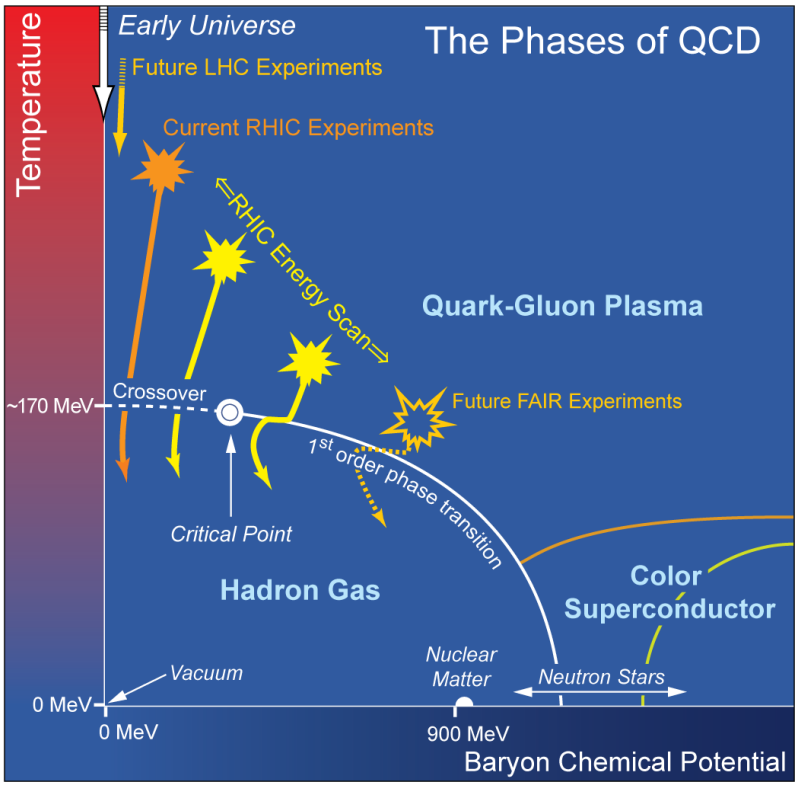

Figure 1.3: The QCD phase diagram, indicating the first order (solid line) and crossover (dotted line) phase transition, critical point (circle), and evolution of several colliders (arrows). Figure taken from [33].

Experiments have been developed to explore the QCD phase diagram and create conditions where the transition to a QGP should be possible in order to test the predictions made by QCD and verify the success of the Standard Model. Various signatures have been suggested to experimentally determine the existence and properties of this new form of matter [34, 35], and these are discussed in the following section.

1.4 Relativistic Heavy Ion Collisions

The *Relativistic Heavy Ion Collider* (RHIC) located at the *Brookhaven National Laboratory* (BNL) was designed and built to exceed the conditions required for QGP formation, and has been successfully colliding heavy ions at relativistic energies since it began operation in 2000. The experimental layout of this facility is described in Chapter 3.

A description of the space-time evolution, energy density, and freeze-out conditions of heavy ion collisions at RHIC are discussed in this section. This is followed by a description of several signatures for the existence of a QGP in heavy ion collisions. A description of useful kinematic variables and other relevant definitions used in heavy ion collisions can be found in Appendix A.

In order to provide further information about the medium created in relativistic heavy ion collisions, the J/ψ vector meson has been extensively studied. This thesis will provide new results on J/ψ production at the STAR detector at RHIC in d+Au and Au+Au collisions at $\sqrt{s_{NN}} = 200$ GeV. These results will be compared to J/ψ production in elementary p+p collisions to determine if there are any modifications from the nuclear environment. A motivation for using heavy quarks to test QCD is provided at the end of this chapter, and a detailed description of J/ψ production in heavy ion collisions is provided in Chapter 2.

1.4.1 Quark Gluon Plasma

The space-time evolution of a heavy ion collision is shown in Fig. 1.4 (right panel). The evolving collision system is shown at various stages for different temperatures/times (right panel), and has been rotated by 90 degrees to schematically describe the various stages of the space-time evolution of the collision. This is only an illustration, and the various stages of the collision do not line up with the edges of any phase in the space-time evolution. The incoming nuclei moving at relativistic speeds are

Lorentz contracted in the direction of motion, forming thin disks. As the nuclei collide, the partons experience *hard* (high-Q^2) interactions in the pre-equilibrium phase from which many particles, including heavy quarks and high-p_T jets, are formed. As the nuclei traverse each other, they create a fireball in which the temperature and density increase and more quark anti-quark pairs are created. As the energy density reaches the critical value, deconfinement sets in and the system undergoes a phase transition to a quark gluon plasma. The pressure of the system causes the fireball to expand, and temperatures and densities begin to decrease until the phase boundary is reached and hadronization occurs. The strong interaction drives the system towards the chemical freeze-out temperature (T_{ch}), after which particle ratios become fixed [36]. This is followed by kinetic freeze-out ($T_{\rm kin}$) after which inelastic collisions cease and particle momenta are fixed [37].

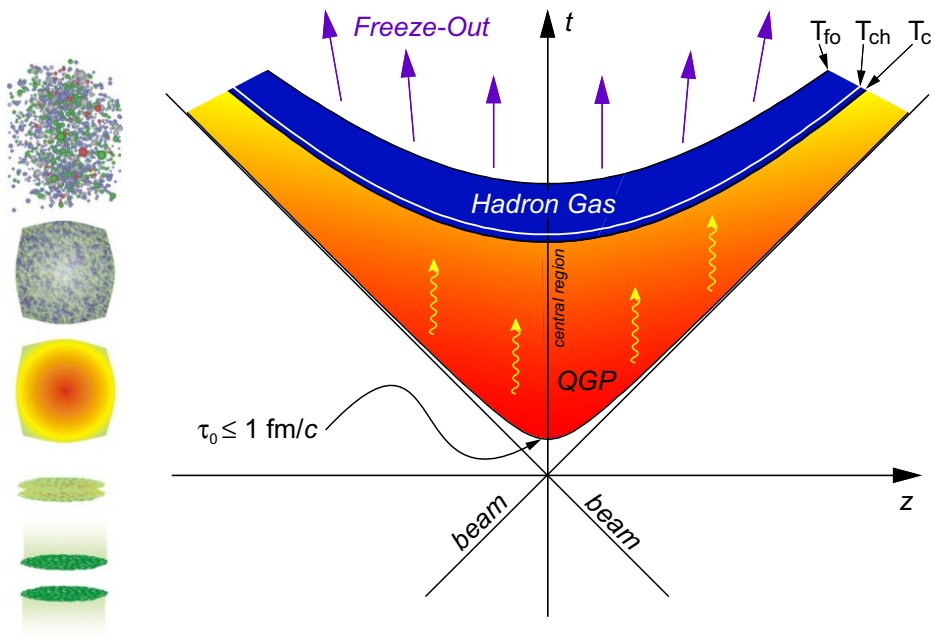

Figure 1.4: The space-time evolution of a heavy ion collision with a phase transition to a quark gluon plasma. Figure taken from [38, 39].

The deconfined state is very short-lived, and hadronization sets in before particles

can be detected. As a result, the quark gluon plasma cannot be directly observed, and indirect methods must be used to infer its properties based on the analysis of hadrons detected in the final state. Strong experimental arguments have been presented to determine whether the conditions created in heavy ion collisions at RHIC exceed those where a phase transition is expected, and indicate that the transition to a QGP has indeed occurred [34, 35]. Some of these features are discussed next.

1.4.2 Initial Energy Density

The formation of a QGP is expected if the energy density exceeds the critical energy density, $\varepsilon_c \gtrsim 1$ GeV/fm^3 [40, 41, 28]. The Bjorken energy density [42] is used as a measure of the peak energy density in created particles, and is defined as

$$\varepsilon_{Bj}(\tau) = \frac{1}{A\tau}\frac{\mathrm{d}E_T(\tau)}{\mathrm{d}y}, \tag{1.5}$$

where A is the area of the overlapping nuclei, τ is the formation time, and $\mathrm{d}E_T(\tau)/\mathrm{d}y$ is the transverse energy per unit of rapidity. The Bjorken energy density is estimated to reach 5.4 GeV/fm^3 at RHIC for $\sqrt{s_{NN}} = 200$ GeV [43], assuming a formation time $\tau = 1$ fm/c. This calculation determines the overlap area of the nuclei using a Monte Carlo simulation and models the nuclei density profile using a Woods-Saxon parameterization, and further details including the values for $\mathrm{d}E_T(\tau)/\mathrm{d}y$ can be found in [44]. However, these estimates for the Bjorken energy require a small crossing time for the nuclei ($\tau < 2R/\gamma = 0.13$ in Au+Au collisions at $\sqrt{s_{NN}} = 200$ GeV at RHIC), and assume a formation time of 1 fm/c without justification. They also rely on a correction to estimate $\mathrm{d}E_T(\tau)/\mathrm{d}y$ from the experimentally measured $\mathrm{d}E_T(\tau)/\mathrm{d}\eta$. As a result, these calculations for the Bjorken energy can only provide an indication for the actual peak energy density.

In order to calculate a more realistic measure of the Bjorken energy density, a lower limit of the measured transverse mass has been used to estimate a formation time of $\tau = 0.35$ fm/c in Au+Au collisions [35], satisfying the condition $\tau > 2R/\gamma$.

Using $\mathrm{d}E_T(\tau)/\mathrm{d}\eta$ rather than an estimaste for $\mathrm{d}E_T(\tau)/\mathrm{d}y$, they obtain a lower limit to the Bjorken energy of $\langle\varepsilon_{Bj}\rangle = 15$ GeV/fm^3. This significantly exceeds the critical energy density required for the formation of a quark gluon plasma, which is estimated to be $\varepsilon_c = 0.7$ GeV/fm^3 for 2-flavor QCD [28].

1.4.3 Temperature and Spectra

The spectra of identified particles has provided abundant information about relativistic heavy ion collisions [34, 35]. The multiplicity density of particles can provide information on the initial gluon density [45], while particle ratios and transverse momentum spectra can be used to measure the chemical and kinetic freeze-out conditions of the collision, respectively [36, 37].

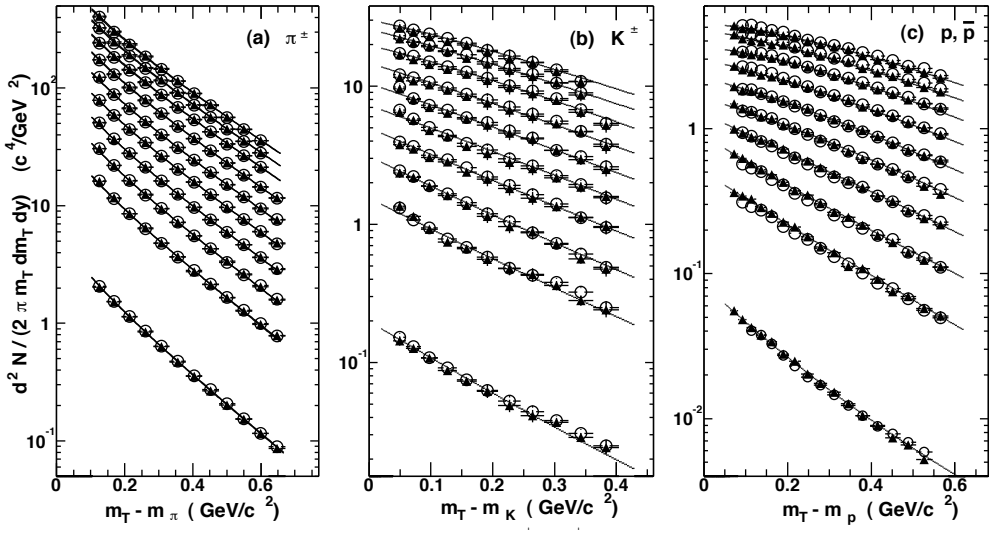

Figure 1.5: The invariant yield versus transverse mass for $\pi^{\pm}$, $K^{\pm}$, p, and $\bar{p}$ in p+p (bottom) and Au+Au 70$-$80% (second bottom) to 0$-$5% (top) at $\sqrt{s_{NN}} = 200$ GeV. Figure taken from [46].

The invariant yield versus transverse mass ($m_T = \sqrt{{p_T}^2 + m^2}$) for identified $\pi^{\pm}$, $K^{\pm}$, p, and $\bar{p}$ at $\sqrt{s_{NN}} = 200$ GeV obtained at the STAR detector at RHIC [46]

are shown in Fig. 1.5 for p+p collisions (bottom), and Au+Au collisions for $0-5\%$ (top), $5-10\%$, $10-20\%$, $20-30\%$, $30-40\%$, $40-50\%$, $50-60\%$, $60-70\%$, and $70-80\%$ (second from bottom) collision centrality. Positively charged particles are shown as open symbols, while negatively charged particles are shown as closed symbols. The proton spectra is scaled by 0.8. The slope of the distributions flattens for heavier particles, which indicates a collectivity of final-state particles increasing with collision centrality.

A hydrodynamically motivated *Blast Wave* [47, 37] model has been used to describe the transverse mass spectra, and is given as:

$$\frac{\mathrm{d}N}{m_T \mathrm{d}m_T} \propto \int_0^R r \mathrm{d}r m_T I_0 \left(\frac{p_T \sinh\rho}{T}\right) K_1 \left(\frac{m_T \cosh\rho}{T}\right), \tag{1.6}$$

where R is the transverse size of the system, I_0 and K_1 represent modified Bessel functions, and T is the freeze-out temperature. The boost angle $\rho = \tanh^{-1}\beta$ depends on the transverse velocity distribution β in $0 \leq r \leq R$, which is parameterized by the surface velocity β_s. The transverse velocity distribution is given as

$$\beta(r) = \beta_s \left(\frac{r}{R}\right)^n, \tag{1.7}$$

where n is treated as a free parameter in [46]. The Blast Wave model has been simultaneously fitted to the $K^{\pm}$, p, $\bar{p}$, and high-p_T ($p_T > 0.5$ GeV/c) part of the $\pi^{\pm}$ spectra with a kinetic freeze-out temperature (T_{kin}) and transverse flow (β) as free parameters [46]. A kinetic freeze-out temperature in $0-5\%$ central Au+Au collisions of $T_{\mathrm{kin}} = 89 \pm 10$ MeV was obtained from the fit.

Thermal models [36, 48, 49] have been used to successfully describe particle ratios observed in heavy ion collisions, and the temperature and baryon chemical potential at freeze-out to be $T_{\mathrm{chem}} = 165 \pm 7$ MeV and $\mu^B_{\mathrm{chem}} = 41 \pm 5$ MeV, respectively [50]. These values depend on the implementation of the thermal model, with some estimates for the temperature reaching 190 MeV. The estimates for the chemical freeze-out temperature are consistent with the critical temperature calculated using lattice QCD. The temperature in the dense fireball created in the initial collision system is

hotter than the temperature at freeze-out, indicating that the critical temperature was exceeded in relativistic heavy ion collisions at RHIC. However, these models do assume that local thermalization of the medium created in heavy ion collisions has been reached, which has not been verified.

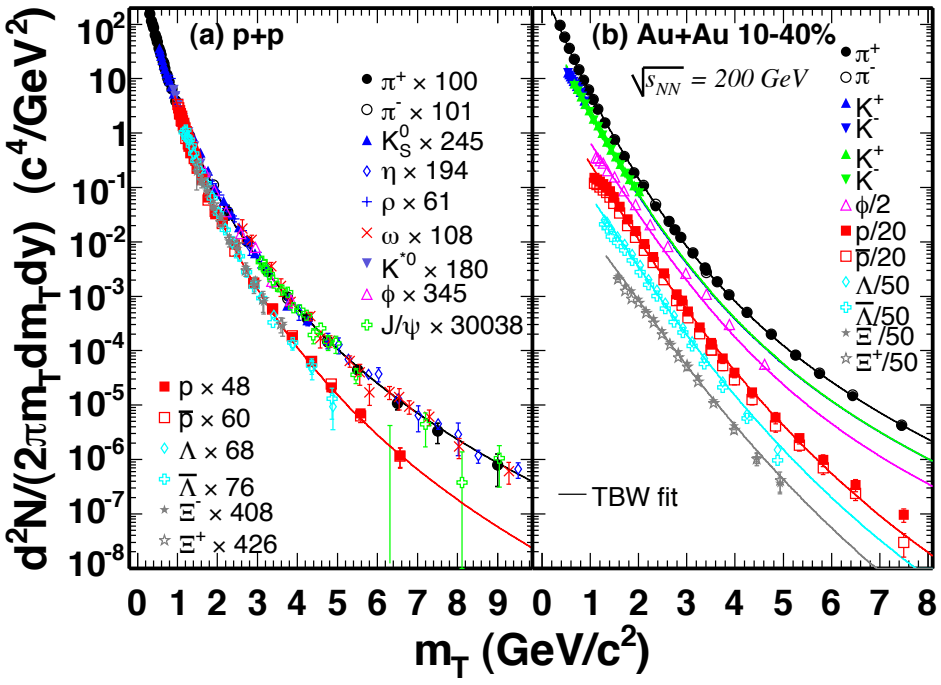

Figure 1.6: The invariant yield versus transverse mass for identified particles in p+p (left) and $10-40\%$ central Au+Au (right) collisions at $\sqrt{s_{NN}} = 200$ GeV with TBW fits. Figure taken from [51].

Blast Wave models assume thermal equilibrium in order to utilize Boltzmann statistics, which is expected to break down at higher p_T where hard processes may dominate. Non-extensive (*Tsallis*) statistics [52, 53] have been used to describe non-equilibrated complex systems, and have been incorporated into a *Tsallis Blast Wave* (TBW) approach, which uses Tsallis statistics and hydrodynamic expansion to describe hadron spectra in p+p and heavy ion collisions in terms of temperature and

flow [54, 51]. The invariant yield for identified particles is shown in Fig. 1.6 for p+p (left) and Au+Au (right) collisions at $\sqrt{s_{_{NN}}} = 200$ GeV at RHIC. The data have been fitted with a TBW model, and a temperature of 128 ± 2 MeV was obtained for $10 - 40\%$ central Au+Au collisions. The centrality dependence of the temperature is described in [54], and very little sensitivity is observed. The TBW model is also able to characterize the degree of thermalization q, where $q = 1$ for a thermalized system. A strong degree of thermalization is observed in $0 - 10\%$ central Au+Au collisions ($q - 1 = 0.018 \pm 0.005$), and this decreases in more peripheral Au+Au and p+p collisions ($q - 1 > 0.06$).

The estimates for the energy density achieved in relativistic heavy ion collisions at RHIC exceed the predicted critical energy density for a phase transition. This, combined with the large system temperatures extracted using thermal and hydrodynamic models, and the high degree of thermalization estimated using the TBW, suggest that the conditions required for a phase transition to a QGP have been reached in relativistic heavy ion collisions at RHIC. Several measurements that suggest the formation of a dense and partonic medium created at RHIC are described next.

1.4.4 Partonic Collectivity

The spatial distribution of colliding nuclei forms an *almond* shape when the nuclei do not overlap completely. This initial spatial anisotropy is converted into a momentum anisotropy due to the differential pressure gradients in the expanding volume. The pressure is largest along the minor axis of the interaction region, and this differential pressure gradient creates a force on the particles. This results in higher momentum particles in the direction that the pressure is greatest. This is illustrated in Fig. 1.7, where nuclei traveling along the z-axis have collided to form the hot almond-shaped collision zone, which contains the participant nucleons ($N_{\rm part}$) of the collision.

The momentum anisotropy, known as *flow*, is determined by decomposing the

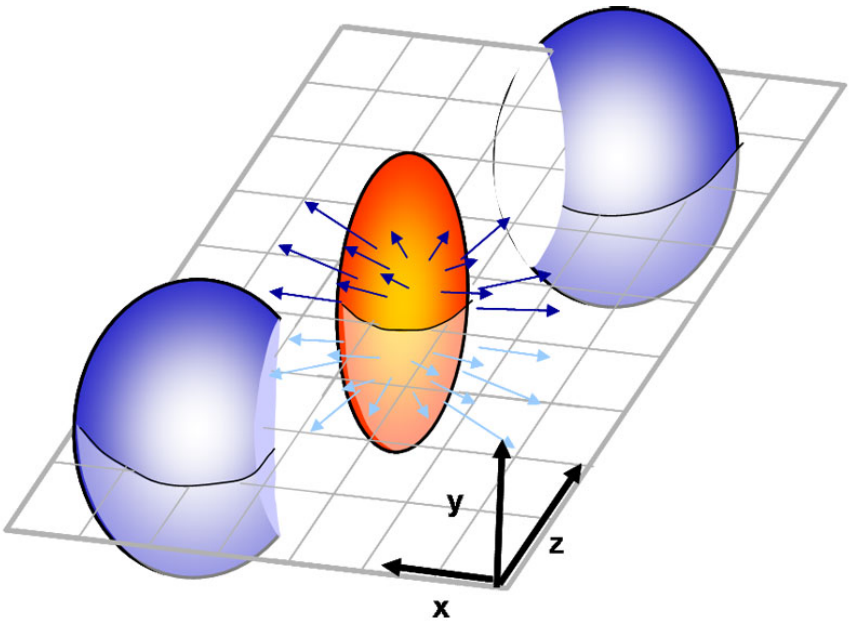

Figure 1.7: A cartoon of a non-central collision. Participant nucleons in the almond-shaped overlap region experience a force from the pressure gradient, while the spectator nucleons continue along the beam axis z. Figure taken from [55].

observed final-state particle distribution into a Fourier expansion, where

$$E\frac{\mathrm{d}^3N}{\mathrm{d}p^3} = \frac{\mathrm{d}^2\mathrm{N}}{2\pi p_T \mathrm{d}p_T \mathrm{d}y}\left(1+\sum_{n=1}^{\infty} 2v_n \cos\left(n\left[\phi-\Psi_{RP}\right]\right)\right). \tag{1.8}$$

The coefficients v_n are defined as:

$$v_n = \langle \cos\left(n\left[\phi-\Psi_{RP}\right]\right)\rangle, \tag{1.9}$$

where Ψ_{RP} is the reaction plane angle in the transverse plane defined by the impact parameter vector of the colliding nuclei. The second harmonic coefficient v_2 (*elliptic flow*) is the largest at midrapidity. The elliptic flow is developed in the early stages of the collision where the pressure gradients are the largest, and provides information about the early collision system and the degree of thermalization.

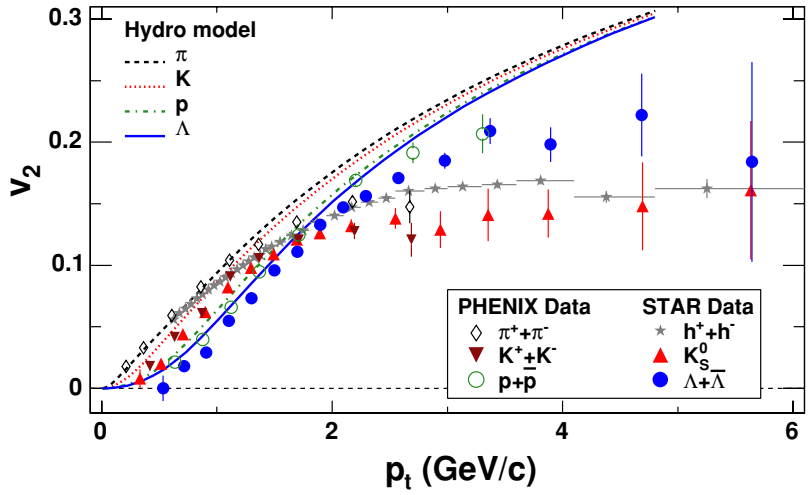

Figure 1.8: The elliptic flow v_2 versus p_T for identified particles in Au+Au collisions at $\sqrt{s_{NN}} = 200$ GeV. Figure taken from [56].

The elliptic flow v_2 has been measured at RHIC, and the results are shown for various identified particles in Au+Au collisions at $\sqrt{s_{NN}} = 200$ GeV in Fig. 1.8. The results have been compared with hydrodynamic models [56], which assume ideal fluid flow and a relaxation time much less than the equilibration time. The hydrodynamic models describe the observed mass-ordering at low-p_T reasonably well, where heavier particles exhibit a smaller flow. The v_2 increases with p_T and saturates above $2-3$ GeV/c. The results indicate a strong collectivity of the early collision system, and the agreement with the hydrodynamic models suggests a highly collective and strongly-interacting medium created in heavy ion collisions at RHIC.

There is an observed difference between the v_2 of baryons and mesons, similar to that observed in the particle spectra shown in Fig. 1.5. The v_2 of particles has been scaled by their number of constituent quarks n_q (2 for mesons, 3 for baryons), and this is shown in Fig. 1.9 (top panel). The ratio of the data to a polynomial fit is also shown (bottom panel), and the results are consistent for different particles with $p_T/n_q > 0.6$ GeV/c, except for pions which are affected by resonance decay effects.

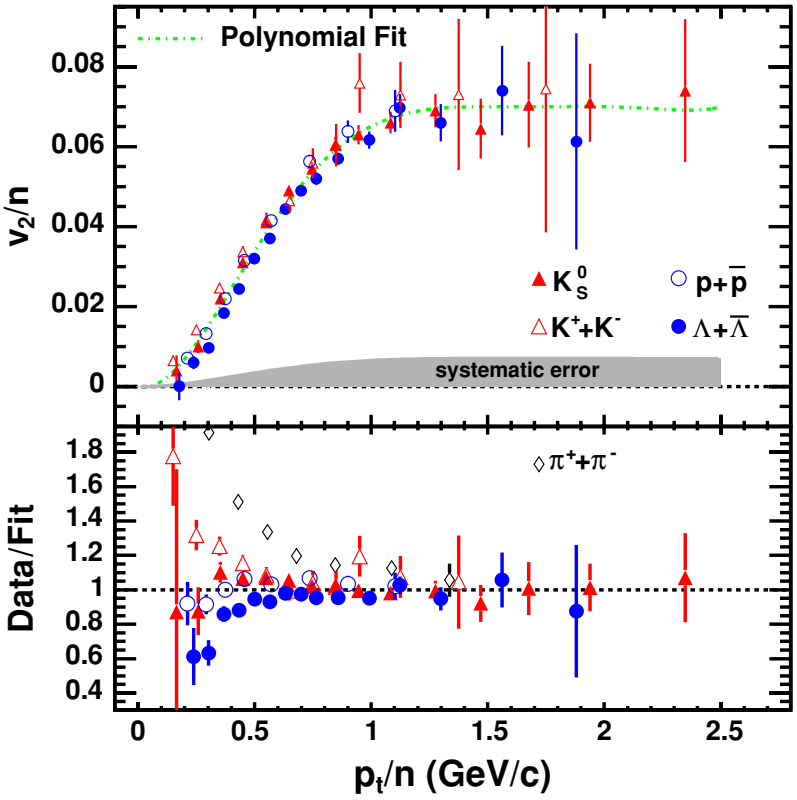

Figure 1.9: The elliptic flow v_2 versus p_T for identified particles in Au+Au collisions at $\sqrt{s_{NN}} = 200$ GeV. Figure taken from [56].

This phenomenon of scaling with the number of constituent quarks (n_q) can be explained by coalescence models [57, 58, 59], which describe the production of hadrons through the coalescing of its constituent quarks from the medium. This suggests that flow is developed in the partonic stage of the collision where quarks are the relevant degrees of freedom, and provides strong support for the creation of a deconfined medium in heavy ion collisions at RHIC.

1.4.5 Energy Loss

Studies of the medium created in heavy ion collisions are performed by observing either the effect of the medium on particles whose properties can be well understood from calculations or elementary p+p collisions where modifications from nuclear matter are not present. High-p_T partons ($p_T \gtrsim 5$ GeV/c) in heavy ion collisions are expected to be created primarily from the initial hard scattering process. This means they can be calculated using perturbative QCD, and provide information on the evolution of the collision system. The fragmentation of high-p_T partons results in a cluster of correlated hadrons known as *jets*, which can be used to probe the matter created in heavy ion collisions by studying how they are modified from their interaction with the medium compared to elementary collisions. High-p_T partons traversing the partonic medium are expected to lose energy from elastic parton scattering and, more significantly, gluon radiation. Such energy loss would result in the softening and broadening of the observed jet structure, known as *jet quenching*.

The *nuclear modification factor* R_{AB} is used to compare experimental observables in the collision system $A + B$ with respect to a reference measurement, generally obtained from p+p collisions at the same energy:

$$R_{AB} = \frac{1}{T_{AB}} \frac{\mathrm{d}^2 N_{AB}/\mathrm{d}p_T\mathrm{d}y}{\mathrm{d}^2\sigma_{pp}/\mathrm{d}p_T\mathrm{d}y}, \tag{1.10}$$

where $T_{AB} = \langle N_{\mathrm{coll}}\rangle/\sigma_{\mathrm{inel}}^{\mathrm{pp}}$ is the nuclear overlap function which takes into account the inelastic cross section in p+p collisions ($\sigma_{\mathrm{inel}}^{\mathrm{pp}}$) and the mean number of nucleon-nucleon collisions in $A + B$ ($\langle N_{\mathrm{coll}}\rangle$). The production of particles originating from the initial hard scattering of the collision is expected to scale with the number of nucleon-nucleon collisions, resulting in $R_{AB} = 1$ if there are no medium modifications.

The nuclear modification factor for charged particles in central Au+Au and d+Au collisions at RHIC [60] is shown versus p_T in Fig. 1.10 (left panel), and some modification is observed in d+Au due to the presence of nuclear matter in the collision system. Very little modification is observed between minimum bias and central d+Au,

despite the increased amount of nuclear matter participating in the collision. However, the conditions required for a phase transition in d+Au are not achieved, even in central collisions. The modification factor decreases significantly in central Au+Au collisions, where $R_{AA} \sim 0.2$ at high-p_T. This implies modifications in addition to any effects from ordinary nuclear matter also present in d+Au collisions, indicating that the suppression in central Au+Au collisions is a final-state effect on jet production resulting from the high density environment.

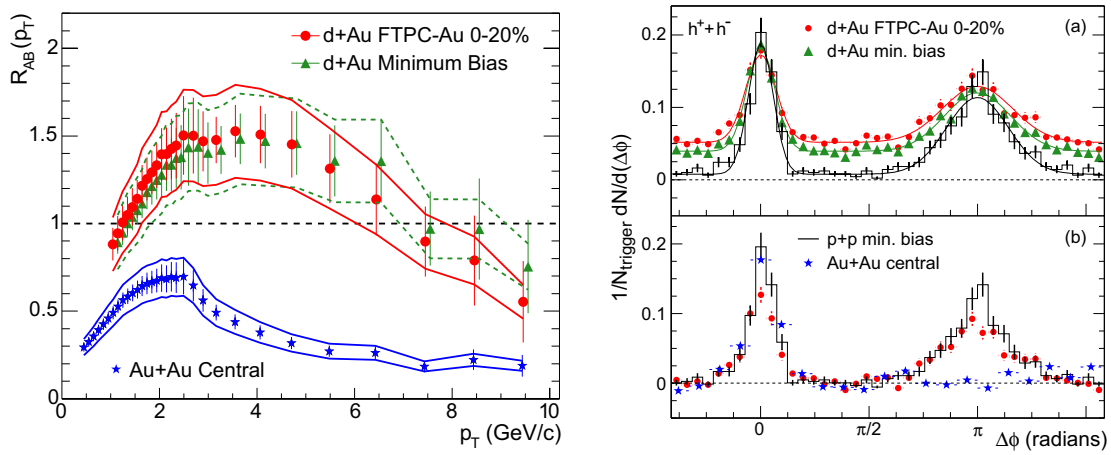

Figure 1.10: Left: R_{AB} in minimum bias d+Au, central d+Au, and central Au+Au. Right: the dihadron azimuthal correlation in p+p, d+Au, and Au+Au collisions. Figure taken from [60].

To understand how the jets are modified, the dihadron azimuthal correlation ($\Delta\phi$) has been measured, where $\Delta\phi = \phi_{\text{Trig.}} - \phi_{\text{Assoc.}}$ is the difference in the azimuthal angle between the trigger hadron and an associated hadron. This is shown in Fig. 1.10 (right panel) for trigger hadrons with $p_T > 4$ GeV/c associated with hadrons of $p_T > 2$ GeV/c [60]. The distribution in p+p exhibits a near-side ($\Delta\phi \sim 0$) peak from jet fragmentation pairs, and an away-side ($\Delta\phi = \pi$) peak from back-to-back pairs. A similar distribution is observed in d+Au, and a slight broadening of the away-side peak is observed from partonic rescattering. The $\Delta\phi$ distribution obtained in central

Au+Au collisions is compared to the results in p+p and d+Au, and the far-side peak in Au+Au is not observed. This is consistent with the jet quenching scenario in which jets experience medium induced energy loss, leading to the production of soft particles below the threshold for associated hadrons. The away-side jets will traverse more of the dense medium, resulting in a suppression of the associated away-side hadrons above the threshold of $p_T > 2$ GeV/c.

1.4.6 Heavy Quarks

Heavy quarks provide a unique tool to probe the medium created in relativistic heavy ion collisions. They are produced primarily in the initial hard scattering of the collision and provide information about the early collision system. Because of their large mass, the production of heavy quarks can be described using pQCD. They are often studied via their leptonic and semileptonic decays, which provide a clean signal as the leptons do not interact strongly with the medium.

The heavy quark anti-quark energy can be parameterized according to the separation distance (r) between the quarks, and is described using the effective Cornell potential,

$$V(r) = \frac{-\alpha}{r} + \sigma r, \tag{1.11}$$

where α is related to the strong coupling constant [61]. The first term arises from single-gluon exchange, and is analogous to the Coulomb potential between electric charges. The second term is associated with confinement, and increases linearly with distance. While light quarks move relativistically, the static Cornell potential can be applied to heavy quarks which are non-relativistic in the hadron rest frame.

In the asymptotic freedom regime where $\alpha_s \to 0$, the potential decreases with increasing temperature. This is illustrated in Fig. 1.11, where the heavy quark anti-quark free energy has been calculated as a function of distance for various temperatures using lattice QCD with three flavors. The bands indicate the Cornell potential

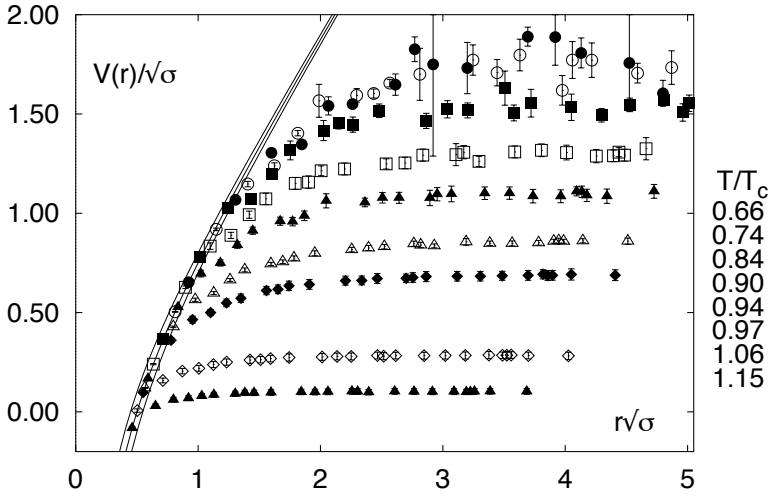

Figure 1.11: Lattice QCD predictions for the temperature dependence of the heavy quark anti-quark free energy for three flavors. Figure taken from [28].

for $\alpha = 0.25 \pm 0.05$ [28]. At a fixed temperature, the heavy quark free energy increases with increasing distance, resulting in the confinement of quarks inside hadrons. However, at high temperatures the quark energy becomes more flat as a function of the quark separation, and less energy is required to free the quarks (color screening). A suppression of heavy quark anti-quark mesons (*quarkonium*) is expected at high temperatures and densities in the presence of a quark gluon plasma, and has been suggested as a signature for the onset of deconfinement [62].

This thesis will present new results on the production of the ground state $c\bar{c}$ vector meson, $J/\psi(1S)$. A description of the J/ψ production mechanism and possible modifications to production in heavy ion collisions are provided in Chapter 2.

Chapter 2

J/ψ Production

The suppression of J/ψ in heavy ion collisions was initially suggested as an unambiguous signature for the formation of a quark gluon plasma [62], therefore providing a direct test of QCD and the Standard Model. This was expected to arise due to color screening in the deconfined medium, which prevents the binding of the $c\bar{c}$ pair. The bound state melts when the Debye screening radius, which depends on the temperature of the system, becomes smaller than the J/ψ radius. Excited $c\bar{c}$ bound states have a smaller binding energy and larger radius and are expected to be dissociated at a lower temperature, thus providing an effective thermometer of the collision system.

Various measurements of J/ψ have been performed in different collision systems and at different energies, and indeed a suppression of J/ψ production in heavy ion collisions has been observed [63, 64, 65]. The J/ψ nuclear modification factor measured at SPS [66] in Pb+Pb collisions and In+In collisions at $\sqrt{s_{_{NN}}} = 17.3$ GeV, and in S+U collisions at $\sqrt{s_{_{NN}}} = 19.4$ GeV, and at PHENIX [67] in Au+Au collisions with a collision energy of $\sqrt{s_{_{NN}}} = 200$ GeV, are shown in Fig. 2.1 versus the number of participant nuclei in the collision. A significant suppression at midrapidity was observed, with R_{AA} reaching $0.2 - 0.4$ in the most central collisions. A similar amount of suppression was observed at SPS and RHIC, despite the increase in collision energy by more than a factor of 10 at RHIC. Furthermore, a larger suppression at forward-rapidity compared to midrapidity was observed at RHIC. These observations indicate

that effects other than color screening are contributing to J/ψ production.

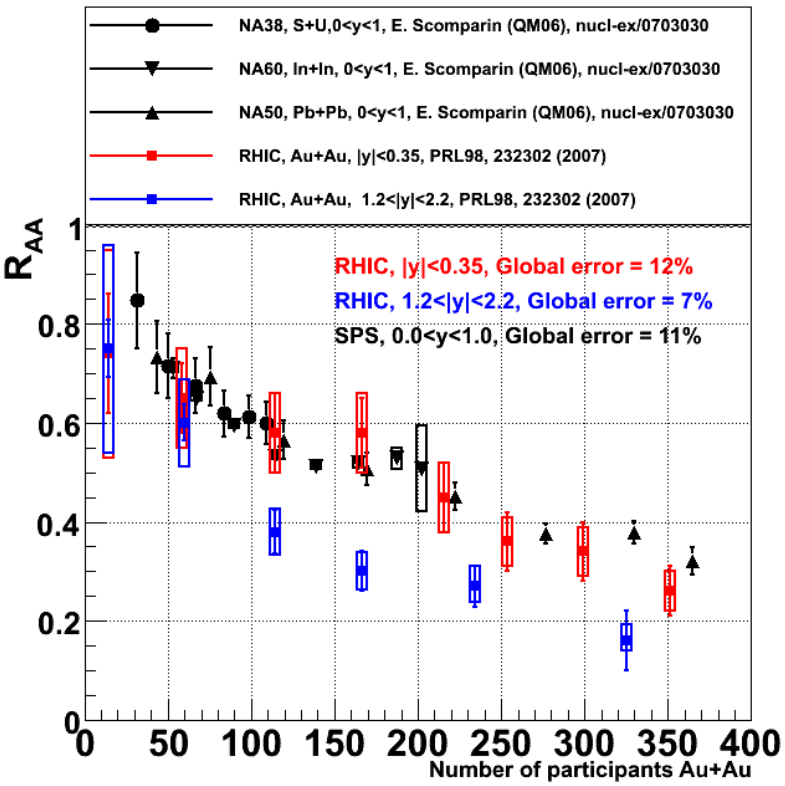

Figure 2.1: The J/ψ nuclear modification factor in Pb+Pb collisions and In+In collisions at $\sqrt{s_{NN}} = 17.3$ GeV at NA50 and NA60, respectively, in S+U collisions at $\sqrt{s_{NN}} = 19.4$ GeV at NA38, and in Au+Au collisions at $\sqrt{s_{NN}} = 200$ GeV at RHIC, as a function of the number of participant nuclei. Figure taken from [68].

The interpretation of J/ψ production in heavy ion collisions is not straightforward, and all possible contributions must be assessed to determine if there are modifications from a QGP phase. The production of J/ψ in p+p collisions provides information on the unmodified J/ψ production mechanism, and while various models have tried to describe J/ψ production, no current model is able to explain all of the J/ψ data. Some of these models are described in Section 2.1. The yields in p+p collisions are

also used as a baseline measurement to determine if there are modifications to production rates in heavy ion collisions.

Modifications to J/ψ production in heavy ion collisions may exist due to the presence of ordinary nuclear matter (*cold nuclear matter*) even if there is no QCD phase transition, and this is described in Section 2.2. To determine if the suppression observed at RHIC is from the presence of a quark gluon plasma, cold nuclear matter effects are studied using d+Au collisions where nuclear matter is present but conditions for a phase transition are not achieved.

Several sources of modification to J/ψ production from a QGP phase have been suggested, and these are described in Section 2.3. The production of J/ψ in d+Au and Au+Au collisions at $\sqrt{s_{NN}} = 200$ GeV is presented in this thesis. The production in d+Au collisions is used to quantify the magnitude of cold nuclear matter effects, and these are subtracted from the production in Au+Au collisions to determine if there are additional modifications to J/ψ production from a QGP phase. Necessary information to understand the production of J/ψ in heavy ion collisions is presented in this chapter.

2.1 Production Mechanism

The production of the heavy $c\bar{c}$ pair in p+p collisions can be calculated using perturbative QCD. The momentum fraction of the parton relative to the proton, knwon as Bjorken x, can be calculated from the momentum transfer of the interaction and the beam energy, where $x \sim (Q^2/s)^{1/2}$. The proton *parton distribution function* (PDF) is shown in Fig. 2.2 versus Bjorken x for $Q^2 = 10$ GeV^2. The distribution is dominated by gluons at low x, which is the region probed by RHIC.

The formation of J/ψ from a $c\bar{c}$ pair is less well understood, and arises from several contributions. Prompt production arises from the direct formation of a $c\bar{c}$ into a J/ψ

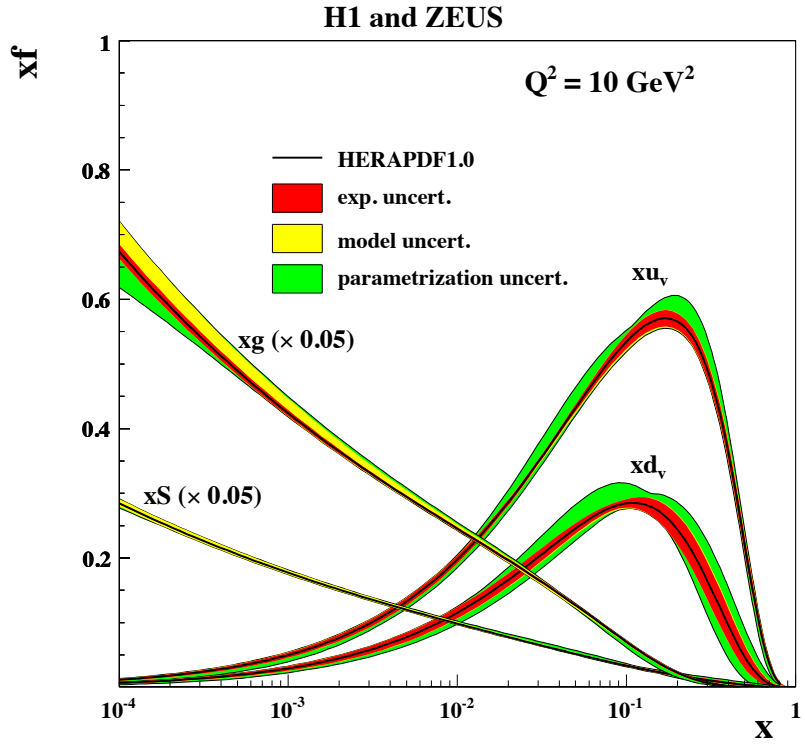

Figure 2.2: The parton distribution functions at $Q^2 = 10$ GeV^2. The distributions are shown for the gluons (g), sea quarks (S) (both scaled down by 20), valence up quarks (u_v), and valence down quarks (d_v). Figure taken from [69] .

bound state in the initial hard scattering of the collision. This also includes indirect contributions from excited states which feed to the J/ψ, such as ψ' and χ_c. In p+p collisions, the contribution from ψ' and χ_c is expected to be $\sim 10\%$ and $\sim 30\%$, respectively [70, 71]. Non-prompt J/ψ production arises from $B \rightarrow J/\psi$ decays, which are estimated to be $\sim 10 - 25\%$ for $p_T > 5$ GeV/c, decreasing at lower p_T [72].

Various models have been used to describe the J/ψ production mechanism, and a detailed review of these can be found in [63]. The *Color Singlet* model (CSM), *Color Octet* (COM) model, and *Color Evaporation* model (CEM) are among the most popular, and provide predictions for the production cross sections. The hadronization

of the charm anti-charm quark pairs is treated non-relativistically due to their large mass compared to $\Lambda_{\rm QCD}$. The production of J/ψ is factorized into the relativistic charm anti-charm production which can be determined using pQCD, and the non-relativistic term describing the bound-state.

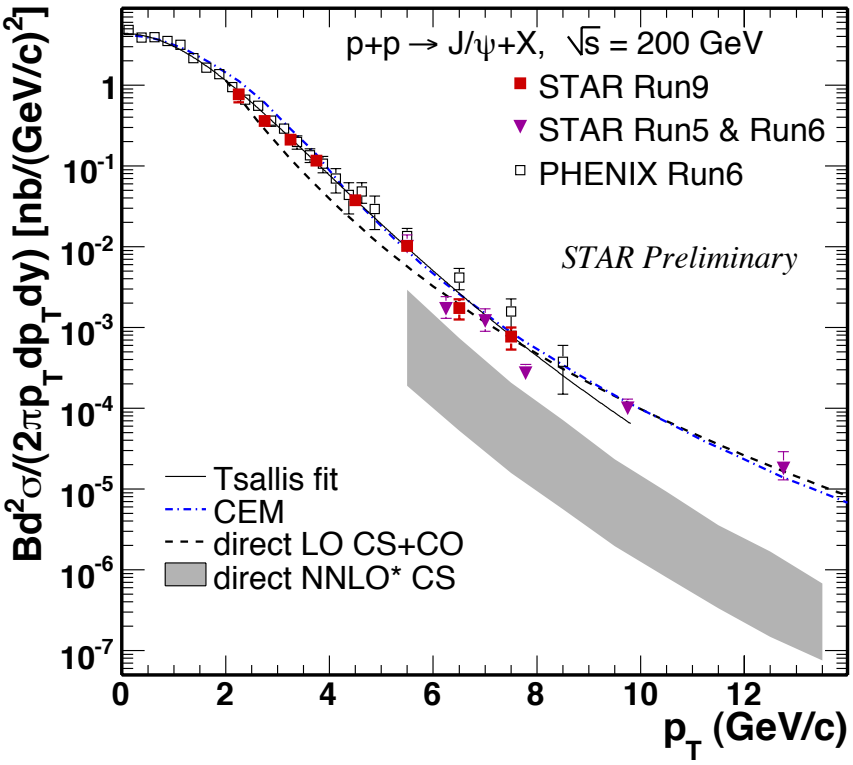

Figure 2.3: The J/ψ p_T spectrum in p+p collisions at $\sqrt{s_{NN}}$ = 200 GeV [73, 74]. The results are compared to various model predictions.

The Color Singlet model (CSM) [75, 76] assumes that the $c\bar{c}$ are formed in a color-singlet state, and the spin and color of the quarks remains unchanged in forming the J/ψ. This model can predict the J/ψ *polarization* (spin-alignment) and cross section without any free parameters, however the value of the polarization is sensitive to the order of the calculation. Leading order CSM predictions were able to successfully describe J/ψ from photo- and hadro-production at lower energies [77, 75],

however it was not able to reproduce the data observed at higher energies. Higher order calculations have improved the agreement, however the predictions significantly under-estimate the high-p_T yield at RHIC in p+p collisions at $\sqrt{s_{NN}} = 200$ GeV [76], as shown in Fig. 2.3. The data are for inclusive J/ψ, while the CSM predictions are for directly produced J/ψ. However the expected contribution from resonances and B decay are not a significant enough contribution to resolve the large discrepancy between the model and data.

The J/ψ polarization measured in p+p collisions at $\sqrt{s_{NN}} = 200$ GeV is shown in Fig. 2.4, and the data are compared to CSM predictions for prompt J/ψ at NLO, which are unable to constrain the polarization very well given the current uncertainties. The precision in the data is currently limited, and the nature of the J/ψ polarization is still not accurately known. Contributions from feed-down in the data further complicate the interpretation of the results.

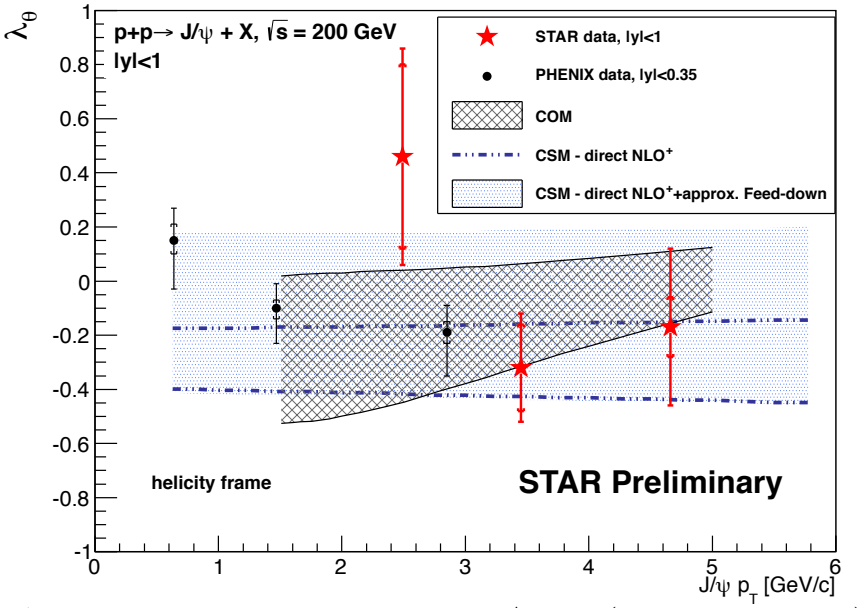

Figure 2.4: The J/ψ polarization in p+p collisions at $\sqrt{s_{NN}} = 200$ GeV [78].

The Color Octet model (COM) was developed in the framework of *Non-Relativistic QCD* (NRQCD). This approach allows for the formation of charmonium in a color-octet state, and a color-singlet state is reached through soft gluon radiation. The COM provided an improved agreement to the data compared to the CSM, and can describe the J/ψ results obtained at RHIC reasonably well across the p_T range [79], shown in Fig 2.3. However, the COM calculation shown in Fig. 2.3 does not include feed-down from resonances and B decays. Resonances are expected to contribute up to 40%, while B feeddown is estimated to increase with p_T and reach $10-25\%$ at high p_T [72]. The COM also predicts a transverse polarization of the J/ψ spin ($\lambda \sim 1$), however the uncertainties on the theory and experimental data of the polarization shown in Fig. 2.4 are too large to constrain this value precisely. This comparison may also be affected by the contributions from resonances in the data.

The Color Evaporation model (CEM) [80, 81, 82, 83] describes the non-relativistic binding term using a constant, and the $c\bar{c}$ pair is summed and averaged over all the color and spin states with the color-singlet state reached through soft gluon emissions. The CEM does not make a prediction for the J/ψ polarization, which is a useful test of charmonium production. While limited, this approach does provide a prediction for the cross section shape and agrees reasonably well with data. The J/ψ p_T spectrum in p+p collisions at RHIC is shown in Fig. 2.3, and the CEM (dot-dashed blue line) shown in Fig 2.3 is able to reproduce the J/ψ p_T spectrum in p+p collisions at RHIC reasonably well [84]. While this CEM calculation does not include B feed-down, this effect is negligible on a decade scale.

In summary, none of the J/ψ production mechanisms provide a complete description of the data. The CEM is able to reproduce measurements from hadron collisions reasonably well, but does not include B feed-down. In addition, it does not provide predictions for the J/ψ polarization, which can be used as a crucial test of the production mechanism. The CSM does make predictions for the polarization, and while these are not strongly constrained they are consistent with the data. However, the

CSM significantly under-estimates the measured J/ψ cross section. The COM provides a better description of the cross section, however it leaves very little room for feed-down contributions. Furthermore, it predicts a transverse polarization for the J/ψ, which is not seen in the data.

2.2 Cold Nuclear Matter Effects

In order to identify the modification to J/ψ from the presence of a quark gluon plasma, all other nuclear effects need to be understood and quantified. *Cold Nuclear Matter* effects from the presence of nuclear matter in the initial-state and final-state of heavy ion collision as compared to p+p can modify the production of J/ψ. These effects do not arise from a QCD phase transition, and must be quantified to determine the effects of a quark gluon plasma on J/ψ production in heavy ion collisions. This is done experimentally using $p+\mathrm{A}$ and $\mathrm{d}+\mathrm{A}$ collisions where the formation of a QGP is not possible but nuclear matter is present. The modifications of cold nuclear matter on J/ψ production are separated into initial- and final-state effects.

Initial-State Effects

The parton distribution functions within a proton, as shown in Fig. 2.2, are modified by the presence of nuclear matter and cannot be treated as a superposition of nucleons. The modification of the *nuclear Parton Distribution Function* (nPDF), is defined by the ratio

$$R_i(x, Q^2, A) = f_i^A(x, Q^2)/A \cdot f_i^p(x, Q^2), \tag{2.1}$$

where the Bjorken x is the fraction of the nucleon momentum carried by parton i, Q^2 is the momentum transfer, A is the nucleus size, and f_i^A and f_i^p are the parton distributions in a nucleus and proton, respectively. The modification of parton densities has been measured by probing quark distributions in DIS experiments from e+A and $e+p$ collisions [5, 6], and from π^0 charged-hadron correlations in d+Au collisions at RHIC [85]. Drell-Yan measurements have also been used to provide information on

the anti-quark densities. Since gluons do not carry electromagnetic charge, the gluon distributions cannot be measured directly and are poorly constrained [86]. Since J/ψs are produced primarily via gluon fusion, their production is sensitive to the modification of the gluon nPDF. As a result, there is some uncertainty in the expected modification to J/ψ production from the modified nuclear parton distribution functions.

The modification of the nPDFs for gluons in a gold nucleus relative to a proton is shown in Fig. 2.5 for $Q^2 = m^2_{J/\psi}$. The distribution has been obtained using various parameterizations of the parton distribution functions (nDS, nDSg [87], EKS98 [88], HKN [89], EPS08 [90]), and these exhibit sizable differences. The shaded boxes indicate the x range probed by various experiments, with RHIC shown at the bottom and covering $0.02 \lesssim x \lesssim 0.1$. The region probed by RHIC is dominated by a suppression of the gluon distribution (*shadowing*), however there are large uncertainties on the magnitude of this effect depending on the nPDF used. Recently, the EPS09 [86] calculations have been performed using a global analysis of the nPDFs at LO and NLO, including a detailed error analysis which was not present in the other calculations.

There are other initial-state modifications to J/ψ production, including multiple parton scattering (*Cronin Effect*) [92] and partonic energy loss. However, shadowing is expected to be the dominant initial-state modification from CNM to J/ψ production at RHIC [86].

Final-State Effects

The J/ψs created in heavy ion collisions at $\sqrt{s_{NN}} = 200$ GeV are produced primarily in the initial partonic hard scattering of the collision, and are exposed to the subsequent evolution of the collision system. As they traverse the nuclear medium, they experience inelastic collisions with nucleons in the dense collision system. The *nuclear absorption* [91, 93] of J/ψ refers to the break-up of the $c\bar{c}$ pair from the surrounding nuclear medium. The nuclear absorption cross section for J/ψ ($\sigma_{\rm abs}$) measures the rate at which J/ψs are destroyed from inelastic collisions with nucleons, and increases

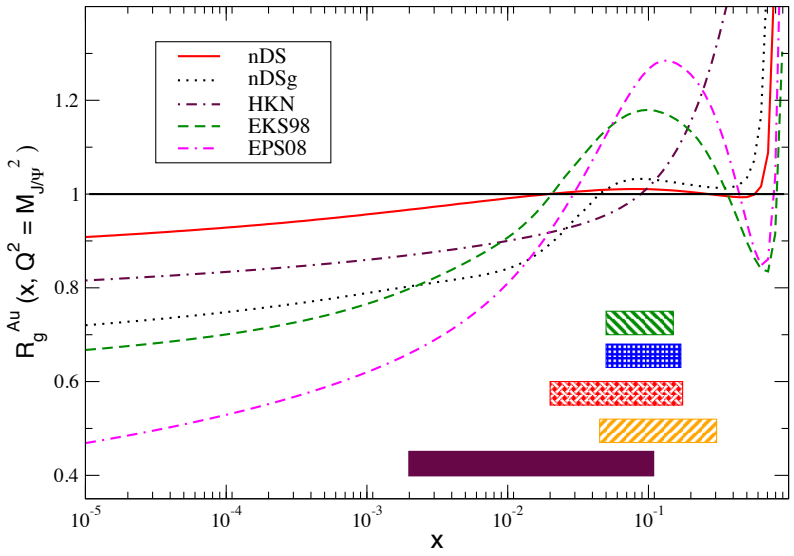

Figure 2.5: The ratio of the gluon distribution in gold relative to a proton versus Bjorken x for $Q^2 = m^2_{J/\psi}$. The boxes indicate the range of x probed by each experiment from bottom to top: RHIC, HERA-B, FNAL, SPS, NCM. Figure taken from [91].

with the increase of nucleon number. The nuclear absorption of J/ψ is implemented by weighting the J/ψ production cross section with a survival probability $S^{\rm abs}$, such that [93]

$$S^{\rm abs}\left(\vec{b}-\vec{s},z'\right) = \exp\left\{-\int_{z'}^{\infty} {\rm d}z''\rho_A\left(\vec{b}-\vec{s},z''\right)\sigma_{\rm abs}\left(z''-z'\right)\right\}, \qquad (2.2)$$

where z' is the longitudinal production point, z'' is the absorption point, and ρ_A is the nucleon density in a nucleus A. The nuclear absorption cross section is expected to have a strong dependence on the J/ψ kinematics and decrease with increasing collision energy [94]. Values of the absorption cross section have been extracted from various data sets using the EPS08 [90] parameterization, and this is shown in Fig. 2.6 versus collision energy (left) and parton momentum fraction (right). There are large uncertainties on the absorption cross section from most experiments.

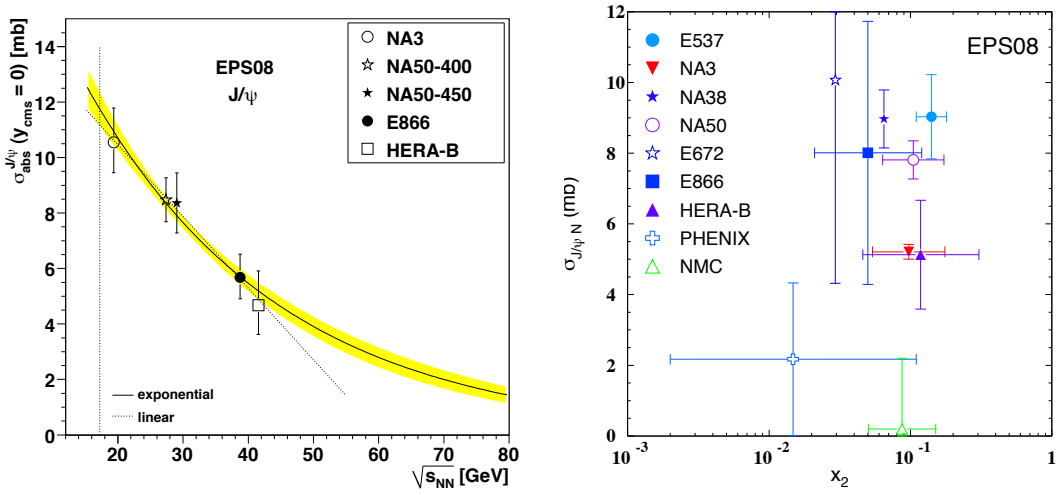

Figure 2.6: The J/ψ nuclear absorption cross section from various experiments extracted using EPS08 as a function of collision energy (left) and momentum fraction (right). Figure taken from [91] and [94].

The absorption of J/ψ from other particles has been described by the *Comovers Interaction Model* [95, 96], and has been used to explain the J/ψ suppression observed in heavy ion collisions at SPS [66] without any contributions from a QCD phase transition [97]. However this effect is challenging to experimentally separate from nuclear absorption, and the absorption cross section generally combines these effects.

There are large uncertainties on the magnitude of cold nuclear matter effects to J/ψ production, and quantifying these effects relies primarily on experiment. The production of J/ψ in d+Au collisions is presented in this thesis to determine the magnitude of cold nuclear matter effects on J/ψ production. The results are compared to predictions for shadowing obtained using the EKS98 [88], nDSg [87], and EPS09 [86] parameterizations of the nPDFs, which are used to determine the J/ψ nuclear absorption cross section [98, 99] in d+Au. The cold nuclear matter effects are compared to the modification of J/ψ in Au+Au collisions from the same experimental configuration to determine if there is an additional suppression of J/ψ production in

Au+Au collisions that can be attributed to a QGP phase.

2.3 Hot Nuclear Matter Effects

To determine if there is any suppression of J/ψ production in relativistic heavy ion collisions arising from the onset of deconfinement, all sources of possible modification to J/ψ production in addition to cold nuclear matter effects must be explored. In the initial formulations of J/ψ suppression, the $c\bar{c}$ bound state were produced very early in the collision and were subsequently exposed to the hot suppression zone of the collision system. However, if the prompt $c\bar{c}$ pair only forms a resonant state later on relative to the formation and lifetime of the QGP, they may be able to escape suppression from the hot and dense medium (*leakage* [100]). While there is no clear picture of the J/ψ formation time relative to the QGP formation, the p_T dependence of J/ψ production may provide some information on this, as faster J/ψs are more likely to escape the suppression zone.

The regeneration of J/ψ from the statistical coalescence of charm quarks in the QGP sea may also contribute to the observed J/ψ yield. This was suggested to explain the similar suppression patterns observed at SPS and RHIC [66, 67] despite the increase in collision energy, as the increased regeneration from the larger charm quark density could compensate for the additional suppression from color screening. This also explains why RHIC observes a stronger suppression at forward rapidity where the charm quark density is lower. The J/ψs from the coalescence of charm quarks in the QGP sea will populate midrapidity and low p_T, in contrast to direct J/ψ production from the initial hard scattering which generally have a higher p_T. Furthermore, the contribution from regeneration will be more significant in central collisions where the charm quark density is highest. These kinematic expectations provide tools to observe the contributions from regeneration and leakage, and disentangle them from the suppression due to color screening.

In order to understand these effects and quantify a modification of J/ψ due to the formation of a quark gluon plasma, the production of J/ψ has been studied in Au+Au collisions at $\sqrt{s_{NN}} = 200$ GeV at the STAR detector at RHIC for J/ψ with $p_T < 10$ GeV/c and $|y| < 1$. The centrality and p_T dependence of J/ψ production in Au+Au collisions have been used to investigate the evolution of the modifications with energy density, and to separate recombination at low-p_T from leakage effects at high-p_T. These results are compared to the cold nuclear matter effects calculated in d+Au collisions using the same kinematics and experimental setup to determine if there are any modifications to J/ψ production from a deconfined QCD phase. The results are also compared to model predictions which account for the various modifications to J/ψ production discussed in this chapter.

2.4 Thesis Outline

A brief overview of particle physics, the Standard Model, and Quantum Chromodynamics has been provided. Some properties of QCD have been described, the most interesting of which is the expected transition from hadronic matter to a quark gluon plasma phase. The conditions required for the formation of a QGP have been discussed, and results obtained from RHIC have been used to verify that these conditions are met in relativistic heavy ion collisions at $\sqrt{s_{NN}} = 200$ GeV.

In order to test the predictions of QCD, the J/ψ meson has been used as a probe of the medium created in heavy ion collisions. While a suppression of J/ψ production is expected in the presence of a QGP, modifications from cold nuclear matter effects need to be constrained before this effect can be quantified. This thesis will present the analysis of J/ψ in d+Au and Au+Au collisions at the STAR detector. The cold nuclear matter effects calculated from d+Au will be compared to the production of J/ψ in Au+Au collisions to determine if there are modifications from a QGP phase.

The next chapters provide an overview of the experimental facility and detectors

used in the analysis of J/ψ in d+Au and Au+Au at the STAR detector at RHIC, followed by a description of the data and analysis methods. The results obtained for J/ψ production in d+Au and Au+Au at $\sqrt{s_{NN}} = 200$ GeV at STAR are then discussed. The dielectron mass spectrum is presented, followed by the efficiency-corrected p_T spectrum and nuclear modification factor as a function of J/ψ p_T and collision centrality. The results are compared to other measurements and theoretical models of J/ψ production in order to determine if there are modifications relative to p+p collisions from the nuclear environment. Finally, the uncertainties associated with the analysis methods are discussed, and a summary is given. Supporting documents, including a description of useful kinematic variables in heavy ion collisions, are provided in the Appendix.

The analysis of J/ψ production at STAR presented in this thesis is my own work. I have calculated the p_T spectrum and nuclear modification factor in d+Au and Au+Au collisions for $|y| < 1$ and $p_T < 5$ GeV/c at $\sqrt{s_{NN}} = 200$ GeV/c as a function of transverse momentum and collision centrality, and these results are presented in Chapter 5. This is the first analysis of J/ψ at low p_T in d+Au collisions at STAR, and the first high-statistics analysis of low p_T J/ψ in Au+Au collisions at STAR. The calculation of the J/ψ nuclear modification factor in d+Au and Au+Au collisions at STAR uses the J/ψ cross section in p+p collisions at STAR. The J/ψ cross section in p+p collisions at STAR has been calculated by other authors, and a description of these analyses can be found in [72, 101]. The results in Au+Au collisions have been combined with high-p_T ($3 < p_T < 5$ GeV/c) data from STAR to extend the coverage of J/ψ production to $p_T < 10$ GeV/c. The high-p_T results have been calculated by another author, and a description of this analysis can be found in [72].

Chapter 3

Experimental Setup

3.1 The Relativistic Heavy Ion Collider

The Relativistic Heavy Ion Collider (RHIC) is located at the Brookhaven National Laboratory in New York, USA. Until November 2010, when the Large Hadron Collider (LHC), located at the Conseil Européen pour la Recherche Nucléaire (CERN) in Geneva, Switzerland, began to collide heavy ions, RHIC was the most powerful heavy ion collider in the world, capable of accelerating a variety of particle species to ultrarelativistic speeds. The primary goal of the heavy ion program at RHIC is to produce a new form of matter, Quark Gluon Plasma (QGP), and to study Quantum Chromodynamics (QCD) at high energies and temperatures. RHIC is also able to collide spin-polarized proton beams, and is still the most powerful polarized-proton collider.

The RHIC facility is shown in Fig. 3.1. The 3.8 km circumference RHIC tunnel houses an intersecting two-ring superconducting hadron collider. Protons are injected directly into the pre-existing Alternating Gradient Synchotron (AGS) from the 200 MeV linac, while heavy ions are first partially stripped and accelerated to 1 MeV/c using the Tandem Van de Graaff accelerator, sent through the Tandem-to-Booster line to the Booster Synchrotron, further stripped and accelerated, and injected into the AGS. The ions are stripped of their remaining electrons, and ions/protons are

Figure 3.1: The RHIC facility located at the Brookhaven National Laboratory [33].

bunched together and accelerated to 10.8 GeV/A and transferred to RHIC. In the RHIC storage rings, the counter-rotating beams are steered and accelerated with the use of superconducting magnets, and intersect at six collision points on the ring. Heavy ions are accelerated to a maximum center-of-mass energy of $\sqrt{s_{NN}} = 200$ GeV per nucleon, and protons to $\sqrt{s_{NN}} = 500$ GeV. In addition, RHIC can also collide heavy ions at lower energies. This has been utilized by the recent Beam Energy Scan (BES) program at RHIC, which has collided Au+Au ions at various energies from $\sqrt{s_{NN}} = 7.7$ GeV to $\sqrt{s_{NN}} = 62.4$ GeV. Since RHIC has independent rings and ion sources, it can also collide unequal ion species, such as d+Au and Cu+Au. The acceleration pattern for gold ions at the RHIC facility is shown in Fig. 3.2

The initial performance specifications for the RHIC luminosity were 2×10^{26} cm^{-2}s^{-1} for Au+Au, and 1.4×10^{31} cm^{-2}s^{-1} for protons [102]. There have been various improvements to the facilities [103], such as stochastic cooling [104], which have increased

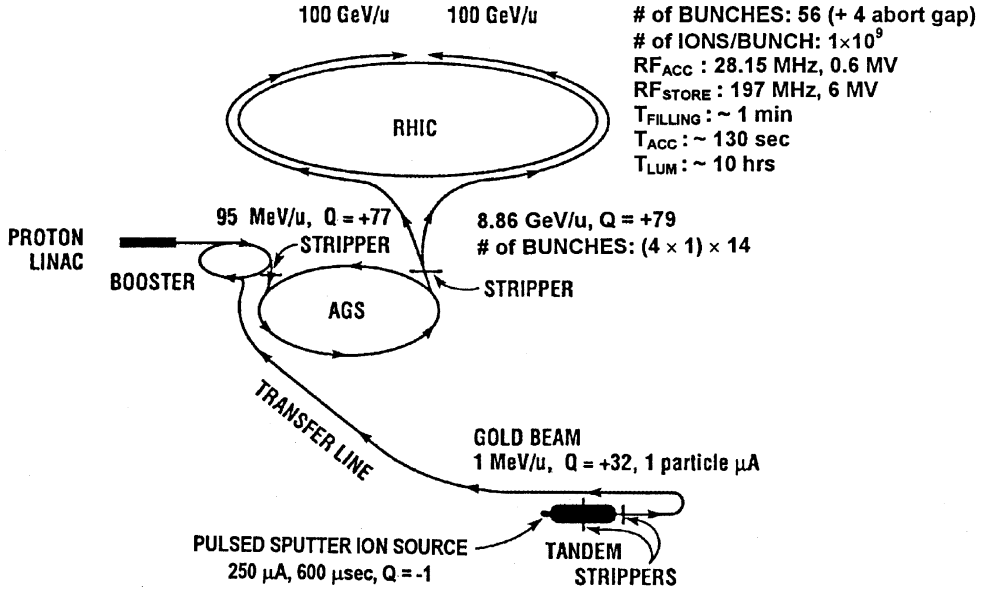

Figure 3.2: The RHIC acceleration pattern for gold ions. Figure taken from [102].

the average luminosity for Au+Au to 30×10^{26} cm^{-2}s^{-1}, and peak luminosity for p+p to 4.6×10^{31} cm^{-2}s^{-1} [105]. More details on the RHIC facility can be found in [102].

Over the years, RHIC has collided p+p, d+Au, Cu+Cu, and Au+Au, using isotopes $^{63}_{29}$Cu and $^{197}_{79}$Au for the heavy ion beams. In 2012, RHIC collided for the first time Cu+Au and U+U ($^{238}_{92}$U) at $\sqrt{s_{NN}} = 200$ GeV, exploring new energy densities and eccentricities. There is a planned upgrade to eRHIC, an electron-ion collider [106], which will further expand the range of collision species, and increase the range of momentum fraction (x) that can be probed at RHIC.

The RHIC project houses experiments at four of the collision points: STAR [55], PHENIX [107], BRAHMS [108], and PHOBOS [109], with only STAR and PHENIX currently in operation. The STAR detector, located at 6 o'clock on the ring, is described below.

3.2 The Solenoidal Tracker at RHIC

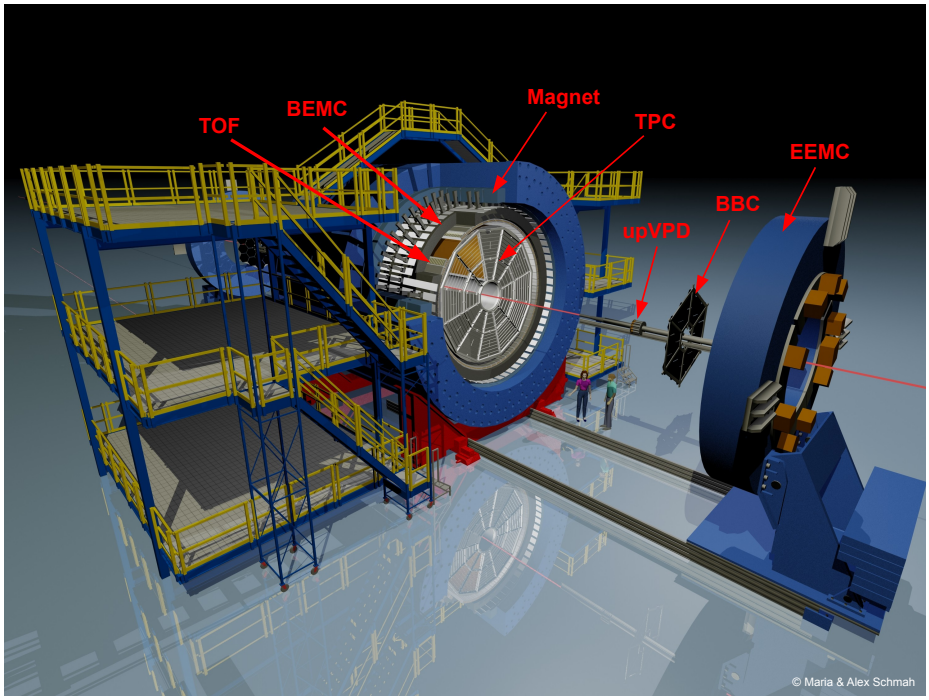

Figure 3.3: The STAR detector at RHIC. Figure taken from [33].

The Solenoidal Tracker at RHIC (STAR) is a multi-purpose large-acceptance detector, covering an azimuthal angle of $0 < \phi \leq 2\pi$ and tracking capabilities out to pseudorapidity $|\eta| < 1.8$ [110]. The STAR detector comprises of various subsystems, shown in Fig. 3.3.

Prior to 2008, the innermost detectors of STAR were the Silicon Vertex Tracker (SVT) [112] and Silicon Strip Detector [113], which provided tracking capabilities close to the beam line and improved the secondary vertex reconstruction resolution. These have been removed and the low-material Heavy Flavor Tracker (HFT) [114, 115], which will provide inner tracking using the existing SSD along with the Intermediate Silicon Tracker (IST) and the PIXEL detector, is scheduled to be installed and

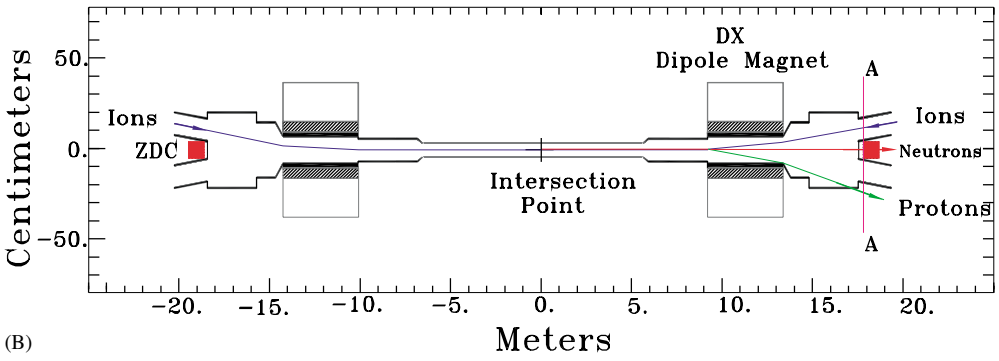

Figure 3.4: The STAR ZDCs located outside of the RHIC dipole magnets. Figure taken from [111].

operational by 2014. Surrounding the inner detectors is the Time Projection Chamber (TPC) [116], the Time Of Flight (TOF) [117], and the Barrel Electromagnetic Calorimeter (BEMC) [118], all of which have full azimuthal coverage at midrapidity. In addition, there are several forward detectors, such as the Endcap Electromagnetic Calorimeter (EEMC) [119], Beam-Beam Counter (BBC), Photon Multiplicity Detector (PMD) [120], Forward Pion Detector (FPD), Forward Muon Spectrometer (FMS), and Forward Time Projection Chamber (FTPC) [121] which was decommissioned in 2010. The STAR magnet [122] surrounds the central subsystems with an outer radius of 7.32 m and a length of 6.85 m, and is capable of producing a uniform magnetic field (B) of 0.25 T (half field) and 0.5 T (full field) along the beam axis. The primary Vertex Position Detector (pVPD) [123], shown in Fig. 3.3, and Zero Degree Calorimeter (ZDC) [124], shown in Fig. 3.4, are located outside of the STAR magnetic field.

The primary detectors used in this analysis are the TPC, TOF, and BEMC. In addition, the pVPD, ZDC, and BBC are used for event triggering and beam monitoring, and the FTPC is used for forward tracking and measuring collision centrality in d+Au collisions. These detectors are discussed below.

3.2.1 Time Projection Chamber

The Time Projection Chamber, described in detail in [116], is the heart of the STAR detector and provides tracking in $0 < \phi \leq 2\pi$ and $|\eta| < 1.8$. It is a 4.2 m long cylinder with an inner radius of 0.5 m and an outer radius of 2 m. It is filled with P10 gas, which contains 10% methane and 90% argon, and is regulated at 2 mbar above atmospheric pressure. Separating the East and West hemispheres of the TPC is the central membrane, which is held at a voltage of -28 kV. The endcaps are instrumented with multi-wire proportional chambers (MWPC) and are grounded. In combination with the concentric inner and outer field-cage cylinders, the endcaps and central membrane create a uniform electric field of ~ 135 V/cm. This setup is illustrated in Fig. 3.5.

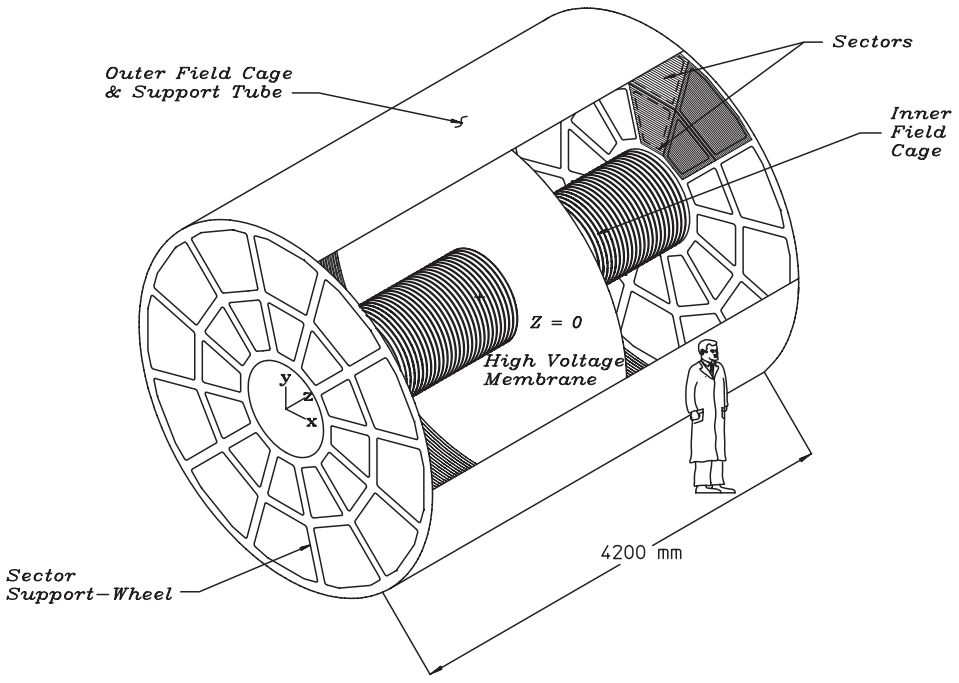

Figure 3.5: The STAR Time Projection Chamber. Figure taken from [116].

Charged particles that traverse the volume of the TPC will ionize atoms in the P10 gas. The ionization electrons drift towards the endcaps at a constant velocity of ~ 5.45 cm/μs, resulting in a maximum drift time in the TPC of ~ 40 μs. The endcaps are split into 12 sectors, each with 45 pad rows. Each sector consists of an inner and outer sector with 13 and 32 pad rows, respectively. The sector coordinates describe the local x as along the direction of the pad row, local y as perpendicular to the pad row and pointing from the beam line outwards, and z as along the beam axis. The inner pad dimensions are chosen to optimize the (x, y) position resolution of the ionization electron deposition, and differ from the outer sectors because of the higher track densities at smaller radius. The outer sectors have continuous pad coverage to optimize the resolution of the energy deposited by the ionization electrons.

The arrival time of the ionization electrons is determined relative to the collision time to calculate the z position of the particle. This, combined with the (x, y) position obtained from the sectors, provides tracking for charged particles in the TPC. The ionization energy loss per unit length, $\mathrm{d}E/\mathrm{d}x$, is obtained from the energy of the ionization electrons, and is used for particle identification. The layout of a single sector is described in Fig. 3.6, and details of the TPC readout system can be found in [125]. The tracking and particle identification capabilities of the TPC are described below.

Tracking

The tracking is performed using the reconstructed spatial hits from the pad rows. The (x, y) position of ionization clusters is determined by the charge measured by adjacent pads within a pad row. The z position of a cluster is determined by measuring the drift time of ionization electrons relative to the start of the collision, and dividing this by the average drift velocity. To accurately determine the z position, the drift velocity must be precisely known. To minimize variations of the drift velocity, the cathode voltage is set so that the electric field corresponds to the peak drift velocity.

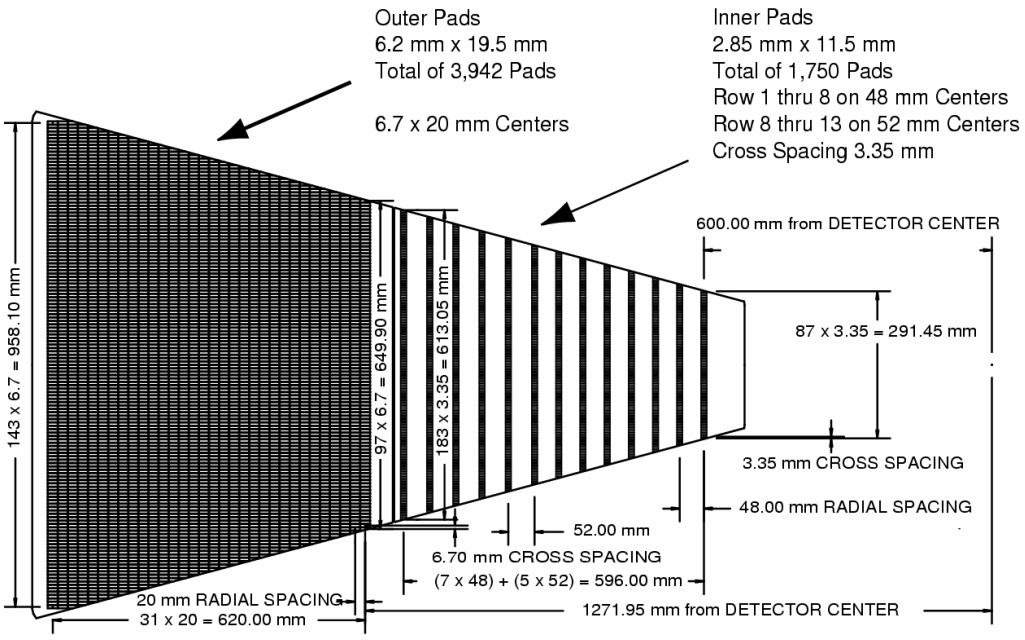

Figure 3.6: A full sector of the anode pad plane on the TPC. Figure taken from [116].

This means the drift velocity is less sensitive to pressure and temperature fluctuations. In addition, every few hours during data taking the drift velocity is measured using laser beams [126]. These create artificial tracks that do not bend in the presence of a magnetic field. The position resolution of the tracking depends primarily on the number of ionized electrons and their diffusion in the gas.

The reconstructed position of the hits can be affected by various factors, and distortions from the high radiation environment as well as the relative and global alignment of the TPC sectors are studied and calibrations are applied to correct for these effects [127]. The tracking algorithm is used to associate the reconstructed spatial hit points to form tracks. To first order, the track is described by a helix, with the direction of the curvature determined by the charge of the particle, and the magnitude of curvature determined by the transverse momentum of the particle. However, due to second order effects such as energy loss, trajectories slightly deviate from the helix.

Since tracks may originate from the primary vertex (located near the center of the detector), from a secondary decay vertex, or even from out-of-time (pile-up) events, the STAR tracker [128] does not assume a particle origin. The association of tracks to a common vertex is done after the tracking is complete, and uses the reconstructed tracks to determine the vertex position. The canonical Kalman filter [129] is used to calculate track parameters and form tracks from the hits. It does so by starting towards the outer layers of the TPC, where track densities are smaller and there is less ambiguity in track formation. This begins with a track seed, which is identified as a collection of a few hits. The Kalman filter then extrapolates inwards along the approximate direction and curvature obtained from the hit distribution. It looks to match hits in the next layer based on a radius of confidence determined by the error on the parameters of the track. A nearby hit is associated if the χ^2 of the track is below some maximum, and for multiple matches, the hit resulting in the smallest χ^2 is chosen. The Kalman track model is then used to determine an updated curvature and direction to extrapolate to the next layer, with each additional hit improving the precision of the track parameters. The tracking stops once the inner-most layer is reached, and the fit is redone to improve the parameters of the outer-most hits. Hits from the TPC are combined with information from inner tracking systems, if they are available, and the Kalman filter matches hits across all active detector layers and must take into account energy loss and multiple Coulomb scattering across the TPC inner field cage. Once the initial tracking is complete, the filter attempts to merge tracks that have been split due to sector boundary effects.

Tracks can have a maximum of 45 hits, however this maximum depends on the curvature and pseudorapidity of the track and can be affected by inactive regions in the detector. These effects, combined with hit merging and losses across sector boundaries, result in a tracking efficiency of $\sim 80 - 90\%$ in p+p and peripheral Au+Au collisions. This has been determined using Monte Carlo simulations, and is shown for π^+ with $|y| < 0.7$ in Au+Au collisions with $B = 0.25$ T for several collision centralities in Fig. 3.7. The tracking efficiency decreases in more central events due to the increased difficulty in resolving hits in the high occupancy environment. Below

200 MeV/c, the tracking efficiency decreases as tracks may not reach the outer field cage under the curvature of the magnetic field.

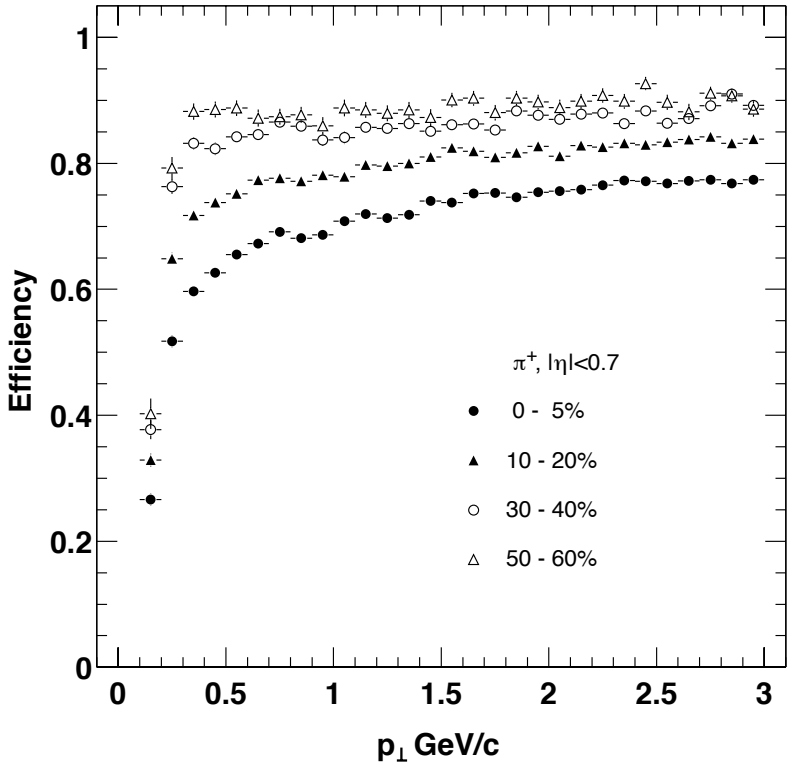

Figure 3.7: The tracking efficiency for π^+ with $|y| < 0.7$ in Au+Au collisions with a magnetic field strength of 0.5 T. Figure taken from [116].

Tracks are required to have at least 10 hits in the pad rows to remove split tracks and ensure a precise track reconstruction. The complete collection of tracks, known as *global tracks*, are used to determine the vertex position of the collision. This is done by extrapolating all the tracks in the TPC to the origin and finding the global average. The vertex reconstruction methods vary depending on the collision environment. The Pile-up Proof Vertexer (PPV) is used in p+p collisions, and performs a 1-dimensional truncated log-likelihood method to determine the z-position of the vertex. In A+A

collisions, the Minuit Vertex Finder (MinuitVF) is used, which determines the vertex position by minimizing the distance of closest approach (DCA) for all tracks [130]. The vertex position resolution depends on the number of tracks used in the vertex finding, and the dependence is shown in Fig. 3.8. Tracks within 3 cm of the vertex position are associated to the vertex and are known as *primary tracks*.

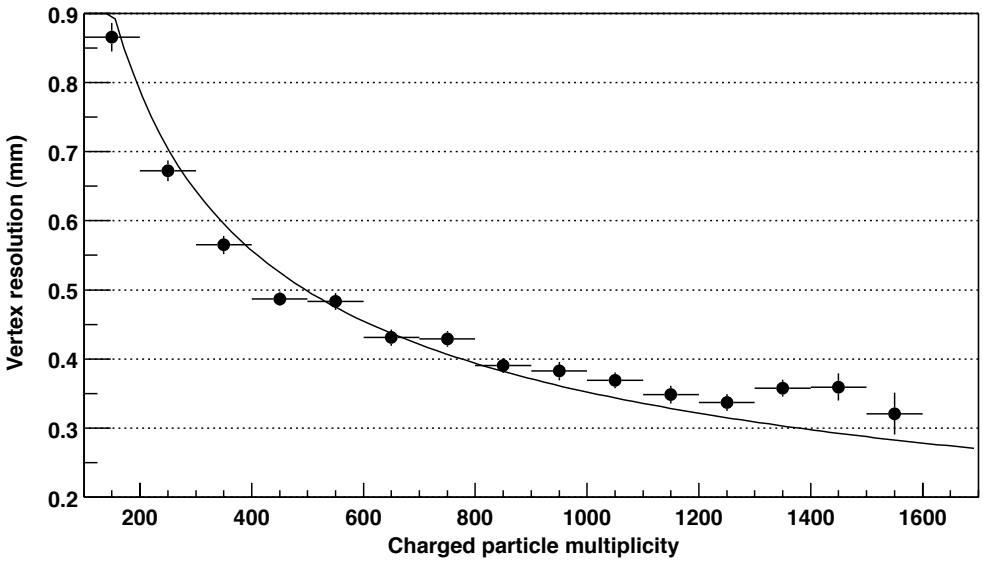

Figure 3.8: The primary vertex resolution in the $x - y$ plane versus the charged particle multiplicity in the TPC. Figure taken from [116].

The primary vertex position is added to the collection of hit points for the primary tracks, and the track fitting is performed again. The additional constraint of the vertex position improves the transverse momentum resolution ($\Delta p_T/p_T$) of the primary tracks. The transverse momentum resolution for π^- and $\bar{p}$ with more than 15 hits is shown versus transverse momentum in Fig. 3.9. This has been obtained using Monte Carlo simulations embedded into real minimum bias collisions in a 0.25 T magnetic field. The resolution is dominated by multiple Coulomb scattering at low-p_T. At higher p_T the track curvature dominates the resolution, and linearly increases with p_T.

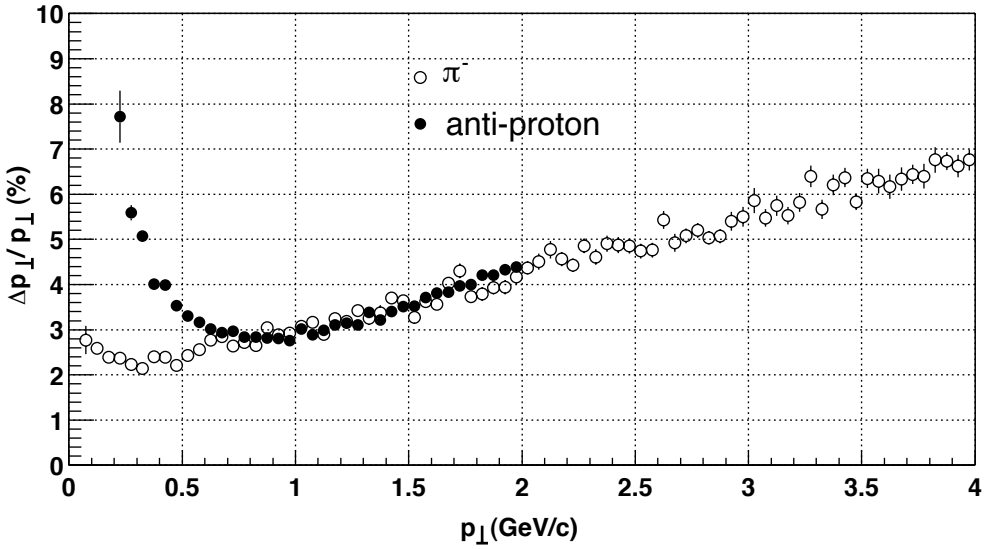

Figure 3.9: The transverse momentum resolution for π^- (open circles) and $\bar{p}$ (closed circles) with greater than 15 hits. Results were obtained using a Monte Carlo simulation for minimum bias collisions with $B = 0.25$ T. Figure taken from [116].

Particle Identification

The ionization energy loss ($\mathrm{d}E/\mathrm{d}x$) is measured from the charge collected by the TPC pad rows, and a track can have a maximum of 45 $\mathrm{d}E/\mathrm{d}x$ hits. The $\mathrm{d}E/\mathrm{d}x$ measurement capabilities are limited by finite track length and ionization fluctuations. To reduce fluctuations, the truncated mean of the $\mathrm{d}E/\mathrm{d}x$ hits is calculated, which rejects the 30% highest $\mathrm{d}E/\mathrm{d}x$ values.

The energy loss for charged particles as a function of momentum in Au+Au collisions is shown in Fig. 3.10. The most probable $\mathrm{d}E/\mathrm{d}x$ for charged particles in the TPC is obtained from the Bichsel functions [13, 131, 132], and these are indicated (symbols). The hadrons obey a mass ordering of the $\mathrm{d}E/\mathrm{d}x$ at lower momentum, with heavier particles losing more energy. The energy loss decreases with momentum until it reaches a minimum and begins to increase in the relativistic rise. Electrons

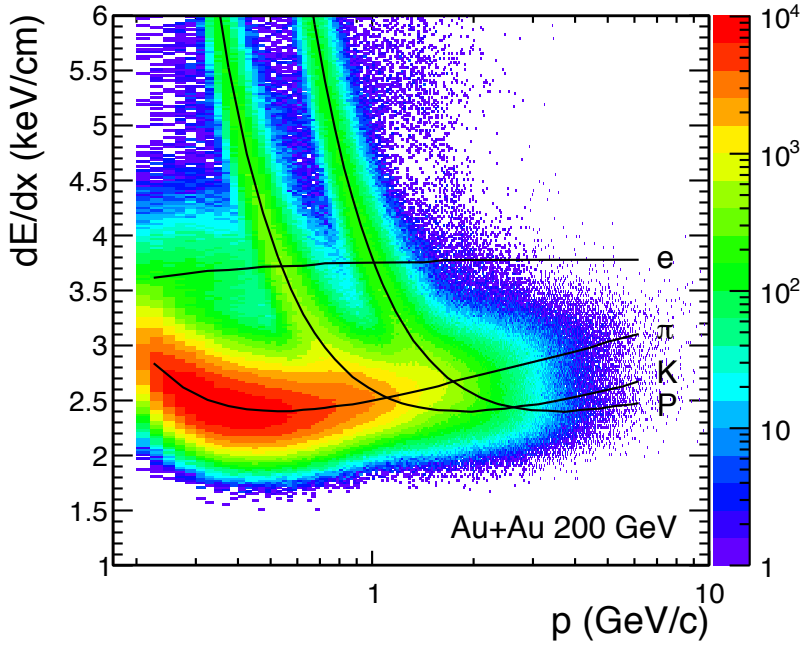

Figure 3.10: Top: The TPC $\mathrm{d}E/\mathrm{d}x$ versus momentum in Au+Au collisions for charged particles. The expected value for various particles is indicated by the symbols and is obtained from the Bichsel functions [131].

are much lighter than the hadrons and are highly relativistic in this momentum region. Their $\mathrm{d}E/\mathrm{d}x$ increases slightly with momentum until it saturates at ~ 1 GeV/c.

The TPC provides essential track reconstruction and particle identification for various particle species across a range of momentum. This method of particle identification is less effective in momentum regions where the $\mathrm{d}E/\mathrm{d}x$ of different particles overlaps, and at high-p_T where the $\mathrm{d}E/\mathrm{d}x$ separation decreases due to the relativistic rise. This becomes particularly challenging for less abundant particles such as electrons, and the TOF and BEMC are used to improve the particle identification capabilities of the TPC at low- and high-p_T, respectively.

3.2.2 Time of Flight

The Time of Flight was fully installed in 2010 [133, 134], and is used to measures the time it takes for a particle to travel between two points, $\Delta t = t_1 - t_0$. The start time (t_0) and stop time (t_1) are determined by the pVPD (described below) and TOF, respectively, and this achieves an average overall time resolution of $\sim$ 87 ps [123]. The TOF consists of 120 trays that cover $|\eta| < 1$ and $0 < \phi \leq 2\pi$. The detector uses Multi-gap Resistive Plate Chamber (MRPC) technology [135], and each tray contains 32 MRPC modules, with each module containing 6 pads. The trays have dimensions $95 \times 8.5 \times 3.5$ inches, covering 6 degrees and one unit in pseudorapidity, and surround the TPC at a radius of $\sim$ 2.2 m. A detailed description of the TOF can be found in [111, 117, 134].

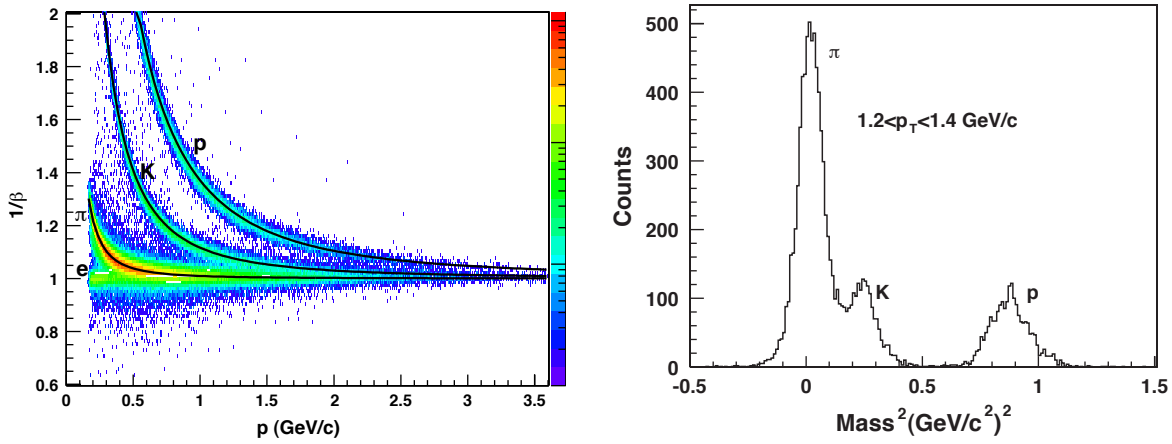

Figure 3.11: The TOF $1/\beta$ versus momentum (left) and m^2 for $1.2 < p_T < 1.4$ GeV/c (right) for charged particles in d+Au collisions at $\sqrt{s_{NN}} = 200$ GeV. Figure taken from [134].

Particle Identification

Tracks reconstructed in the TPC are matched to hits in the TOF. From the time of flight (Δt) the inverse velocity ($1/\beta$) can be calculated:

$$1/\beta = c\frac{\Delta t}{\Delta s}, \tag{3.1}$$

where Δs is the track pathlength. The mass (m) of the particle can be determined from $1/\beta$ and the momentum (p) where

$$m = \frac{p}{\beta\gamma c} = \frac{p\sqrt{1-\beta^2}}{\beta c} = \frac{p}{c}\sqrt{\left(\frac{1}{\beta}\right)^2 - 1}. \tag{3.2}$$

The $1/\beta$ distribution versus momentum and m^2 distribution for $1.2 < p_T < 1.4$ GeV/c obtained from TOF are shown in Fig. 3.11 in the left and right panel, respectively, and are obtained from d+Au collisions at $\sqrt{s_{NN}} = 200$ GeV. The expected $1/\beta$ for electrons, pions, kaons, and protons are obtained using the particle masses from the Particle Data Group (PDG) [136], and are indicated in the plot (lines). The $1/\beta$ distribution exhibits a mass ordering, with heavier particles traveling slower than lighter ones. As the momentum increases, the velocity of all particles converges to c.

The TOF provides excellent capabilities for particle identification, and is particularly effective in separating electrons from heavier hadrons at low momentum. This is challenging using the TPC alone, as the $\mathrm{d}E/\mathrm{d}x$ of the electrons overlaps with the kaons at $\sim$ 500 MeV/c, and with the protons at $\sim$ 1 GeV/c. This is illustrated in Fig. 3.12, where the $\mathrm{d}E/\mathrm{d}x$ distribution in d+Au collisions is shown for charged particles (top panel), and for particles satisfying $|1/\beta - 1| < 0.03$ (bottom panel). Heavier particles such as the protons and kaons have been removed using the TOF, and the electron and pion $\mathrm{d}E/\mathrm{d}x$ bands are clearly distinguishable. A high purity sample of electrons can be obtained by further using $\mathrm{d}E/\mathrm{d}x$ to remove the pions. In this way the TOF and TPC can provide high quality particle identification at low momentum, and can be used to effectively identify electrons for $p < 1.5$ GeV/c. The TOF matching efficiency and acceptance is $\sim 65 - 70\%$ above 500 MeV/c, and decreases below this.

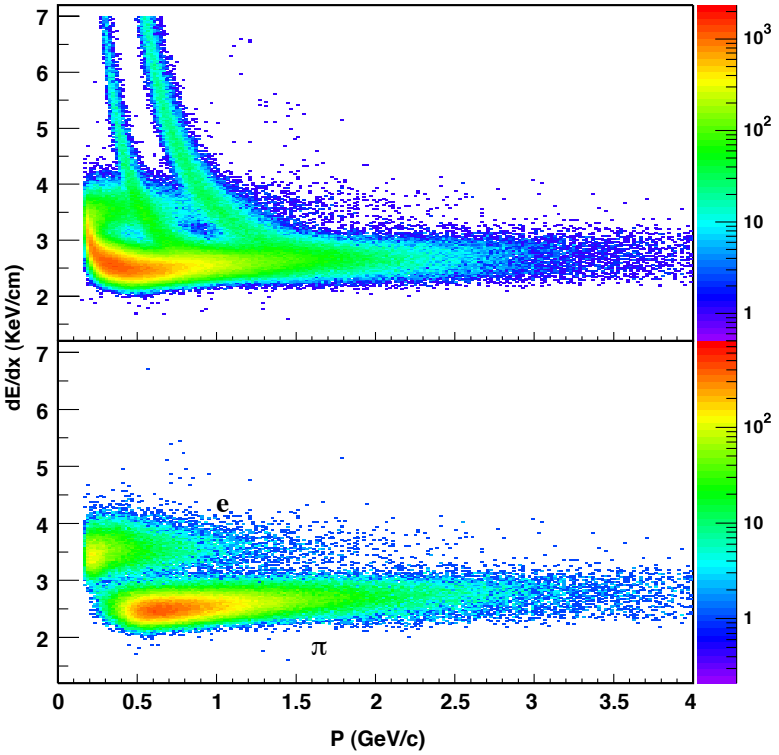

Figure 3.12: Top: The TPC $\mathrm{d}E/\mathrm{d}x$ as a function of momentum in d+Au collisions at $\sqrt{s_{NN}} = 200$ GeV for charged particles. Bottom: The $\mathrm{d}E/\mathrm{d}x$ for particles that satisfy $|1/\beta - 1| < 0.03$. Figure taken from [134].

3.2.3 Barrel Electromagnetic Calorimeter

The Barrel Electromagnetic Calorimeter [118] surrounds the TPC and TOF with full azimuthal coverage and pseudorapidity coverage of $|\eta| < 1$. The BEMC is contained within the STAR magnet, with the front face located at a radius of 223.5 cm. It consists of 120 calorimeter modules, each covering 6 degrees (26 cm) and one unit in pseudorapidity (293 cm), with a depth of 23.5 cm and an additional 6.6 cm of structural plates. The modules are segmented into 40 towers, and each of the 4800 towers covers $\Delta\eta \times \Delta\phi = 0.05 \times 0.05$. Each tower points back to the interaction region, and covers an area of $\sim 10 \times 10$ cm at $\eta = 0$.

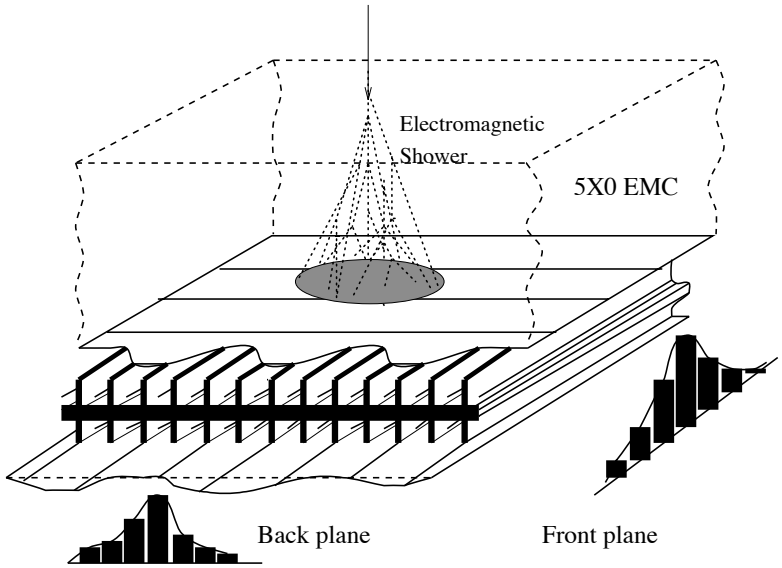

Figure 3.13: The calorimeter BSMD, with two independent wire layers that provide shower shapes along the η and ϕ direction. Figure take from [118]

.

The BEMC is a sampling calorimeter, consisting of alternating layers of lead absorber plates and scintillator plates. Charged particles traversing the lead absorber plates will produce an electromagnetic shower, and the ionized electrons from these showers are converted into light by the scintillator plates to determine the energy of the shower. There are 20 layers of 5 mm thick lead plates which alternate with 21 scintillator plates. The scintillator plates are also 5 mm thick, except the first two layers which are associated with the Pre Shower Detector (PSD) and are 6 mm thick. A Barrel Shower Maximum Detector (BSMD) is located between the 5^{th} and 6^{th} lead-scintillator stack. It consist of two layers of gas wire pad chambers along the η and ϕ planes with dimensions of $\Delta\eta \times \Delta\phi = 0.01 \times 0.05$ and 0.05×0.01, respectively, and provides a two-dimensional shower shape as described in Fig. 3.13.

The BEMC amounts to a total radiation length of $\sim 20X_0$, where the radiation length X_0 is defined as the mean distance over which a high energy electron loses all but $1/e$ (37%) of its energy by Bremsstrahlung [13]. The light created by particles striking the scintillating plates is transported by wavelength shifting (WLS) optical fibers to photomultiplier tubes (PMTs) outside of the STAR magnetic field. A side view of a calorimeter module is shown in Fig. 3.14 (left), and displays the projective nature of the towers and the sandwich geometry of the lead-scintillator plates. The core structure of each module is held together at a pressure of 15 *psi* using 30 straps that are connected to the non-magnetic front and back plates of the module. This ensures stability of the calorimeter layers regardless of the orientation. A side view of a BEMC module is shown in detail in Fig. 3.14 (right), and describes the dimensions and structure of the module.

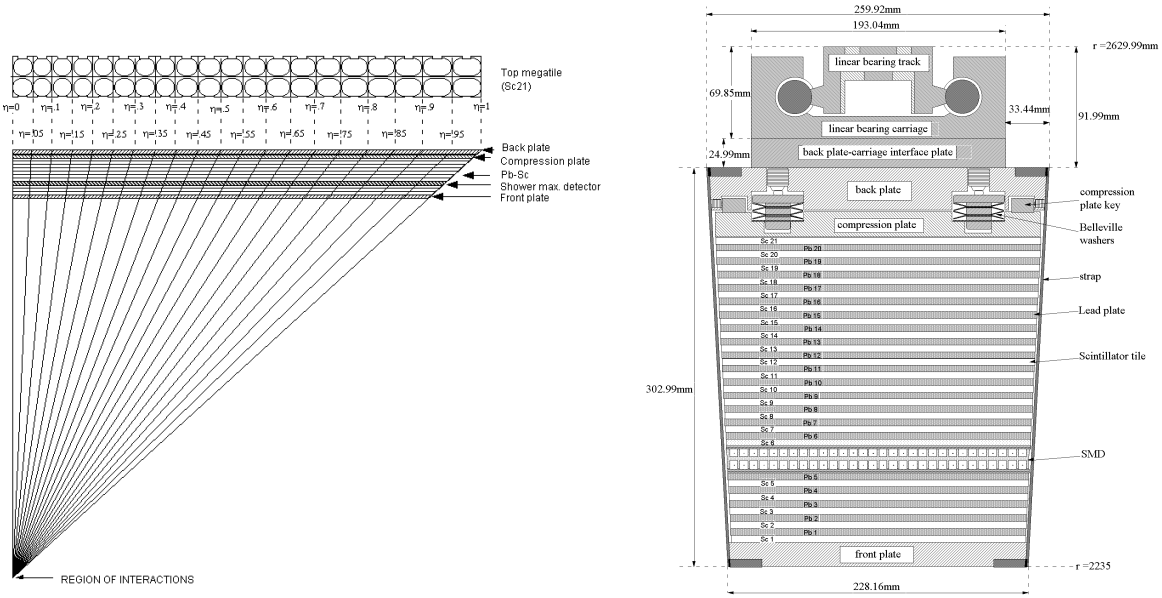

Figure 3.14: A side view of a BEMC module, showing projective tower geometry (left), and dimensions and mechanical structure of the lead-scintillator plates, compression plate, and rail mounting (right). Figure take from [118].

Particle Identification

The BEMC towers (BTOW) provide information on the amount of energy deposited in the calorimeter with an energy resolution of $\mathrm{d}E/E \sim 16\%/\sqrt{E}$. With a depth of $20X_0$, electrons are expected to deposit their entire energy in the calorimeter. Hadrons have a much smaller interaction cross section with the lead, and generally pass through the material as minimum ionizing particles (MIPs). As a result, they deposit far less energy in the calorimeter. Since electrons are massless on the MeV scale and above, the energy (E) that they deposit into the calorimeter is roughly equal to their momentum. Combining the energy obtained from the BEMC with the momentum obtained from the TPC provides a means of identifying electrons via their energy-to-momentum ratio, $E/p \sim 1$. The electron-hadron discrimination power is poor for $p < 1$ GeV/c, as there is a significant contribution from hadrons with $E/p \sim 1$. As the momentum increases, the average hadron E/p decreases and the discrimination power improves. The discrimination also depends on the resolution of the energy and momentum, which is dominated by the energy resolution at low momentum and by the momentum resolution at high momentum. The efficiency of matching an electron to an energy deposit in the BEMC is $\sim 80 - 90\%$ above 1 GeV/c, and decreases below this.

The BSMD is located at $5X_0$, and provides information on the shape and position of a shower. Electromagnetic showers are much broader than those of hadronic showers, and at this depth electrons are expected to have a fully developed shower shape. This is in contrast to hadrons, whose shower shape is not expected to have developed. As a result, electromagnetic showers can be identified by a large number of active η and ϕ strips ($\sim \geq 2$) in the BSMD. The shower shape and position in the BSMD can be combined with the BTOW energy to provide an improved resolution on the cluster position and size.

The particle identification methods and associated efficiencies for each detector used in this analysis are discussed in detail in Chapter 4.

3.2.4 Trigger Detectors

The luminosities delivered to STAR have increased drastically over the lifetime of RHIC, and not every collision can be recorded. Special consideration is taken to decide on what collisions to trigger on and record. The STAR trigger system [137] uses a pipelined setup in which information from the fast detectors is examined at the bunch crossing rate. This information is used to determine whether to begin amplification digitization acquisition (ADA) for slower detectors which are required for tracking and additional particle identification. The triggering performs multiple levels of logic, with the final level ($L3$) based on tracking from the slow detectors [138], while the first three trigger levels are based on information from the fast detectors [137].

The primary detectors used to trigger on collisions with minimum bias are the BBC, pVPD, and ZDC, which are located to the East and West of the collision region with large rapidities. These detectors measure the scattering of the collided nuclei and coincidences between their East and West components to detect whether a collision took place. More advanced trigger logic can be implemented to bias the event selection toward rare or interesting events. The BEMC, which is a fast detector with a readout time of ~ 10 ns, is used to trigger on events containing a large energy deposit in a single tower or tower cluster, corresponding to the production of a jet or high-p_T particle. The TOF is used in addition to other detectors to trigger on central heavy ion collisions by requiring a high occupancy of hits. In general, these conditions are applied in addition to the minimum bias trigger conditions. In this analysis, only minimum bias and central triggered events are considered, and these rely on triggering using the pVPD. The ZDC and BBC are used for additional triggering conditions and for monitoring the beam and background rates. These detectors are briefly described next.

The BBCs are located at a distance of 3.5 m from the interaction region and surround the beam pipe. They are segmented into of two layers of hexagonal tiles, with the inner layer consisting of smaller tiles, and larger tiles making up the outer layer. The layout of the BBC is shown in Fig. 3.15. The BBC can be used to determine

the vertex position and collision centrality, however they are restricted by their large granularity and non-uniform efficiency. In this analysis, the BBCs have been used to monitor beam conditions and background rates.

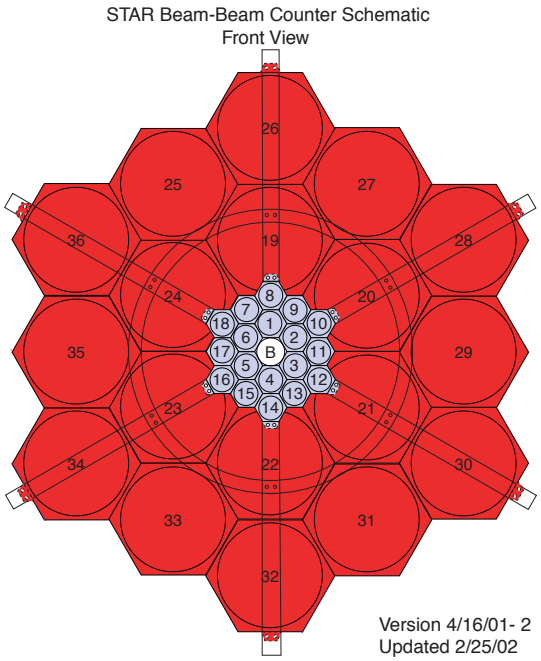

Figure 3.15: The BBC layout at STAR. Figure taken from [139].

The pVPD detectors are located around the beam pipe outside of the STAR magnet at a distance of 5.6 m from the interaction region. They consist of lead-scintillator layers coupled to 19 PMTs, 10 on the inner ring and 9 on the outer ring. Fragments from the colliding nuclei, which generally do not participate in the collision, travel at near the speed of light towards the pVPDs. The start resolution achieved by the pVPD is $\sim$ 24 ps [123], and the time difference between the signals received at the East and West pVPD is used to determine the vertex position of the collision. In general, events are only triggered if they occur within $30 - 60$ cm of the interaction region to ensure a near uniform efficiency and acceptance of the detector. The pVPD has been used as the primary minimum bias trigger in this analysis.

The ZDCs are located along the beam line and outside of the RHIC dipole magnets. This means that charged particles are bent away from the ZDCs as they exit the interaction region. Spectator neutrons from the collision are detected by the ZDC, which uses alternating layers of tungsten plates and wavelength shifting fibers connected to PMTs to detect Cherenkov radiation. The ZDCs have been used in this analysis for monitoring the beam conditions and background rates, and for event triggering in addition to the pVPD.

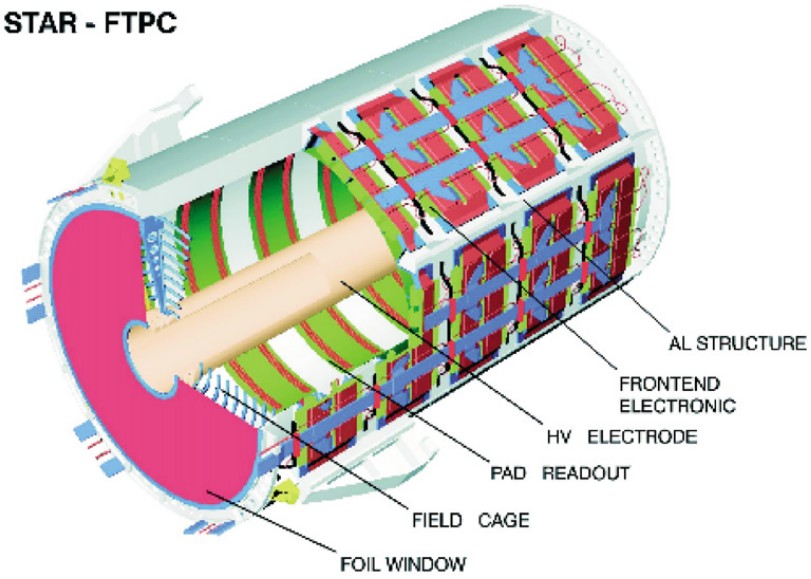

Figure 3.16: A description of the FTPC layout at STAR. Figure taken from [121].

The FTPCs, shown in Fig. 3.16, are located at $2.5 < |\eta| < 4$ and are cylindrical in shape with a diameter of 75 cm and a length of 120 cm. They use the radial drift of ionization electrons in a low diffusion gas (50% Ar, 50% CO_2) to provide tracking in a similar way to the TPC. Tracks with $|\eta| < 1$ are considered in this analysis, and the FTPC is only used to determine the centrality of d+Au collisions. Further details on the FTPC can be found in [121].

The exact trigger requirements for the data used in this analysis are described in Chapter 4.

3.2.5 Data Acquisition

The STAR Data Acquisition System (DAQ) is responsible for accumulating data from the various detectors on an event level. It assembles the detector information into larger data structures that describe the detector response to the collision environment. The RHIC Computing Facility (RCF) manages the data storage using a High Performance Storage System (HPSS). The DAQ is responsible for reading data from the STAR detectors, reducing the data rate, and storing the data using HPSS. The DAQ applies the $L3$ trigger conditions before storing the data to decide whether the data should be recorded. The $L3$ decision in based on tracking, and requires a farm of ~ 50 CPUs integrated with the DAQ to perform this. The delay between receiving the event information and the $L3$ deciding on whether to build/reject the event means that the DAQ must be able to deal with multiple events at different stages of completion. The DAQ was designed to operate at an event rate of ~ 100 Hz. An upgrade to the DAQ1000 [140] has increased the event rate to 1 kHz. In order to deal with the large amounts of data, events are first compressed to reduce the event size by a factor ~ 10. The $L3$ trigger is then used to decide which events to write to tape, and this reduces the data stream by a factor of ~ 100. A detailed description of the tasks, performance, and components of the DAQ system can be found in [141, 142].

Chapter 4

Data Analysis

The suppression of J/ψ in heavy ion collisions has been proposed as a signature of the formation of a Quark Gluon Plasma due to the Debye screening of the heavy quark potential in a deconfined medium [62]. However there are various other modifications that need to be considered in order to quantify a suppression due to color screening. The presence of nuclear matter in the initial-state of the collision can modify production rates as nuclei cannot be treated as a superposition of nucleons. Similarly, interactions with nuclear matter in the final-state can also cause modifications to observed production rates. These *cold nuclear matter* (CNM) effects [93] are unrelated to a phase transition into a deconfined medium, and can be studied in p + A and d + A collisions where nuclear matter is present but a transition to a QGP is not possible. There may also be modifications to J/ψ production in heavy ion collisions other than CNM effects and color screening, such as the recombination of $c\bar{c}$ quarks. A systematic study of J/ψ in d + A and A+A is needed in order to disentangle the various effects and quantify a suppression due to color screening.

The data and analysis methods used to reconstruct J/ψ via their dielectron decay channel in d+Au and Au+Au collisions at $\sqrt{s_{NN}} = 200$ GeV at the STAR detector are described in this chapter. The dataset and trigger configurations are discussed, followed by a description of the event selection requirements and centrality selection

details. The track selection requirements and electron identification methods, including their associated efficiencies, are presented. Finally, the total J/ψ efficiency and acceptance correction is described.

4.1 Data and triggers

In 2008, STAR recorded collisions of d+Au at $\sqrt{s_{NN}} = 200$ GeV for 9 weeks. This was the first run after the removal of the inner tracking detectors, which greatly reduced the amount of material and as a result the dielectron background. While STAR also recorded d+Au collisions at $\sqrt{s_{NN}} = 200$ GeV in 2003, the statistics were inadequate to study rare particles such as J/ψ.

There have been several Au+Au runs at RHIC, and a detailed history of these can be found in [105]. This analysis uses the Au+Au data recorded in 2010, which was the first Au+Au run after the removal of the inner tracking detectors. STAR recorded Au+Au collisions at $\sqrt{s_{NN}} = 200$ GeV for 10.9 weeks before proceeding to the Beam Energy Scan (BES) where Au+Au beams were collided at 62.4, 39, 11.5, and 7.7 GeV. In 2011, the BES was extended to include 19.6 and 27 GeV, and another 6.4 weeks of Au+Au data at $\sqrt{s_{NN}} = 200$ GeV were recorded. The data recorded in 2011 at $\sqrt{s_{NN}} = 200$ GeV were not included in this analysis.

The data consists of several trigger configurations which have been used to identify specific types of collisions. Rare particles such as J/ψ and Υ can be enhanced by triggering on a high-p_T electrons or electron-pairs, which are identified by a large energy deposit in the BEMC. These are not effective for low-p_T J/ψ due to the large background from π^0 decay. As a result, this analysis only uses data obtained from the minimum bias (MB) trigger. The minimum bias trigger for d+Au and Au+Au required a coincidence between the East and West VPD, selecting on collisions within 30 cm of the interaction region along the beam line on the $z-$axis. For triggering on d+Au collisions, the deuteron was required to fragment the gold ion. This was

done by identifying a neutron in the East ZDC which faces the incoming gold nuclei, corresponding to an ADC count above 5. The sampled luminosity and number of minimum bias d+Au events recorded in 2008 are shown in Fig. 4.1, and a total of 46 M events were used in this analysis.

An additional central-biased trigger (CENT) was used to enhance central Au+Au collisions accepted by the MB trigger. This was done by requiring a high occupancy in the TOF detector, corresponding to a large particle multiplicity. The recorded number of events for the MB and CENT trigger in Au+Au collisions are shown in Fig. 4.2, and a total of 304 M minimum bias and 234 M central events were analyzed, respectively.

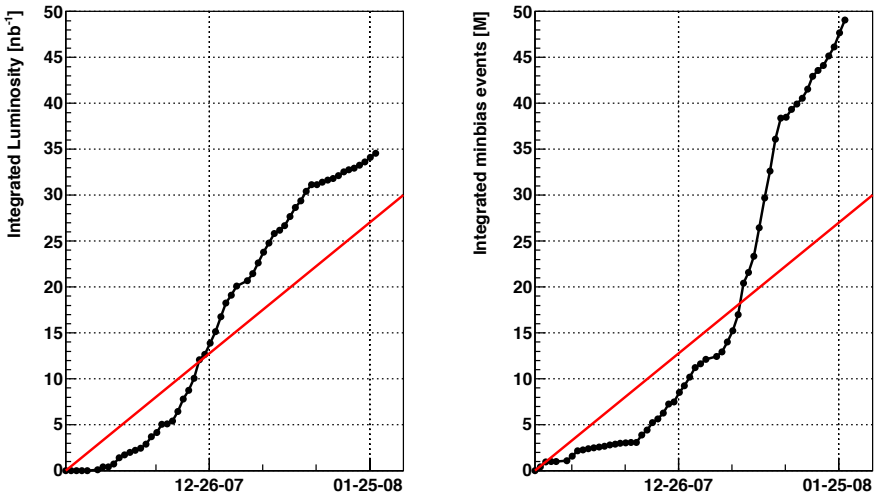

Figure 4.1: The integrated luminosity (left) and number of minimum bias events (right) versus time, recorded for d+Au collisions at $\sqrt{s_{NN}} = 200$ GeV. The recorded data (circles) exceeds the goal for the run (line). Figure taken from [143].

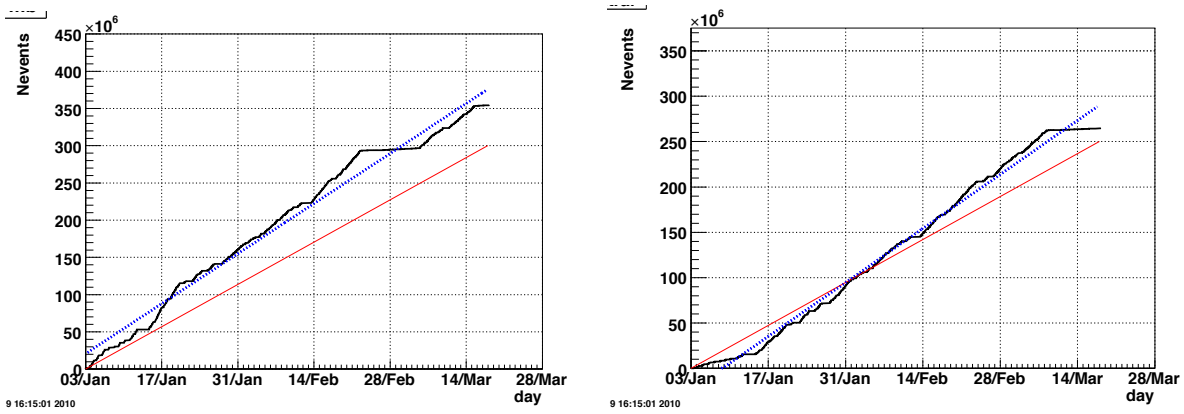

Figure 4.2: The number of minimum bias events recorded for Au+Au collisions at $\sqrt{s_{NN}} = 200$ GeV versus time, using the MB trigger (left) and Central trigger (right). The recorded data (black) and projections (blue) are compared to the goals for the run (red). Figure taken from [144].

4.2 Event Selection

The minimum bias trigger identifies collisions that occur within $|V_Z| < 30$ cm, and this online vertex position is determined from the time difference in the East and West VPD signals. The offline vertex position is determined by the vertex finding algorithm implemented for d+Au and Au+Au collisions (MinuitVF), which minimizes the distance of closest approach of the reconstructed tracks at the origin. The z-vertex position is shown in Fig. 4.3 for minimum bias d+Au collisions (dotted line). The vertex position obtained from MinuitVF is required to be within $|V_Z| < 30$ cm in d+Au and Au+Au collisions to ensure a uniform detector efficiency.

The VPD trigger is less efficient in low multiplicity collisions, which causes losses in peripheral d+Au and Au+Au collisions. These events are rejected or corrected for inefficiencies to remove any bias from the centrality selection. A reweighting of the multiplicity distribution in d+Au collisions was performed, and this is described below. Only data in $0 - 60\%$ central Au+Au collisions, where the VPD inefficiency is negligible, were used in this analysis. The central trigger recorded $0 - 10\%$ central

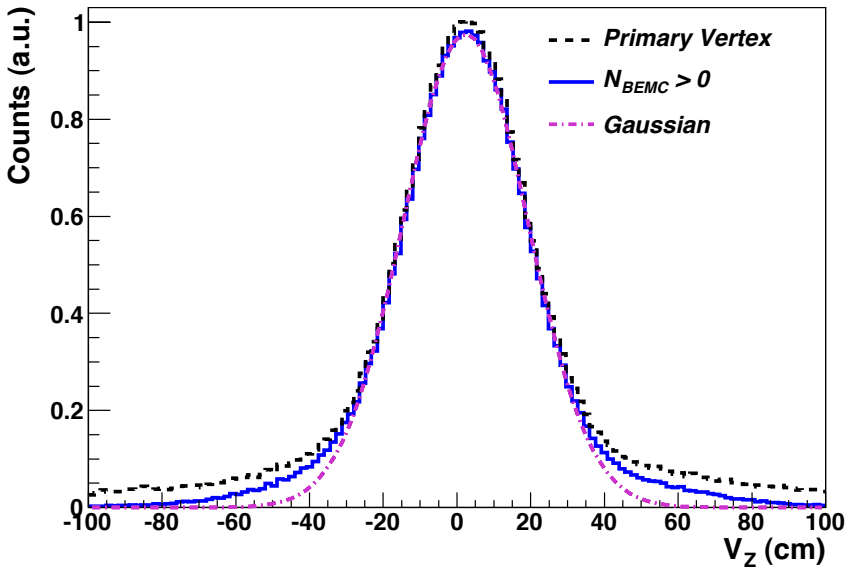

Figure 4.3: The primary vertex position for all events (dashed line), and for events with $N_{\mathrm{BEMC}} > 0$ (solid line), in d+Au collisions. The distribution with $N_{\mathrm{BEMC}} > 0$ is fitted with a Gaussian (dot-dash line).

Au+Au events, however this also experiences inefficiencies for the less central collisions. As a result, only $0-5\%$ central Au+Au collisions from the central trigger were considered.

4.2.1 Pile-up Removal

Due to the high beam luminosity ($\sim 100-300$ kHz) compared to the TPC readout time ($\sim$ 80 μs) at STAR, tracks from multiple events can be drifting through the TPC at the same time. As a result, multiple vertices per event were reconstructed by MinuitVF in d+Au and Au+Au collisions. The BEMC is a fast detector (readout time $\sim$ 10 ns) and is not sensitive to pile-up. To ensure that the reconstructed vertex triggered the event, pile-up events in d+Au collisions were removed by requiring at least 1 track in the TPC to be matched to an energy deposition in the BEMC. The vertex distribution in d+Au with $N_{\mathrm{BEMC}} > 0$ is shown in Fig. 4.3 (solid line), and

is fitted with a Gaussian function (dot-dashed line). A total of 30 M d+Au events satisfying $|V_Z| < 30$ cm and $N_{\rm BEMC} > 0$ were accepted and analyzed. The event selection criteria and number of events in d+Au collisions is summarized in Table 4.1.

The VPD V_Z distribution in Au+Au collisions is shown in Fig. 4.4 versus the reconstructed V_Z obtained using MinuitVF (left panel). A clear correlation is seen, however there is a significant amount of out-of-time events which exhibit no correlation. To remove these pile-up events, a correlation between the VPD and MinuitVF V_Z position was required. The difference between the VPD and reconstructed V_Z position (ΔV_Z) is shown in Fig. 4.4, and the distribution has a width of 0.6 cm. Pile-up events have been identified and removed by requiring $|\Delta V_Z| < 3$ cm. The remaining pile-up within $|\Delta V_Z| < 3$ cm amounts to less than 1% of events. A total of 189 M minimum bias events in $0-60\%$ centrality and 87 M central events in $0-5\%$ centrality with $|V_Z| < 30$ cm and $|\Delta V_Z| < 3$ cm were used in this analysis. The event selection requirements for Au+Au collisions are summarized in Table 4.2.

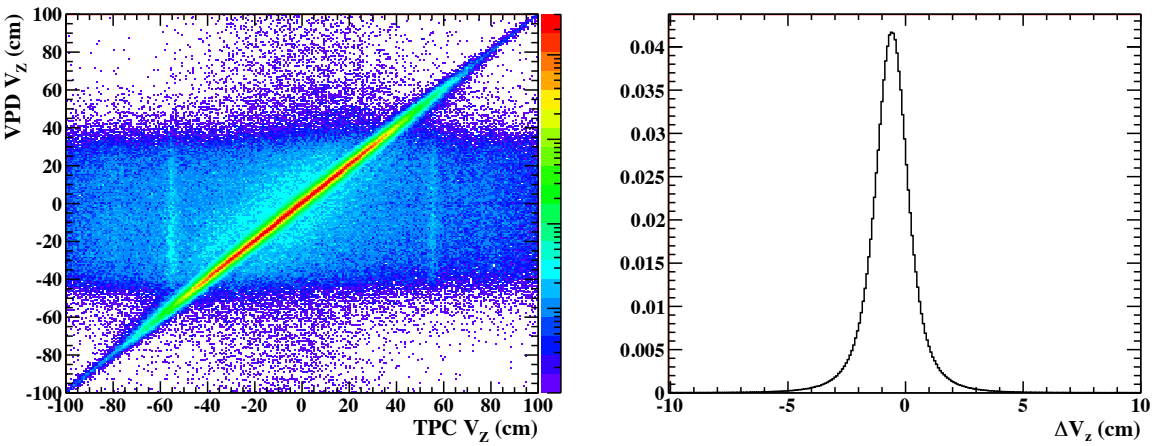

Figure 4.4: The VPD V_Z versus the reconstructed V_Z position in Au+Au collisions (left panel), and the difference between these vertex positions, ΔV_Z (right panel).

Table 4.1: Event selection in d+Au collisions.

Trigger	Condition	Events
Minimum Bias	None	46 M
	$\|V_Z\| < 30$ cm	31 M
	$N_{\mathrm{BEMC}} > 0$	30 M

Table 4.2: Event selection in Au+Au collisions.

Trigger	Condition	Events
Minimum Bias	None	304 M
	$0 - 60\%$	222 M
	$\|V_Z\| < 30$ cm	191 M
	$\|\Delta V_Z\| < 3$ cm	189 M
Central	None	234 M
	$0 - 5\%$	96 M
	$\|V_Z\| < 30$ cm	87 M
	$\|\Delta V_Z\| < 3$ cm	87 M

4.2.2 Corrupt Scaler Rates

The BBC and ZDC detectors monitor the beam collision and background rates (*scaler rates*) during each run, and some of these rates are used to understand and correct for distortion effects in the TPC. During the recording of d+Au collisions in 2008, there were instances when the scaler boards were faulty and the rates from the BBC and the ZDC recorded values 2 or 3 times higher than the correct values. Although such

instances only account for $\sim 0.1\%$ of the total statistics, it is necessary to understand and correct for these effects, especially for the analysis of rare particles. A method to exclude these corrupt events was developed, and is described next.

Identifying and removing events with incorrect scaler rates during data production has been implemented for subsequent runs. However, since this problem was discovered after the recording and production of the d+Au data, a solution that could be implemented on the analysis level was necessary. Since the beam luminosity decreases over time, it is periodically dumped and re-filled. Within each *fill* of the beam, the luminosity monotonically decreases and there is a large variation of the scaler rates over time in a single fill, making it hard to identify problematic scaler rates directly. To remove the variation of beam rates within a fill, ratios of different scaler rates were computed. From these ratios, clear instances of events with problematic scaler rates could be identified and removed. This is illustrated in Fig. 4.5, where the ratio of the ZDC coincidence rate and BBC coincidence rate is plotted versus the beam fill number. While most events have a ratio of approximately 0.3, instances where this value is a factor of 2 higher or lower are clearly observed. The distortion corrections do not rely on the BBC coincidence rate, and no consideration was taken for events where this rate was problematic. Events with incorrect ZDC coincidence rates were identified as having a ratio above 0.42 and were removed.

For some scaler channels, where this approach did not completely remove the in-fill fluctuations and no clear structure where the doubling of scaler rates could be identified, a slightly more complicated approach was taken. By using a Principle Component Analysis (PCA), the rates of interest were approximated from a combination of other scaler rates. The actual scaler rate was divided by the approximation, yielding a ratio approximately equal to unity. Outliers represented corrupt events and were removed. The total number of events rejected due to problematic scalers corresponds to $\sim 1\%$ of the total statistics.

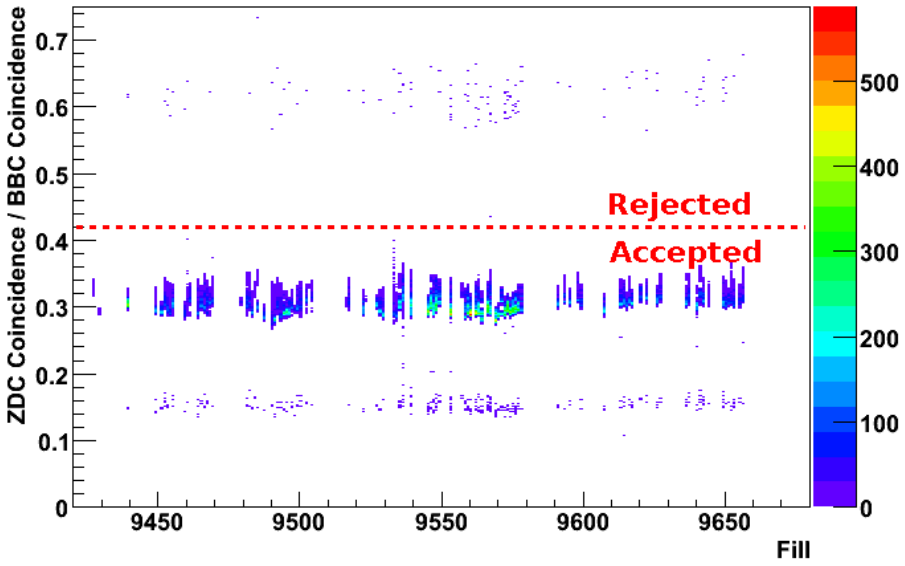

Figure 4.5: The ratio of the ZDC coincidence an BBC coincidence rates. Outliers are instances of hardware failures resulting in incorrect rates (above dotted line), and are removed.

4.3 Event Centrality

The centrality of a collision is a description of the amount of transverse overlap in the colliding nuclei. Central collisions, which have a large overlap region of the nuclei, will on average produce a more energetic system and result in a larger particle multiplicity. In order to understand the evolution of modifications to J/ψ production with energy density, an understanding of the charged particle multiplicity and a measure of the collision centrality is required. The centrality of a collision cannot be directly measured, and is generally determined from the observed particle multiplicity. The TPC was used to determine the charged particle multiplicity and centrality selection in Au+Au collisions. To remove correlations between the centrality selection and the observed event in the lower multiplicity d+Au environment, the FTPC multiplicity was also used in d+Au for the centrality selection. A description of the event multiplicity and centrality in d+Au and Au+Au collisions is given below.

4.3.1 Multiplicity

The charged particle reference multiplicity (`refMult`) in the TPC and FTPC is defined as the number of primary tracks passing the requirements listed in Table 4.3. Constraints are placed on the number of reconstructed hit points (`nHitsFit`) to ensure a good track fit quality, and on the detector acceptance using transverse momentum (p_T) and pseudorapidity (η). The distance of closest approach between tracks and the reconstructed vertex (`DCA`) is required to be within 3 cm to ensure they originate from the primary collision vertex.

Pile-up events were removed by requiring that a track was matched to the BEMC in d+Au, and by requiring a correlation between the VPD and the reconstructed track vertex position in Au+Au. However, pile-up tracks (out-of-time tracks that originate from a different collision vertex) can still be associated with the triggered collision because of the high bunch crossing rate crossing compared to the TPC read-out time, and this effect becomes more pronounced at higher luminosity. This is reflected in the mean charged particle multiplicity in the TPC as a function of beam luminosity in d+Au collisions as shown in Fig. 4.6 (circles), which exhibits a clear increase with luminosity (BBC coincidence rate). Additional constraints applied to tracks in the TPC and FTPC for the d+Au data to remove pile-up are described next.

A class of pile-up tracks which cross the central membrane after the collision, known as *Post-Crossing* tracks, were identified during data production. These tracks are formed by associating an out-of-time track to a triggered vertex. The time offset shifts the reconstructed z-position of the track, and this can artificially move the reconstructed track position across the central membrane, which is not physically possible. These tracks were flagged and removed by requiring `flag` < 1000. The mean `refMult` after removing post-crossing tracks is shown in Fig. 4.6 (square). The luminosity dependence has decreased but is still apparent, indicating further pile-up.

Table 4.3: Charged particle event multiplicity requirements.

TPC	FTPC
$\|\eta\| < 0.5$	$-3.8 < \eta < -2.8$
$p_T > 0.15$ GeV/c	$p_T < 3$ GeV/c
`nHitsFit` > 16	$5 <$ `nHitsFit` < 12
$\|$`DCA`$\| < 3$ cm	*$\|$`DCA`$\| < 2$ cm
*$\chi^2 < 6$	

(*only applied to d+Au.)

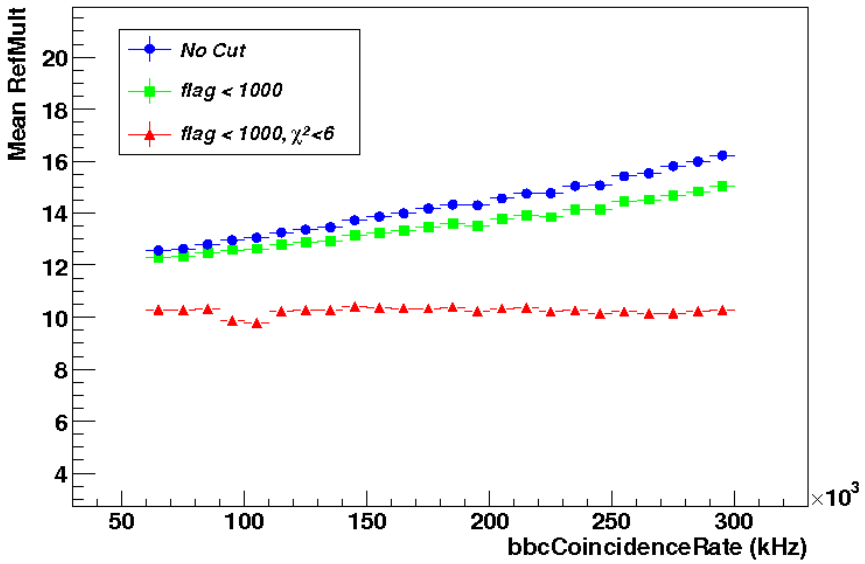

Figure 4.6: The mean charged particle multiplicity for the TPC in d+Au collisions.

Since pile-up tracks do not originate from the triggered collision, they will have a poor extrapolation to the collision vertex. Primary tracks include the vertex position

in track fitting, resulting in a large χ^2 for pile-up primary tracks. The remaining pile-up in the d+Au data was removed by applying an upper limit on the track χ^2. To ensure a constant mean `refMult` as a function of luminosity, a value of $\chi^2 < 6$ on the fit quality of primary tracks was required. This results in a constant mean `refMult` as a function of luminosity in d+Au, as shown in Fig. 4.6 (triangles). The χ^2 values are not as well tuned in the FTPC, and so a similar approach was taken to remove pile-up by looking at the `DCA` of tracks to the vertex. A stable `refMult` was obtained by requiring $|\texttt{DCA}| < 2$ cm in the FTPC.

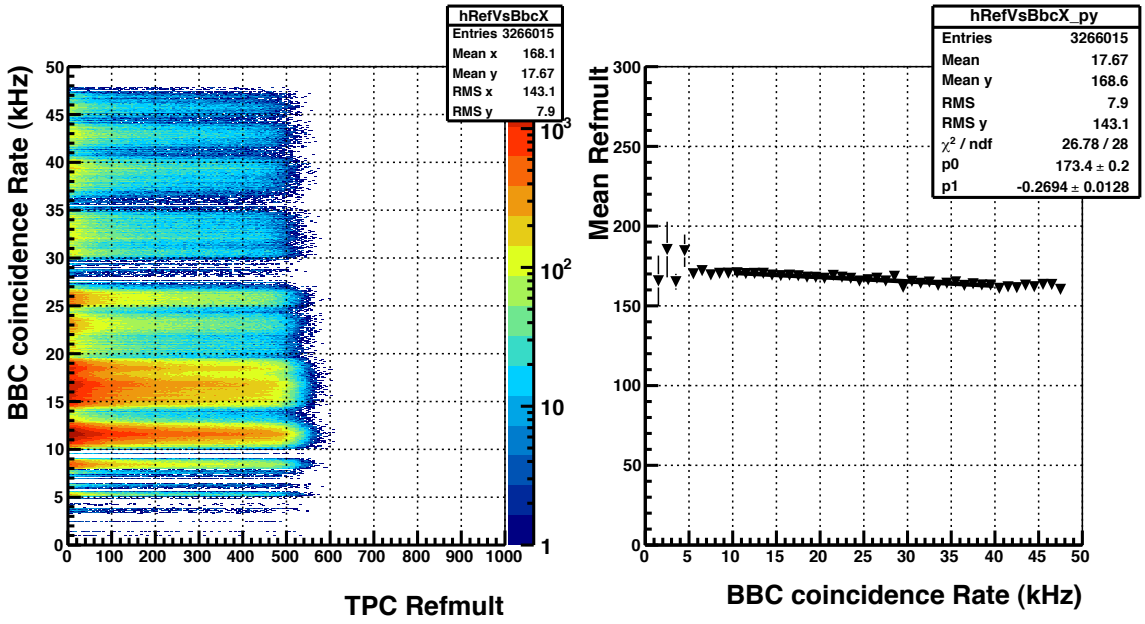

Figure 4.7: The charged particle multiplicity (left) and mean multiplicity (right) in the TPC as a function of BBC coincidence rate in Au+Au collisions.

The charged particle multiplicity in Au+Au collisions is shown versus the BBC coincidence rates in Fig. 4.7 (left panel). The mean `refMult` has been calculated as a function of the luminosity rates, and fitted with a straight line (right panel). The mean `refMult` decreases slightly at high luminosities due to the high charge occupancy in the TPC. The luminosity dependence of the `refMult` in Au+Au, as well as

the time dependence and z-vertex position dependence, and have been studied and the `refMult` in Au+Au has been corrected event-by-event [145]. The time dependence of the mean `refMult` for Au+Au is shown in Fig. 4.8 before corrections (left panel) and after corrections (right panel). This is stable after the corrections are applied, and outliers (red) were removed from the analysis.

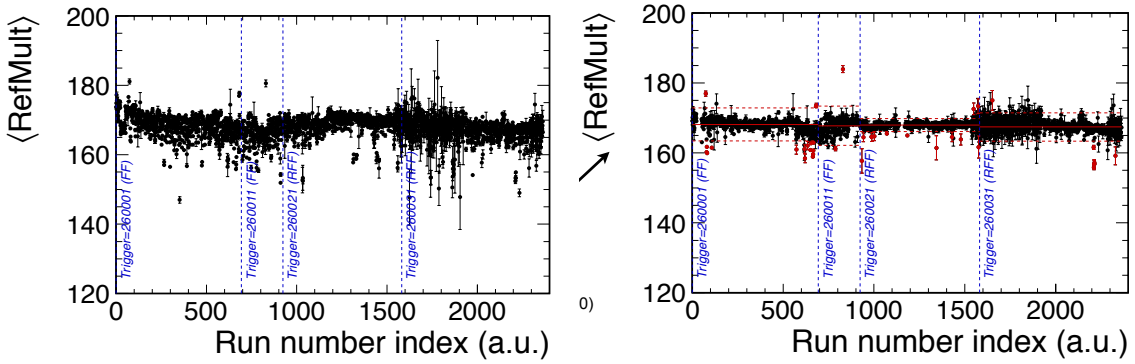

Figure 4.8: The mean multiplicity in the TPC as a function of time before corrections (left) and after corrections (right) in Au+Au collisions. Outliers (red) are removed from the analysis [145].

The mean multiplicity in the FTPC during the d+Au data taking in 2008 exhibits sizable fluctuations across the entire run. The entire run period was subsequently divided into 3 periods, namely

- Run Period 1: Run Number 8340015 - 9008109
- Run Period 2: Run Number 9009007 - 9020089
- Run Period 3: Run Number 9021001 - 9027091

in which the multiplicity was roughly constant. These time periods coincide with hardware changes in the detector. As a result, all centrality selections were calculated in 3 distinct time periods for the d+Au data [146]. The centrality selection in d+Au and Au+Au are discussed below.

4.3.2 Centrality Selection

The transverse overlap of the colliding nuclei cannot be measured directly, and the centrality selection has been determined using a Monte Carlo Glauber calculation [147, 148, 149, 150] which is used to simulate the colliding nuclei. A description of the Glauber model can be found in Appendix A, and has been used to simulate collisions as a function of the collision impact parameter (b). In each collision, the number of participants ($N_{\rm part}$) and binary collisions ($N_{\rm coll}$) was related to the collision centrality and charged particle multiplicity. The measured particle multiplicity from data was compared to the distribution from the Glauber model and used to constrain the centrality of the collision. The centrality in Au+Au collisions was defined using the particle multiplicity measured in the TPC, and this is shown in Fig. 4.9 (black). In d+Au, the centrality selection also relies on the multiplicity measured in the East (gold facing) FTPC (FTPC-E), which has pseudorapidity coverage of $-3.8 < \eta < -2.8$. This was beneficial to the centrality determination in d+Au, as the large gap in pseudorapidity between the TPC and FTPC removes correlations which may bias the centrality selection in the low multiplicity d+Au collision environment.

The multiplicity ranges and corresponding values of $\langle b \rangle$, $\langle N_{\rm part} \rangle$, and $\langle N_{\rm coll} \rangle$ obtained from the Glauber model, along with their uncertainties, are shown in Table 4.4 for d+Au collisions, and Table 4.5 for Au+Au collisions. This has been performed in 3 distinct run periods for d+Au collisions due to instabilities in the FTPC, and the multiplicity range in d+Au for each centrality is the same for run period 1 and 2, and is shown in brackets for run period 3.

4.3.3 Multiplicity Reweighting

The TPC `refMult` is shown in Fig. 4.9 for Au+Au collisions obtained from data (black) and Glauber Monte Carlo simulations (red), and the Glauber distribution has been normalized to the data for `refMult` > 100. There is a discrepancy between

Table 4.4: The centrality definitions in d+Au collisions.

Centrality (%)	*`refMult`	$\langle N_{\rm part} \rangle$	$\langle N_{\rm coll} \rangle$	$\langle b \rangle$ (fm)
$0-20$	$>10(8)$	15.22 ± 1.83	14.59 ± 1.75	3.57 ± 0.43
$20-40$	$>6(4)$	11.37 ± 1.36	10.75 ± 1.29	4.57 ± 0.55
$40-100$	$\leq 6(4)$	5.65 ± 0.68	4.75 ± 0.57	6.65 ± 0.80

(*FTPC-E multiplicity)

Table 4.5: The centrality definitions in Au+Au collisions.

Centrality (%)	`refMult`	$\langle N_{\rm part} \rangle$	$\langle N_{\rm coll} \rangle$	$\langle b \rangle$ (fm)
$0-5$	>446	349.81 ± 2.70	1071.15 ± 28.86	2.32 ± 0.13
$5-10$	>379	300.87 ± 7.04	856.01 ± 27.08	3.97 ± 0.22
$10-20$	>269	235.61 ± 8.83	608.81 ± 31.13	5.66 ± 0.23
$20-30$	>184	167.67 ± 10.55	377.29 ± 33.31	7.33 ± 0.27
$30-40$	>119	115.87 ± 11.10	223.79 ± 30.46	8.69 ± 0.31
$40-50$	>73	76.37 ± 10.70	124.28 ± 24.57	9.87 ± 0.35
$50-60$	>41	47.69 ± 9.44	64.42 ± 17.69	10.92 ± 0.40
$60-70$	>21	27.46 ± 7.77	30.52 ± 11.46	11.88 ± 0.45
$70-80$	>10	14.43 ± 5.26	13.39 ± 6.13	12.81 ± 0.50
$0-20$	>269	280.21 ± 5.97	785.18 ± 28.68	4.41 ± 0.16
$20-40$	>119	141.63 ± 10.65	300.35 ± 31.51	8.01 ± 0.28
$40-60$	>41	62.14 ± 9.97	94.55 ± 20.93	10.39 ± 0.37
$60-80$	>30	21.12 ± 6.21	22.20 ± 8.44	12.33 ± 0.46
$0-60$	>41	161.25 ± 8.87	392.58 ± 26.77	7.61 ± 0.27
$0-80$	>10	127.12 ± 7.53	302.61 ± 21.08	8.76 ± 0.30

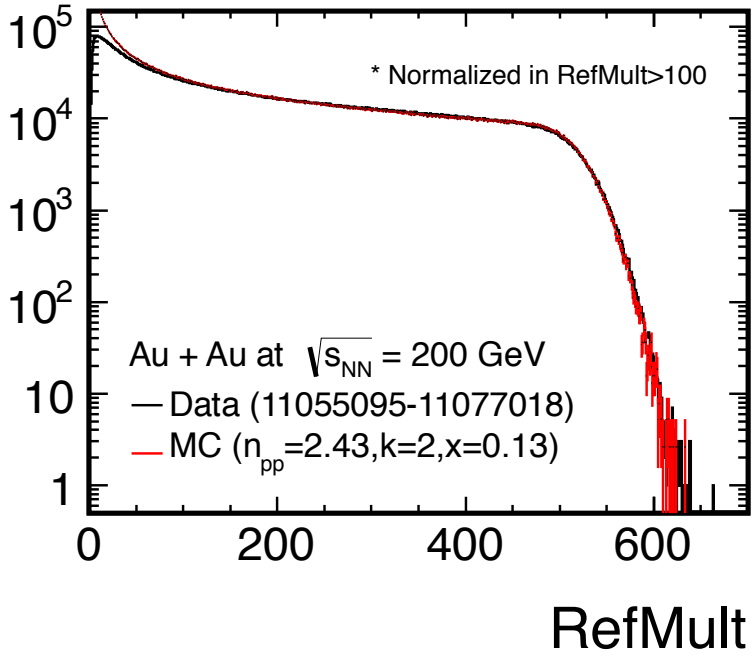

Figure 4.9: The multiplicity distribution in the TPC for minimum bias events in Au+Au collisions from data (black) and Glauber Monte Carlo simulation (red) [145].

the data and simulation for `refMult` < 40, as the VPD is not completely efficient at triggering on low multiplicity events. To correct for the inefficiency at low multiplicity, a reweighting procedure of the `refMult` distribution was carried out. The multiplicity weights were obtained from the ratio of the Glauber prediction to the data and were used to correct the measured `refMult`.

The multiplicity reweighting factor in Au+Au collisions has been calculated by comparing the data and Glauber `refMult` distribution, as shown in Fig. 4.9. The ratio of the Glauber multiplicity to the data is shown in Fig. 4.10, and the weights are large at low multiplicity. These decrease at higher multiplicity, and approach unity for $0-60\%$ central collisions. In this analysis, only $0-60\%$ central Au+Au collisions have been analyzed, and no reweighting of the multiplicity has been applied.

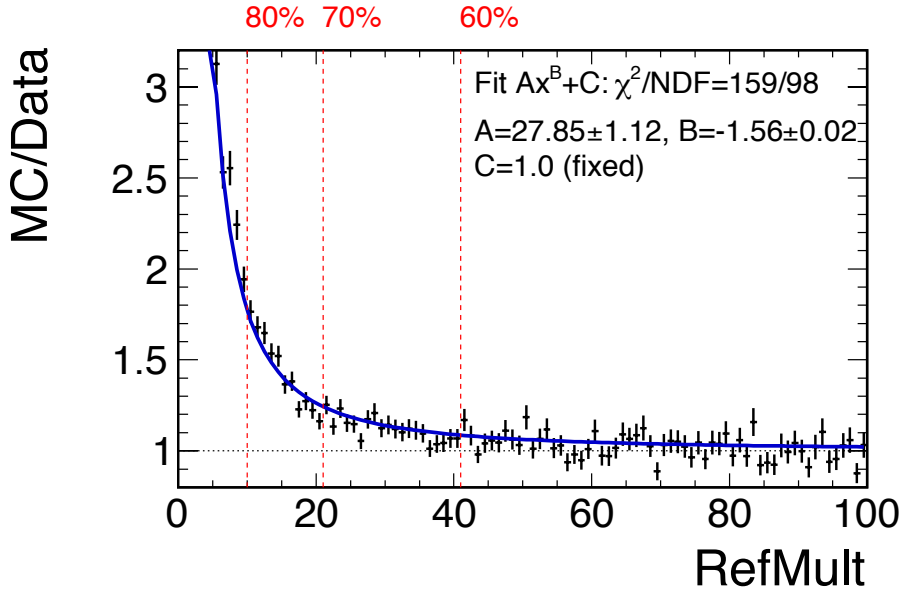

Figure 4.10: The TPC multiplicity weights for Au+Au collisions [145].

The East FTPC `refMult` distribution obtained from data and Glauber simulations in d+Au collisions is shown Fig. 4.11, and the data also exhibits an inefficiency for low multiplicity events. The distributions are normalized for `refMult` > 6, and there are significant losses in the multiplicity from data for `refMult` < 6. The effect is negligible for $0 - 20\%$ and $20 - 40\%$ central collisions, but has a large effect on $40 - 100\%$ central d+Au collisions. This represents a large fraction of the data, and a reweighting of the multiplicity was carried out to correct for this.

The weights used to correct the multiplicity in d+Au collisions were calculated as a function of the TPC and FTPC multiplicities, and were obtained from the ratio of the FTPC-E multiplicity distribution between data and Glauber simulations for each TPC multiplicity. For each event, the TPC and FTPC-E multiplicities were determined after the removal of pile-up, and the corresponding weight was obtained and used to correct the multiplicity. The TPC `refMult` for d+Au collisions is shown in Fig. 4.12 for $40 - 100\%$ central events. The unweighted multiplicity distribution

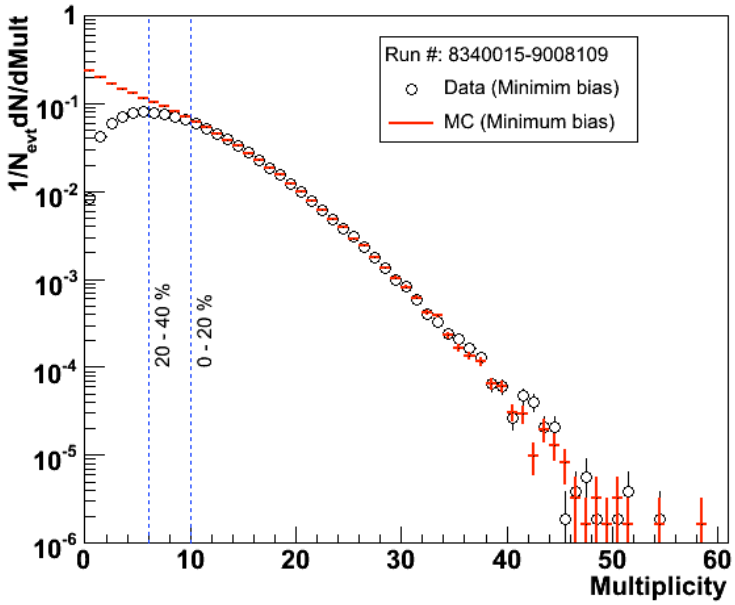

Figure 4.11: The East FTPC particle multiplicity distribution in d+Au collisions for run period 1 from data (open circle) and Glauber simulations (line) [146].

(black) is compared to the multiplicity after reweighting (blue). The distributions are also compared to the multiplicity distribution from previous d+Au collisions recorded in 2003 (red). An additional efficiency factor has been applied to to compensate for losses due to pile-up removal in the high luminosity 2008 data. The reweighting effect is negligible in central and mid-central collisions, but has a significant impact on low multiplicity collisions in $40 - 100\%$ centrality.

4.4 Track Selection

The TPC provides tracking for charged particles with full azimuthal coverage and pseudorapidity coverage at midrapidity. The acceptance of the TPC is illustrated in Fig. 4.13, and shows the pseudorapidity versus azimuthal angle (left) and transverse momentum versus azimuthal angle (right) in Au+Au collisions. Tracks are required

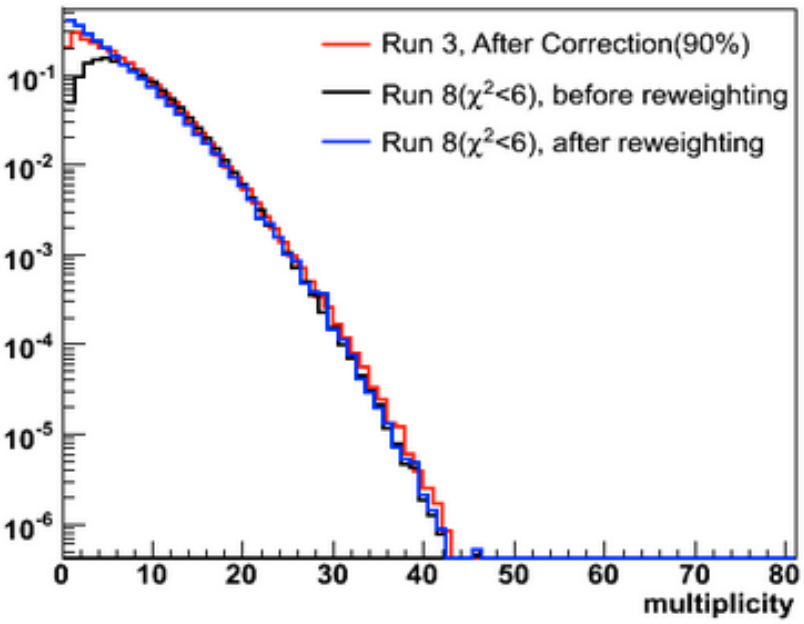

Figure 4.12: The TPC charged particle multiplicity for $40-100\%$ central d+Au collisions before weighting (black) and after weighting (blue). The data are compared to the 2003 d+Au data (red). The distributions are normalized for multiplicity > 5.

to have $p_T > 0.2$ GeV/c in order to reach the outer radius of the TPC. The TPC sector 20 was disabled during the 2010 data taking, corresponding to the losses for $-1 < \phi < 0$ and $-1 < \eta < 0$. There is also a decrease in statistics for $1 < \phi < 2$ and $-1 < \eta < 0$, due to the temporary masking of sector 24.

The pseudorapidity distribution for charged particles in d+Au collisions is shown in Fig. 4.14 for various ranges of vertex position. Due to the asymmetry of the d+Au collision system, more particles are created with $\eta < 0$ (gold-facing direction). Only events which have $|V_Z| < 30$ cm are accepted in this analysis, and the pseudorapidity distribution exhibits non-uniform behavior beyond this. The tracking efficiency is uniform for $|\eta| < 1$, and decreases outside of this. As a result, only tracks with $|\eta| < 1$ are accepted in this analysis.

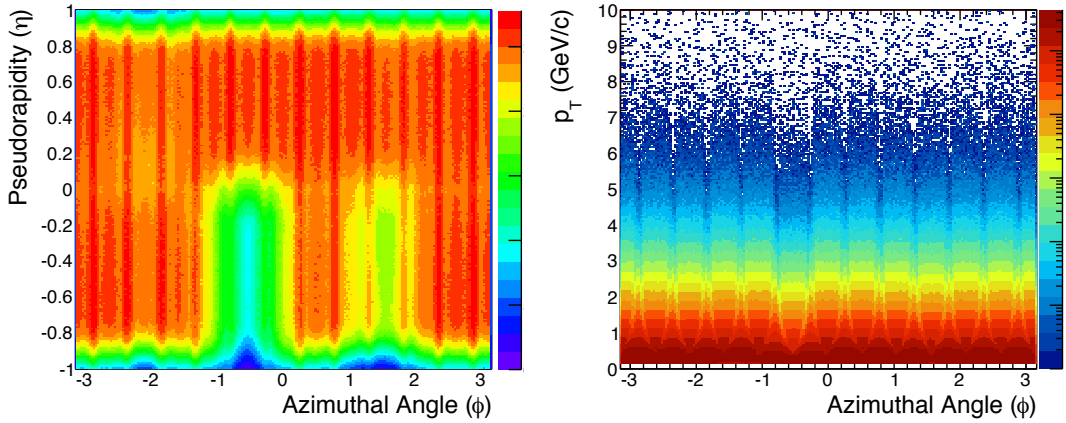

Figure 4.13: The TPC azimuthal angle versus pseudorapidity (left) and transverse momentum (right) for charged particles in Au+Au collisions. The losses correspond to masked out/disabled sectors in the TPC.

To ensure a high track reconstruction quality, requirements are placed on the number of reconstructed hit points (`nHitsFit`), the ratio of reconstructed hit points to possible hit points (`nHitsRatio`), the number of $\mathrm{d}E/\mathrm{d}x$ hit points ($nHitsDedx$), and the distance of closest approach between the track and the vertex (`DCA`). Tracks are required to have `nHitsFit` ≥ 20 (16), `nHitsRatio` > 0.52 (0.52), $nHitsDedx \geq 16$ (12), and $|$`DCA`$| < 3$ (2) cm in d+Au (Au+Au) collisions. The value for `nHitsRatio` was chosen to ensure the removal of split tracks, while the minimum number of spatial and $\mathrm{d}E/\mathrm{d}x$ hits were chosen to remove poorly reconstructed tracks while not significantly decreasing statistics. The Au+Au data exhibit a smaller mean number of hits per track due to the high occupancy environment, and more stringent requirements have been placed on the number of hits in d+Au. Similarly, a tighter requirement has been placed on the `DCA` of tracks to the collision vertex in Au+Au because of the higher track density.

Tracks are also given a flag during the fitting process to indicate the fit quality and detector used in the fitting. Tracks that are poorly reconstructed have `flag` < 0 and are not considered. Post-crossing tracks, which are from pile-up, have `flag` > 1000

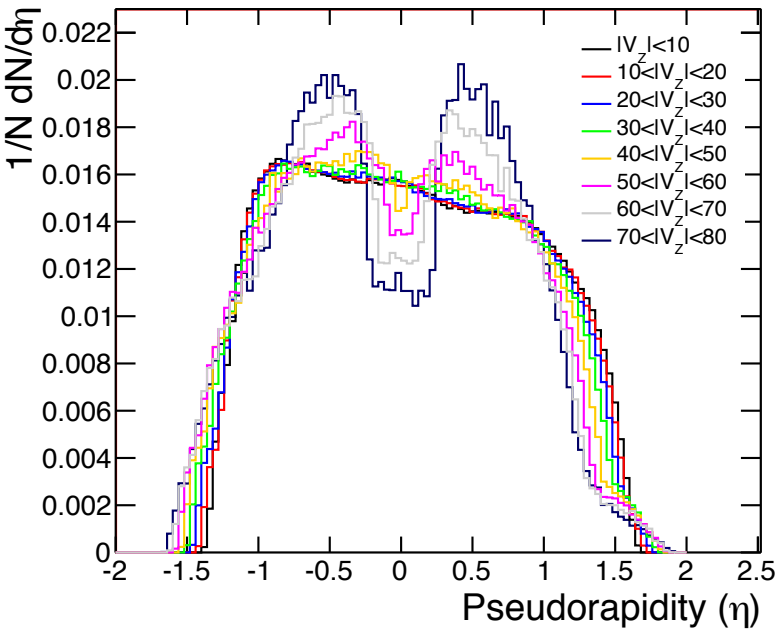

Figure 4.14: The pseudorapidity distribution for charged particles in d+Au collisions for a range of different vertex positions.

and are also removed. Tracks in the TPC that have a good reconstruction quality are given a flag of 301, and only these tracks are selected for this analysis. The quality requirements for tracks reconstructed in d+Au and Au+Au collisions are summarized in Table 4.6, and the conditions in Au+Au are shown in brackets when different.

4.5 Electron Identification

Electrons can provide a very clean probe of early conditions and the evolution of the collision environment as they do not strongly interact with the medium. The TPC has been used as the primary tool for electron identification in STAR, and utilizes the reconstructed momentum and ionization energy loss per unit length ($\mathrm{d}E/\mathrm{d}x$). The TOF and BEMC have been used to further discriminate between electrons and

Table 4.6: Primary track selection in d+Au (Au+Au) collisions.

Transverse Momentum	$p_T > 0.2$ GeV/c
Pseudorapidity	$\|\eta\| < 1.0$
Track Flag	`flag` $== 301$
Spatial Hits	`nHitsFit` ≥ 20 (16)
Hits / Possible Hits	`nHitsRatio` ≥ 0.52
dE/dx Hits	$nDedxHits \geq 16$ (12)
`DCA`	$\|$`DCA`$\|$ < 3 (2) cm

hadrons at low and high p_T, respectively. The TOF was only partially installed in 2008, and has not been included in the d+Au analysis due to limited acceptance. The details of the electron identification methods using the TPC, BEMC, and TOF, including the associated efficiencies of these detectors, are described below.

4.5.1 TPC dE/dx

The Time Projection Chamber has been used for track reconstruction and measuring particle ionization energy loss per unit length (dE/dx). The track momentum and dE/dx have been used to identify electrons, and this is illustrated in Fig. 4.15 for charged particles in Au+Au collisions. The expected dE/dx values for various particles obtained from the Bichsel functions [131] are also shown (lines).

In order to identify electrons, the dE/dx is normalized to the expected dE/dx for electrons obtained from the Bichsel functions (dE/d$x_{\rm Bichsel}$) and scaled by the dE/dx resolution ($\sigma_{{\rm d}E/{\rm d}x}$) to obtain the variable $n\sigma_e$. The variable $n\sigma_e$ is constructed to

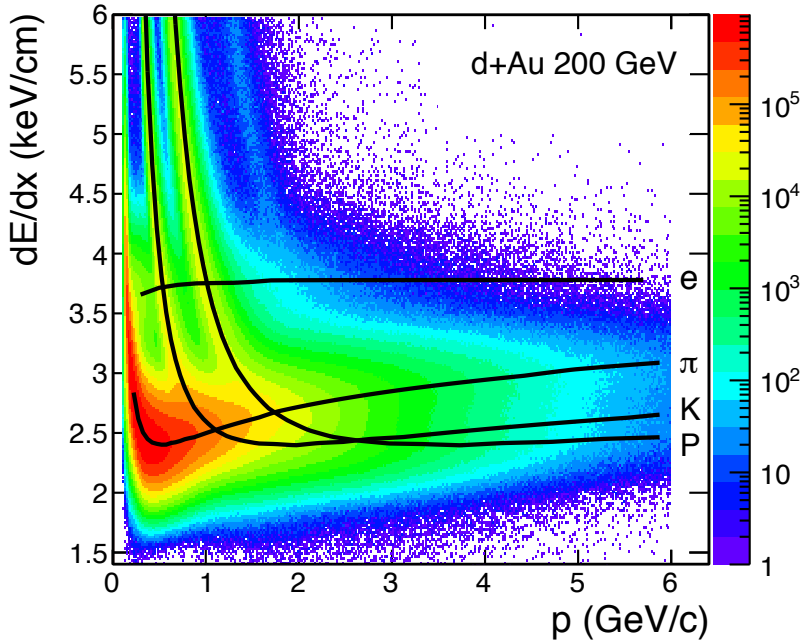

Figure 4.15: The energy loss per unit length, $\mathrm{d}E/\mathrm{d}x$, of charged particles in d+Au collisions. The solid lines indicate the expected $\mathrm{d}E/\mathrm{d}x$ obtained from the Bichsel functions [131].

follow a Gaussian distribution with a mean of 0 and width of 1, where

$$n\sigma_e = \log\left(\frac{\mathrm{d}E/\mathrm{d}x_{\mathrm{Measured}}}{\mathrm{d}E/\mathrm{d}x_{\mathrm{Bichsel}}}\right)/\sigma_{\mathrm{d}E/\mathrm{d}x}. \tag{4.1}$$

The measured mean and width of the $n\sigma_e$ distribution are not exactly equal to 0 and 1, respectively, and must be determined from data. Due to the overlap of the $\mathrm{d}E/\mathrm{d}x$ of different particles and significant contamination from hadrons, the electron $n\sigma_e$ shape cannot be directly extracted from the data. The $n\sigma_e$ distribution has been projected into small momentum bins and fitted with multiple Gaussian functions to take into account the various particle contributions so that the electron distribution can be understood. This is challenging as there are regions in which the $\mathrm{d}E/\mathrm{d}x$ of different particles overlaps completely, and this can cause ambiguity in the fitting. This becomes more difficult in Au+Au collisions where the background is higher.

The $n\sigma_e$ distribution has been calculated using the $\mathrm{d}E/\mathrm{d}x$ of all particles in Au+Au collisions, and is shown in Fig. 4.16 (black) for $0.8 < p < 0.9$ GeV/c (left panel) and $2.5 < p < 3$ GeV/c (right panel). The red shaded region ($n\sigma_e = 0 \pm 1$) indicates $\mathrm{d}E/\mathrm{d}x$ values close to the expected electron $\mathrm{d}E/\mathrm{d}x$ shown in Fig. 4.15, and represents the approximate mean and width of the electron distribution. However, the electrons cannot be seen clearly due to the significant hadron contamination. In order to suppress the hadron contamination in Au+Au collisions, the TOF has been used to identify electrons. The TOF is unable to separate pions from electrons, but can remove most other hadron contamination for $p < 1.5$ GeV/c. In addition to using the TOF, a small pair-wise mass of particles, $m_{\mathrm{ee}} < 10$ MeV/c^2, was required to select electrons from photon conversions to further reduce the background in Au+Au. The electron $n\sigma_e$ distribution obtained after applying both of these conditions is shown in Fig. 4.16 (green), and the electron peak is clearly visible.

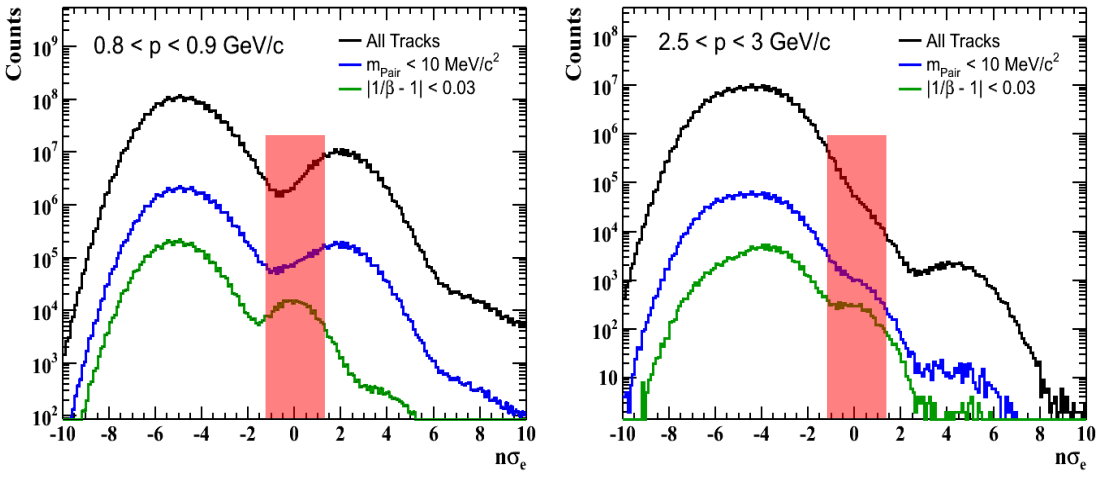

Figure 4.16: The $n\sigma_e$ distribution in Au+Au collisions for $0.8 < p < 0.9$ GeV/c (left) and $2.5 < p < 3$ GeV/c (right). The red band represents the approximate $\mathrm{d}E/\mathrm{d}x$ for electrons.

After enhancing the electron contribution in the $n\sigma_e$ distribution by using the TOF and selecting photonic electrons, multiple Gaussian fitting was performed on

the $n\sigma_e$ distribution to determine the shape of the electron contribution. This is shown for $1.8 < p < 2$ GeV/c in Au+Au collisions in Fig. 4.17, and the data (black histogram) has been fitted with a sum of Gaussian (solid line) to determine the electron (long dashed line), proton and kaon (dot-dahsed line), and pion (short dashed line) contributions. In this momentum range the TOF cannot completely remove the heavier hadrons, and the proton and kaon dE/dx bands cannot be distinguished and are described by a single Gaussian. The peak at $n\sigma_e \sim 5$ has been excluded from the fit, and is caused by merged pions whose tracks could not be distinguished in the TPC. The Bichsel functions have been used to determine the expected mean value of the hadrons along the $n\sigma_e$ axis (vertical lines), and the number of dE/dx hit points from data has been used to estimate the uncertainty in the expected mean dE/dx (shaded bands). This determines the fit range for the mean of each particle, which is indicated by the shaded bands in Fig. 4.17. The Gaussian fitting to the $n\sigma_e$ distribution has been performed as a function of momentum and collision centrality in Au+Au collisions. These results are summarized in Appendix B.2, along with further details on the fitting procedure.

The same approach has been used to fit the $n\sigma_e$ distribution in d+Au collisions, however the TOF was not available to remove the contribution from heavier hadrons. To avoid the large hadron contamination due to the overlap of kaons and protons with the electron dE/dx at ~ 0.6 GeV/c and ~ 1 GeV/c, respectively, only electrons with $p > 1.2$ GeV/c have been used for J/ψ reconstruction in d+Au collisions. As a result, the $n\sigma_e$ fitting in d+Au collisions has been performed for $p > 1$ GeV/c. In this range, the kaon dE/dx cannot be distinguished from the protons, and the kaons are included in the proton fit. Gaussian functions are fitted to the electron, pion, proton, and deuteron dE/dx. The deuteron contribution becomes negligible for $p > 2$ GeV, and they are excluded from the fitting in this range. To improve the fit to the electron Gaussian, the mean and width of the $n\sigma_e$ distribution for a high purity sample of photonic electrons was obtained. The values of $\mu = -0.3$ and $\sigma = 0.9$ were obtained and used to constrain the fitting to the electron $n\sigma_e$. A summary of the momentum dependence of the $n\sigma_e$ distributions and multiple Gaussian fitting in d+Au, as well

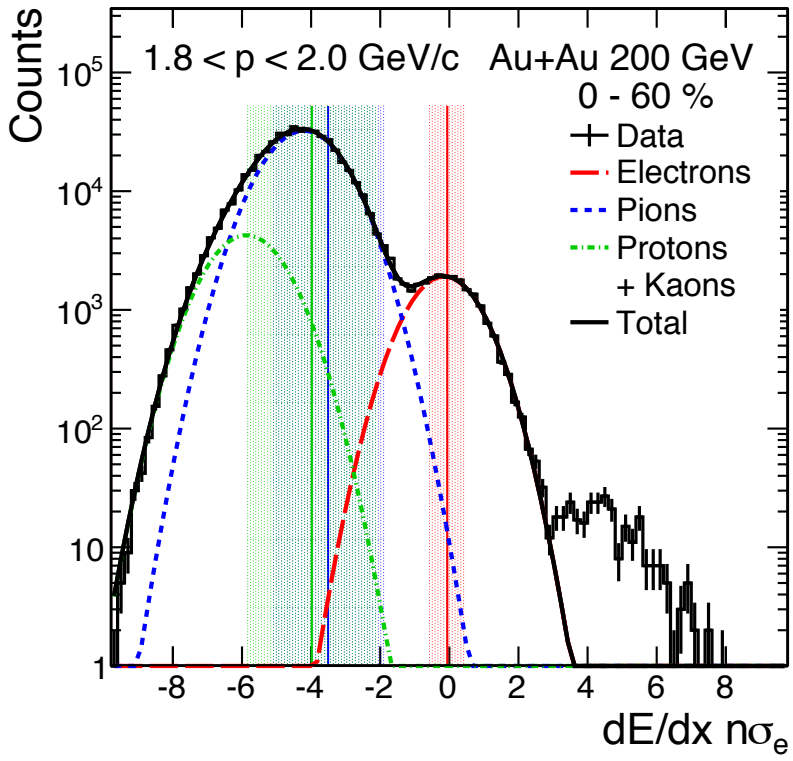

Figure 4.17: The $n\sigma_e$ distribution for $1.8 < p < 2$ GeV/c in $0-60\%$ central Au+Au collisions (black histogram). Gaussian distributions have been fitted to the data to obtain the electron (red), proton (green), and pion (blue) contributions.

as a detailed description of the fitting procedure, is provided in Appendix B.1.

The Gaussian fit parameters extracted from the $n\sigma_e$ distribution for various particles in d+Au and Au+Au collisions are summarized in Fig. 4.18 and Fig. 4.19, respectively. No fitting was performed to deuterons and protons with $p < 1.8$ GeV/c in Au+Au, as these were removed by the TOF. The kaons have also been removed by the TOF at low momentum, and their $\mathrm{d}E/\mathrm{d}x$ merges with the $\mathrm{d}E/\mathrm{d}x$ of other hadrons above 1 GeV/c. The Gaussian height (left), mean (middle), and width (right) exhibit a smooth behavior for each particle for most of the momentum range. There are some fluctuations in regions where the fitting was under-constrained due to the

overlap in $\mathrm{d}E/\mathrm{d}x$ of different particles. These fluctuations in the fit parameters have been taken into account in the systematic uncertainties, described in Chapter 6. The electron mean and width in Au+Au collisions exhibit a momentum dependence. This may be due to a momentum dependence on the normalization of the electron $\mathrm{d}E/\mathrm{d}x$, or an artificial effect from hadron contamination. This is also included in the systematic uncertainties. The centrality dependence of the $n\sigma_e$ distributions and Gaussian fit parameters in Au+Au collisions can be found in Appendix B.2.

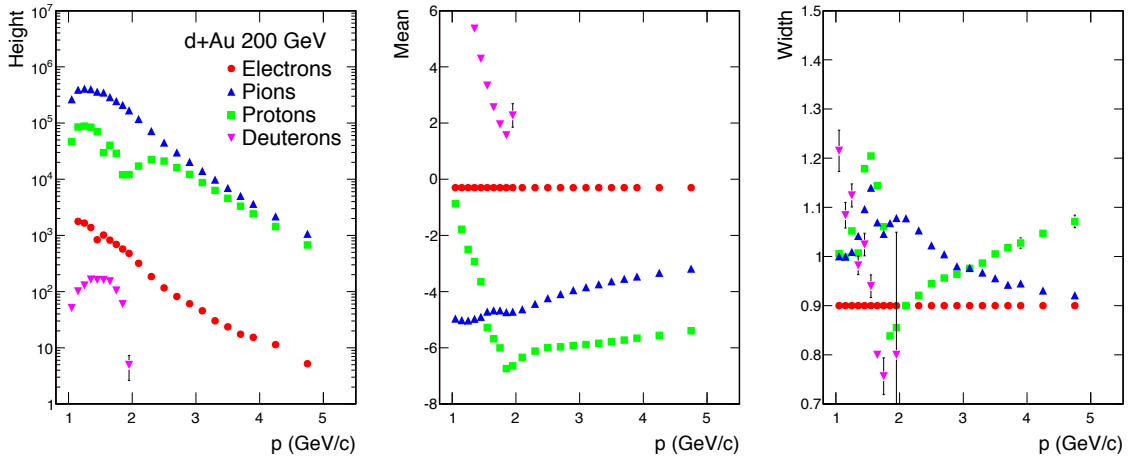

Figure 4.18: The height (left), mean (middle), and width (right) of the Gaussian functions fitted to the electrons (red circles), pion (blue upward triangles), protons (green squares), and deuterons (magenta downward triangles) in d+Au collisions versus momentum.

Tracks in d+Au collisions were required to have $|n\sigma_e| < 2.4$ to select electrons, and hadrons were rejected by requiring $|n\sigma_p| > 2.2$ and $|n\sigma_\pi| > 2.5$. These values were chosen to optimize the statistics and purity of the electron sample. Furthermore, only tracks with a transverse momentum of $p_T > 1.0$ GeV/c and momentum $p > 1.2$ GeV/c were accepted to remove hadron contamination from the protons and kaons.

In Au+Au collisions, the TOF was used to remove the contribution from heavier

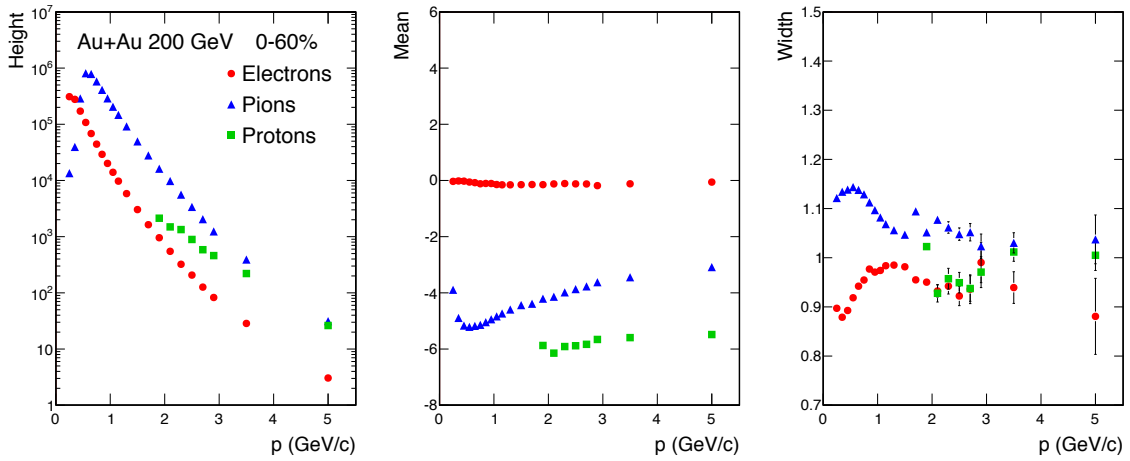

Figure 4.19: The height (left), mean (middle) and width (right) of the Gaussian functions fitted to the electrons (red circles), pions (blue triangles), and protons (green squares) in Au+Au collisions versus momentum.

particles such as kaons and protons at low momentum where their $\mathrm{d}E/\mathrm{d}x$ overlaps with that of the electrons. As a result, no conditions on track momentum or hadron $\mathrm{d}E/\mathrm{d}x$ were required in Au+Au. The TOF cannot separate pions and electrons, and was unable to reject other hadrons above 1.5 GeV/c. These contributions were removed by requiring $-1 < n\sigma_e < 2$, and an asymmetric cut was chosen to reject the large hadron contamination from pions and protons with $p > 1.5$ GeV/c which have $n\sigma_e \lesssim -1$. This requirement accepts most electrons while rejecting the large majority of hadrons, as can be seen in Fig. 4.17. The efficiency and purity associated to identifying electrons using $\mathrm{d}E/\mathrm{d}x$ are discussed in the following section.

4.5.2 TOF $1/\beta$

The mass of electrons is negligible in the momentum range considered in this analysis, and as a result they have a velocity $\beta \equiv v/c \sim 1$. Heavier particles will travel slower at a given momentum, and the TOF can be used to separate these from the electrons by measuring the particle flight time and velocity. As the momentum of particles

increases, their velocity approaches c and hadrons can no longer be separated from electrons. The TOF can be used to separate electrons from heavier hadrons up to $p \sim 1.5$ GeV/c, but cannot remove pions due to their small mass.

Tracks in the TPC are matched to the TOF in order to calculate their flight time and velocity. The TOF $1/\beta$ distribution is shown in Fig. 4.20 as a function of TPC momentum for all charged particles in Au+Au collisions (left panel). The expected $1/\beta$ has been calculated using the mass of each particle [136], and these are also shown (lines). The $1/\beta$ distribution for electrons with $0.2 < p < 0.4$ GeV/c is shown in Fig. 4.20 (right panel), and has been fitted with a Gaussian function to obtain a width of $\sigma = 0.01$. Electrons are identified by requiring $|1/\beta - 1| < 0.03$, corresponding to a 3σ cut around $1/\beta = 1$.

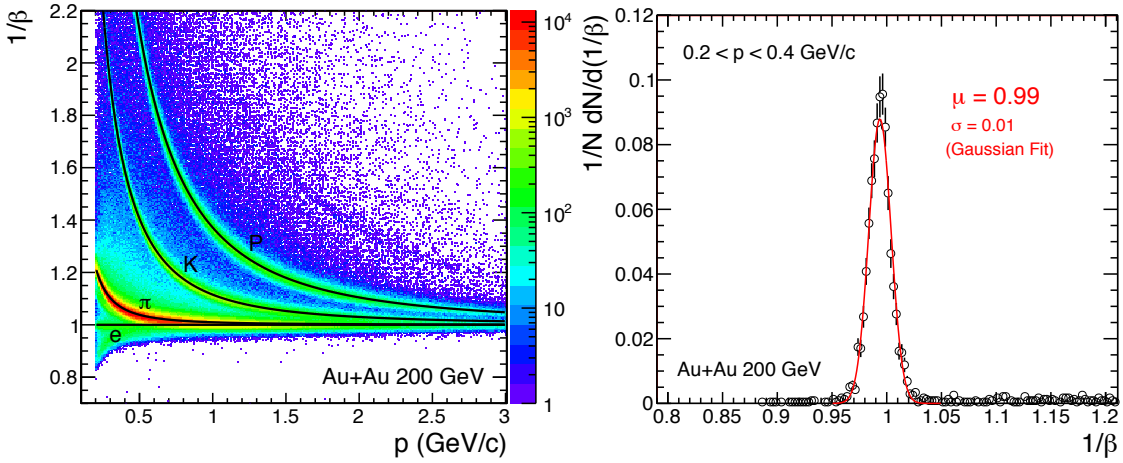

Figure 4.20: The TOF $1/\beta$ versus TPC momentum for all charged particles in Au+Au collisions (left panel). The lines indicate the expected value for various particles. The $1/\beta$ for electrons with $0.2 < p < 0.4$ GeV/c (right panel) is fitted with a Gaussian.

The dE/dx distribution for charged particles in Au+Au collisions is shown in Fig. 4.21 before using the TOF (left panel), and after matching to the TOF and requiring $|1/\beta - 1| < 0.03$ (right panel). This illustrates the electron identification

capabilities of the TOF, as heavier hadrons such as kaons, protons, and deuterons, have been removed. The pion and electron dE/dx bands are clearly visible, and the remaining hadrons were removed using dE/dx by requiring $-1 < n\sigma_e < 2$. The TOF is less effective at separating heavier hadrons from electrons at high momentum, and is only used to identify electrons with $p < 1.5$ GeV/c in Au+Au collisions. The TOF was not fully installed during the 2008 d+Au taking and has not been used for particle identification in d+Au collisions.

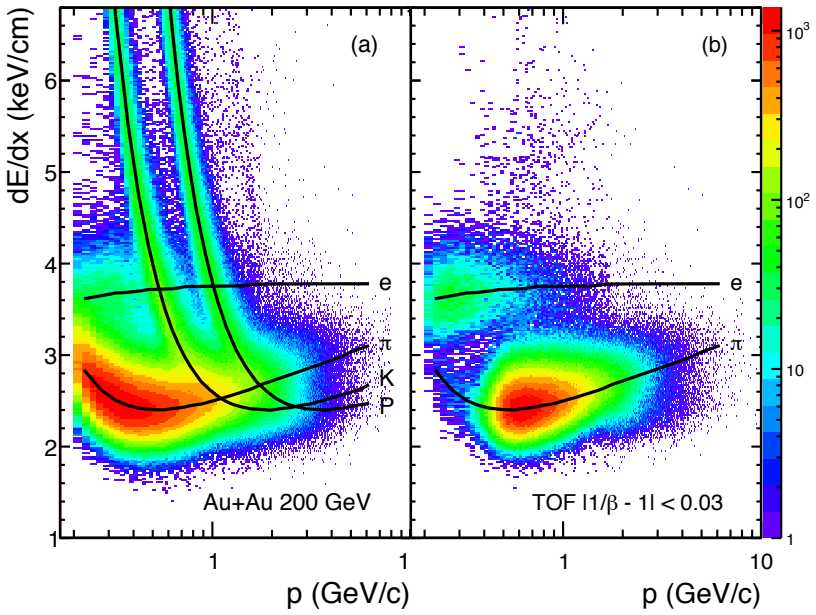

Figure 4.21: The TPC dE/dx versus momentum for charged particles in Au+Au collisions (left panel). Heavier hadrons are removed using the TOF by requiring $|1/\beta - 1| < 0.03$ (right panel). The expected values for various particles are shown (lines) and are obtained from the Bichsel functions [131].

4.5.3 BEMC E/p

The BEMC has been used to discriminate between electrons and hadrons and to improve the purity of the electron candidates used for J/ψ reconstruction. This was done by considering the energy deposited in the BEMC towers (BTOW), and the shower shape obtained by the BEMC shower maximum detector (BSMD). The energy deposited by electrons in the BTOW is approximately equal to their momentum, and electrons can be identified from their energy-to-momentum ratio $E/p \sim 1$. Electromagnetic showers are also more developed than hadronic showers, and the BSMD η and ϕ strips can be used to distinguish between electrons and hadrons. The BSMD can also be used to determine the position of the shower more accurately than the BTOW.

Tracks in the TPC were projected outwards to the BEMC to determine the η and ϕ coordinates of the particle as it struck the BEMC. The simplest method used to reconstruct the energy of a particle in the BEMC was to identify the tower that the particle struck (t_1) and obtain the corresponding tower energy (E_1). The struck tower was identified by matching the track and tower η and ϕ coordinates, and the position of the energy deposition was taken as the center of the tower position. Towers were required to have an energy greater than the threshold energy $E_T = 200$ MeV to remove false matches due to noise in the electronics. This value was obtained by fitting a Gaussian function to the noise peak in the energy spectrum at $E = 0$ GeV and excluding energies within 5σ.

The Molière radius for electrons in lead is $R_M \sim 1.6$ cm, and electrons will deposit $\sim 95\%$ of their shower in a cylinder of radius $2R_M$ [118]. At midrapidity, the BEMC tower size is $\sim 10 \times 10$ cm^2, and electrons that strike near the center of a tower will deposit their entire energy into a single tower. However, electrons that hit near the edge of a tower may deposit their energy in more than one tower. In order to reconstruct the full electron energy in d+Au, neighboring towers were clustered together to form the tower cluster energy E_n. The clustering was performed by identifying t_1 and considering this and the 8 surrounding towers, forming a 3×3 tower grid.

Smaller clusters were formed by considering the 3 closest towers to the TPC track at the BEMC surface within the 3×3 tower grid. The BEMC energy spectrum for particles with $p > 1$ GeV/c in d+Au collisions is shown in Fig. 4.22. The energy obtained from a single tower (circles) has been compared to the energy obtained from a 3 tower cluster (squares) and a 9 tower cluster (triangles). There is an increase in the energy when using more than one tower for the energy reconstruction, resulting in a more accurate measure of the electron energy, however no improvement was found when using more than 3 towers. The final BEMC energy used in d+Au collisions was obtained from the 3 tower cluster energy E_3.

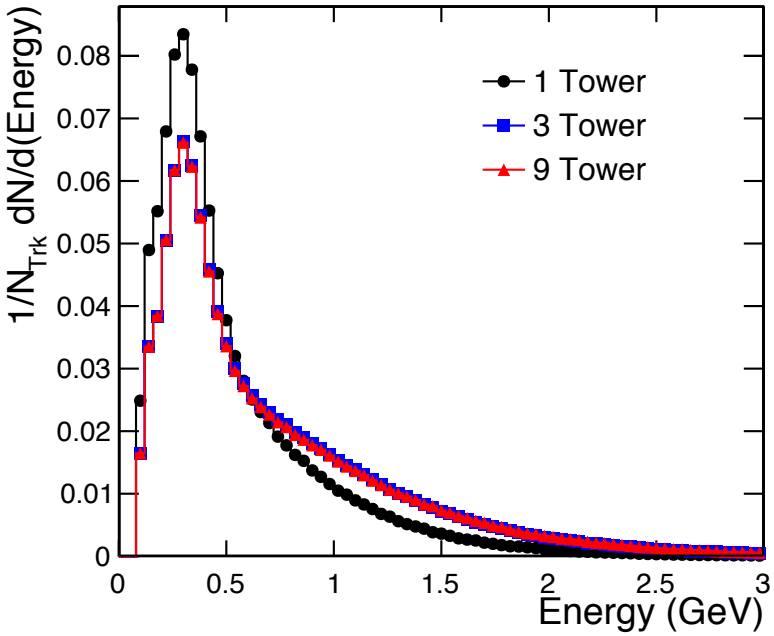

Figure 4.22: The BEMC energy spectrum for particles with $p > 1$ GeV/c in d+Au collisions.

The energy reconstructed in the BEMC has been used to identify electrons from their energy-to-momentum ratio E/p, where E is BEMC energy, and p is the momentum obtained from the TPC. Electrons in d+Au have been identified using the

TPC by requiring $|n\sigma_e| < 2.4$, $|n\sigma_p| > 2.2$, and $|n\sigma_\pi| > 2.5$, and the E/p distribution for tracks satisfying these constraints with $2 < p < 3$ GeV/c is shown in Fig. 4.23 (circles). There is a significant amount of hadron contamination which populates the low E/p. The electron E/p, which is approximately Gaussian with a mean of 1, can be seen in excess of the hadron contamination. The E/p distribution from a pure hadron sample (triangles) obtained by requiring $|n\sigma_e| > 3$ has been scaled using the purity obtained from the $n\sigma_e$ distributions, and replicates the hadron contamination well. This illustrates the electron-hadron discrimination capabilities of the BEMC, and hadrons in d+Au have been rejected by requiring $E/p > 0.5$.

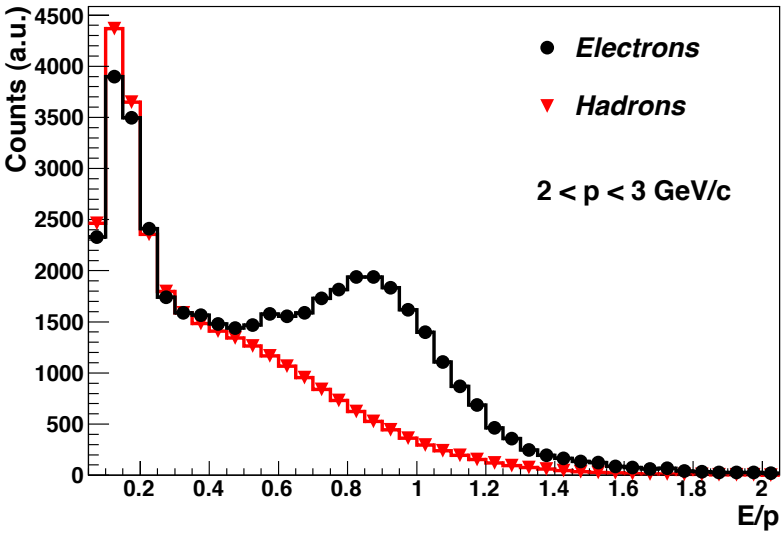

Figure 4.23: The E/p distribution for electron candidates (circles) and hadrons (triangles) with $2 < p < 3$ GeV/c in d+Au collisions.

To understand the shape of the E/p distribution for electrons, a high purity sample of electrons has been obtained by applying more stringent requirements on dE/dx. An electron sample with a purity of $> 95\%$ has been obtained in d+Au, however this is only used to study the detector response to electrons as the statistics

are too limited for J/ψ reconstruction. The E/p distribution for a high-purity electron sample with $1 < p < 1.5$ GeV/c in d+Au is shown in Fig. 4.24 (black). The distribution is fitted with a Gaussian (dashed line), which describes the distribution well for $0.7 < E/p < 1.2$. The E/p distribution in d+Au has also been obtained using a Monte Carlo simulation, where electrons are embedded into real data events to determine the BEMC response, and this is shown in Fig. 4.24 (red). The distribution from simulation is slightly narrower than the data, which may be due to an under-estimated energy or momentum resolution in the simulation, or from hadron contamination in the data. The difference between these distributions is included in the systematic uncertainties, and these are discussed in Chapter 6.

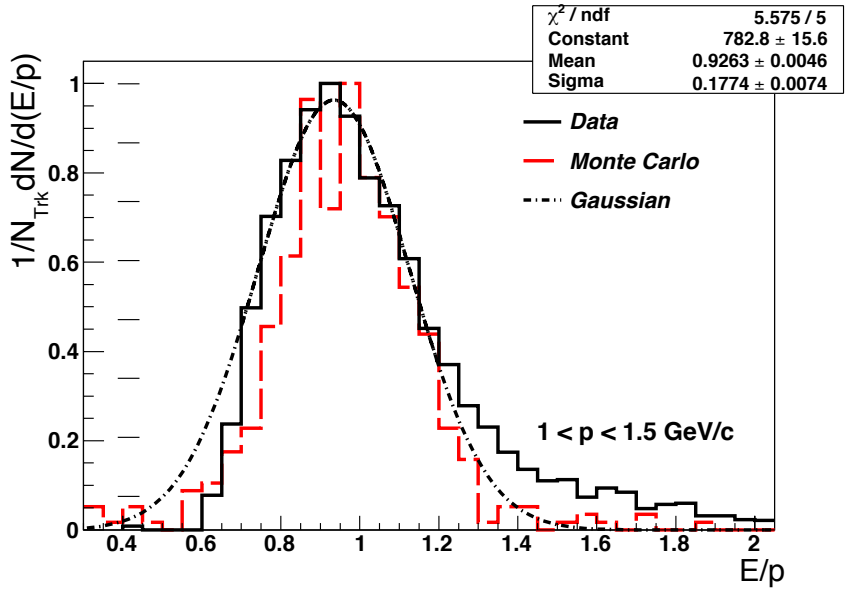

Figure 4.24: The BEMC E/p distribution for electrons with $1 < p < 1.5$ GeV/c in d+Au collisions from data (solid line) and simulation (dashed line). A Gaussian is fitted to the data (dot-dashed line).

The clustering of neighboring towers in the BEMC is an effective tool in reconstructing the electron energy in the low occupancy d+Au environment. However, due to the high background rates in the more energetic Au+Au collisions, this method can

over-estimate the energy of electrons. Instead, only a single tower was used to determine the electron energy in Au+Au. The E/p distribution for a high-purity electron sample in Au+Au has been obtained using $\mathrm{d}E/\mathrm{d}x$, TOF, and selecting electrons from photonic conversions, and this is shown in Fig. 4.25 for various energy reconstruction methods. The E/p shape obtained using the single tower energy E_1 (black circles) peaks at 0.9, and has a non-Gaussian low-E/p tail due to energy being shared between towers. In order to improve the energy reconstruction in Au+Au collisions, the 3 closest towers to the electron track were considered and the tower with the highest energy (E') was used. The E/p distribution obtained using E', the highest-energy of the 3 closest towers, is also shown (blue triangles). The non-Gaussian low-E/p tail has disappeared, illustrating the improvement of using the maximum energy tower. The BSMD has been used to improve the reconstruction of the energy in the BEMC. Information on the position of the energy deposit from the BSMD has been combined with the tower energy from the BTOW to form *hits*. The E/p distribution obtained using the highest energy tower within the hit is shown (green closed squares), and is consistent with the E/p distribution obtained without the BSMD. The E/p distribution has also been obtained using the sum of the energy of the towers associated to the hit (magenta open squares). This distribution has a mean greater than one and a non-Gaussian tail at high E/p, illustrating that this method over-estimates the energy in Au+Au due to the large background.

The distance (R) between a track and an energy deposit is calculated in $\eta - \phi$ coordinates at the BEMC radius, where $R = \sqrt{\Delta\eta^2 + \Delta\phi^2}$. The resolution of the distance is limited by the tower size of $\Delta\eta \times \Delta\phi = 0.05 \times 0.05$. The distance R between tracks and the matched tower t_1 for electrons in Au+Au collisions is shown in Fig. 4.26 (black circles). The distribution shape is defined by the tower size and has a maximum of 0.035 and peaks at 0.025. The distance between electrons and the tower with the maximum energy (t') is also shown in Fig. 4.26 (blue triangles). The distribution exhibits a softer peak and a tail extending beyond 0.035, corresponding to instances where a neighboring tower containing more energy was selected instead.

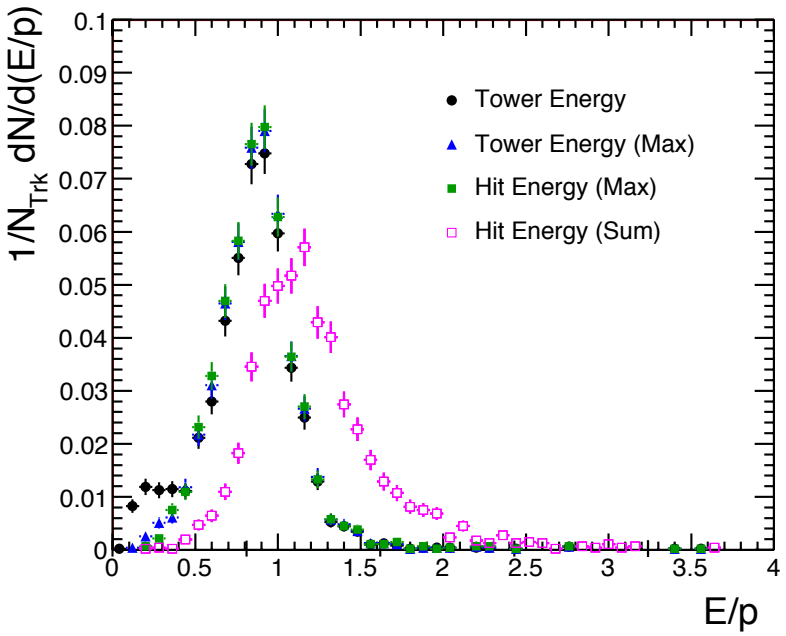

Figure 4.25: The E/p distribution for electrons with $2 < p < 5$ GeV/c in Au+Au collisions obtained using the single tower energy (black closed circles), the maximum tower energy (blue closed triangles), the hit maximum tower energy (green closed squares), and the hit summed tower energy (magenta open squares).

The BSMD measures the shape and position of electromagnetic showers in the BEMC using wire chambers along η and ϕ, which have dimensions of $\Delta\eta \times \Delta\phi = 0.01 \times 0.05$ and 0.05×0.01, respectively. The shower position from the BSMD has been combined with the energy in the BTOW to form hits in the BEMC to improve the matching precision, and the distance between electrons and the hit position obtained using the BSMD for Au+Au collisions is shown in Fig. 4.26 (green squares). The distribution is narrower than when using the BTOW only, and peaks at 0.005. The number of BSMD η and ϕ strips can also be used to further discriminate between electrons and hadrons from their shower shape, but this was not used in this analysis due to the impact on statistics.

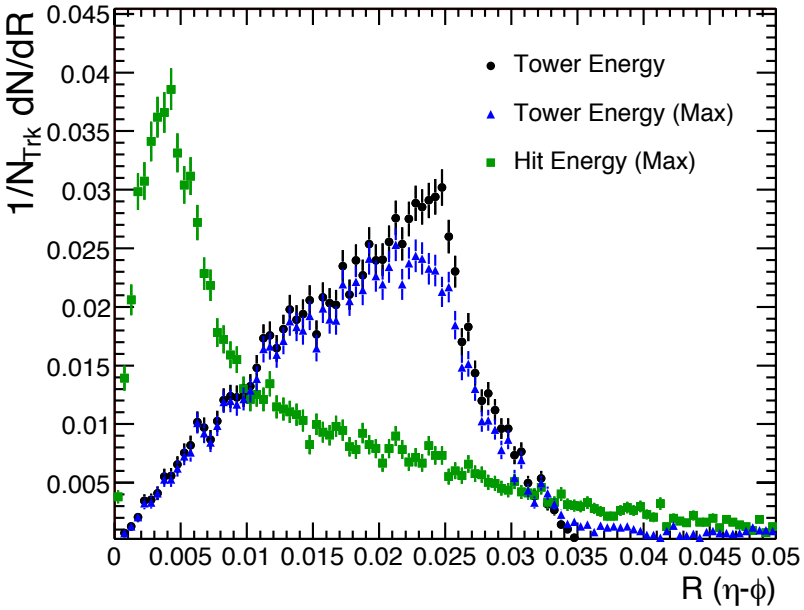

Figure 4.26: The distance in $\eta - \phi$ coordinates between electron tracks from the TPC and energy depositions in the BEMC in Au+Au collisions.

The distance and E/p distributions obtained using the BTOW+BSMD in Au+Au have been compared to the distributions obtained from simulation, and this is shown in Fig. 4.27 for electrons with $3 < p < 5$ GeV/c. The data (circles) exhibit a slightly wider distribution the simulation (triangles), consistent with the trend observed in the d+Au data. Electrons in Au+Au have been identified by requiring $0.5 < E/p < 1.5$. To remove false matches to the BEMC in Au+Au collisions, electrons were required to have $R < 0.035$. A detailed comparison of the distance and E/p distributions in Au+Au can be found in Appendix C.2. At lower momentum, the BEMC efficiency decreases and the electron-hadron discrimination is poor. As a result, the BEMC has been used for $p > 1.5$ GeV/c in Au+Au collisions to compliment the electron identification capabilities of the TOF.

In summary, electron identification in d+Au has been performed using the TPC

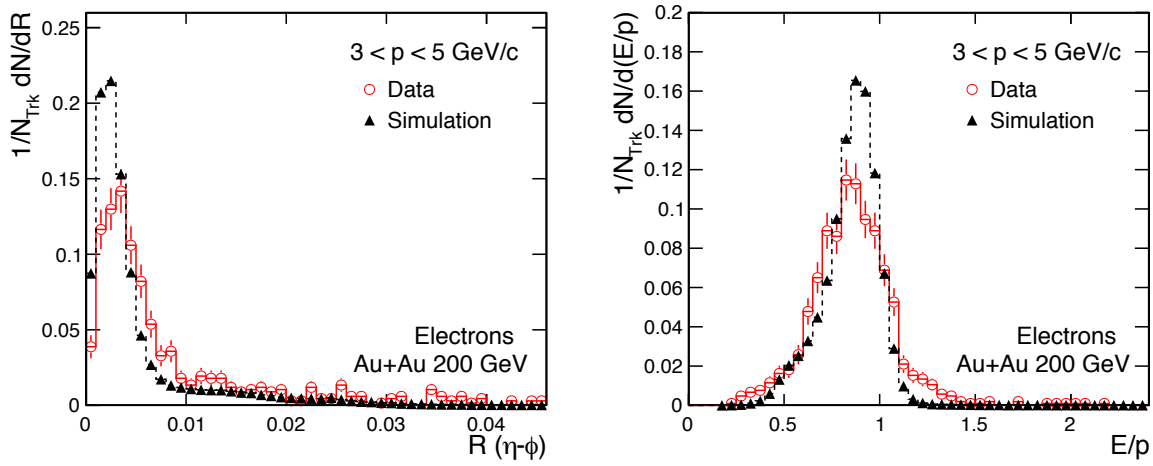

Figure 4.27: The distance between electrons and energy deposits in the BEMC (left) and the E/p ratio for electrons with $R < 0.035$ (right) from simulation (circles) and data (triangles) for electrons with $3 < p < 5$ GeV/c in Au+Au collisions.

dE/dx and BEMC E/p. To remove hadron contamination, tracks in d+Au collisions were required to have $p > 1.2$ GeV/c and $p_T > 1$ GeV/c. This was not necessary in Au+Au, as the TOF $1/\beta$ was used in addition to dE/dx to provide improved electron identification for $p < 1.5$ GeV/c in Au+Au, while the BEMC E/p was used for $p > 1.5$ GeV/c. The electron identification requirements are summarized in Table 4.7 for d+Au collisions, and in Table 4.8 for Au+Au collisions. The efficiencies associated with the electron identification requirements are described in the following section.

4.6 Identification Efficiency

Tracks reconstructed in the TPC that pass the quality cuts discussed earlier in this chapter have been subjected to various electron identification requirements using the TPC, TOF, and BEMC. These conditions, summarized in Table 4.7 and 4.8, have been chosen to maximize the number of accepted electrons while removing as much hadron contamination as possible in order to obtain a high quality J/ψ signal. The

Table 4.7: Electron identification requirements in d+Au collisions.

TPC	$p_T > 1$ GeV/c
	$p > 1.2$ GeV/c
	$\lvert n\sigma_e \rvert < 2.4$
	$\lvert n\sigma_p \rvert > 2.2$
	$\lvert n\sigma_\pi \rvert > 2.5$
BEMC	$E/p > 0.5$

Table 4.8: Electron identification requirements in Au+Au collisions.

TPC	$-1 < n\sigma_e < 2$
TOF ($p < 1.5$ GeV/c)	$\lvert 1/\beta - 1 \rvert < 0.03$
BEMC ($p > 1.5$ GeV/c)	$0.5 < E/p < 1.5$
	($R < 0.035$)

efficiency of reconstructing a J/ψ using the analysis methods described in this chapter was calculated to correct the measured J/ψ spectrum for detector effects to obtain the invariant J/ψ yield. The TPC acceptance and tracking efficiency, including the track quality constraints on `nHitsFit`, `nHitsRatio`, and `DCA`, were determined using a simulation of Monte Carlo J/ψs embedded into real data, and details on this are provided in the following section. Tracks passing these conditions were subjected to the electron identification requirements, and the electron identification efficiency is defined as the fraction of electrons satisfying these conditions. The TPC, TOF, and BEMC electron identification efficiencies are described below.

4.6.1 TPC $\mathrm{d}E/\mathrm{d}x$

The TPC has been used to identify electrons and reject hadrons using $\mathrm{d}E/\mathrm{d}x$, and the $n\sigma$ electron identification requirements are listed in Table 4.7 and 4.8. Multiple Gaussians have been fitted to the $\mathrm{d}E/\mathrm{d}x$ $n\sigma_e$ distribution to determine the electron and hadron contributions, and the details are described in Appendix B.1 and Appendix B.2 for d+Au and Au+Au collisions, respectively. The electron identification efficiency (ε) is defined as the fraction of electrons that satisfy the identification requirements:

$$\varepsilon = \frac{\text{accepted electrons}}{\text{all electrons}}. \tag{4.2}$$

Some hadrons may also pass the identification requirements, and the electron purity (p) is defined as the fraction of accepted tracks that are electrons:

$$p = \frac{\text{accepted electrons}}{\text{accepted electrons + accepted hadrons}}. \tag{4.3}$$

The $\mathrm{d}E/\mathrm{d}x$ identification efficiency was determined using the Gaussian fit parameters summarized in Fig. 4.18 and 4.19. In Au+Au collisions, electrons were identified by requiring $-1 < n\sigma_e < 2$. The Gaussian function fitted to the electron $n\sigma_e$ distribution was used to determine the efficiency by calculating the fraction of electrons satisfying $-1 < n\sigma_e < 2$. The resulting $n\sigma_e$ electron identification efficiency in Au+Au collisions for $0-60\%$ collision centrality is shown in Fig. 4.28 (solid circle), and ranges from $78-88\%$. The purity (open square) has been calculated from the data used in the $n\sigma_e$ electron Gaussian fitting which satisfy $|1/\beta - 1| < 0.03$ and $m_{\mathrm{ee}} < 10$ MeV/c^2, with the additional requirement that $-1 < n\sigma_e < 2$. The $n\sigma_e$ fit parameters, efficiency, and purity as a function of momentum and collision centrality can be found in Appendix B.2, and the efficiency decreases in more central events.

The $\mathrm{d}E/\mathrm{d}x$ efficiency calculation in d+Au was less straightforward, as rejection cuts were placed on the pions and protons since the TOF was not available. To determine the combined efficiency of these cuts, the fraction of electrons passing all of

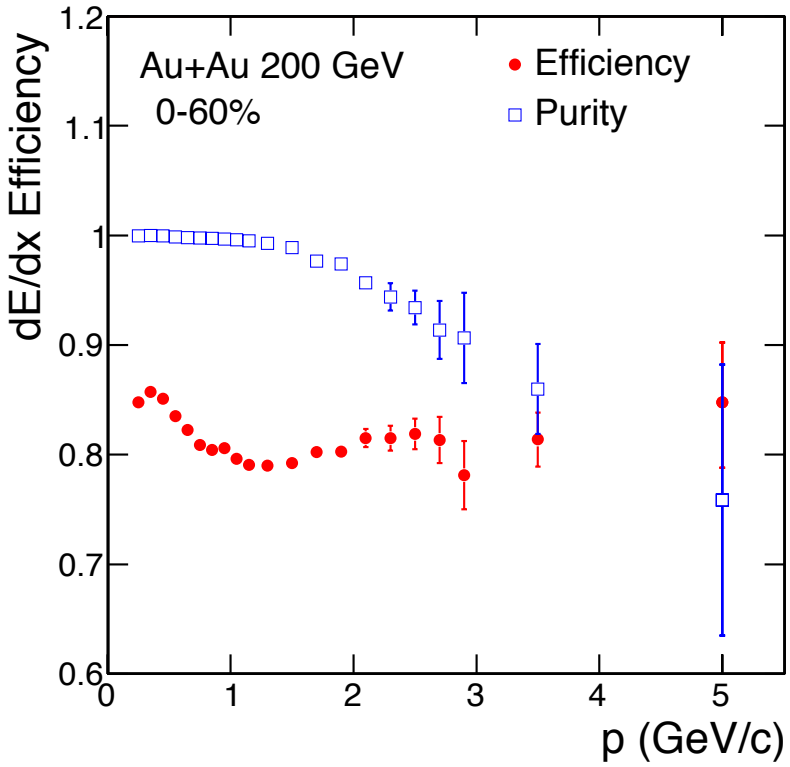

Figure 4.28: The $n\sigma_e$ electron identification efficiency for 0-60% central Au+Au collisions (solid circle). The purity of photonic electrons within $-1 < n\sigma_e < 2$ from the $n\sigma_e$ fit distributions is also shown (open square).

these conditions must be computed. This requires knowing the distribution shape of electrons in $n\sigma_p$ and $n\sigma_\pi$, which has been determined using a Monte Carlo simulation. Protons, pions, and deuterons were generated according to a Gaussian distribution with $\mu = 0$ and $\sigma = 1$ in $n\sigma_p$, $n\sigma_\pi$, and $n\sigma_d$ space, respectively. Electrons were simulated according to the mean and width extracted from the Gaussian fitting to the $n\sigma_e$ distribution. The relative particle abundances in each momentum bin were also determined from the Gaussian fits to the $n\sigma_e$ distribution. Within each momentum bin, particle yields were assumed to have an exponential drop-off with momentum, $dN/dp \sim \exp(-p/T)$. To determine which particles satisfy the $n\sigma$ requirements, values of $n\sigma_e$, $n\sigma_p$, and $n\sigma_\pi$ were calculated for each particle. This was done using the

expected $\mathrm{d}E/\mathrm{d}x$ for each particle obtained from the Bichsel functions and the mean and width obtained from the Gaussian fitting to the $n\sigma_e$ distribution.

The electron $\mathrm{d}E/\mathrm{d}x$ identification efficiency in d+Au is shown in Fig. 4.29 (circles), and is $\sim 80-97\%$ in $1.5 < p < 5$ GeV/c. The efficiency drops off below this because of the overlap of the electron and proton $\mathrm{d}E/\mathrm{d}x$ at $p \sim 1$ GeV/c. The purity of the electrons passing the $n\sigma$ cuts is also shown (triangles) and is $\sim 25-40\%$. The purity increases to $\sim 45-70\%$ when applying the BEMC E/p requirements (squares). The bars on the data points represent the statistical errors, and the color bands represent the systematic uncertainty. The sources for the systematic uncertainty are primarily from the method used to calculate the efficiency from the Gaussian fit parameters, and are described in Chapter 6.

A higher $\mathrm{d}E/\mathrm{d}x$ efficiency was obtained for $p > 1.4$ GeV/c in d+Au collisions compared to Au+Au collisions. This is because tighter selection criteria were placed on $n\sigma_e$ in Au+Au due to the increased background from hadrons. To improve the Gaussian fitting to the $n\sigma_e$ distribution, this background was suppressed by using the TOF to select electrons and by requiring $m_{\mathrm{ee}} < 10$ MeV/c^2 to select a pure sample of electrons from photonic conversions. The purity of this electron sample (shown in Fig. 4.28) is not an indication of the purity of the electrons used for J/ψ reconstruction in Au+Au collisions. The purity for electrons satisfying $-1 < n\sigma_e < 2$ in Au+Au collisions is smaller than the efficiency shown in Fig. 4.28, and decreases in central collisions.

4.6.2 TOF $1/\beta$

The efficiency and acceptance of matching a track to the TOF in Au+Au collisions was obtained from a high purity sample of electrons ($> 95\%$) from data by requiring $0 < n\sigma_e < 2$ and $m_{\mathrm{ee}} < 10$ MeV/c^2. The efficiency was calculated from the ratio of all electron candidates to those which were successfully matched to the TOF. The

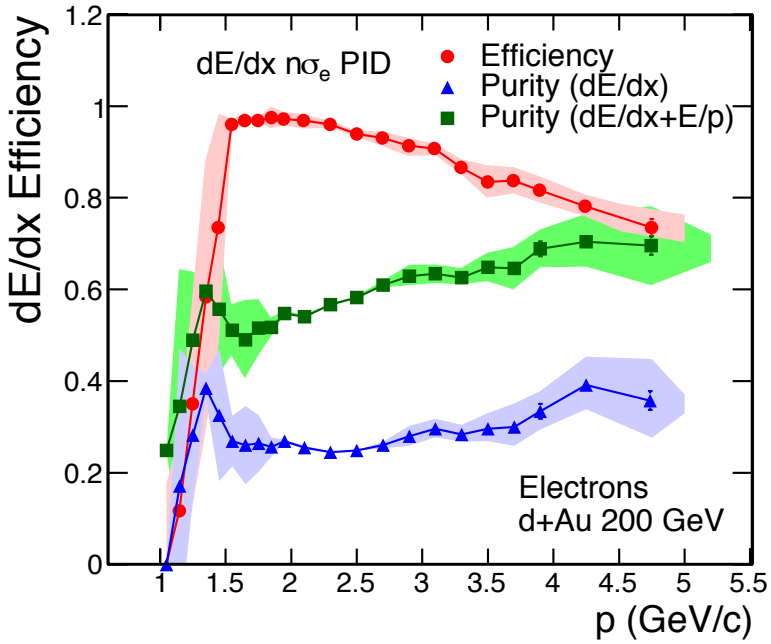

Figure 4.29: The electron dE/dx identification efficiency (circles), and purity (triangles) in d+Au. The purity for tracks satisfying the dE/dx and E/p requirements is also shown (squares). The systematic uncertainties are indicated by the shaded bands.

TOF efficiency is shown versus momentum in Fig. 4.30 (left panel) for $0-60\%$ central Au+Au collisions (red open circles). The purity of the electron sample is poor for $p_T < 1$ GeV/c due to the dE/dx crossing of the electrons with kaons and protons, and the efficiency in this range is biased towards the hadron efficiency. The TOF matching efficiency has been obtained for hadrons using $|n\sigma_e| > 3$, and this is also shown (blue open circles). Above 1 GeV/c the hadrons and electrons exhibit a similar trend, with the electron matching efficiency systematically above that of the hadrons.

The electron and hadron TOF matching efficiency have been compared as a function of momentum, pseudorapidity, and centrality, and the details can be found in Appendix C.1. The two distributions exhibit a similar behavior for $p_T > 1.2$ GeV/c

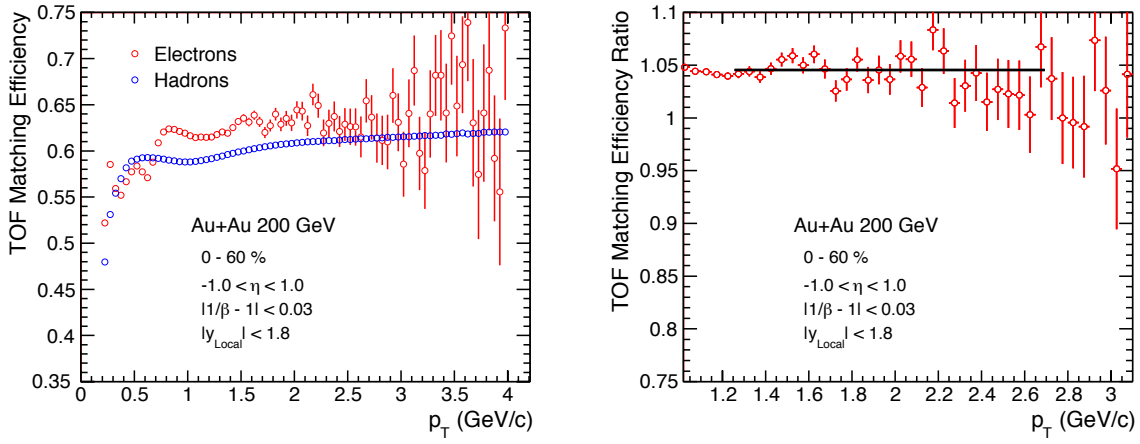

Figure 4.30: Left: The TOF matching efficiency versus p_T for electrons (red circles) and hadrons (blue circles) in 0-60% central collisions. Right: The ratio of the TOF matching efficiency for electrons and hadrons (open circles). A constant function has been fitted to the data for $p_T > 1.2$ GeV/c.

where the purity of the electron sample is high, and across the pseudorapidity and centrality range. Since the electron statistics are limited, and a pure electron sample for low momentum is hard to achieve, the TOF matching efficiency obtained from hadrons has been used to correct the data. The ratio of the electron and hadron matching efficiency is shown in Fig. 4.30 (right panel), and a constant function has been fitted to this for $p_T > 1.2$ GeV/c. The TOF matching efficiency for electron was found to be $4.5 \pm 0.3\%$ higher than that of hadrons, and this has been used to scale the hadron efficiency. The TOF matching efficiency from scaled hadrons in Au+Au has been used to correct the data as a function of transverse momentum, pseudorapidity, and collision centrality, and the centrality dependence is shown in Fig. 4.31. The efficiency exhibits a centrality ordering, with a higher efficiency achieved in more peripheral events due to the decreased occupancy in the detectors. The pseudorapidity dependence can be found in Appendix C.1, and the efficiency decreases towards $|\eta| \sim 1$.

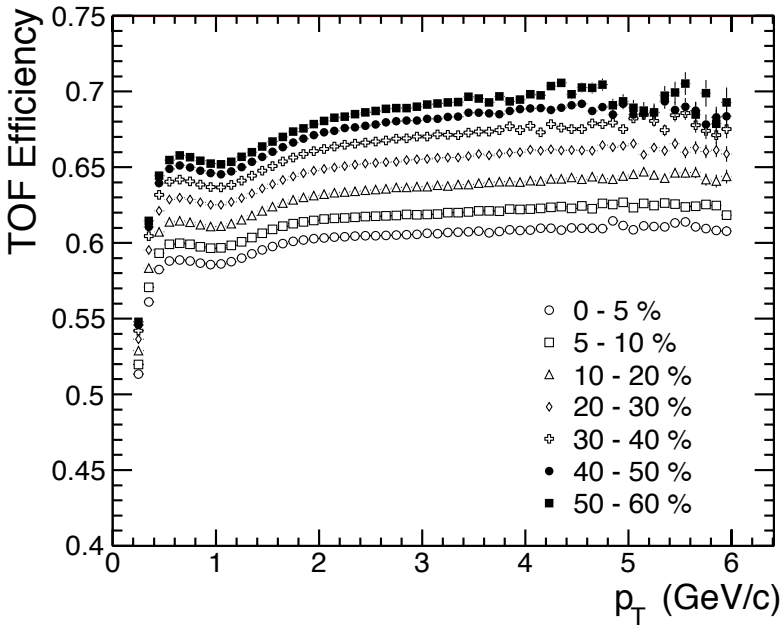

Figure 4.31: The centrality dependence of the TOF matching efficiency for $|\eta| < 1$ in Au+Au collisions. The efficiency is obtained from hadrons and scaled to match the electrons.

Once tracks are matched to the TOF, they are required to have $|1/\beta - 1| < 0.03$ to select electrons and reject heavier hadrons. The $1/\beta$ distribution is shown in Fig. 4.20 for electrons with $0.2 < p < 0.4$ GeV/c. The distribution has been fitted with a Gaussian function in various momentum bins, and is shown in Appendix C.1. The efficiency is determined from the fraction of electrons with $|1/\beta - 1| < 0.03$, and is $\sim 96 - 99\%$. The distributions do not exhibit a strong momentum dependence or centrality dependence. The efficiency has been calculated as a function of momentum, and no centrality dependence have been taken into account. The uncertainties from the TOF matching and $1/\beta$ efficiency are described in Chapter 6.

4.6.3 BEMC E/p

Electron candidates in the TPC are projected to the BEMC and matched to an energy cluster to determine their energy-to-momentum ratio E/p. In d+Au, the energy of the 3 closest towers to the track were summed to determine the cluster energy, E_3. In Au+Au, only the highest energy tower was used, as background levels were too high to sum neighboring towers. Furthermore, constraints were placed on the distance between tracks and energy deposits in Au+Au collisions, as the probability of false matching increases significantly from d+Au. To improve the precision of the energy position in the BEMC, the BSMD was used in addition to the BTOW in Au+Au collisions.

The efficiency of matching an electron to the BEMC has been determined by obtaining a high purity electron sample from data, and computing the fraction of electrons that are successfully matched to the BEMC with a reconstructed energy above $E_T = 200$ MeV. The efficiency of matching electrons in $0 - 60\%$ central Au+Au collisions to the BEMC with $R < 0.035$ is shown in Fig. 4.32 using the BTOW only (circles), and using the BTOW+BSMD (squares). The efficiency obtained using the BTOW only is consistent with the BEMC matching efficiency in d+Au collisions, and is $\sim 85\%$ for $p > 1.5$ GeV/c. This decreases for $p < 2$ GeV/c when using the BSMD.

The same methods of matching tracks to the BEMC were performed in simulation. Monte Carlo electrons were embedded into real data events and propagated through the detector. The tracks reconstructed from the Monte Carlo electrons were matched to the BEMC to determine the detector performance. The BEMC matching efficiency obtained using the BTOW+BSMD with $R < 0.035$ in Au+Au collisions is shown in Fig. 4.33 for data (open circles) and simulation (triangles). The efficiency from data is lower than the simulation, and the same trend is observed when using the BTOW only. This is mostly due to the difference in the distance between tracks and energy clusters in simulation and data. The distance and E/p distributions from simulation and data are compared in Appendix C.2, and the differences are discussed in Chapter 6.

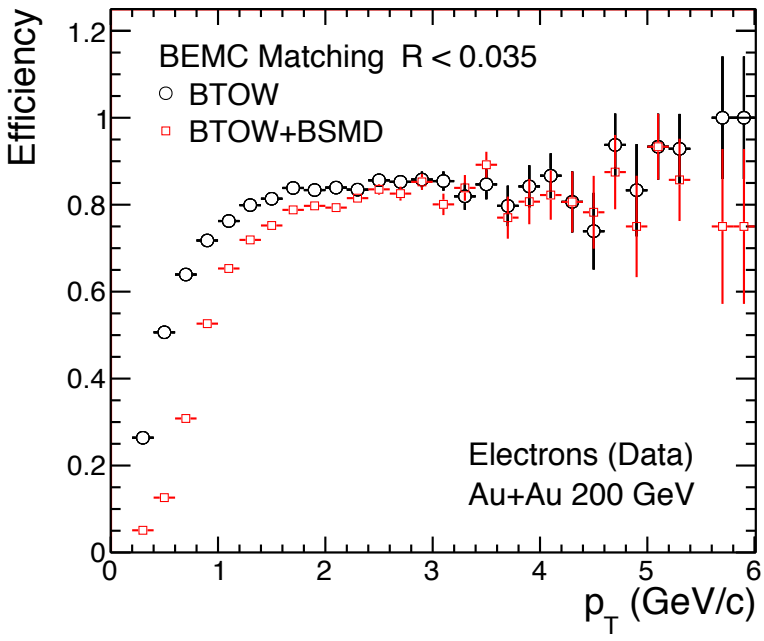

Figure 4.32: The BEMC matching efficiency versus p_T for $|\eta| < 1$ in Au+Au collisions obtained from data using the BTOW with $R < 0.035$ (circles), and using the BTOW+BSMD with $R < 0.035$ (squares).

The transverse momentum, centrality, and pseudorapidity dependence of the BEMC matching efficiency in Au+Au can be found in Appendix C.2, and no significant centrality or pseudorapidity dependence was observed. The BEMC matching efficiency obtained from simulation has been used to correct the final results as a function of transverse momentum.

Electron candidates matched to the BEMC were required to have $E/p > 0.5$ in d+Au collisions. An upper-limit was required for Au+Au collisions due to the increased background, and electrons were identified using $0.5 < E/p < 1.5$. The E/p efficiency in d+Au and Au+Au collisions has been calculated from a pure sample

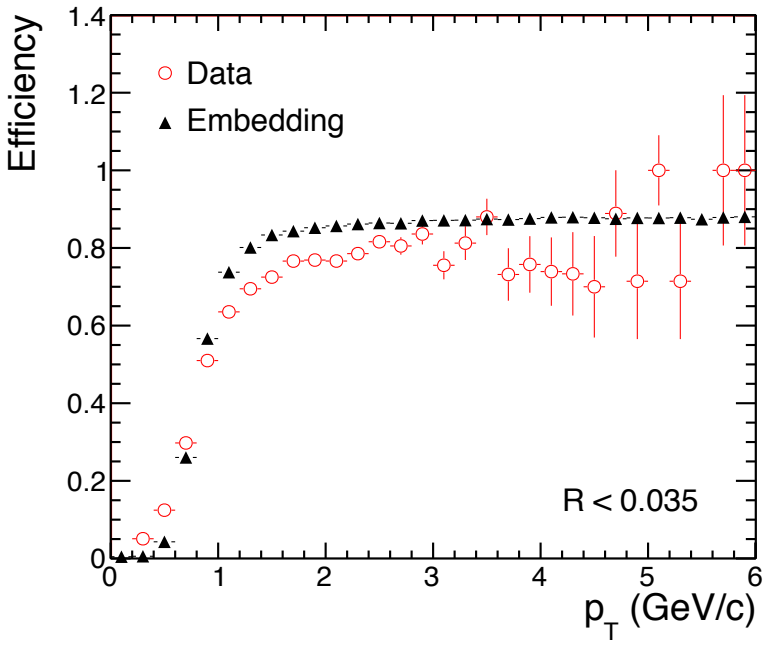

Figure 4.33: The BEMC matching efficiency versus p_T for $|\eta| < 1$ in $0-60\%$ central Au+Au collisions obtained from data (open circles) and simulation (closed triangles). Electrons are matched to a cluster using the BTOW+BSMD with $R < 0.035$.

of electrons by computing the fraction of electrons with $0.5 < E/p < 1.5$. The efficiency has also been calculated using simulated electrons embedded into real events, and the E/p distribution from data and simulation are shown in Fig. 4.24 for d+Au, and Fig. 4.27 for Au+Au. A detailed comparison of the E/p distribution between data and simulation as a function of momentum in Au+Au collisions can be found in Appendix C.2. The agreement is reasonably good, however the data exhibits a broader distribution than the simulation in general. The electron E/p efficiency in Au+Au obtained using the BTOW+BSMD with $R < 0.035$ is shown in Fig. 4.34. An efficiency of $> 95\%$ was obtained for electrons with $E/p > 0.5$ in d+Au collisions, and for electrons with $0.5 < E/p < 1.5$ in Au+Au collisions.

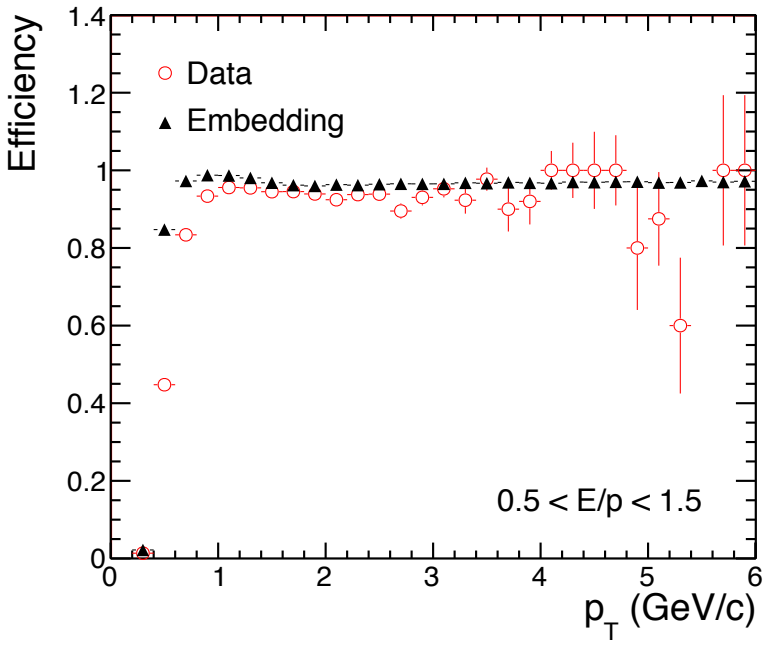

Figure 4.34: The BEMC E/p cut efficiency versus p_T for $|\eta| < 1$ in $0-60\%$ central Au+Au collisions obtained from data (open circles) and simulation (closed triangles). Electrons are matched to a cluster using the BTOW+BSMD with $R < 0.035$.

4.7 J/ψ Efficiency

4.7.1 Tracking Efficiency and Acceptance

In order to determine the TPC tracking efficiency and acceptance, Monte Carlo J/ψs were embedded and decayed into real data events. A GEANT simulation was used to determine the interaction of the electron daughters with the detector material, after which the TPC Response Simulator was used to model the ionization energy and detector response. Flat input spectra for the Monte Carlo J/ψ transverse momentum and rapidity distributions were used to reduce CPU time and increase statistics at higher p_T. These distributions were subsequently weighted with physical distributions to take the J/ψ p_T and rapidity shape into account in the efficiency calculation. A Gaussian and a power-law function were fitted to J/ψ spectra from PYTHIA and

used to model the rapidity and transverse momentum of the J/ψ, respectively. The unweighted and weighted input J/ψ p_T and rapidity distribution for d+Au collisions are shown in Fig. 4.35.

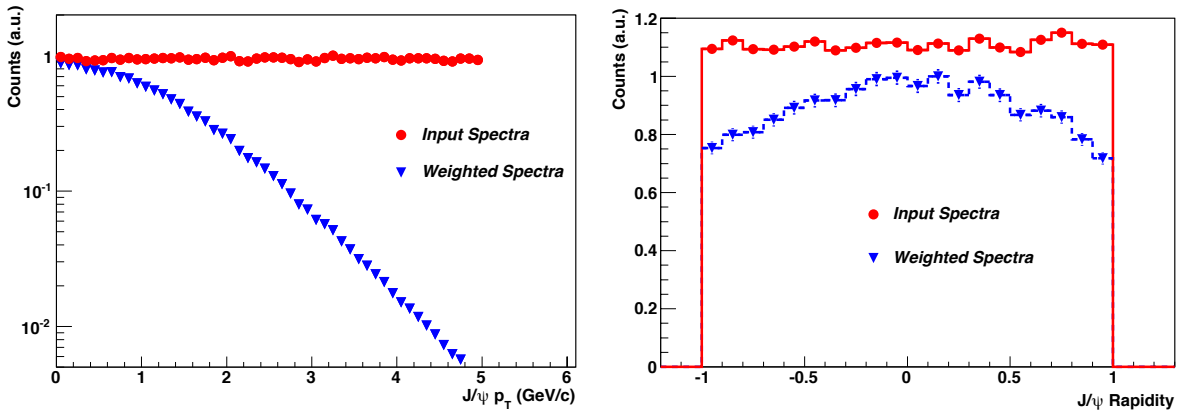

Figure 4.35: The input J/ψ transverse momentum (left) and rapidity (right) used in simulation in d+Au. The unweighted (circles) and weighted (triangles) distributions are shown.

The Monte Carlo electron daughters that passed through the TPC acceptance and were reconstructed by the tracking software were subjected to the same track quality requirements as the real data. Those that passed the quality selection requirements were reconstructed into their parent J/ψ. The acceptance and tracking efficiency for J/ψ in $|y| < 1$ were folded together by comparing the input Monte Carlo J/ψ distribution to the reconstructed J/ψ distribution obtained after applying the acceptance and track quality cuts previously discussed. A comparison of distributions obtained from simulation and data can be found in Appendix D.1 and D.2 for d+Au and Au+Au collisions, respectively, and the distributions agree well. There is a slight discrepancy in the `nHitsFit` distribution between simulation and data, and this was accounted for in the systematic uncertainties, as described in Chapter 6.

The J/ψ tracking efficiency $\times$ acceptance are shown in Fig. 4.36 as a function of transverse momentum for various centrality (left panel) and rapidity (right panel)

ranges in Au+Au collisions, and in Fig. 4.37 as a function of transverse momentum for d+Au collisions. The tracking efficiency decreases in more central events due to the higher occupancy in the detector. The J/ψ tracking efficiency is $\sim 20-35\%$ for $p_T < 5$ GeV/c, and decreases for $0.5 < p_T < 1.5$ in d+Au due to the p_T requirements used for electron identification.

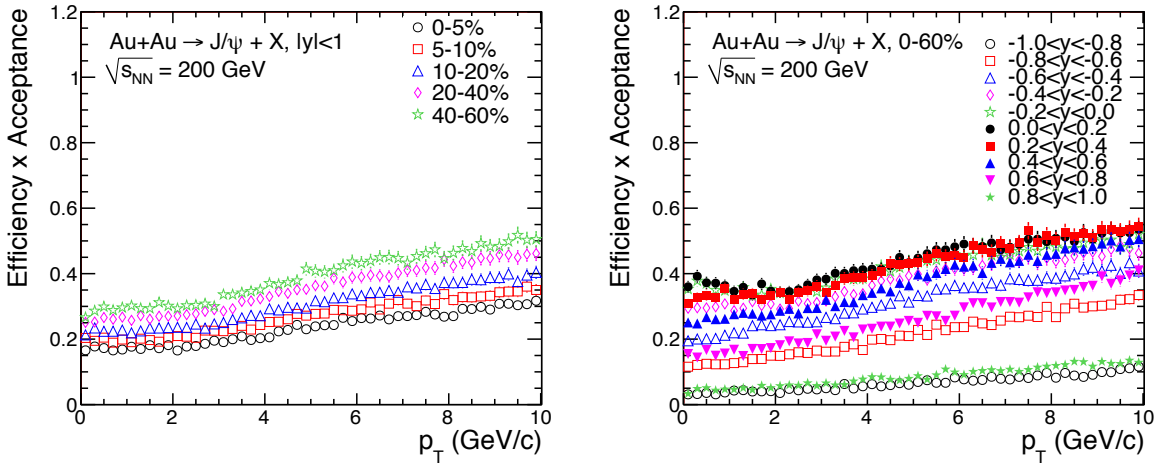

Figure 4.36: The J/ψ tracking efficiency and acceptance versus p_T for various centrality bins (left panel) and rapidity bins (right panel) in Au+Au collisions.

4.7.2 Total J/ψ Efficiency

The total J/ψ efficiency and acceptance was determined by combining the J/ψ tracking efficiency and acceptance with the electron identification efficiencies. Because J/ψ reconstruction is performed using electron pairs, the electron identification efficiencies contribute in quadrature to the final efficiency. The various efficiency contributions were combined using the J/ψ decay kinematics from simulation. The resulting total efficiency in d+Au is shown in Fig. 4.37 using the TPC only (open squares), and using the TPC and BEMC (closed squares). The total efficiency is $\sim 12-20\%$ when using the TPC only, and decreases to $7-12\%$ when using the TPC and BEMC. The p_T and centrality dependence of the total J/ψ efficiency correction in Au+Au collisions

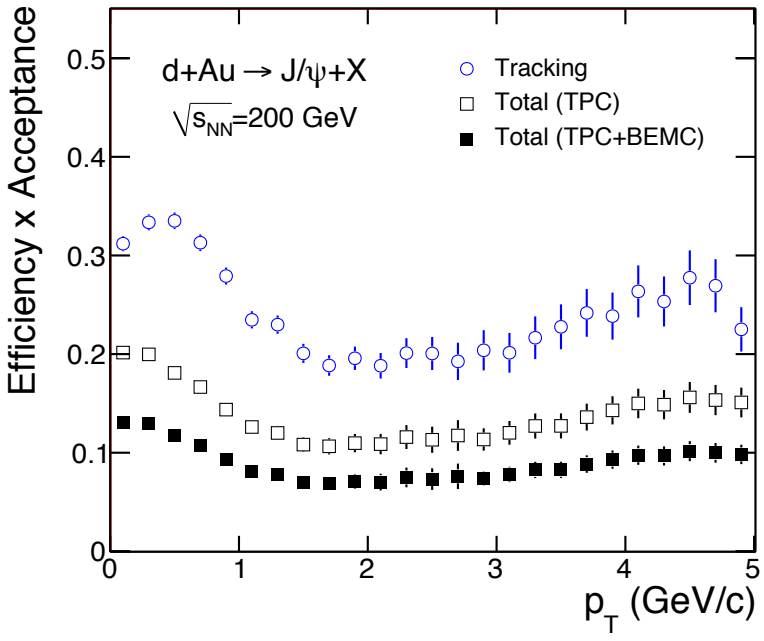

Figure 4.37: The J/ψ tracking efficiency and acceptance (circles) and total efficiency using the TPC only (open squares) and using the TPC and BEMC (closed squares) versus p_T for $|y| < 1$ in d+Au collisions.

are shown in Fig. 4.38. The efficiency increases with p_T and decreases in more central collisions, and ranges from $4 - 18\%$ for $p_T < 5$ GeV/c.

The total efficiency and acceptance corrections shown in Fig. 4.37 and Fig. 4.38 have been used to correct the measured J/ψ p_T spectrum to determine the invariant J/ψ yield in d+Au and Au+Au collisions. The J/ψ signal and invariant yield in d+Au and Au+Au collisions are described in Chapter 5.

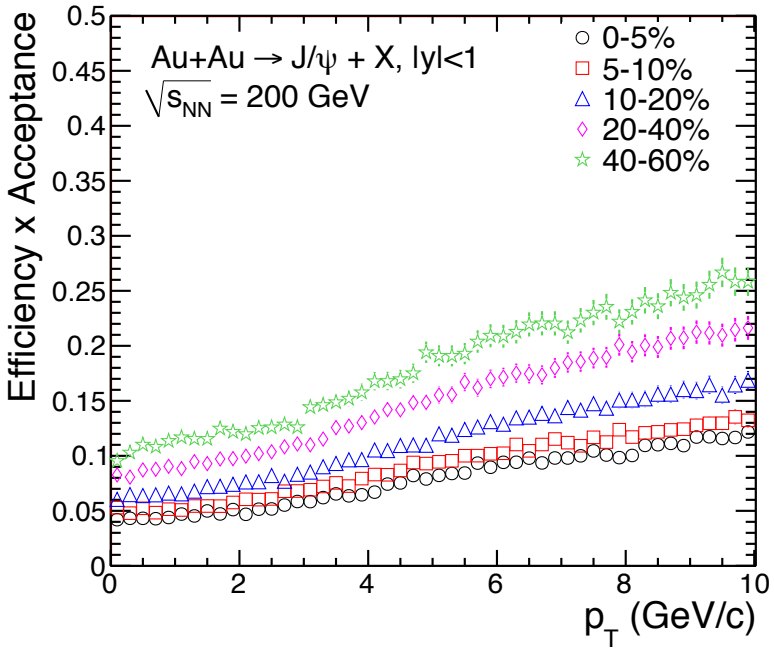

Figure 4.38: The J/ψ total efficiency and acceptance versus p_T for various centrality bins in Au+Au collisions.

Chapter 5

Results

The reconstruction of J/ψ has been performed in d+Au and Au+Au collisions at STAR via the dielectron decay channel:

$$J/\psi \rightarrow e^+ + e^- \ (B = 5.94 \pm 0.06\%), \tag{5.1}$$

where B is the branching ratio of the J/ψ decay to dielectrons [136]. The identification requirements used to identify electrons are discussed in Chapter 4, and those listed in Table 4.7 have been applied to the d+Au data, and 30 million events have been analyzed. Similarly, the electron identification requirements listed Table 4.8 have been applied to the Au+Au data, and a total of 235 million minimum bias collisions and 72 million central collisions have been analyzed.

The J/ψ yield has been obtained from the dielectron invariant mass spectrum and corrected using the efficiency described in Section 4.7.2 to obtain the J/ψ p_T spectrum in d+Au and Au+Au collisions. The results have been compared to the J/ψ cross section in p+p collisions to determine if there are any modifications to J/ψ production in heavy ion collisions. The dielectron invariant mass spectrum in d+Au and Au+Au collisions is presented below, followed by a description of the J/ψ yield extraction and efficiency correction. Finally, the J/ψ invariant p_T spectrum and nuclear modification factor in both collision systems are presented.

5.1 Dielectron Mass Spectrum

Electron pairs that originate from the collision vertex within the same event have been used to reconstruct the dielectron invariant mass spectrum. Like-sign pairs ($e^+ + e^+$ and $e^- + e^-$) have been used to estimate the background from random combinations of opposite-sign pairs ($e^+ + e^-$). The number of background (combinatorial) pairs, N_{BG}, is calculated using the geometric mean of the like-sign pairs:

$$N_{BG} = 2\sqrt{N_{++} \times N_{--}}, \tag{5.2}$$

where N_{++} (N_{--}) is the number of $e^+ + e^+$ ($e^- + e^-$) pairs. The statistical uncertainty in the background contributes to the uncertainty in the J/ψ signal, and to minimize this a mixed-event background calculation was used in Au+Au collisions. The mixed-event background was obtained by mixing opposite-sign electron pairs from different events with similar event conditions such as collision centrality and vertex position. The event centrality and vertex position were both divided into 10 bins to ensure that the mixing was done between tracks from similar events. All combinations of opposite sign pairs in a given collision centrality and V_Z range were used to reconstruct the mixed-event background once at least 20 positive and negative charged electron candidates were obtained. This process was repeated across the entire data set, providing a significant increase in the statistics used in the mixed-event background compared to the like-sign background. The mixed-event background requires a normalization factor, and this was obtained by normalizing to the like-sign background in the range $2.6 < m < 3.6$ GeV/c^2. The statistics in d+Au were limited, and significant fluctuations in the like-sign background resulted in a large normalization uncertainty of the mixed-event background. As a result, a mixed-event background was not considered in d+Au and a like-sign background was used instead. The amount of background is quantified using the signal-to-background ratio, $S : B$, where $S = N_{J/\psi} = N_{+-} - N_{BG}$ and $B = N_{BG}$. The signal strength is defined by it's significance, $S/\delta S$, where

$$\delta S = \sqrt{S + 2B}. \tag{5.3}$$

The dielectron invariant mass spectrum for $|y| < 1$ and $p_T < 5$ GeV/c in $0-100\%$ central d+Au collisions is shown in Fig. 5.1. The results have been obtained without (left panel) and with (right panel) the use of the BEMC to illustrate the reduction in the background when using this detector. A peak in the opposite-sign dielectron mass spectrum (open circles) around the J/ψ mass range is visible above the like-sign background (closed triangles). The signal-to-background ratio obtained without the BEMC is $S : B = 2 : 1$. Using the BEMC and requiring $E/p > 0.5$ decreases the background substantially, resulting in $S : B = 12 : 1$. However, the additional inefficiency in matching electrons to the BEMC decreases the number of identified electrons and reduces statistics in the dielectron mass spectrum.

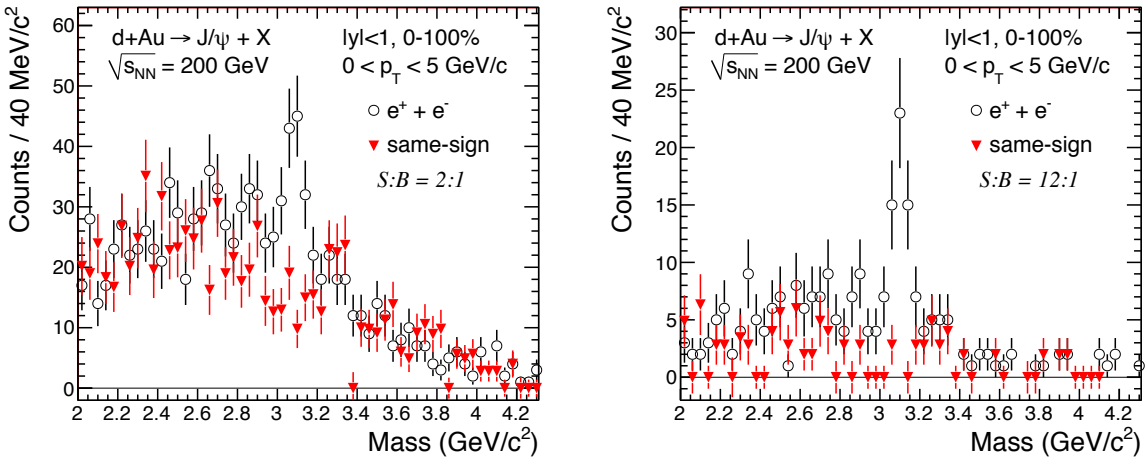

Figure 5.1: The dielectron mass spectrum from d+Au collisions obtained without (left panel) and with (right panel) the BEMC.

The dielectron invariant mass spectrum for $|y| < 1$ and $p_T < 5$ GeV/c in Au+Au collisions is shown in Fig. 5.2 (open circles) for minimum bias triggered data in $0-60\%$ central collisions (left) and central triggered data in $0-5\%$ central collisions (right). The like-sign (upward triangles) and mixed-event (downward triangles) background are shown, and a strong signal-to-background ratio has been achieved using the TPC, TOF, and BEMC, with $S : B = 1 : 4$ in $0-60\%$. This increases from $S : B = 1 : 9$

in $0-5\%$ central to $S:B=1$ in $40-60\%$ central Au+Au collisions. The dielectron mass spectrum in $0-20\%$ and $40-60\%$ central Au+Au collisions is shown in Fig 5.3 to illustrate the centrality dependence of the background, which decreases in more peripheral collisions. The like-sign (upward triangles) and mixed-event (downward triangles) background are shown, and the improvement in the statistical uncertainty of the mixed-event background can be clearly seen in $40-60\%$ central collisions.

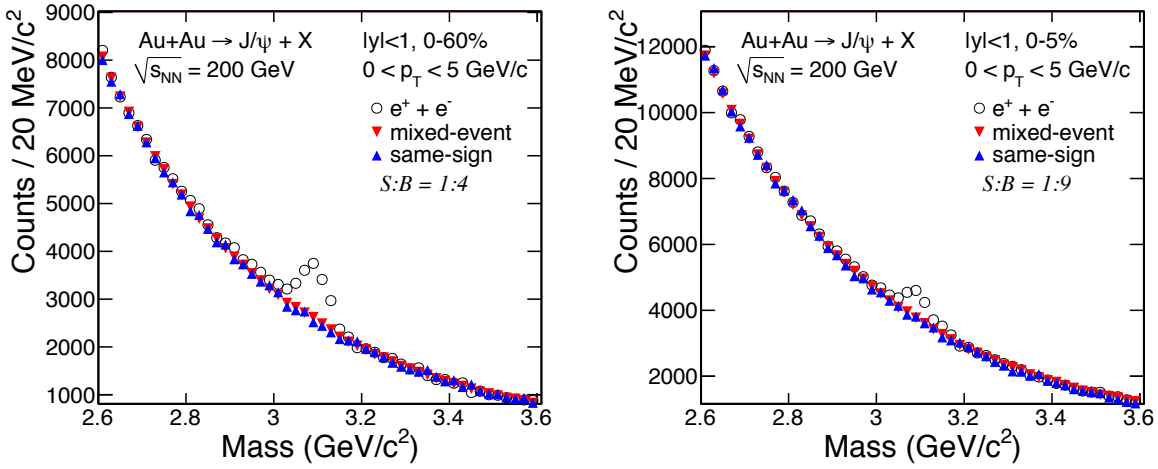

Figure 5.2: The dielectron mass spectrum from minimum bias data in $0-60\%$ central collisions (left) and central triggered data in $0-5\%$ central collisions (right) in Au+Au collisions.

5.2 J/ψ Signal

The combinatorial background has been subtracted from the opposite-sign dielectron invariant mass spectrum to obtain the J/ψ signal. This is shown for $|y|<1$ and $p_T<5$ GeV/c in $0-100\%$ central d+Au collisions in Fig. 5.4 (open circles), and for $0-60\%$ central Au+Au collisions in Fig. 5.5.

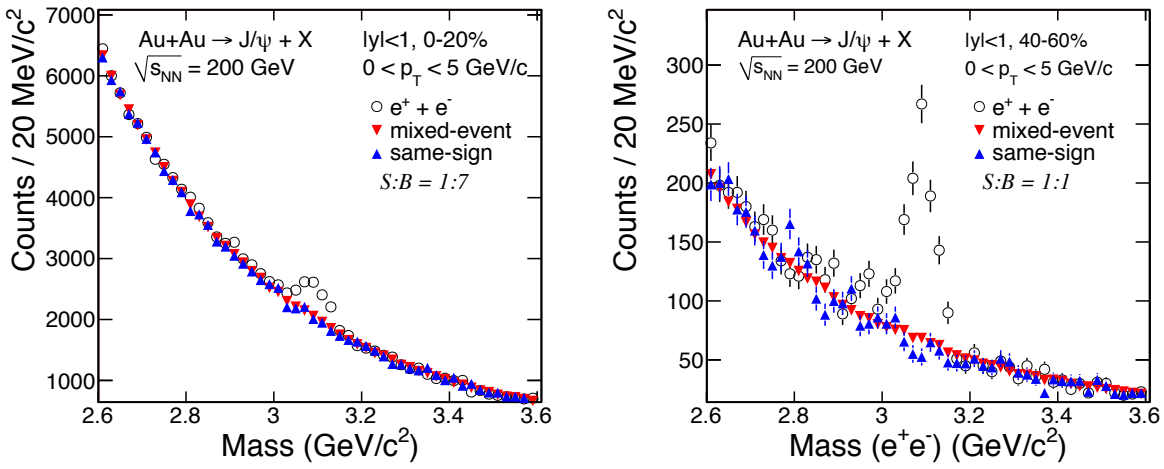

Figure 5.3: The dielectron mass spectrum in $0-20\%$ central (left) and $40-60\%$ central (right) Au+Au collisions.

The J/ψ signal shape was determined from simulation by embedding Monte Carlo J/ψs into real data, and results from the momentum resolution of the TPC and the radiative energy loss of electrons (Bremsstrahlung) interacting with the material in the detector. The J/ψ signal shape from simulation has been fitted to the dielectron mass spectrum after background subtraction to determine the J/ψ yield, and has been combined with a straight line to account for any residual background from $c\bar{c}$ and Drell-Yan contributions. While this residual background is expected to decrease exponentially with increasing mass, both a straight line and an exponential fit result in consistent estimates for the background within the mass range shown.

The J/ψ signal shape from simulation has been fitted to the d+Au data in the mass range $2 < m < 3.8$ GeV/c, and is shown in Fig. 5.4. There is a good agreement between the simulation and data, and a $\chi^2/\texttt{dof}$ of 33/44 was achieved. The J/ψ yield is obtained from the integral of the signal shape from simulation after subtracting the residual background, and a total of 53 ± 9 J/ψs with a significance of 5.9σ were reconstructed in $0-100\%$ central d+Au collisions using the TPC and BEMC. While there is an increase in the number of reconstructed J/ψs by $\sim 50\%$ when the

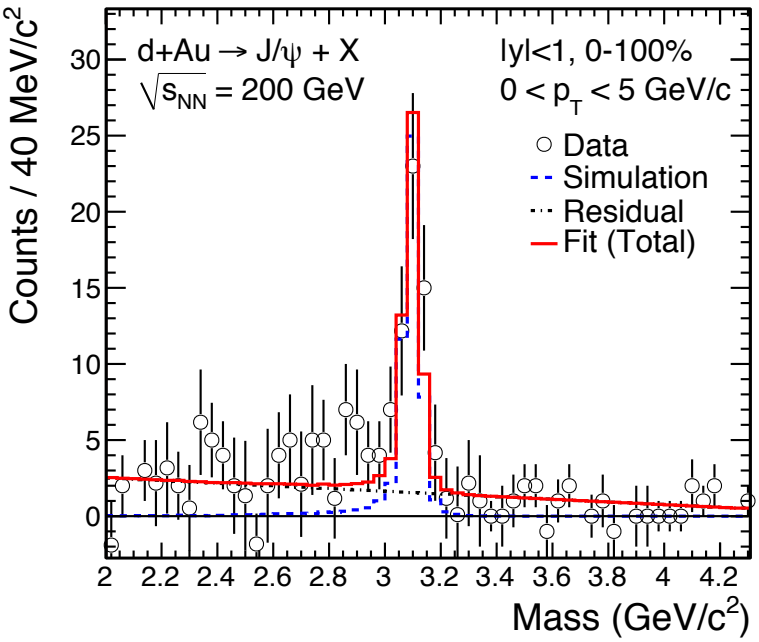

Figure 5.4: The J/ψ signal in $0-100\%$ central d+Au collisions after like-sign background subtraction.

BEMC is not used, the decrease in the background obtained when using the BEMC improves the significance of the J/ψ signal.

A data-driven correction has been performed to improve the agreement between the signal shape from data and simulation in Au+Au collisions, and has been done by including an additional Gaussian smearing of the electron momentum resolution. A detailed description of this can be found in Appendix E, and a smearing resolution of $0.61\% \times p_T$ was used to correct the data, improving the χ^2 of the fit between the data and signal shape from 33/14 to 6/14 . The J/ψ signal shape from simulation obtained after applying the additional momentum smearing has been fitted to the Au+Au data, and is shown in Fig. 5.5. A total of 5502 ± 119 J/ψs have been reconstructed in minimum bias $0-60\%$ central Au+Au collisions, with a signal significance of 27σ. A total of 3651 ± 228 J/ψs were reconstructed in central bias $0-5\%$ central Au+Au

collisions, with a signal significance of 16σ. To avoid double-counting of events that satisfy the minimum bias and central trigger, the $0-5\%$ central collisions in minimum bias triggered data were discarded, and the higher statistics central triggered data in $0-5\%$ central trigger data were combined with the $5-60\%$ minimum bias trigger data.

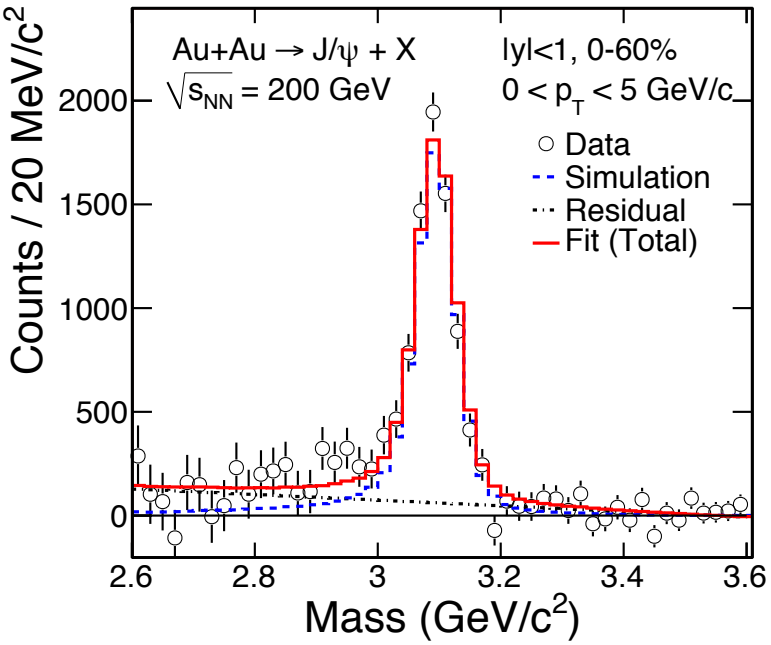

Figure 5.5: The J/ψ signal in $0-60\%$ central Au+Au collisions (minimum bias and central trigger).

The final J/ψ yield in $|y| < 1$ and $p_T < 5$ GeV/c has been extracted as a function of transverse momentum and collision centrality using the signal shape from simulation. The yield has also been calculated by counting the entries in the dielectron mass spectrum after background subtraction. The difference between these two methods is included in the systematic uncertainties, and is discussed in Chapter 6. The yield has been obtained in 5 p_T bins with $\Delta p_T = 1$ GeV/c, and is also divided into 3 centrality bins in d+Au, and 7 centrality bins in Au+Au. Due to limited statistics

in d+Au, only the centrality-integrated p_T spectrum and p_T-integrated centrality dependence have been obtained in d+Au, and the results from $3 < p_T < 4$ GeV/c and $4 < p_T < 5$ GeV/c have been combined in the d+Au p_T spectrum. The dielectron mass spectrum and signal shape, including the fits from simulation, as a function of p_T and centrality can be found in Appendix F.1 for d+Au collisions, and Appendix F.2 for Au+Au collisions.

The J/ψ yield, signal-to-background ratio, and significance obtained in each p_T and centrality bin in d+Au and Au+Au collisions are summarized in Table 5.1 and Table 5.2, respectively. As a result of the limited statistics for J/ψ in d+Au, the sum of the J/ψ yields in different centrality/p_T bins does not equal the centrality-/p_T-integrated J/ψ yield. This is due to fluctuations in the invariant mass background, and this is taken into account in the systematic uncertainties. The $0-60\%$ central Au+Au results combine the data from minimum bias $5-60\%$ central collisions with the high statistics $0-5\%$ central data obtained from the central trigger.

Table 5.1: The J/ψ uncorrected signal $N_{J/\psi}$, signal-to-background ratio S/B and significance $S/\delta S$ obtained in d+Au collisions.

Centrality (%)	p_T (GeV/c)	$N_{J/\psi}$	S/B	$S/\delta S$ (σ)
$0-100$	$0-5$	52 ± 9	10.72	6.0
	$0-1$	15 ± 5	9.83	3.1
	$1-2$	23 ± 6	–	4.1
	$2-3$	7 ± 3	–	2.1
	$3-5$	5 ± 3	–	1.6
$0-20$	$0-5$	15 ± 5	11.35	3.2
	$0-1$	4 ± 3	4.23	1.5
	$1-2$	1 ± 2	–	0.3
	$2-3$	1 ± 2	–	0.5
	$3-5$	5 ± 3	–	1.5
$20-40$	$0-5$	13 ± 5	7.27	2.6
	$0-1$	4 ± 3	–	1.1
	$1-2$	4 ± 3	–	1.5
	$2-3$	5 ± 3	–	1.7
	$3-5$	0 ± 0	–	0.0
$40-100$	$0-5$	18 ± 5	–	3.7
	$0-1$	9 ± 6	–	1.7
	$1-2$	16 ± 5	–	3.2
	$2-3$	9 ± 17	–	0.6
	$3-5$	0 ± 0	–	0

Table 5.2: The J/ψ uncorrected signal $N_{J/\psi}$, signal-to-background ratio S/B and significance $S/\delta S$ obtained in Au+Au collisions.

Centrality (%)	p_T (GeV/c)	$N_{J/\psi}$	S/B	$S/\delta S$ (σ)
$0-60$	$0-5$	8423 ± 297	0.13	28.3
	$0-1$	2056 ± 156	0.10	13.2
	$1-2$	3265 ± 186	0.14	17.6
	$2-3$	1972 ± 139	0.15	14.2
	$3-4$	919 ± 95	0.18	9.6
	$4-5$	352 ± 57	0.15	6.2
$0-5$	$0-5$	3667 ± 237	0.09	15.4
	$0-1$	880 ± 113	0.06	7.8
	$1-2$	1439 ± 150	0.10	9.6
	$2-3$	894 ± 110	0.10	8.1
	$3-4$	375 ± 75	0.11	5.0
	$4-5$	119 ± 44	0.09	2.7
$5-10$	$0-5$	738 ± 96	0.12	7.7
	$0-1$	248 ± 51	0.11	4.9
	$1-2$	248 ± 59	0.13	4.2
	$2-3$	128 ± 44	0.10	2.9
	$3-4$	82 ± 27	0.19	3.0
	$4-5$	38 ± 19	0.11	2.0
$10-20$	$0-5$	1351 ± 109	0.16	12.4
	$0-1$	316 ± 57	0.15	5.6
	$1-2$	538 ± 65	0.15	8.2
	$2-3$	304 ± 52	0.15	5.9
	$3-4$	130 ± 35	0.25	3.7
	$4-5$	72 ± 23	0.21	3.2

Centrality (%)	p_T (GeV/c)	$N_{J/\psi}$	S/B	$S/\delta S$ (σ)
$20-30$	$0-5$	1033 ± 78	0.27	13.3
	$0-1$	218 ± 39	0.21	5.5
	$1-2$	388 ± 46	0.26	8.4
	$2-3$	277 ± 37	0.38	7.5
	$3-4$	142 ± 26	0.36	5.4
	$4-5$	23 ± 15	0.16	1.5
$30-40$	$0-5$	808 ± 55	0.49	14.8
	$0-1$	207 ± 28	0.45	7.4
	$1-2$	285 ± 33	0.47	8.6
	$2-3$	182 ± 25	0.55	7.3
	$3-4$	104 ± 18	0.62	5.6
	$4-5$	44 ± 12	0.59	3.6
$40-50$	$0-5$	533 ± 38	0.92	14.0
	$0-1$	116 ± 19	0.82	6.2
	$1-2$	221 ± 23	1.07	9.5
	$2-3$	95 ± 17	0.68	5.5
	$3-4$	51 ± 12	1.18	4.2
	$4-5$	31 ± 9	1.76	3.5
$50-60$	$0-5$	320 ± 26	1.80	12.5
	$0-1$	77 ± 12	1.64	6.2
	$1-2$	117 ± 15	1.85	7.6
	$2-3$	81 ± 13	2.38	6.5
	$3-4$	30 ± 8	3.15	3.8
	$4-5$	21 ± 6	5.96	3.7

5.3 Invariant p_T Spectrum

The analysis details of J/ψ production for $p_T < 5$ GeV/c in d+Au and Au+Au collisions at $\sqrt{s_{NN}} = 200$ GeV/c at the STAR detector are presented in this thesis. The J/ψ invariant yield has been calculated as a function of p_T and collision centrality for $p_T < 5$ GeV/c and $|y| < 1$ in d+Au and Au+Au collisions at $\sqrt{s_{NN}} = 200$ GeV. In the following figures, the results from the Au+Au analysis described in this thesis are combined with the high-p_T ($3 < p_T < 10$ GeV/c) J/ψ invariant yield to extend the coverage of the J/ψ p_T spectrum to $p_T < 10$ GeV/c at STAR. The details of the high-p_T analysis can be found in [72].

To obtain the J/ψ invariant p_T spectrum, the J/ψ yield in d+Au and Au+Au are corrected using the efficiency in Fig. 4.37 and Fig. 4.38, respectively, and normalized to the number of events and phase space used in the analysis. The invariant p_T spectrum is defined as:

$$B\frac{\mathrm{d}^2N}{p_T\mathrm{d}p_T\mathrm{d}y\mathrm{d}\phi} = \frac{1}{2\pi p_T}\frac{N_{J/\psi}}{\Delta p_T \Delta y}\frac{1}{\epsilon \times a}, \tag{5.4}$$

where $\Delta y = 2$ for $|y| < 1$, p_T is the mean transverse momentum in a bin of width Δp_T, and $\epsilon \times a$ is the efficiency and acceptance correction.

To determine if there are modifications to the J/ψ yield in d+Au and Au+Au collisions, the J/ψ p_T spectrum in p+p collisions has been used as a baseline. The efficiency-corrected p_T spectrum in p+p collisions at STAR is shown in Fig. 5.6 (left panel) for $|y| < 1$ (closed symbols) [72, 101], and is compared to PHENIX data in $|y| < 0.35$ (open black triangles) [74]. The results are also compared to theoretical predictions obtained from the Color Evaporation Model [83], NNLO* CS model [75, 76] and NLO CS+CO model [79]. The CEM predictions are consistent with the data across the p_T range. The CS+CO model predictions are also consistent with the data but do not make predictions for the yield at low-p_T, while the CS model underestimates the J/ψ yield. The models are for prompt J/ψ production, and do not account for B feed-down which may be up to 25% at high-p_T [72].

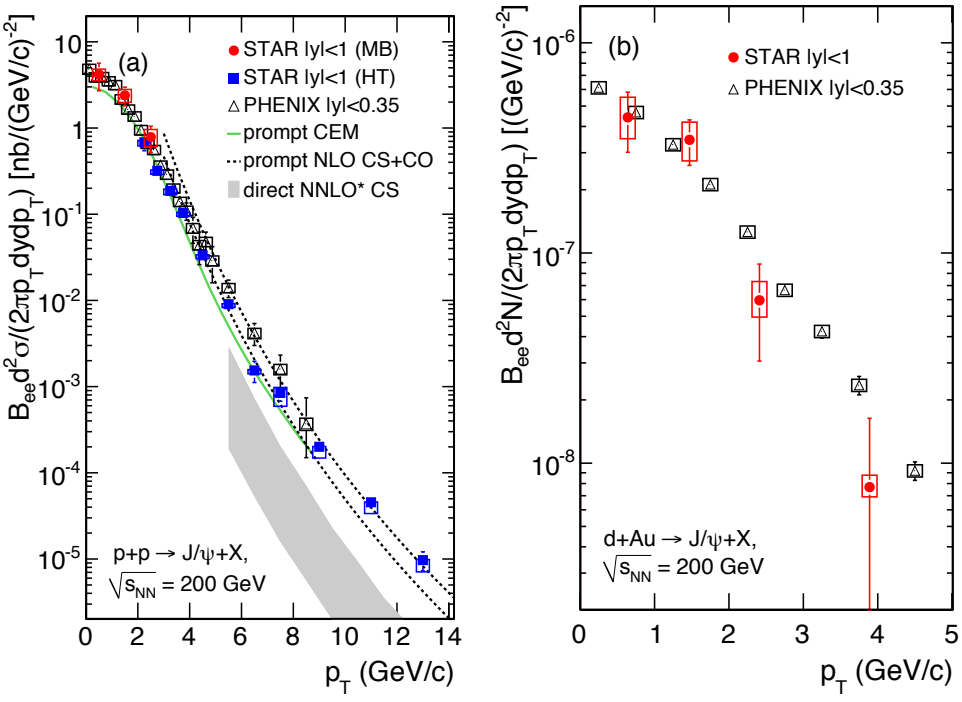

Figure 5.6: Left: The J/ψ cross section in p+p collisions at STAR (closed symbols) [151, 101] and PHENIX (open triangles) [74]. The results are compared to various model predictions [75, 79, 83]. Right: The J/ψ invariant p_T spectrum in $0-100\%$ central d+Au collisions at STAR (closed red circles) and PHENIX (open black triangles) [152].

The efficiency-corrected J/ψ p_T spectrum in $|y| < 1$ is shown in Fig. 5.6 (right panel) for $0-100\%$ central d+Au collisions (closed red cirlces). The bars represent the statistical uncertainties, and the boxes represent the systematic uncertainties, which are described in Chapter 6. The results are compared to PHENIX data at the same energy in $|y| < 0.35$ [152] (open black triangles), and the results are consistent within errors.

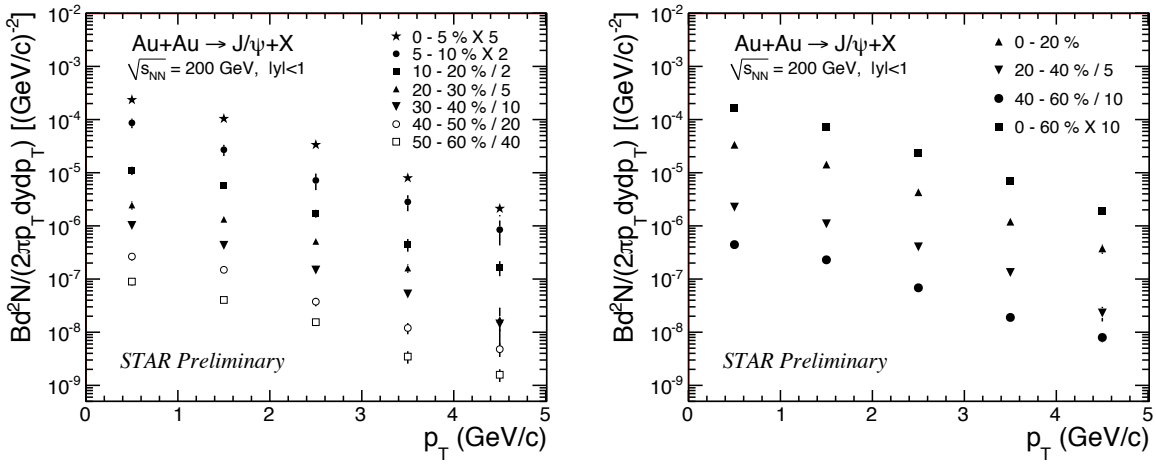

Figure 5.7: The J/ψ invariant p_T spectrum in Au+Au collisions at $\sqrt{s_{NN}} = 200$ GeV for all centralities (left) and merged centralities (right).

The efficiency-corrected J/ψ p_T spectrum for each centrality bin in Au+Au collisions is shown in Fig. 5.7 (left panel), and the bars indicate the statistical uncertainties. The yields have been scaled to enlarge the separation of the p_T spectrum for different centrality bins. The shape of the spectrum is similar in each centrality bin, with higher yields observed in more central collisions. The results have been merged into central $(0-20\%)$, mid-central $(20-40\%)$, and peripheral $(40-60\%)$ collisions to probe different collision conditions, improve statistics, and allow for a direct comparison to other results. The resulting p_T spectrum is shown in Fig. 5.7 (right panel).

The J/ψ invariant p_T spectrum for $|y| < 1$ and $p_T < 5$ GeV/c in Au+Au collisions is shown in Fig. 5.8 (closed red circles) for (a) $0-60\%$, (b) $0-20\%$, (c) $20-40\%$, and (d) $40-60\%$ central collisions. The data are compared to high-p_T STAR data [72] in $|y| < 1$ (open red circles) and low-p_T PHENIX data [67] in $|y| < 0.35$ (open black squares). The boxes represent the systematic uncertainties, and are described in Chapter 6. The STAR and PHENIX results are consistent within errors. The results are also compared to other measurements the J/ψ cross section in p+p collisions at

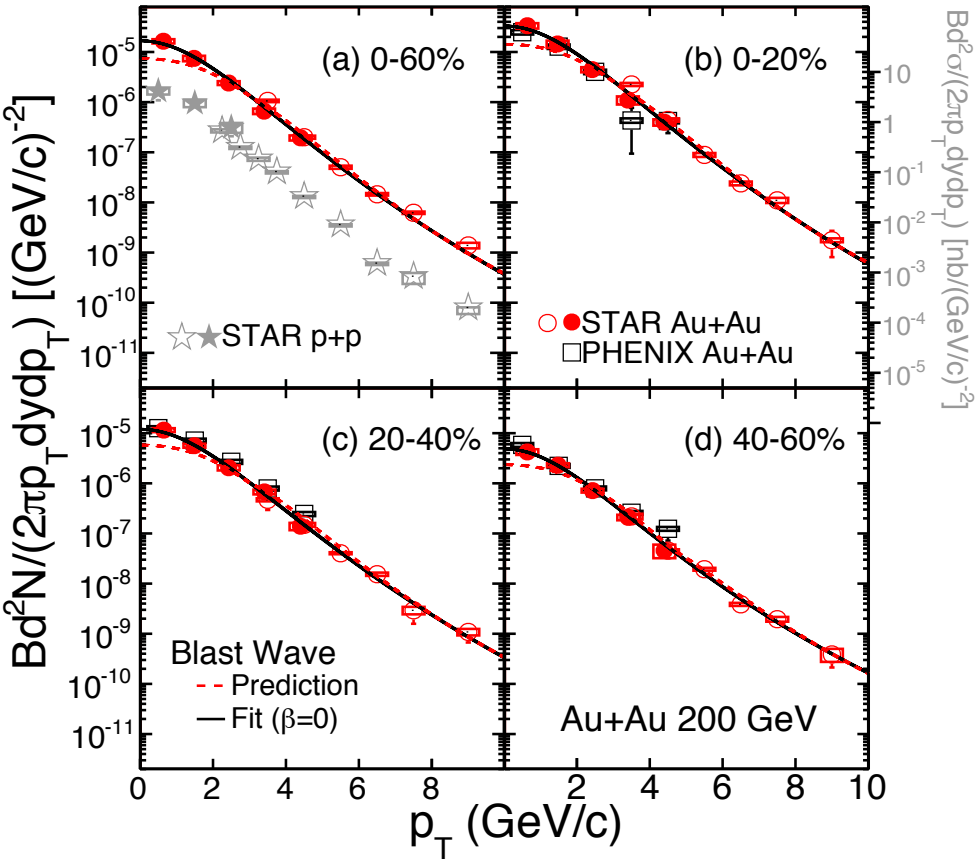

Figure 5.8: The J/ψ invariant p_T spectrum for $p_T < 5$ GeV/c in Au+Au collisions (closed red circles) for (a) $0-60\%$, (b) $0-20\%$, (c) $20-40\%$, and (d) $40-60\%$ central collisions. The results are compared to high-p_T STAR data [72] (open red circles) and PHENIX data [67] (open black squares). The Au+Au data are compared to Tsallis Blast Wave predictions [51, 54]. The J/ψ cross section in p+p collisions [72, 101] (grey stars) is also shown in (a).

$\sqrt{s_{NN}} = 200$ GeV/c at STAR [72, 101] in panel (a). The y-axis for the J/ψ cross section in p+p collisions is shown on the right. The p_T spectrum in Au+Au collisions has been compared to a Tsallis Blast Wave (TBW) model [54], which uses non-extensive Tsallis statistics and hydrodynamic expansion to describe hadron spectra in heavy ion collisions in terms of temperature and flow. The TBW predictions obtained from

lighter hadrons [51, 54], shown in Fig. 5.8 (dashed line), agrees with the data well for $p_T > 2$ GeV/c, but under-estimates the yield below this. The STAR data have been fitted with a TBW model assuming a zero radial flow, $\beta = 0$ (solid line) [54], which improves the agreement to the data at low-p_T. This suggests that there may be contributions from recombination at low-p_T, or that the J/ψ has a small radial flow compared to lighter hadrons.

The J/ψ yield $B\mathrm{d}^2N/\mathrm{d}y\mathrm{d}p_T$ for $|y| < 1$ in Au+Au collisions at STAR is shown on a linear scale in Fig. 5.9 for low p_T (closed red circles) and high p_T (open red circles) in (a) $0-60\%$, (b) $0-20\%$, (c) $20-40\%$, and (d) $40-60\%$ central collisions. The results are compared to predictions from viscous hydrodynamics using a J/ψ decoupling temperature of $T = 120$ MeV (dot-dashed line) and $T = 165$ MeV (dot-dot-dashed line) [153]. The predictions assume a zero chemical potential for J/ψ at kinetic freeze-out, and the scale of the predictions is determined from a fit to the data in $p_T < 5$ GeV. The data favors the higher decoupling temperature and is well described for $2 < p_T < 5$ GeV/c. However, the hydrodynamic calculations fail to describe the low p_T J/ψ yield ($p_T < 2$ GeV/c).

The data in Fig. 5.9 are also compared to theoretical predictions for J/ψ production in a transport model with initial production and continuous regeneration of J/ψ (solid line). The individual contributions from initial production (short dashed line) and regeneration (long dashed line) are also shown. Initial production dominates in peripheral events, and decreases in more central events as the suppression from color screening increases. In contrast, the contribution from regeneration is small in peripheral events, and increases in central events where the charm quark density is larger. The J/ψs from regeneration also have a lower average p_T than those from initial production. The calculations are able to describe the data well for each collision centrality across the p_T range. Furthermore, the predictions for the J/ψ yield from initial production and from regeneration have been separately fitted to the data with their scales left as a free parameter, and the quality of these fits decreased as compared to fitting the data with the predictions for a combination of initial production

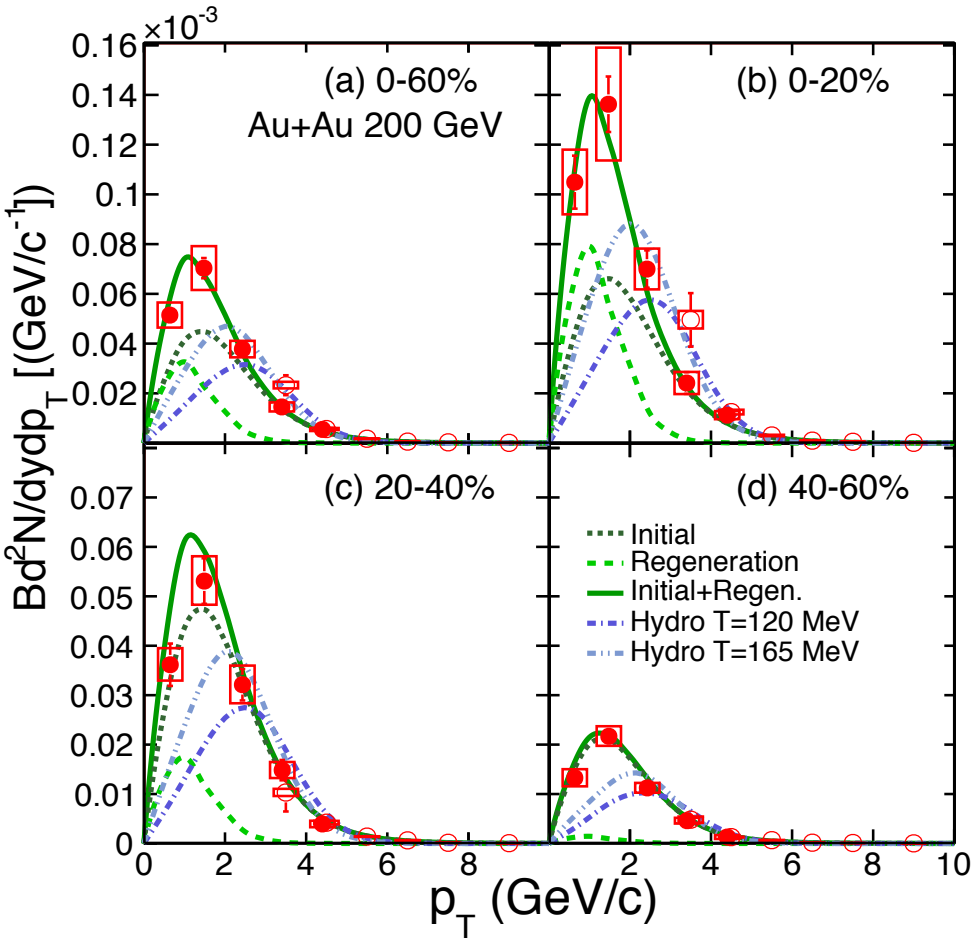

Figure 5.9: The J/ψ yield in Au+Au collisions for low p_T (closed red circles) and high p_T [72] (open red circles) in (a) $0-60\%$, (b) $0-20\%$, (c) $20-40\%$, and (d) 40--60% central collisions. The results are compared to hydrodynamic calculations [153] and transport model calculations including initial production and regeneration of J/ψ [154].

and regeneration. This indicates that the observed J/ψ yield in Au+Au collisions at $\sqrt{s_{NN}} = 200$ GeV consists of a mixture of J/ψs from initial production and regeneration, with initial production dominating in more peripheral events and at higher p_T, and regeneration becoming significant at low p_T in central collisions.

5.4 Nuclear Modification Factor

In order to determine if there is any modification to the production of J/ψ in d+Au and Au+Au collisions, the production rates are compared to those from p+p collisions and scaled by the number of binary nucleon collisions ($N_{\rm coll}$). The nuclear modification factor (R_{AB}) is defined as

$$R_{AB} = \frac{1}{T_{AB}} \frac{\mathrm{d}^2 N_{AB}/\mathrm{d}p_T\mathrm{d}y}{\mathrm{d}^2\sigma_{pp}/\mathrm{d}p_T\mathrm{d}y}, \tag{5.5}$$

where $\mathrm{d}^2N_{AB}/\mathrm{d}p_T\mathrm{d}y$ is the invariant J/ψ yield in $A+B$ collisions and $\mathrm{d}^2\sigma_{pp}/\mathrm{d}p_T\mathrm{d}y$ is the J/ψ cross section in p+p collisions. The nuclear overlap function is defined as $T_{AB} = \langle N_{\rm coll}\rangle/\sigma^{\rm pp}_{\rm inel}$, and takes into account the inelastic cross section in p+p collisions ($\sigma^{\rm pp}_{\rm inel} = 42 \pm 3$ mb [155]) and the number of nucleon-nucleon collisions in $A+B$ collisions. The production of J/ψ in heavy ion collisions should scale with the $N_{\rm coll}$, as the J/ψ production cross section can be described using pQCD.

The nuclear modification factor has been investigated in d+Au collisions to determine the cold nuclear matter effects to J/ψ production. These have been subtracted from the modifications to J/ψ production in Au+Au collisions to determine if there is a suppression from a QGP phase. The nuclear modification factor in Au+Au collisions has also been compared to theoretical predictions involving cold nuclear matter effects, color screening, and regeneration, and the results are described below.

5.4.1 Nuclear Modification in d+Au

The nuclear modification factor for J/ψ with $p_T < 5$ GeV/c in d+Au collisions has been calculated versus $N_{\rm coll}$, and is shown in Fig. 5.10. The point-to-point errors are statistical (lines) and systematic (boxes), and the systematic uncertainties are described in Chapter 6. The boxes on the vertical axis represent the normalization uncertainty on $N_{\rm coll}$ and the p+p cross section. The results are compared to published data at the same energy with $|y| < 0.35$ [156] (open circles). The results are consistent within errors, and suggest a small suppression in central d+Au collisions.

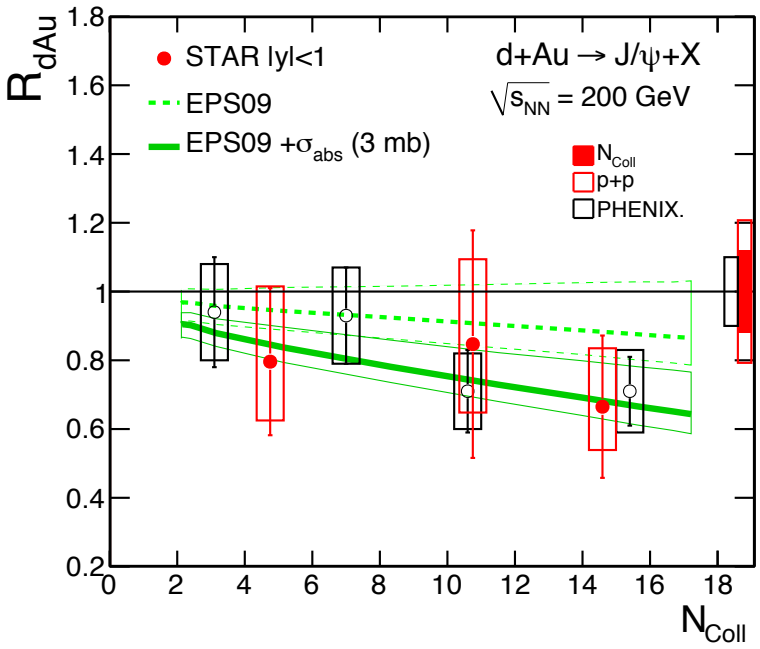

Figure 5.10: The J/ψ nuclear modification factor versus $N_{\rm coll}$ in $|y| < 1$ (closed circles) for $p_T < 5$ GeV/c in d+Au collisions at STAR. The results are compared to PHENIX data in $|y < 0.35|$ (open circles) [156]. The green band indicates the expected modification due to shadowing only (dashed line) and due to shadowing and nuclear absorption (solid line) [98, 99]. The bands indicate the uncertainty on the shadowing from the EPS09 calculations [86].

Using various parameterizations of the nuclear Parton Distribution Functions (EPS09 [86], EKS98 [88], and nDSg [87]), the expected modification of the J/ψ production due to an initial-state shadowing has been calculated [98, 99]. The various nPDFs predict a small suppression of J/ψ in $|y| < 1$, increasing with increasing collision centrality. The J/ψ nuclear modification factor obtained using the EPS09 calculations for shadowing is shown in Fig. 5.10 (dashed lines). The EPS09 calculation includes an error analysis which the other parameterizations do not, and this is indicated by the band in Fig. 5.10 (dashed lines). The shadowing predictions from

the EKS98 and nDSg calculations are consistent within the EPS09 uncertainties. The EPS09 predicts a nuclear modification factor of $R_{dA} = 0.88^{+0.15}_{-0.07}$ in $0 - 20\%$ central d+Au collisions at $\sqrt{s_{NN}} = 200$ GeV for J/ψ with $|y| < 1$.

In addition to an initial-state shadowing, a final-state J/ψ absorption cross section ($\sigma_{\rm abs}$) has also been included in the predictions [98, 99], which describes the rate that J/ψs are absorbed or broken up by other nucleons participating in the collision. The value of the absorption cross section has been obtained from a fit to the STAR data in Fig. 5.10. A χ^2 minimization was performed to determine the most probable value of the absorption cross section, and the χ^2 distributions for each nPDF as a function of the absorption cross section are shown in Fig 5.11. The minimum χ^2 ranges from $\sim 2 - 4$ mb depending on the nPDF used, and a central value obtained from the EPS09 parameterization of

$$\sigma_{\rm abs} = 2.8^{+3.5}_{-2.6}\ (\text{stat.})\ ^{+4.0}_{-2.8}\ (\text{syst.})\ ^{+1.8}_{-1.1}\ (\text{EPS09})\ \text{mb} \tag{5.6}$$

was obtained. The minimum χ^2 for each nPDF is small ($\chi^2 < 1$), and results from the large statistical and systematic uncertainties in the data. As a result, a value for the absorption cross section cannot be well constrained. There are additional uncertainties on the shadowing obtained from the nPDFs, and these are estimated to be significant using the EPS09 calculations.

The nuclear modification factor shown in Fig. 5.10 is compared to the expected R_{dA} obtained using the EPS09 nPDF parameterization combined with a J/ψ nuclear absorption cross section of $\sigma_{\rm abs} = 3$ mb (solid lines). The band indicates the uncertainty from the EPS09 calculations of $^{+1.8}_{-1.1}$ mb. There is a small contribution to the observed suppression from the initial-state modification to the PDFs within a nucleus (dashed lines). Further suppression arises due to the absorption of J/ψ from the surrounding nuclear matter in the final-state. The number of nucleon-nucleon collisions increases with increasing collision centrality, resulting in a stronger suppression of J/ψ due to nuclear absorption in more central events. This is consistent with the

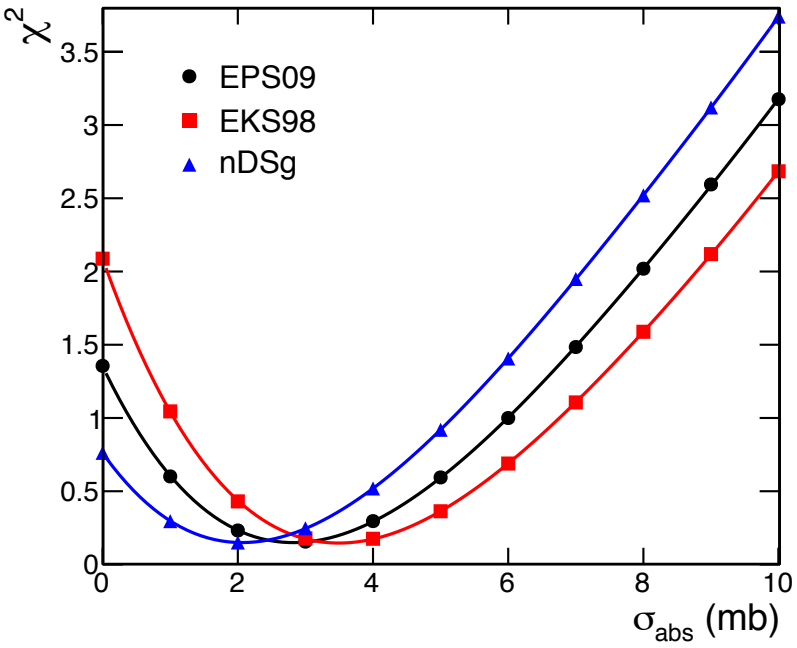

Figure 5.11: The χ^2 between the R_{dA} from data and model predictions as a function of $\sigma_{\rm abs}$ using the EPS09 [98, 99], EKS98 [88], and nDSg [87] nPDFs.

trend observed in the data. The results are consistent with more accurate calculations of the absorption cross section at the same energy of $\sigma_{\rm abs} = 2.8^{+1.7}_{-1.4}$ mb [157, 156] obtained using the EKS98 nPDFs. This indicates that cold nuclear matter effects are not a strong modification of J/ψ production at midrapidity in 200 GeV collisions.

The nuclear modification factor as a function of p_T for J/ψ in $0-100\%$ central d+Au collisions is shown in Fig. 5.12. The shaded band represents the statistical uncertainty from p+p collisions, and the boxes on the vertical axis represent the normalization uncertainty from $N_{\rm coll}$ of 12% and $\sigma^{\rm pp}_{\rm inel}$ of 8%. There are large uncertainties for $p_T > 2$ GeV/c due to limited statistics. The results are consistent with other measurements in $|y| < 0.35$ [152] (open circles). The predicted p_T dependence of the nuclear modification factor in d+Au has been determined from the EPS09 paramaterization of the nPDFs and combined with an absorption cross section of

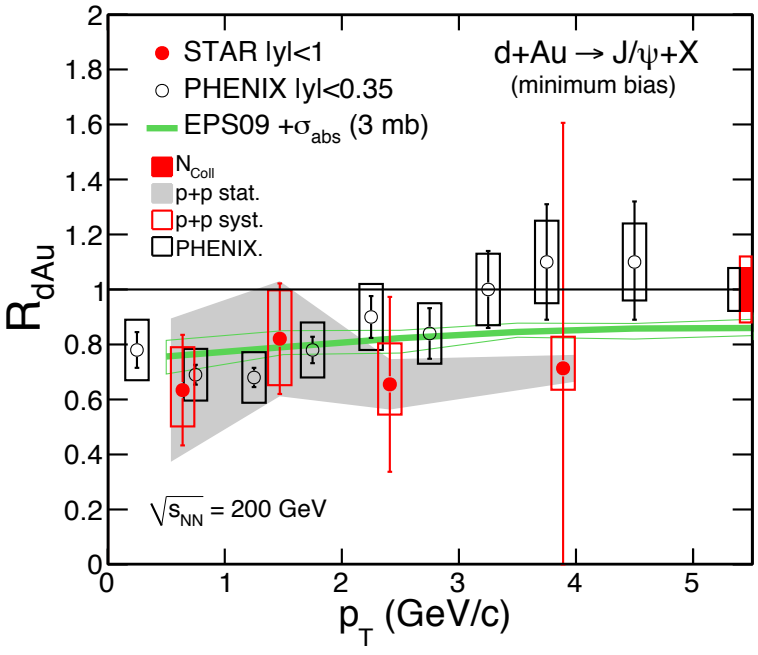

Figure 5.12: The J/ψ nuclear modification factor versus p_T in $|y| < 1$ (closed circles) for $0 - 100\%$ central d+Au collisions. The results are compared to published data with $|y| < 0.35$ [152] (open circles). The green band indicates the expected value and uncertainties due to shadowing and nuclear absorption [98, 99].

$\sigma_{\rm abs} = 3$ mb. This is shown in Fig. 5.12 (green band), and is consistent with the data. The predictions indicate a suppression of R_{dA} at low p_T. The R_{dA} increases at higher p_T from the modification of the initial-state nuclear PDFs, however the p_T dependence is not significant.

The values for the nuclear modification factor for $|y| < 1$ versus p_T in $0 - 100\%$ central collisions and versus $N_{\rm coll}$ for $p_T < 5$ GeV/c in d+Au are summarized in Table 5.3. The uncertainties are separated into (A) statistical, (B) systematic, and (C) global uncertainties which arise from the uncertainty on $N_{\rm coll}$ and the uncertainty in the p+p cross section. The nuclear modification factor in Au+Au is presented in the following section, and the cold nuclear matter effects calculated in d+Au have

been used to determine if there is an additional suppression in Au+Au compatible with a QGP phase.

Table 5.3: The J/ψ invariant yield and nuclear modification factor for $|y| < 1$ in d+Au collisions at $\sqrt{s_{NN}} = 200$ GeV with (A) statistical, (B) systematic, and (C) global uncertainties.

Centrality (%)	p_T (GeV/c)	R_{dA}	(A)	-(B)	+(B)	(C)
$0-100$	$0-1$	0.634	0.201	0.156	0.132	0.411
	$1-2$	0.821	0.201	0.176	0.169	0.255
	$2-3$	0.655	0.318	0.149	0.110	0.140
	$3-5$	0.712	0.890	0.114	0.078	0.130
$0-20$	$0-5$	0.677	0.211	0.173	0.128	0.164
$20-40$	$0-5$	0.863	0.337	0.251	0.203	0.164
$40-100$	$0-5$	0.811	0.218	0.223	0.174	0.164

5.4.2 Nuclear Modification in Au+Au

The p_T-integrated nuclear modification factor for J/ψ in Au+Au collisions as a function of $N_{\rm part}$ is shown in Fig. 5.13 (closed circles). The point-to-point errors are statistical (lines) and systematic (boxes), and the systematic uncertainties are described in Chapter 6. The shaded bands represent the uncertainty on $N_{\rm coll}$, and the boxes on the vertical axis represent the normalization uncertainty from the statistical error in p+p collisions combined with the uncertainty on $\sigma^{\rm pp}_{\rm inel}$ of 8%. The results are compared to PHENIX data [67] (open circles) and agree within errors, exhibiting a decrease of R_{AA} with increasing $N_{\rm part}$.

The results are compared to predictions for the nuclear modification factor in Au+Au based on cold nuclear matter effects only [158]. The shadowing effect determined using the EKS98 calculations [88] has been combined with an absorption cross section $\sigma_{\rm abs} = 3$ mb obtained from data to determine the J/ψ nuclear modification factor in Au+Au from cold nuclear matter effects only, and the results are shown in Fig. 5.13 (squares). The shadowing from the EKS98 is slightly smaller than that from the EPS09, however the two are consistent within the uncertainties provided for the EPS09 calculations. The suppression from cold nuclear matter effects has been subtracted from the J/ψ nuclear modification factor, and this is shown in Fig. 5.14. The central values of the STAR data indicate a suppression of $0.1 - 0.2$ beyond cold nuclear matter effects, and this does not exhibit a strong centrality dependence. The central values of the PHENIX data are consistent with no additional suppression for $N_{\rm part} \lesssim 200$, above which the suppression increases with $N_{\rm part}$. However, due to the large statistical, systematic, and global uncertainties in the STAR and PHENIX data, a suppression beyond cold nuclear matter effects cannot be claimed.

To understand the medium modifications to J/ψ in Au+Au collisions, the nuclear modification factor has been compared to results from Cu+Cu collisions, and this is shown in Fig. 5.15. There are fewer participant nucleons in Cu+Cu collisions, resulting in a lower temperature and in-medium path length, and the Cu+Cu results are consistent with no suppression within the current uncertainties.

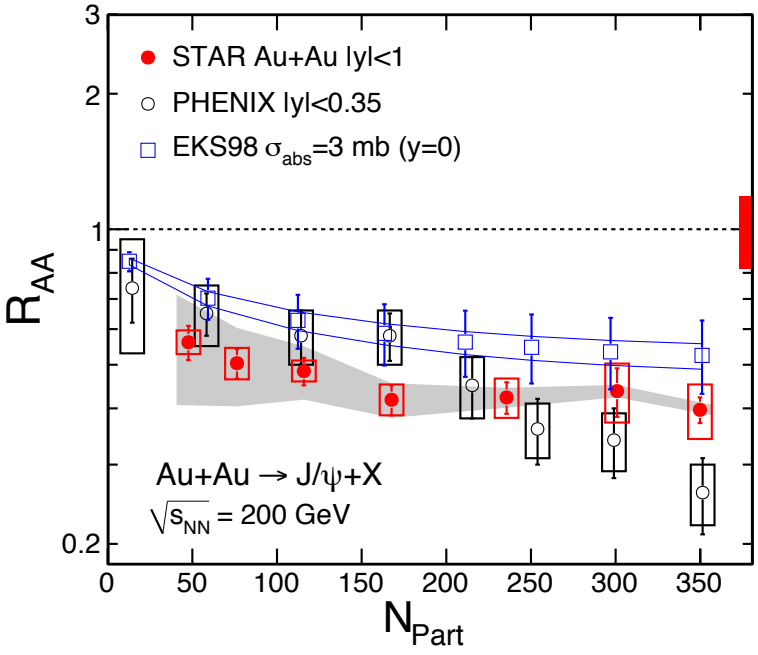

Figure 5.13: The J/ψ nuclear modification factor in Au+Au collisions (closed circles). The results are compared to PHENIX data in $|y| < 0.35$ (open circles) [67]. The predicted modification from cold nuclear matter effects is also shown (squares) [158].

The J/ψ nuclear modification factor has also been compared to theoretical predictions involving the suppression and regeneration of J/ψ from charm quarks (solid line [159] and dashed line [154]), and the latter also includes B feed-down and formation-time effects. The models also include cold nuclear effects, such as initial-state shadowing and parton scattering, and a final-state nuclear absorption of $\sigma_{\rm abs} = 1.5$ mb and 3 mb, respectively. These are consistent with the absorption cross section extracted from the STAR d+Au data, and the predictions in [159] decrease by 8% when using $\sigma_{\rm abs} = 2.7$ mb. The predictions are similar and describe the data well, indicating contributions from color screening and statistical regeneration in addition to cold nuclear matter effects. Both the data and models exhibit a decrease of R_{AA} in more central events from the suppression of J/ψ due to color screening.

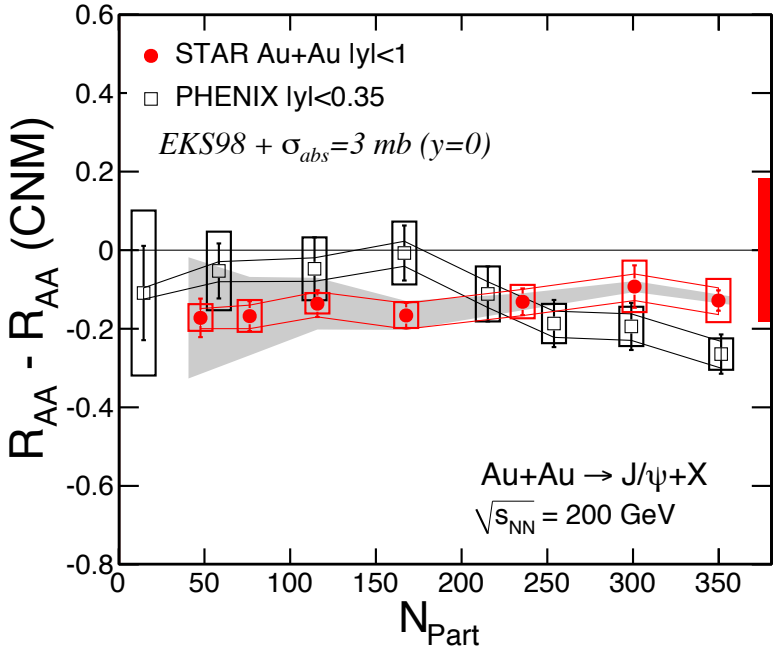

Figure 5.14: The J/ψ nuclear modification factor in Au+Au collisions after the subtraction of cold nuclear matter effects [158].

There are multiple $c\bar{c}$ pairs created in central heavy ion collisions at RHIC, and the increased number of $c\bar{c}$ pairs in central collisions is expected to result in an increase of J/ψ production at low p_T from the coalescence of thermalized charm quarks. Depending on the formation time of J/ψ relative to the QGP, high-p_T J/ψs may escape the suppression zone leading to an enhancement in R_{AA} at high-p_T [100]. In order to understand more about the suppression of J/ψ in heavy ion collisions and disentangle modifications from color screening to those from regeneration and leakage, the p_T dependence of the nuclear modification factor has been calculated.

The nuclear modification factor for J/ψ in Au+Au collisions as a function of transverse momentum for various collision centralities is shown in Fig. 5.16 (closed circles). The shaded band indicates the statistical uncertainty from p+p collisions,

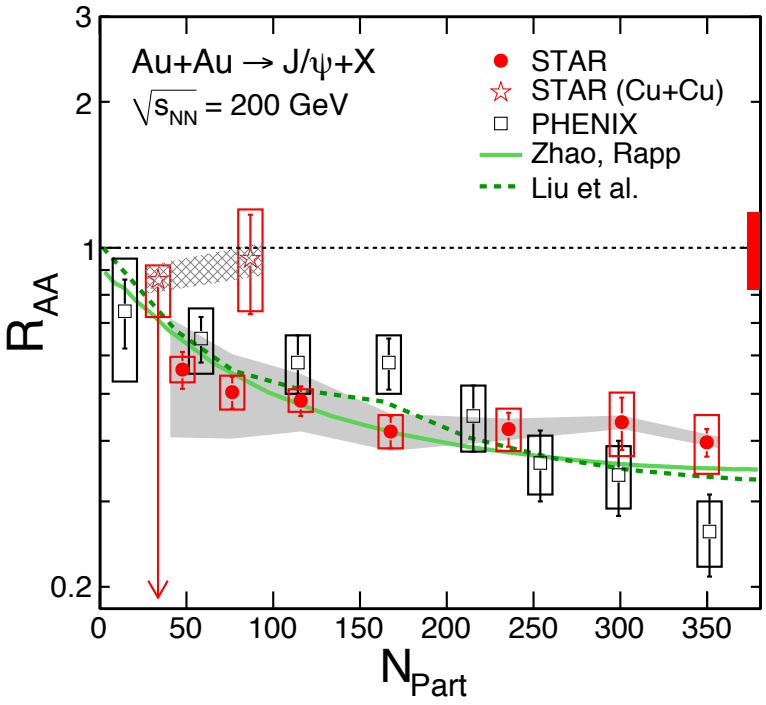

Figure 5.15: The J/ψ nuclear modification factor in Au+Au collisions (closed circles). The results are compared to STAR Cu+Cu results (open stars), published data in $|y| < 0.35$ [74] (open circles), and and theoretical predictions (solid line [159] and dashed line [154]).

and the box on the vertical axis represents the normalization uncertainty from $N_{\rm coll}$ and $\sigma^{\rm pp}_{\rm inel}$. The results are compared to STAR high-p_T data [72] (open circles) and PHENIX [67] (open squares), and are consistent within errors, exhibiting an increase of R_{AA} at high p_T.

The nuclear modification factor has been compared to the same theoretical predictions for J/ψ involving a suppression due to color screening and regeneration from charm quarks in addition to cold nuclear matter effects (solid line [159], dashed line [154]), and these models describe the data reasonably well. The data and models exhibit an increase for $p_T > 1$ GeV/c, with R_{AA} approaching unity for $p_T > 4$ GeV/c

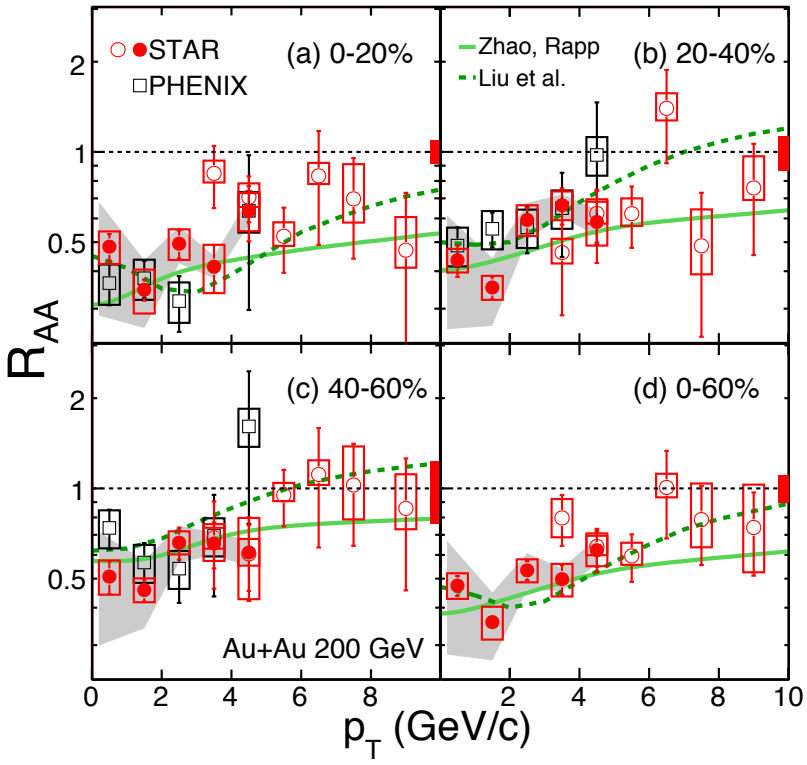

Figure 5.16: The J/ψ nuclear modification factor in Au+Au collisions (closed circles). The results are compared to STAR high-p_T results [72] (open circles), published data in $|y| < 0.35$ [74] (open squares), and and theoretical predictions (solid line [159] and dashed line [154]).

in $40-60\%$ central collisions. This can be explained by the escape of high-p_T J/ψ from the hot suppression region created in heavy ion collisions, or from initial-state multiple gluon scattering which provides additional p_T to the J/ψ in comparison to p+p collisions. A significant suppression is observed for $p_T < 3$ GeV/c for all centralities ($R_{AA} < 0.6$ in $0-20\%$ and $20-40\%$), which is expected to arise from the color screening of J/ψ in the deconfined medium, and competes with various modifications such as regeneration from charm quarks and formation time effects to create the observed p_T dependence. Given the current uncertainties, the data cannot distinguish between either model prediction.

The centrality and p_T dependence of the J/ψ nuclear modification factor exhibits some interesting features in the data and in the model predictions. The cold nuclear matter effects have been studied in d+Au, and have been subtracted from the modification of J/ψ production in Au+Au collisions to determine the effects of a deconfined medium. However, current uncertainties prevent an accurate measurement of the modification to J/ψ production in addition to CNM effects. The J/ψ R_{AA} has been compared to model predictions involving several sources of modification to J/ψ production, and these reproduce the data well. In addition to cold nuclear matter effects, an overall suppression compatible with color screening dominates the modification and results in a suppression of J/ψ production. The models suggest a low-p_T enhancement from regeneration, and an increase of R_{AA} with increasing p_T from the escape of J/ψ from the suppression zone due to formation time effects, consistent with the trend observed in data. These observations are consistent with the formation of a QGP phase.

The J/ψ invariant yield and nuclear modification factor in Au+Au collisions are summarized in Table 5.4. The uncertainties are separated into (A) statistical, (B) systematic, and (C) global uncertainties which arise from the uncertainty in $N_{\rm coll}$ and the uncertainty in the p+p cross section. The systematic uncertainties are discussed in Chapter 6.

Table 5.4: The J/ψ invariant yield and nuclear modification factor for $|y| < 1$ in Au+Au collisions at $\sqrt{s_{NN}} = 200$ GeV with (A) statistical, (B) systematic, and (C) global uncertainties.

Cent.	p_T	Yield	±(A)	+(B)	-(B)	scale	R_{AA}	(A)	+(B)	-(B)	(C)
$0-60$	$0-1$	16.38	1.23	$+1.60$	-1.62	$\times10^{-6}$	0.47	0.04	$+0.05$	-0.05	0.20
	$1-2$	7.46	0.43	$+0.93$	-0.94	$\times10^{-6}$	0.36	0.02	$+0.04$	-0.05	0.09
	$2-3$	2.40	0.18	$+0.21$	-0.21	$\times10^{-6}$	0.53	0.04	$+0.05$	-0.05	0.08
	$3-4$	0.66	0.07	$+0.08$	-0.08	$\times10^{-6}$	0.50	0.06	$+0.06$	-0.06	0.06
	$4-5$	0.19	0.03	$+0.02$	-0.02	$\times10^{-6}$	0.62	0.10	$+0.07$	-0.07	0.08
$0-20$	$0-1$	33.39	3.39	$+4.12$	-4.16	$\times10^{-6}$	0.48	0.05	$+0.06$	-0.06	0.20
	$1-2$	14.46	1.18	$+2.40$	-2.42	$\times10^{-6}$	0.35	0.03	$+0.06$	-0.06	0.09
	$2-3$	4.45	0.48	$+0.52$	-0.52	$\times10^{-6}$	0.49	0.05	$+0.06$	-0.06	0.07
	$3-4$	1.10	0.20	$+0.20$	-0.20	$\times10^{-6}$	0.41	0.07	$+0.08$	-0.08	0.04
	$4-5$	0.40	0.08	$+0.06$	-0.06	$\times10^{-6}$	0.64	0.13	$+0.09$	-0.09	0.07
$20-40$	$0-1$	11.51	1.36	$+1.02$	-1.07	$\times10^{-6}$	0.44	0.05	$+0.04$	-0.04	0.18
	$1-2$	5.63	0.49	$+0.51$	-0.53	$\times10^{-6}$	0.35	0.03	$+0.03$	-0.03	0.10
	$2-3$	2.04	0.20	$+0.24$	-0.25	$\times10^{-6}$	0.59	0.06	$+0.07$	-0.07	0.10
	$3-4$	0.67	0.09	$+0.07$	-0.07	$\times10^{-6}$	0.66	0.09	$+0.07$	-0.07	0.09
	$4-5$	0.14	0.04	$+0.02$	-0.02	$\times10^{-6}$	0.58	0.16	$+0.10$	-0.10	0.09
$40-60$	$0-1$	4.23	0.53	$+0.55$	-0.56	$\times10^{-6}$	0.51	0.06	$+0.07$	-0.07	0.24
	$1-2$	2.30	0.19	$+0.20$	-0.22	$\times10^{-6}$	0.46	0.04	$+0.04$	-0.04	0.15
	$2-3$	0.72	0.09	$+0.06$	-0.06	$\times10^{-6}$	0.66	0.08	$+0.06$	-0.06	0.17
	$3-4$	0.21	0.04	$+0.03$	-0.03	$\times10^{-6}$	0.65	0.11	$+0.08$	-0.08	0.16
	$4-5$	0.05	0.01	$+0.01$	-0.01	$\times10^{-6}$	0.61	0.19	$+0.18$	-0.19	0.15
$0-5$	$0-5$	448.45	29.34	$+61.71$	-61.83	$\times10^{-6}$	0.40	0.03	$+0.05$	-0.05	0.07
$5-10$	$0-5$	394.34	48.35	$+58.60$	-59.30	$\times10^{-6}$	0.44	0.05	$+0.06$	-0.07	0.07
$10-20$	$0-5$	271.57	21.83	$+26.81$	-27.42	$\times10^{-6}$	0.42	0.03	$+0.04$	-0.04	0.07
$20-30$	$0-5$	166.12	12.53	$+12.90$	-13.36	$\times10^{-6}$	0.42	0.03	$+0.03$	-0.03	0.08
$30-40$	$0-5$	114.14	7.95	$+5.89$	-6.32	$\times10^{-6}$	0.48	0.03	$+0.02$	-0.03	0.10
$40-50$	$0-5$	66.08	4.92	$+5.23$	-5.41	$\times10^{-6}$	0.50	0.04	$+0.04$	-0.04	0.13
$50-60$	$0-5$	38.11	3.33	$+2.23$	-2.38	$\times10^{-6}$	0.56	0.05	$+0.03$	-0.04	0.18

Chapter 6

Systematic Uncertainties

The primary sources of uncertainty in the data analysis, yield extraction, and efficiency correction for J/ψ in d+Au and Au+Au collisions are described below.

1. dE/dx Efficiency. The dE/dx electron identification efficiency is shown in Fig 4.29 and 4.28 for d+Au and Au+Au, respectively. The uncertainty associated with the electron dE/dx identification efficiency can be separated into several components, and these are discussed below.

(a) Fit Constraints. In order to determine the various particle contributions to the $n\sigma_e$ distributions, multiple Gaussians are fitted to account for the electrons, pions, protons and deuterons. The details and results of the fitting are described in Appendices B.1 and B.2. There is some ambiguity in the fitting in regions where the hadron dE/dx overlaps the electrons. Constraints on the Gaussian fit parameters have been used in some regions to improve the fitting, and these constraints were relaxed and varied to determine the effect on the fitting. The fit parameters were also varied within the errors obtained by the fitting procedure, and all of these variations resulted in an uncertainty of $\sim 2\%$.

(b) Momentum dependence. The mean and width of the electron $n\sigma_e$ distributions in Au+Au exhibit a momentum dependence, which may be due to calibration

effects, or from a residual hadron contamination underneath the electron peak that is not removed by the TOF or photonic electron requirements. To understand this effect, the mean and width were assumed to be constant, and fitted with a constant function in the range $0.2 < p < 5$ GeV/c. The efficiency calculated using the corresponding constant mean and width resulted in a change in the final yield of $4 - 6\%$, which has been included in the systematics.

(b) Efficiency Calculation. The Gaussian fit parameters obtained from the $n\sigma_e$ distribution have been used to determine the efficiency of the $n\sigma$ electron identification requirements. In Au+Au, electrons are identified using $n\sigma_e$ only, and the efficiency is calculated directly from the electron mean and width extracted from the Gaussian fits. The uncertainty associated to the fitting is described above. The TOF was not available in d+Au, and hadrons were rejected using $n\sigma_e$, $n\sigma_p$, and $n\sigma_\pi$. The uncertainty from the efficiency calculation of these requirements is discussed below.

The dE/dx efficiency in d+Au was calculated using a multiple Gaussian fitting to the $n\sigma_e$ distribution combined with a Monte Carlo simulation, and is shown in Fig. 6.1 (right panel). The simulation was used to determine the fraction of electrons and hadrons satisfying the dE/dx requirements, and this is explained in detail in Chapter 4. The efficiency was also calculated from data without a Monte Carlo simulation. The accepted number of electrons was obtained from the electron candidates in data satisfying the dE/dx requirements, and the total number of electrons was calculated from the Gaussian fit to the electron contribution in the $n\sigma_e$ distribution. This is illustrated in Fig. 6.1 (left panel), and shows the $n\sigma_e$ distribution for $3 < p < 3.2$ GeV/c in d+Au (histogram) and Gaussian fits to the electron (red), pion, (blue), and proton (green). The electron candidates from data satisfying the dE/dx requirements are also shown (red shaded histogram), and the hadron contamination can be seen by the excess counts in the data above the electron Gaussian. The efficiency has been calculated by comparing the number of electron candidates from data that lie below the electron Gaussian distribution to the integral of the electron Gaussian. This method assumes that the only hadron contribution is in the

excess above the Gaussian function, which may not be valid at low momentum. The dE/dx efficiency obtained using this method is compared to the efficiency used to correct the final results in Fig. 6.1 (right panel), and the two methods agree well for $p > 1.6$ GeV/c. Below this, the proton dE/dx is steeply falling and overlaps the electrons, resulting in an uncertainty in the estimate for the hadron contamination from data. The difference between the two methods results in a systematic uncertainty of $\sim 14\%$ in the final results.

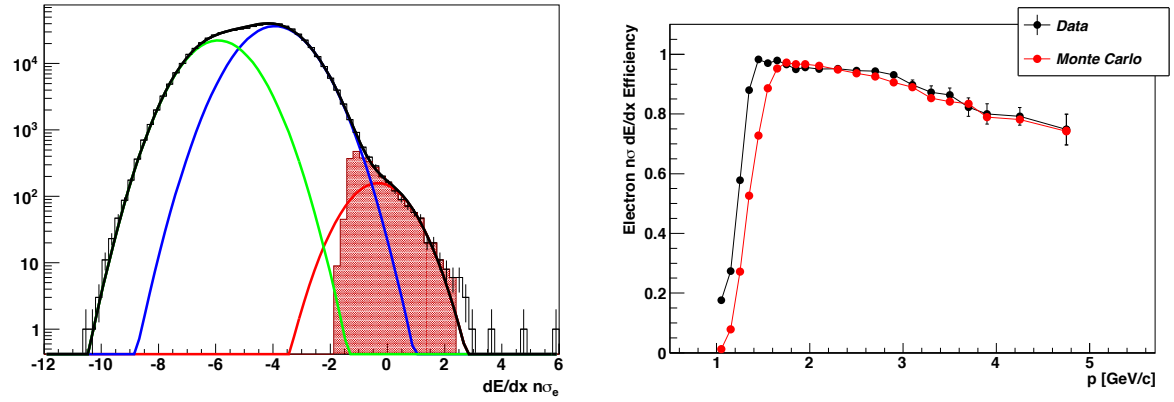

Figure 6.1: The $n\sigma_e$ distribution for $3 < p < 3.2$ GeV/c in d+Au collisions (left) for all particles (histogram), and for electrons satisfying the $n\sigma$ requirements. The associated efficiency (right) is obtained from data and simulation.

2. TOF Efficiency. There are several uncertainties associated with the TOF matching efficiency and $1/\beta$ cut efficiency used to correct the Au+Au data, and these are described below.

(a) Matching Efficiency. The TOF matching efficiency was obtained from data, and the purity of the electrons used to obtain the efficiency was poor for $p < 1.2$ GeV/c. Instead, the TOF matching efficiency was obtained from a scaled hadron TOF matching efficiency, which provides significantly more statistics than can be obtained using electrons. The ratio of the electron and hadron matching efficiency

was calculated for $p > 1.2$ GeV/c a region where the electron purity was high. The ratio of 1.045 was obtained and used to scale the hadron matching efficiency, which was then used to correct the data. To determine the uncertainty on the efficiency, the results were also obtained using the hadron efficiency without any scaling, and using the electron efficiency with limited purity. These resulted in an uncertainty of $\sim 2-3\%$ and $\sim 1\%$, respectively. The pseudorapidity dependence of the matching efficiency was also investigated by correcting the data with a different number of pseudorapidity bins, and resulted in an uncertainty of $\sim 1-3\%$.

(b) $1/\beta$ Efficiency. The $1/\beta$ cut efficiency was calculated by determining the fraction of electrons with $|1/\beta - 1| < 0.03$. This was done by obtaining a high-purity electron sample and counting the entries in $|1/\beta - 1| < 0.03$. The efficiency was also estimated by fitting a Gaussian function to the $1/\beta$ distribution to remove any non-Gaussian contributions to the tails of the distribution from hadron contamination. The centrality dependence of the efficiency was also considered, and this was found to be a small effect ($\sim 1\%$). The total uncertainty on the $1/\beta$ efficiency was found to be $\sim 1-3\%$.

3. BEMC Efficiency. The uncertainty due to the BEMC was primarily from the disagreement between simulation and data. The matching and E/p cut efficiency from simulation and data are compared in Fig. 4.33 for Au+Au collisions. The distribution of the distance between tracks and BEMC clusters from data is wider than from simulation, and the same trend was observed in the E/p distributions in d+Au and Au+Au. This results in an efficiency from data that is systematically lower that that from simulation by $\sim 2-10\%$. The uncertainty from the BEMC is obtained by comparing the results obtained from simulation and data, and results in an uncertainty in the final results of $< 10\%$ in d+Au collisions, and $\sim 14-18\%$ in Au+Au collisions.

4. Tracking Efficiency. The tracking efficiency of the TPC was determined by embedding Monte Carlo J/ψs into real data events, allowing the J/ψ to decay

into its daughter electrons, and using GEANT to model how the electrons interact with the detector material. How well the simulation mimics the interaction between charged particles and the TPC was determined by comparing the distributions from simulation and data, such as $nHitsFit$, $nHitsDedx$, and DCA. These distributions are compared in Appendices D.1 and D.2, and there is an observed shift between the data and simulation of $\sim 1-2$ hits. The uncertainty from the tracking efficiency was obtained from the differences between the simulation and data, resulting in an uncertainty of $\sim 6\%$ in Au+Au and $\sim 12\%$ in d+Au.

5. Yield Extraction. The J/ψ yield was obtained by subtracting a combinatorial background from the opposite sign dielectron mass spectrum, and fitting this with a signal shape obtained from simulation. The uncertainties associated with this are described below.

(a) Counting. The yield was also obtained by counting the number of entries in the dielectron mass spectrum in the range $3 < m < 3.2$ GeV/c^2 after background subtraction. The number of counts was corrected using the fraction of J/ψs outside of this mass range ($\sim 15\%$), which was determined using the signal shape from simulation. This was compared to the results obtained from fitting the signal shape from simulation to the mass spectrum, and resulted in an uncertainty of $\sim 2-20\%$ in Au+Au, depending on p_T and collision centrality. The uncertainty was largest for $3 < p_T < 4$ GeV/c (see Fig. 6.2), and results from statistical fluctuations in the invariant mass distribution. The comparison was performed for $p_T < 5$ GeV/c in $0-100\%$ central d+Au collisions to enhance statistics and minimize the effects from fluctuations, and resulted in an uncertainty of the J/ψ yield of 12.5%.

(b) Fitting. A mixed-event background was used in Au+Au and has been fitted to the like-sign background in the range $2.6 < m < 3.6$ GeV/c^2. The signal shape from simulation has been combined with a residual background (straight line) and fitted to the background-subtracted mass spectrum in the range $2.6 < m < 3.6$ GeV/c^2

to determine the J/ψ yield. The fit range for the mixed-event background and the signal shape have been varied, and result in an uncertainty on the final yield in Au+Au of $\sim 3-10\%$.

(c) Signal Shape. An additional Gaussian smearing was applied to the momentum resolution in simulation to improve the fit quality between the data and simulation in Au+Au collisions. The additional smearing factor was determined by performing a χ^2 minimization of the signal shape to the data. The uncertainty on the smearing coefficient was obtained from the χ^2 distribution and resulted in an uncertainty in the final yield in Au+Au of $\sim 2-5\%$.

6. Efficiency Correction. The J/ψ p_T spectrum in $0-100\%$ central d+Au collisions was calculated for $p_T < 5$ GeV/c with $\Delta p_T = 1$, and corrected using the efficiency in Fig. 4.37. Due to limited statistics, only the p_T-integrated yield in each centrality bin was calculated. The p_T-integrated efficiency was calculated from an unweighted and weighted average of the p_T-dependent efficiency correction. The weighted efficiency was determined using the J/ψ p_T spectrums from PYTHIA, and the difference in these two efficiencies resulted in an uncertainty in the final d+Au yield of $< 9\%$.

The statistical uncertainties from the particle identification efficiencies and the tracking efficiency have been combined to obtain an uncertainty of $4-5\%$, which has been added to the systematic uncertainties.

7. Normalization uncertainty. The nuclear modification factor was calculated by normalizing the invariant yield in d+Au and Au+Au collisions to the yield in p+p collisions, scaled to the number of binary collisions in each centrality bin. The normalization uncertainties include the uncertainty of the J/ψ cross section p+p collisions of 16%, the 8% uncertainty on the inelastic cross section in p+p collisions ($\sigma^{\rm pp}_{\rm inel}$), and the uncertainty on $N_{\rm coll}$, which is 12% in d+Au and $3-20\%$ in Au+Au (increasing with decreasing collision centrality). While the uncertainties on $N_{\rm coll}$ and

$\sigma_{\rm inel}^{\rm pp}$ are correlated, they have been added in quadrature and therefore the normalization uncertainty represents an upper limit.

The systematic uncertainties described above are summarized in Table 6.1 versus p_T for $0-100\%$ central d+Au collisions, and in Table 6.2 for $0-60\%$ central Au+Au collisions. The p_T and centrality dependence of the total systematic uncertainty for J/ψ in Au+Au collisions is shown in Fig. 6.2.

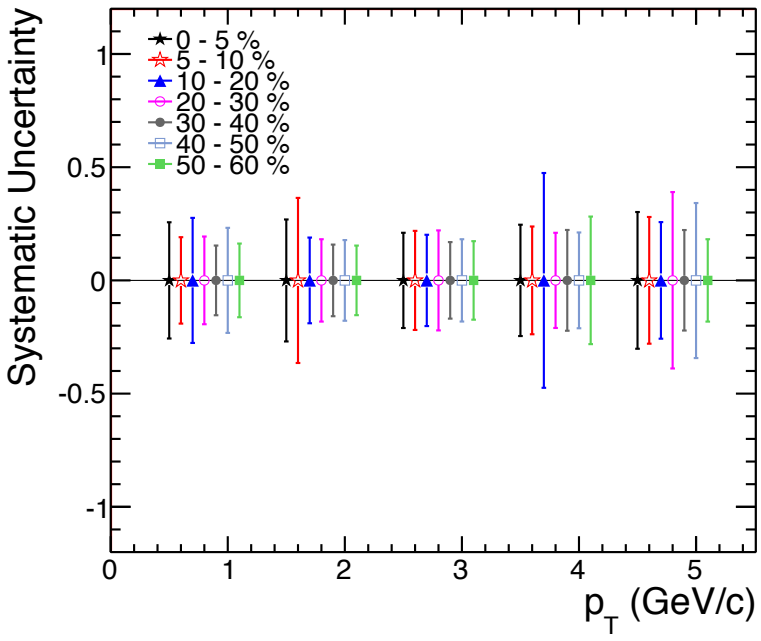

Figure 6.2: The p_T and centrality dependence of the total systematic uncertainty for J/ψ in Au+Au collisions.

Table 6.1: The J/ψ systematic uncertainties in $0-100\%$ central d+Au collisions.

Source	$0-1$ GeV/c (%)	$1-2$ GeV/c (%)	$2-3$ GeV/c (%)	$3-4$ GeV/c (%)	$4-5$ GeV/c (%)
$n\sigma$ fit	+2.8 -1.5	+1.7 -0.9	+0.9 -0.5	+2.5 -1.5	+4.6 -2.8
$n\sigma$ method	+15.7 -15.4	+10.5 -15.4	+13.6 -10.2	+7.7 -7.7	+7.7 -3.4
Tracking	±11.7	±11.7	±11.7	±11.7	±11.7
Yield	+12.5	+12.5	+12.5	+12.5	+12.5
Efficiency	±8.3	±8.3	±8.3	±8.3	±8.3
BEMC	±11.1	±10.8	±10.3	±9.3	±9.3

Table 6.2: The J/ψ systematic uncertainties in $0-60\%$ central Au+Au collisions.

Source	$0-1$ GeV/c (%)	$1-2$ GeV/c (%)	$2-3$ GeV/c (%)	$3-4$ GeV/c (%)	$4-5$ GeV/c (%)
$n\sigma_e$ (fit)	$+1.1$	$+1.0$	$+0.7$	$+1.5$	$+1.8$
	-1.1	-1.0	-0.7	-1.5	-1.8
$n\sigma_e$ (const.)	$+5.8$	$+5.7$	$+5.4$	$+5.0$	$+4.4$
	-5.8	-5.7	-5.4	-5.0	-4.4
TOF	$+2.3$	$+2.8$	$+2.5$	$+2.1$	$+1.8$
	-2.3	-2.8	-2.5	-2.1	-1.8
$1/\beta$	$+2.2$	$+2.5$	$+1.9$	$+1.5$	$+1.3$
	-1.7	-2.3	-2.0	-1.7	-1.4
BEMC / E/p	$+13.9$	$+14.1$	$+14.5$	$+16.5$	$+17.3$
	-13.9	-14.1	-14.5	-16.5	-17.3
Tracking	$+5.9$	$+6.2$	$+6.5$	$+6.3$	$+5.9$
	-5.9	-6.2	-6.5	-6.3	-5.9
Efficiency	$+4.0$	$+4.0$	$+4.1$	$+4.1$	$+4.2$
	-4.3	-4.3	-4.3	-4.4	-4.4
Yield (counts)	$+5.2$	$+9.0$	$+1.9$	$+11.9$	$+8.4$
	-5.2	-9.0	-1.9	-11.9	-8.4
Yield (fit)	$+0.5$	$+0.1$	$+2.7$	$+4.0$	$+2.8$
	-0.5	-0.1	-2.7	-4.0	-2.8
Yield (smear)	$+1.7$	$+2.2$	$+2.6$	$+2.7$	$+1.9$
	-2.0	-2.5	-2.5	-2.2	-1.5

Chapter 7

Summary

The production of J/ψ with $p_T < 5$ GeV/c and $|y| < 1$ in d+Au and Au+Au collisions at $\sqrt{s_{NN}} = 200$ GeV at the STAR detector at RHIC was presented in this thesis. The reconstruction of J/ψ has been performed via the dielectron decay channel, and the electron identification and J/ψ reconstruction methods used in this analysis have been described. The J/ψ p_T spectrum has been calculated and compared to the production in p+p collisions to determine the modification to J/ψ in d+Au and Au+Au collisions. The collision centrality and transverse momentum dependence of the yield, efficiency correction, and nuclear modification factor have been calculated in both collision systems, and a description of the uncertainties associated with these measurements has been provided.

The nuclear modification factor in d+Au was compared to predictions for cold nuclear matter effects. Modifications of the nuclear parton distribution functions were combined with a J/ψ nuclear absorption cross section of

$$\sigma_{\rm abs} = 2.8^{+3.5}_{-2.6}\ (\text{stat.})\ ^{+4.0}_{-2.8}\ (\text{syst.})\ ^{+1.8}_{-1.1}\ (\text{EPS09})\ \text{mb},$$

which was obtained from a fit to the data using the EPS09 nPDFs [86, 98]. While the uncertainties on the J/ψ absorption cross section are large, the results are consistent with other measurements at the same energy [152, 156, 157].

A suppression of J/ψ production in Au+Au collisions was observed, with $R_{AA} < 0.5$ in $0-20\%$ central collisions. The cold nuclear matter effects obtained from d+Au collisions have been subtracted from the J/ψ modification factor in Au+Au collisions [158], and the data suggest an additional suppression of $\sim 0.1-0.2$, consistent with the formation of a QGP phase. However, the current uncertainties prevent a measurement of the suppression beyond cold nuclear matter effects, and more precise data and theoretical models are needed to quantify this amount.

The nuclear modification factor in Au+Au was compared to predictions involving various modifications to J/ψ production in heavy ion collisions in addition to the cold nuclear matter effects measured in d+Au collisions. The models were able to describe the J/ψ suppression in Au+Au well, and included a suppression from color screening, regeneration of J/ψ from charm quarks in the QGP sea, feed-down from excited states and B decay, and escape of high-p_T J/ψ from the suppression zone due to formation time effects. The color screening from a deconfined phase results in an overall suppression which increases with increasing collision centrality. This competes with contributions from regeneration at low-p_T and high-p_T leakage. These trends are observed in the data, with R_{AA} increasing with p_T and reaching unity for $p_T > 5$ GeV/c in $40-60\%$ central collisions. Regeneration is expected to populate low p_T, and while an increase for $R_{AA} < 1$ GeV/c was observed, the current precision does not allow for a measurement of this contribution.

In summary, the cold nuclear matter effects to J/ψ production in d+Au collisions have been determined and subtracted from the modifications in Au+Au collisions. However, given the current uncertainties in the data, a suppression beyond cold nuclear matter effects could not be determined. The collision centrality and p_T dependence of the J/ψ nuclear modification factor in Au+Au collisions are in good agreement with predictions involving the color screening of J/ψ in a deconfined medium and the regeneration of J/ψ from the coalescence of charm quarks, and a suppression compatible with the formation of a quark gluon plasma was observed.

Bibliography

[1] Thomas McEvilley. *The shape of ancient thought: comparative studies in Greek and Indian philosophies*. Allworth Press. ISBN 1-58115-203-5, 2002.

[2] B.J. Bjorken and S.L. Glashow. *Phys. Lett.*, 11:255, 1964.

[3] M. Kobayashi and T. Maskawa. *Prog. Th. Phys.*, 49:652, 1973.

[4] H. Harari. *Physics Letters B*, 57B:265, 1975.

[5] E.D. Bloom et al. *Phys. Rev. Lett.*, 23:930, 1969.

[6] M. Breidenbach et al. *Phys. Rev. Lett.*, 23:935, 1969.

[7] S.W. Herb et al. *Phys. Rev. Lett.*, 39:252, 1977.

[8] F. Abe et al. *Phys. Rev. Lett.*, 74:2626, 1995.

[9] S. L. Glashow. *Nucl. Phys.*, 22:579, 1961.

[10] P. W. Higgs. *Phys. Rev. Lett*, 13:508, 1964.

[11] S. Weinberg. *Phys. Rev. Lett*, 19:1264, 1967.

[12] CERN press release. `http://press.web.cern.ch/press/PressReleases/Releases2012/PR17.12E.html`, 2012.

[13] J. Beringer et al. *Phys. Rev. D*, 86:010001, 2012.

[14] T. van Ritbergen, J. Vermaseren, and S. Larin. *Phys. Lett. B*, 400:379, 1997.

[15] Siegfried Bethke. *Eur. Phys. J*, C64:689, 2009.

[16] G. Sterman et al. *Rev. Mod. Phys.*, 67:157, 1995.

[17] P. Petreczky. *Nucl. Phys.*, B140:78, 2004.

[18] J. B. Kogout. *Rev. Mod. Phys.*, 55:775, 1983.

[19] S. Durr et al. *Science*, 322:1224, 2008.

[20] C. T. H. Davies et al. *Phys. Rev.*, D78:114, 2008.

[21] Z. Fodor and S. D. Katz. *Phys. Lett.*, B534:87, 2002.

[22] E. V. Shuryak. *Phys. Rept.*, 61:71, 1908.

[23] S. Digal, P. Petreczky, and H. Satz. *Phys. Rev. D*, 64:094015, 2001.

[24] F. Karsch, D. Kharzeev, and H. Satz. *Phys. Lett. B*, 637:75, 2006.

[25] P. Braun-Munzinger and J. Stachel. *Nature*, 448:302, 2007.

[26] Y. M. K. Yagi and T. Hatsuda. *From Big Bang to Little Bang*. Cambridge University Press, 2006.

[27] Berndt Muller. *The physics of the quark-gluon plasma*. Springer-Verlag, 1985.

[28] F. Karsch. *Nucl. Phys.*, A698:199, 2002.

[29] Z. Fodor, S. D. Katz, and K. K. Szabo. *Phys. Lett.*, B568:73, 2003.

[30] Z. Fodor and S. D. Katz. *Journ. High Energy Phys.*, 04:50, 2004.

[31] R. V. Gavai and S. Gupta. *Phys. Rev.*, D71:114014, 2005.

[32] M. M. Aggarwal et al. 2010, arXiv:1007.2613v1.

[33] RHIC home page. `http://www.bnl.gov/rhic`.

[34] J. Adams et al. *Nucl. Phys.*, A757:102, 2005.

[35] K. Adcox et al. *Nucl. Phys.*, A757:184, 2005.

[36] P. Braun-Munzinger, I. Heppe, and J. Stachel. *Phys. Lett.*, B465:15, 1999.

[37] E. Schnedermann, J. Sollfrank, , and U. Heinz. *Phys. Rev.*, C48:2462, 1993.

[38] Duke University home page. `http://www.phy.duke.edu`.

[39] H. Caines. *J. Phys.*, G31:S101, 2005.

[40] E. Laermann and O. Philipsen. *Ann. Rev. Nucl. Part. Sci.*, 53:163, 2003.

[41] F. Karsch. *Lect. Notes Phys.*, 583:209, 2002.

[42] J.D. Bjorken. *Phys. Rev. D*, 27:140, 1983.

[43] S. Adler et al. *Phys. Rev.*, C71:034908, 2005.

[44] S. Adler et al. *Phys. Rev. C*, 71:034908, 2005. Erratum-ibid.C71:049901.

[45] D. Kharzeev and E. Levin. *Phys. Lett.*, B523:79, 2001.

[46] J. Adams et al. *Phys. Rev. Lett.*, 92:112301, 2004.

[47] E. Schnedermann, J. Sollfrank, and U. Heinz. *Phys. Rev. C*, 48:2462, 1993.

[48] P. Braun-Munzinger, J. Stachel, J. Wessels, and N. Xu. *Phys. Lett.*, B344:43, 1995.

[49] J. Cleymans, D. Elliott, H. Satz, , and R. L. Thews. *Z Pys.*, 74:319, 1997.

[50] W. Broniowski, W. Florkowski, and M. Michalec. *Acta Phys. Polon.*, B33:761, 2002.

[51] Z. Tang. 2011, arXiv:1101.1912.

[52] B. De, S. Bhattacharyya G. Sau, and S. Biswas. *Int. J Mod. Phys.*, E16:1687, 2007.

[53] G. Wilk and Z. Wlodarczyk. *Eur. Phys. J*, A40:299, 2009.

[54] Z. Tang. *Phys. Rev. C*, 79:051901, 2009.

[55] STAR home page. `http://www.star.bnl.gov`.

[56] J. Adams et al. *Phys. Rev. C*, 72:014904, 2005.

[57] S. A. Voloshin. *Nucl. Phys.*, A715:379, 2003.

[58] R. J. Fries, B. Muller, C. Nonaka, and S. A. Bass. *Phys. Rev.*, C68:044902, 2003.

[59] D. Molnar and S. A. Voloshin. *Phys. Rev. Lett.*, 91:092301, 2003.

[60] J. Adams et al. *Phys. Rev. Lett.*, 91:072304, 2003.

[61] D. H. Perkins. *Introduction to High Energy Physics*. Cambridge University Press, 2000.

[62] T. Matsui and H. Satz. *Phys Lett. B*, 178:416, 1986.

[63] J. P. Lansberg. *A Rev. Int. J. Mod. Phys.*, A21:3857, 2006.

[64] M. C. Abreu et al. *Phys. Lett. B*, 449:128, 1999.

[65] R. Arnaldi et al. *Phys. Rev. Lett.*, 99:132302, 2007.

[66] R. Arnaldi et al. *Nucl. Phys.*, A783:261, 2007.

[67] A. Adare et al. *Phys. Rev. Lett.*, 98:232301, 2007.

[68] E. T. Atomssa. 2008, arXiv:0805.4562v1.

[69] R. Placakyte. In *Proceedings of XXXI Physics in Collision*, 2011, arXiv:1111.5452v4.

[70] J. Rafelski, R. L. Thews, and M. Schroedter. *Phys. Lett. B*, 678:72, 2009.

[71] N. Brambilla et al. *Eur. Phys. Journ. C*, 71:1534, 2011.

[72] L. Adamczyk et al. 2011, arXiv:1208.2736v1.

[73] C. B. Powell. *Proceedings of Science (EPS-HEP2011)*, page 485, 2011, arXiv:1111.6944v2.

[74] B. I. Abelev et al. *Phys. Rev. Lett.*, 98:232002, 2007.

[75] R. Baier and R. Ruckl. *Phys. Lett. B*, 102:102, 1981.

[76] P. Artoisenet et al. *Phys. Rev. Lett.*, 101:152001, 2008.

[77] E. L. Berger and D. L. Jones. *Phys. Rev.*, D23:1521, 1981.

[78] B. Trzeciak. In *Proceedings of the International Conference on Strangeness in Quark Matter*, 2011, arXiv:1202.0897v1.

[79] G. C. Nayak, M. X. Liu, and F. Cooper. *Phys. Rev. D*, 71:032001, 2005.

[80] H. Fritzsch. *Phys. Lett. B*, 67:217, 1977.

[81] P. L. Cho and A. K. Leibovich. *Phys. Rev. D*, 53:150, 1996.

[82] P. L. Cho and A. K. Leibovich. *Phys. Rev. D*, 53:6203, 1996.

[83] A.D. Frawley, T. Ullrich, and R. Vogt. *Phys. Rept.*, 462:125, 2008.

[84] M. Bedjidian et al. 2003, arXiv:hep-ph/0311048v1.

[85] B. Meredith. *Nucl. Phys. A*, 830:595, 2009.

[86] K.J. Eskola, H. Paukkunena, and C.A. Salgado. *Nucl. Phys. A*, 830:599, 2009.

[87] D. de Florian and R. Sassor. *Phys. Rev. D*, 69:074028, 2004.

[88] K.J. Eskola, V.J. Kolhinen, and P.V. Ruuskanen. *Nucl. Phys. B*, 535:351, 1998.

[89] M. Hirai, S. Kumano, and M. Miyama. *Phys. Rev. D*, 64:034003, 2001.

[90] K.J. Eskola, H. Paukkunena, and C.A. Salgado. *JHEP*, 0807:102, 2008.

[91] V. Tram and F. Arleo. *Eur. Phys. J. C*, 61:847, 2009.

[92] M. Lev and B. Petersson. *Z. Phys. C*, 21:155, 1983.

[93] R. Vogt. *Phys. Rev. C*, 71:054902, 2005.

[94] C. Lourenco, R. Vogt, and H. Woehri. *JHEP*, 0902:14, 2009.

[95] S. Gavin and R. Vogt. *Nucl. Phys. A*, 610:442, 1996.

[96] A. Capella et al. *Phys. Lett. B*, 393:431, 1997.

[97] N. Armesto, A. Capella, E. G. Ferreiro, A. Kaidalov, and D. Sousa. *Nucl. Phys. A*, 698:583, 2002.

[98] R. Vogt. *Phys. Rev. C*, 81:044903, 2010.

[99] R. Vogt. *Phys. Rev. C*, 71:054902, 2005.

[100] F. Karsch and P. Petronzio. *Z. Phys. C*, 37:627, 1988.

[101] L. Kosarzewski. *Acta Phys. Pol. B*, 5:543, 2012. Proceedings Supplement.

[102] M. Harrison, T. Ludlam, and S. Ozaki. *Nucl. Instr. Meth. in Phys. Research A*, 499:235, 2003.

[103] W. Fischer (BNL). 2010.

[104] M. Blaskiewicz, J. M. Brennan, and K. Mernick. *Phys. Rev. Lett.*, 105:094801, 2010.

[105] W. Fischer. `http://www.agsrhichome.bnl.gov/RHIC/Runs`, 2012.

[106] Abhay Deshpande, Richard Milner, Raju Venugopalan, and Werner Vogelsang. *Ann. Rev. Nucl. Part. Sci.*, 55:165, 2005.

[107] PHENIX home page. `http://www.phenix.bnl.gov`.

[108] BRAHMS home page. `www4.rcf.bnl.gov/brahms/WWW/brahms.html`.

[109] PHOBOS home page. `http://www.phobos.bnl.gov`.

[110] K. H. Ackermann et al. *Nucl. Instr. Meth. A*, 499:624, 2003.

[111] K. Kajimoto. PhD thesis, The University of Texas at Austin, 2009.

[112] R. Bellwied et al. *Nucl. Instr. Meth. A*, 499:640, 2003.

[113] M. Anderson et al. *Nucl. Instr. Meth. A*, 499:652, 2003.

[114] H. H. Weiman et al. `http://rnc.lbl.gov/~wieman/hft_final_submission_version.pdf`, 2007.

[115] J. Bouchet. 2009, arXiv:0907.3407.

[116] M. Anderson et al. *Nucl. Instr. Meth. A*, 499:659, 2003.

[117] W. J. Llope. *Nucl. Instr. Meth. A*, 2010. doi:10.1016/j.nima.2010.07.086.

[118] M. Beddo et al. *Nucl. Instr. Meth. A*, 499:725, 2003.

[119] C. E. Allgower et al. *Nucl. Instr. Meth. A*, 499:740, 2003.

[120] M. M. Aggarwal et al. *Nucl. Instr. Meth. A*, 499:751, 2003.

[121] K. H. Ackermann et al. *Nucl. Instr. Meth. A*, 499:713, 2003.

[122] F. Bergsma et al. *Nucl. Instr. Meth. A*, 499:633, 2003.

[123] W. J. Llope et al. *Nucl. Instr. Meth. A*, 522:252, 2004.

[124] C. Adler et al. *Nucl. Instr. Meth. A*, 499:433, 2003.

[125] M. Anderson et al. *Nucl. Instr. Meth. A*, 499:679, 2003.

[126] J. Abele et al. *Nucl. Instr. Meth. A*, 499:692, 2003.

[127] G. Van Buren et al. `http://arxiv.org/pdf/physics/0512157.pdf`, 2005, arXiv:physics/0512157.

[128] A. Rose. `http://arxiv.org/abs/nucl-ex/0307015`, 2003, arXiv:nucl-ex/0307015.

[129] P .Billoir. *Comp. Phys. Comm.*, 57:390, 1989.

[130] R. Reed et al. *Journ. Phys.: Conf. Series.*, 219:03020, 2010.

[131] H. Bichsel. *Nucl. Instr. Meth. A*, 562:154, 2006.

[132] H. Bichsel. *Phys. Rev.*, A46:5761, 1992.

[133] P. Fachini et al. `http://www.star.bnl.gov/public/tof/publications/TOF_20040524.pdf`, 2004.

[134] W. J. Llope et al. *Nucl. Instr. Meth. A*, 538:243, 2005.

[135] E. C. Zeballosa et al. *Nucl. Instr. Meth. A*, 374:132, 1996.

[136] Particle Data Group. `http://pdg.lbl.gov`.

[137] F. S. Bieser et al. *Nucl. Instr. Meth. A*, 499:766, 2003.

[138] C. Adler et al. *Nucl. Instr. Meth. A*, 499:778, 2003.

[139] E. Judd. `http://www.star.bnl.gov/public/trg/runschool/introduction/index.html`, 2004.

[140] T. Ljubicic et al. `http://drupal.star.bnl.gov/STAR/files/future/proposals/daq1000-3-22-2005.pdf`, 2005.

[141] J. M. Landgraf et al. *Nucl. Instr. Meth. A*, 499:762, 2003.

[142] M. J. Le Vine et al. `http://wjllope.rice.edu/~tof/tofp/Documents/DAQTRG_docs/DAQ_Requirements.pdf`, 1997.

[143] J. Dunlop. `http://www.star.bnl.gov/protected/common/common2008/trigger2008/`.

[144] J. Dunlop. `http://www.star.bnl.gov/protected/common/common2010/trigger2010/`.

[145] H. Masui. `http://www.star.bnl.gov/protected/bulkcorr/hmasui/2011/Centrality_200GeV_Nov08/hmasui_centrality_Run10_AuAu_200GeV_PWGC_Nov08_2011.pdf`, 2011.

[146] C. Jena. `www.star.bnl.gov/protected/lfspectra/cjena/run8_dAu200GeV/dAu_centrality/documentation/centrality_run8_dAu200GeV.html`, 2008.

[147] P. Shukla. 2001, arXiv:nucl-th/1011.4193.

[148] M. L. Miller, K. Reygers, S. J. Sanders, and P. Steinberg. 2007, arXiv:nucl-ex/0701025v1.

[149] H. Masui. Centrality Results in Au+Au at 200 GeV. `http://www.star.bnl.gov/protected/common/common2010/centrality/200GeV/index.html`, 2011.

[150] M. L. Miller. PhD thesis, Yale University, 2004.

[151] B. I. Abelev et al. *Phys. Rev. C*, 80:041902, 2009.

[152] A. Adare et al. 2012, arXiv:1204.0777.

[153] U. W. Heinz and C. Shen. 2011. private communication.

[154] Y. Liu, Z. Qu, N. Xu, and P. Zhuang. *Phys. Lett B.*, 678:72, 2009.

[155] J. Adams et al. *Phys. Lett. B*, 612:181, 2005.

[156] A. Adare et al. *Phys. Rev. C*, 77:024912, 2008. Erratum-ibid.C79:059901,2009.

[157] A. Adare et al. 2008, arXiv:0804.4660v1.

[158] N. Brambilla, S. Eidelman, B. K. Heltsley, R. Vogt, G. T. Bodwin, et al. *Eur. Phys. J.*, C71:1534, 2011.

[159] X. Zhao and R. Rapp. *Phys. Rev. C*, 82:064905, 2010.

[160] A. Timmins. PhD thesis, University of Birmingham, 2008.

[161] D. Kharzeev, E. Levin, and M. Nardi. 2002, arXiv:hep-ph/0212316.

Appendix A

Heavy Ion Collisions

Nuclei that are accelerated to relativistic speeds are Lorentz contracted in the direction of motion, resulting in a disk shape. As heavy ions collide, the partons in the overlapping region of the colliding nuclei undergo inelastic collisions, converting kinetic energy into matter and transverse energy. The rapid expansion of the collision system creates a hot volume referred to as the *fireball*, in which QGP may be formed if temperatures are sufficient. The further expansion and cooling of the system leads to hadronization and finally freeze-out, after which particles no longer interact. The space-time evolution of relativistic heavy ion collisions is discussed in Chapter 1 and illustrated in Fig. 1.4. Observables in heavy ion collision experiments, such as particle multiplicities and momentum spectra, provide information of the system after kinetic freeze-out. These final-state distributions are related to the early collision system, and are used to understand the evolution of the system.

The average number of particles produced in heavy ion collisions increases with the amount overlap of nuclear matter in the collision. The degree of overlap is referred to as the *centrality* of a collision. The nuclear overlap is defined by the impact parameter b, which describes the orthogonal distance between the nuclei centers. Incoming nuclei in a heavy ion collision are illustrated in Fig. A.1. The number of participant nucleons (N_{part}) are shown in red, and the spectator nucleons which do not participate in the interaction are shown in blue. A central collision has a small impact

parameter, whereas a large impact parameter indicates a peripheral collisions. As N_{part} increases, the number of elementary nucleon-nucleon collisions, N_{coll}, increases as ${N_{\text{part}}}^{4/3}$ [150]. Both the increase in soft processes with N_{part} and of hard processes with N_{coll} contribute to particle production.

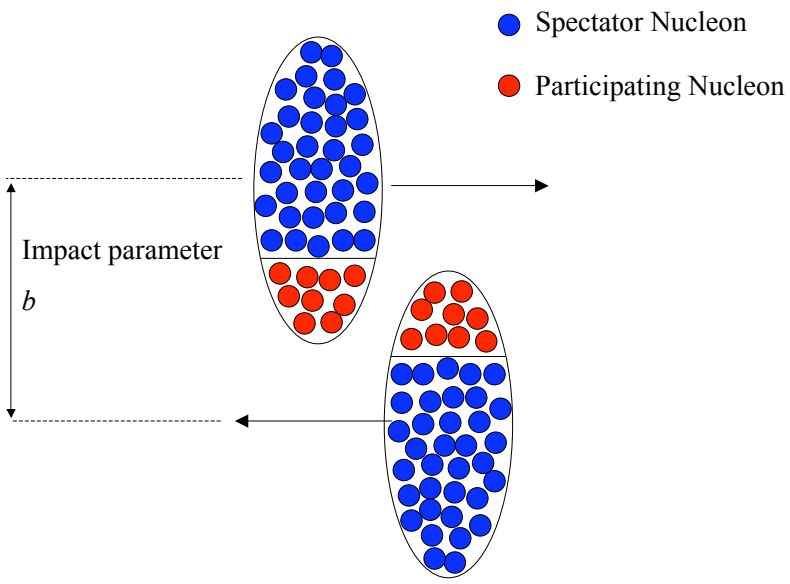

Figure A.1: A schematic diagram of colliding nuclei, indicating the impact parameter b, and the overlap region of the nuclei in red. Figure taken from [160].

Since the impact parameter and the number of participant nucleons cannot be measured directly, the observed particle multiplicity is used as an indirect measure of centrality. Glauber model calculations [147, 150] are used to relate the observed charged particle multiplicity to the collision geometry of the nuclei. This is done by modeling the nucleon-nucleon collisions between the participant nucleons with a given nuclear collision geometry. The distribution of nucleons within a nucleus is described by a Woods-Saxon distribution, where nuclei are assumed to be spherical, and the charge distributions of protons and neutrons are assumed to be the same. The deuteron density is modeled using a Hulthen form [161] for d+Au collisions.

The Glauber model is implemented using a Monte Carlo simulation of the incoming nuclei. Nucleons are distributed according to their density profile, and impact parameters of the nuclei are determined from the relative positions of the nuclei centers, which are randomly selected from uniform distributions in the (x, y) plane. Nucleons interact if their transverse distance is less than $\sqrt{\sigma_{\rm inel}^{\rm pp}/\pi}$, where $\sigma_{\rm inel}^{\rm pp} = 42$ mb is the inelastic nucleon-nucleon cross section at 200 GeV [155]. For a given centrality range, the average impact parameter, number of participant nucleons, and number of nucleon-nucleon collisions is determined and equated to a range in charged particle multiplicity which can be measured experimentally.

Cylindrical coordinates are used to describe the heavy ion collision system, with the z axis oriented along the beam direction. The momentum distributions are separated into components longitudinal and transverse to the beam axis. The momentum vector of a particle ($\boldsymbol{p}$) is separated into the longitudinal momentum (p_z) and boost-invariant transverse momentum (p_T) defined as

$$\begin{aligned} p_z &= |\boldsymbol{p}| \cos\theta, & \text{(A.1)} \\ p_T &= |\boldsymbol{p}| \sin\theta, & \text{(A.2)} \\ &= \sqrt{p_x^2 + p_y^2}, & \text{(A.3)} \end{aligned}$$

where θ is the angle between $\boldsymbol{p}$ and the beam axis (dip angle). The transverse mass, m_T, of a particle with mass m is calculated from its transverse momentum, where

$$m_T = \sqrt{{p_T}^2 + m^2}, \quad \text{(A.4)}$$

and its energy is given by

$$\begin{aligned} E &= \sqrt{|\boldsymbol{p}|^2 + m^2} & \text{(A.5)} \\ &= \sqrt{p_z^2 + m_T^2}. & \text{(A.6)} \end{aligned}$$

From this, the rapidity (y) of a particle can be defined:

$$\begin{aligned} E &= m_T \cosh y, & \text{(A.7)} \\ p_z &= m_T \sinh y, & \text{(A.8)} \end{aligned}$$

from which we obtain

$$y = \frac{1}{2}\ln\left(\frac{E+p_z}{E-p_z}\right), \tag{A.9}$$

which is additive under a Lorentz boost. This allows a direct comparison of both p_T and y distributions between experiments with different collision energies.

For unidentified particles, the pseudorapidity η is used as a similar measure to the rapidity, where

$$\eta = \frac{1}{2}\ln\left(\frac{|\boldsymbol{p}|+p_z}{|\boldsymbol{p}|-p_z}\right) \tag{A.10}$$

$$= -\ln\left[\tan\left(\frac{\theta}{2}\right)\right]. \tag{A.11}$$

In the limit where $E \approx p$, the rapidity and pseudorapidity converge.

The number of particles produced (N) is quantified using the invariant yield:

$$N = \frac{\mathrm{d}^3N}{\mathrm{d}\Omega}, \tag{A.12}$$

where d^3N is the number of particles in a phase-space of volume $\mathrm{d}\Omega$. The boost invariant volume element in momentum-space coordinates is

$$\mathrm{d}\Omega = \frac{\mathrm{d}^3p}{E} \tag{A.13}$$

and the yield is given as

$$N = E\frac{\mathrm{d}^3N}{\mathrm{d}p^3}. \tag{A.14}$$

To make use of the variables p_T and y, we use the coordinate transformation

$$p = (p_x, p_y, p_z) \rightarrow (p_T, \phi, y), \tag{A.15}$$

where ϕ is the azimuthal angle subtended by p_T. The transformation is defined by:

$$p_x = p_T\cos\phi, \tag{A.16}$$

$$p_y = p_T\sin\phi, \tag{A.17}$$

$$p_z = m_T\sinh y. \tag{A.18}$$

The coefficients of the coordinate transformation from x_i to x'_i are obtained from the determinant of the Jacobian matrix $\mathcal{J}$, defined as

$$\mathcal{J}_{ij} = \frac{\partial x_i}{\partial x'_j}. \tag{A.19}$$

For the coordinate transformation defined above, the resulting Jacobian is

$$\begin{aligned}
\mathcal{J} &= \left| \begin{pmatrix} \cos\phi & \sin\phi & \frac{p_T \sinh y}{m_T} \\ -p_T \sin\phi & p_T \cos\phi & 0 \\ 0 & 0 & m_T \cosh y \end{pmatrix} \right| && \text{(A.20)} \\
&= p_T m_T \cos^2\phi \cosh y + p_T m_T \sin^2\phi \cosh y && \text{(A.21)} \\
&= p_T m_T \cosh y. && \text{(A.22)}
\end{aligned}$$

It follows that

$$\begin{aligned}
\frac{\mathrm{d}^3 p}{E} &= \mathcal{J} \frac{\mathrm{d}p_T d\phi dy}{E} && \text{(A.23)} \\
&= \frac{p_T m_T \cosh y}{E} \mathrm{d}p_T \mathrm{d}\phi \mathrm{d}y && \text{(A.24)} \\
&= p_T \mathrm{d}p_T \mathrm{d}\phi \mathrm{d}y, && \text{(A.25)}
\end{aligned}$$

and the invariant yield is then

$$\mathrm{N} = \frac{\mathrm{d}^3 N}{p_T \mathrm{d}p_T \mathrm{d}y \mathrm{d}\phi}, \tag{A.26}$$

The two dimensional invariant yield is obtained by integrating over the azimuthal angle from 0 to 2π, and this is determined experimentally:

$$\mathrm{N} = \frac{1}{2\pi p_T} \frac{\mathrm{d}^2 N}{\mathrm{d}p_T \mathrm{d}y} = \frac{1}{2\pi p_T} \frac{N'}{\Delta p_T \Delta y} \tag{A.27}$$

where N' is the number of particles per event, and Δy and Δp_T describe the experimental acceptance.

To constrain nuclear modifications to J/ψ production in heavy ion collisions, the invariant yield is compared to the J/ψ cross section in p+p collisions at the same energy. The nuclear modification factor R_{AB} in $A+B$ collisions is defined by

$$R_{AB} = \frac{1}{T_{AB}} \frac{\mathrm{d}^2 N_{AB}/\mathrm{d}p_T \mathrm{d}y}{\mathrm{d}^2 \sigma_{\mathrm{inel}}^{\mathrm{pp}}/\mathrm{d}p_T \mathrm{d}y}, \tag{A.28}$$

where $T_{AB} = \langle N_{\mathrm{coll}} \rangle / \sigma_{\mathrm{inel}}^{\mathrm{pp}}$ is the nuclear overlap function which takes into account the inelastic cross section in p+p collisions ($\sigma_{\mathrm{inel}}^{\mathrm{pp}}$) and the number of binary nucleon collisions in $A+B$ ($\langle N_{\mathrm{coll}} \rangle$). The production of particles originating from the initial hard scattering of the collision are expected to scale with the number of nucleon-nucleon collisions, resulting in $R_{AB} = 1$ is there is no nuclear modification.

Appendix B

$\mathrm{d}E/\mathrm{d}x$ $n\sigma_e$ Fitting

B.1 $\mathrm{d}E/\mathrm{d}x$ $n\sigma_e$ Fitting in d+Au

Multiple Gaussians have been fitted to the $\mathrm{d}E/\mathrm{d}x$ distribution as a function of momentum to determine the relative particle contributions of electrons and various hadrons. The $\mathrm{d}E/\mathrm{d}x$ was normalized to the expected electron $\mathrm{d}E/\mathrm{d}x$ obtained from the Bichsel functions to obtain the probability of whether a particle is an electron ($n\sigma_e$).

The electron $\mathrm{d}E/\mathrm{d}x$ overlaps the kaon, proton, and deuteron $\mathrm{d}E/\mathrm{d}x$ at ~ 0.6, ~ 1, and ~ 1.6 GeV/c, respectively, which causes some uncertainty in the fitting procedure. As a result, careful consideration has been taken in performing the Gaussian fitting to each particle contribution by constraining the fit parameters in the regions where the $\mathrm{d}E/\mathrm{d}x$ overlaps. Electrons identified in d+Au were required to have $p > 1.2$ GeV/c to remove the significant hadron contamination below this. The $n\sigma_e$ fitting in d+Au was performed for $p > 1$ GeV/c, and in this range the kaons cannot be distinguished from the other hadrons and were excluded from the fit. A complete description of the fitting procedure in d+Au is given below.

The fitting is done in an iterative way starting with fitting to the proton and pion contributions only as these are the most abundant particles. The electron and

deuteron contributions were excluded by fitting in the range $-15 < n\sigma_e < -1$. The fitting was performed without any constraints, and the fit quality is good outside of $1.4 < p < 1.8$ GeV/c, where the proton and pion dE/dx overlap.

To improve the fitting, loose requirements were placed on the fit parameters. The proton height was required to be less than that of the pions, and the proton and pion widths were constrained to be between 0.8 and 1.2. Polynomials were fitted to the Gaussian fit values for the mean of the protons and pions versus momentum. The polynomials were then used to obtain initial values for the next set of fitting and provide fit constraints in $1.4 < p < 2.2$ GeV/c and $p > 3.4$ GeV/c where the fitting was poor. The fitting was repeated with these constraints, and the resulting fit parameters were used to describe the protons and pions in subsequent fits.

The proton and pion Gaussians were then fixed to their previous fit values, with the parameter limits set to 5 times the uncertainty on the fit values. Electrons were then included in the fitting process, and the fitting was performed with no constraints on the electron fit parameters. The $n\sigma_e$ mean and width of the Gaussian fit to the electrons were found to be mostly constant with momentum and were fitted to obtain a value of $\mu \sim -0.3$, and $\sigma \sim 0.9$, respectively.

With the electron, proton, and pion contributions determined, the deuterons were included in the fit for $p < 2$ GeV/c. The deuteron statistics are limited, and several constraints were required for the fitting to distinguish the deuteron and electron contributions. The deuteron mean was forced to be distinct from the electron mean, and the width to be between 0.7 and 1.3. These limits were motivated by looking at the fits without any constraints. The $n\sigma_e$ distributions for each momentum bin is shown in Fig. B.1 and Fig. B.2, and the Gaussian fits describe the various particle contributions well. The Gaussian fit parameters, which are summarized in Fig. 4.18, have been used to determine the dE/dx electron identification efficiency and purity, and this is described in Chapter 4.

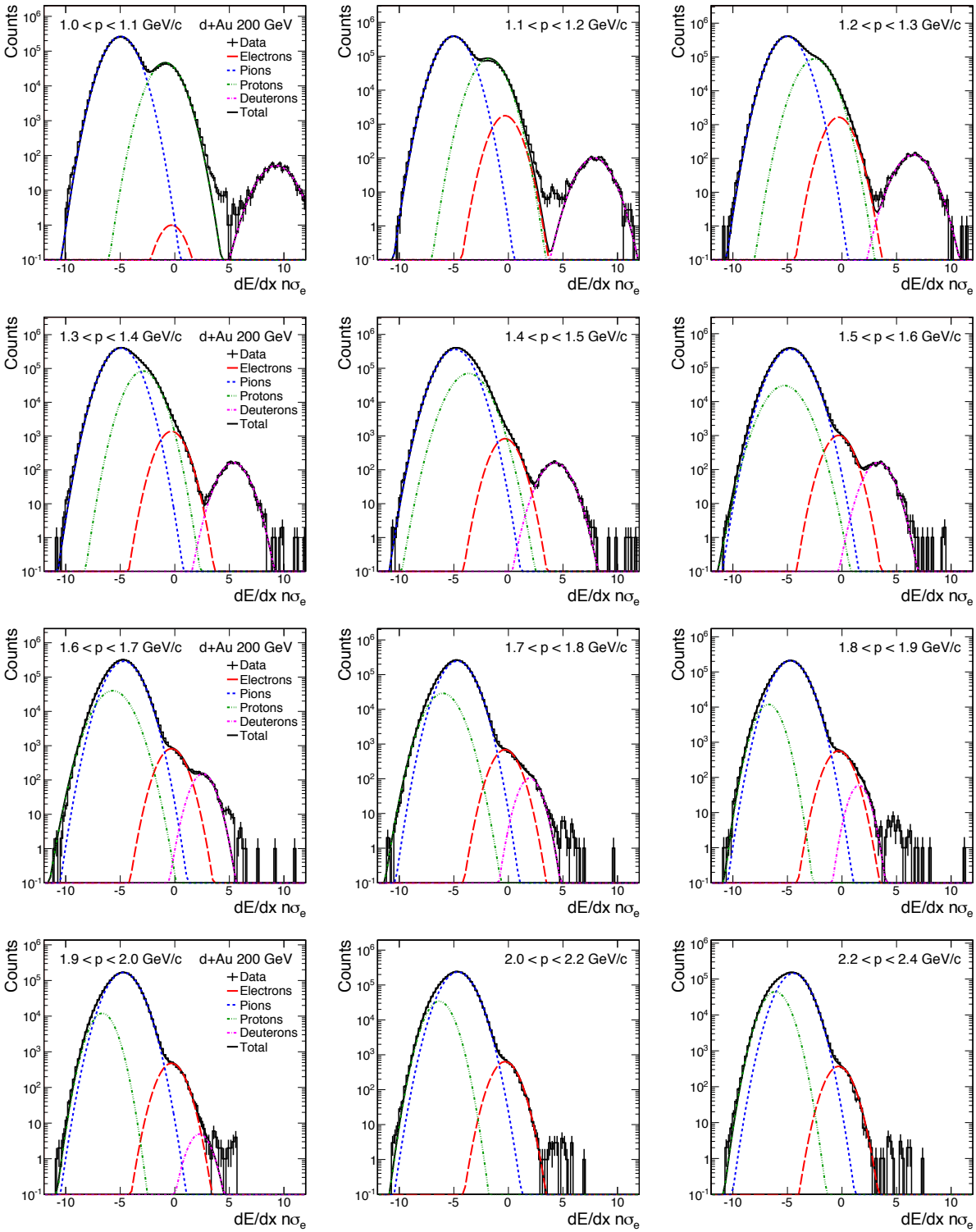

Figure B.1: The $n\sigma_e$ distribution in d+Au collisions. Multiple Gaussians have been fitted to the different particle contributions.

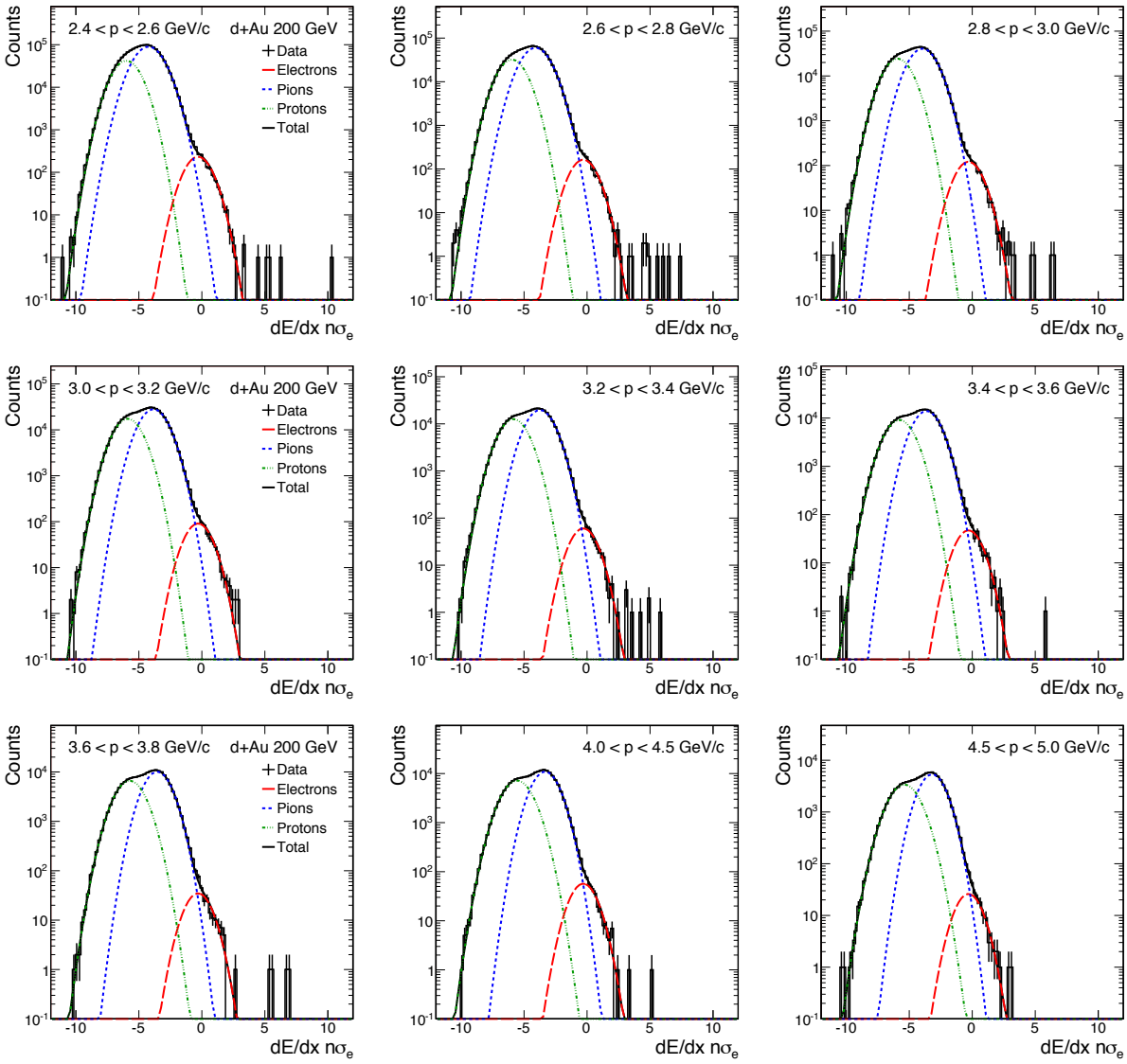

Figure B.2: The $n\sigma_e$ distribution in d+Au collisions. Multiple Gaussians have been fitted to the different particle contributions.

B.2 $\mathrm{d}E/\mathrm{d}x$ $n\sigma_e$ Fitting in Au+Au

A similar approach to fitting the $n\sigma_e$ distribution in d+Au described in Appendix B.1 has been used for the $n\sigma_e$ distribution in Au+Au collisions. To remove contributions from heavier particles such as protons, kaons, and deuterons, the TOF has been used to select electrons by requiring $|1/\beta - 1| < 0.03$ in Au+Au, which was not available in the d+Au data. Furthermore, the pair-wise mass of tracks was required to be less than 10 MeV/c^2 to enhance the electron purity by select on electrons from photonic conversions. As a result, there was less uncertainty in the Gaussian fitting to the $n\sigma_e$ distribution in Au+Au as compared to Au+Au, as most of the hadron contamination has been removed from the regions where the $\mathrm{d}E/\mathrm{d}x$ of electrons and hadrons overlaps. However, due to the large range of multiplicities in Au+Au collisions, the centrality dependence of the $n\sigma_e$ distribution has been taken into account, which was not necessary for d+Au collisions. Loose constraints have been applied to the fit parameters to improve the fitting, and these are described below.

For momentum $p < 1.8$ GeV/c, only electrons and pions are taken into account in the fitting, and are fitted in the range $-10 < n\sigma_e < 2$ to exclude merged tracks with large $\mathrm{d}E/\mathrm{d}x$. The TOF $1/\beta$ and photonic electron requirements remove the majority of the kaons, deuterons, and protons at low momentum. An additional Gaussian can be included in the fit to take into account merged pions which have a value of $n\sigma_e \sim 5$. However, there is a non-Gaussian contribution to this $n\sigma_e$ region which cannot easily be accounted for. Thus it is more appropriate to only fit the Gaussians for $n\sigma_e < 2$ and exclude the merged pions. Above this momentum range, protons are also included in the fitting. The Bichsel functions have been used to determine the predicted mean value of the hadrons along the $n\sigma_e$ axis, and the uncertainty from the number of $\mathrm{d}E/\mathrm{d}x$ hit points from data has been used to estimate the fit range of the mean $n\sigma_e$ value for the hadrons. For each centrality, the fitting is performed without any fit parameters, and the fitting describes the data well for most momentum ranges. For $1 < p < 1.8$ GeV/c, there is some residual hadron contamination under the electron distribution, and centrality-dependent constraints are placed on

the fitting of the electron mean and width. These are obtained by extrapolating from outside of this momentum range and estimating the expected mean and width. A similar approach is taken for the protons and pions to ensure the fitting does not confuse these contributions when their $\mathrm{d}E/\mathrm{d}x$ overlaps.

The $n\sigma_e$ distributions are shown in various momentum slices in Fig. B.3 and Fig. B.4 for $0-60\%$ central Au+Au collisions. Gaussian functions have been fitted to the various particle contributions, indicated by the lines, and the fit range of the Gaussian mean for each particle is indicated by the shaded bands.

The Gaussian fit parameters are summarized in Fig. B.5 and Fig. B.6 for each centrality bin, and are shown in Chapter 4 in Fig. 4.19 for $0-60\%$ central collisions. The efficiency of requiring $-1 < n\sigma_e < 2$ has been calculated from the mean and width of the Gaussian fits to the electron contribution is also shown, and ranges from $75-88\%$. The purity of the electron candidates with $|1/\beta - 1| < 0.03$ and $m_{\mathrm{ee}} < 10$ MeV/c^2 is also shown. This is $\sim 98\%$ for $p < 1.5$ GeV/c, and decreases above 1.5 GeV/c due to the rise of the pion $\mathrm{d}E/\mathrm{d}x$.

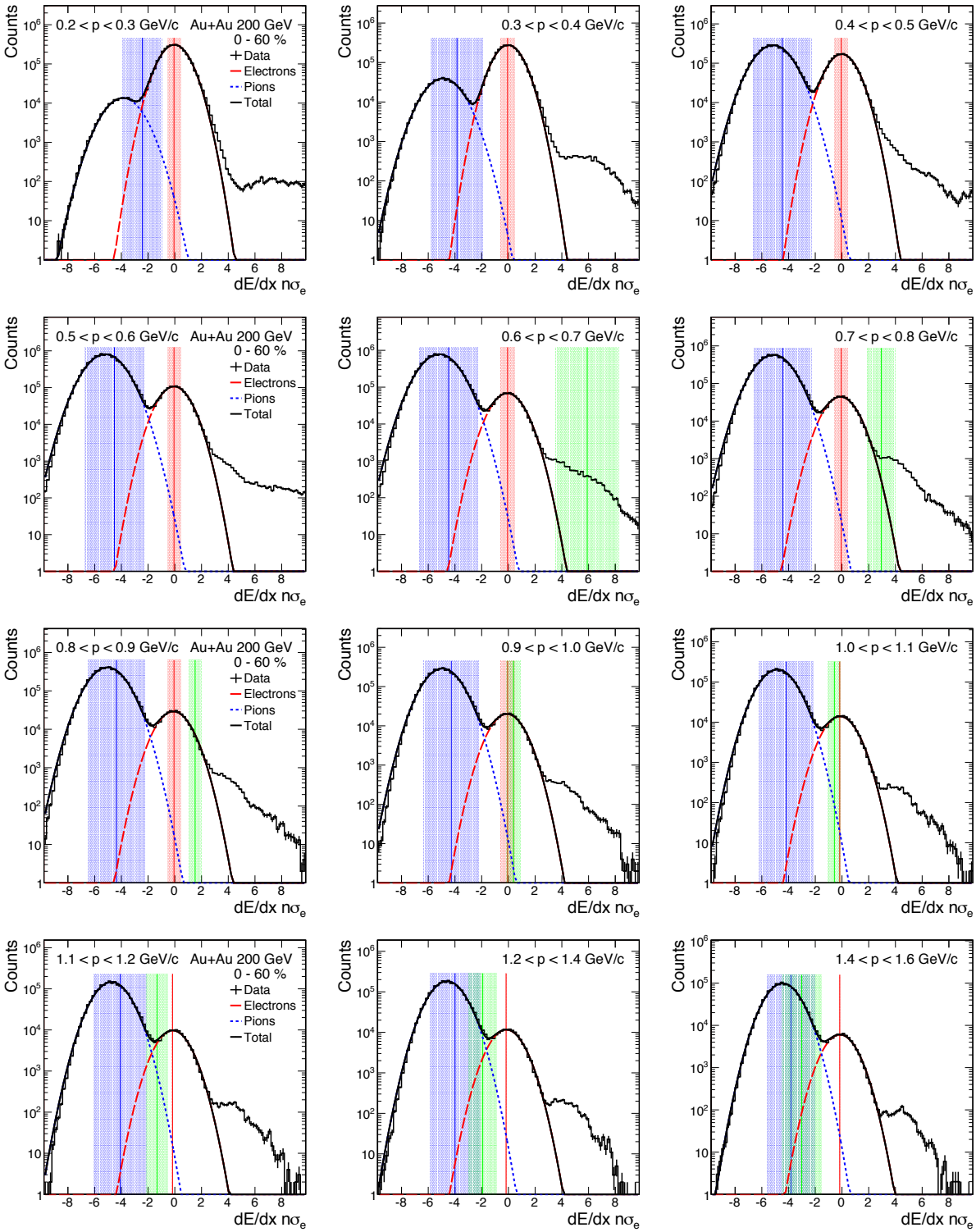

Figure B.3: The $n\sigma_e$ distribution in $0-60\%$ central Au+Au collisions. Multiple Gaussians have been fitted to the different particle contributions.

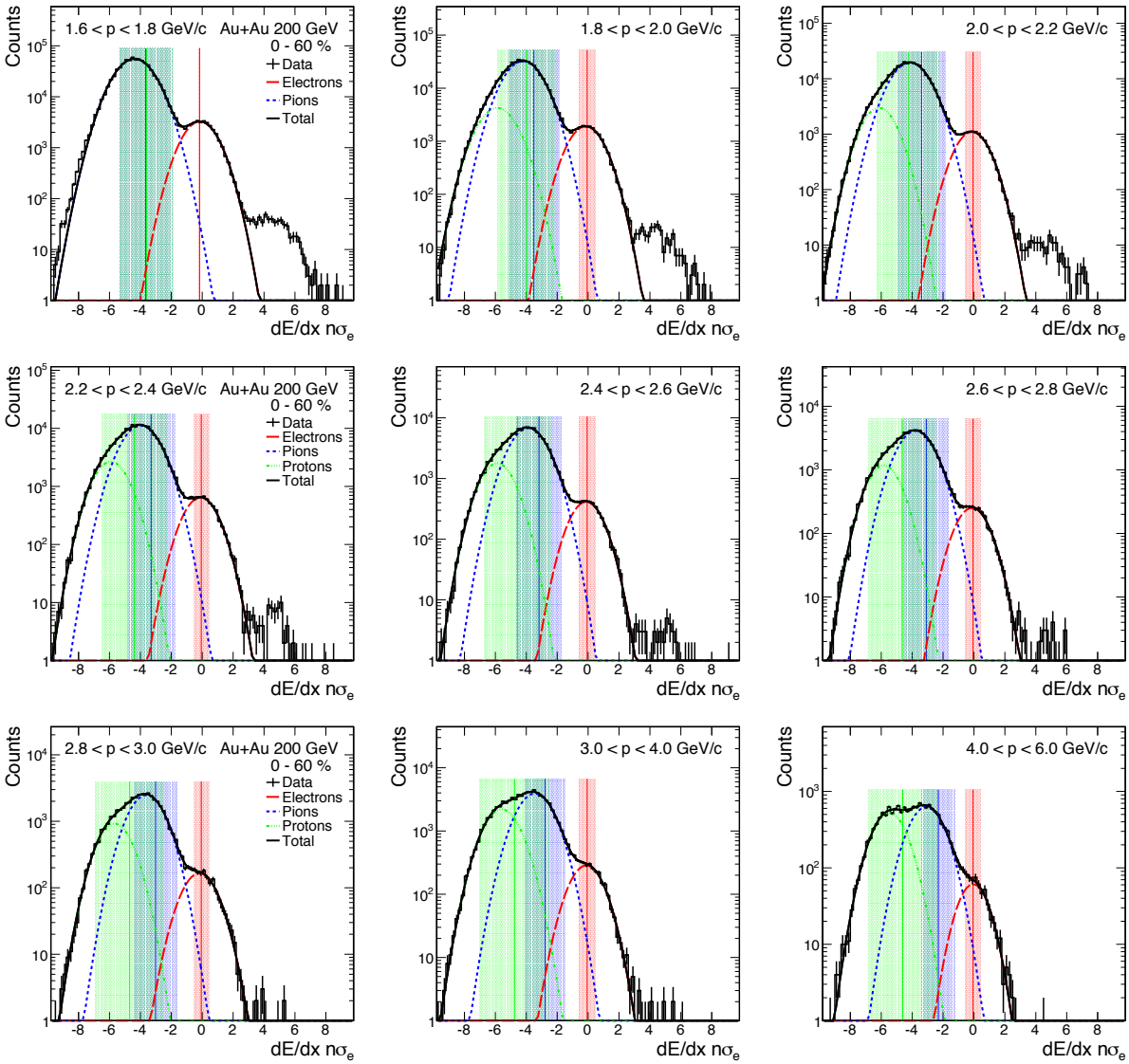

Figure B.4: The $n\sigma_e$ distribution in $0-60\%$ central Au+Au collisions. Multiple Gaussians have been fitted to the different particle contributions.

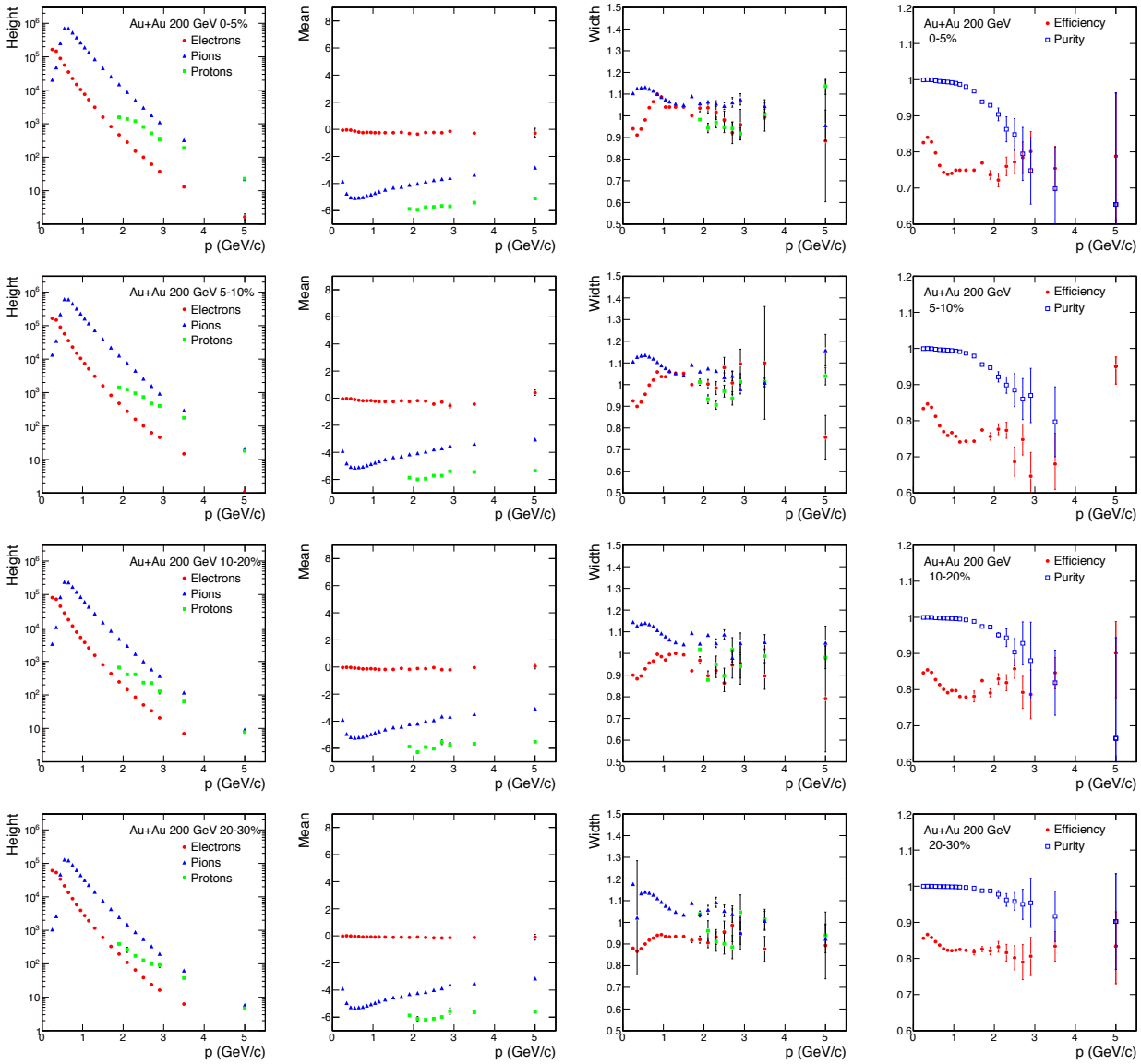

Figure B.5: From left to right: The height, mean, width, and efficiency (circles) and purity (squares) for $-1 < n\sigma_e < 2$, obtained from the Gaussian functions fitted to the electrons (circles), pions (triangles), and protons (squares) in Au+Au collisions in $0-5\%$ centrality (top) to $20-30\%$ centrality (bottom).

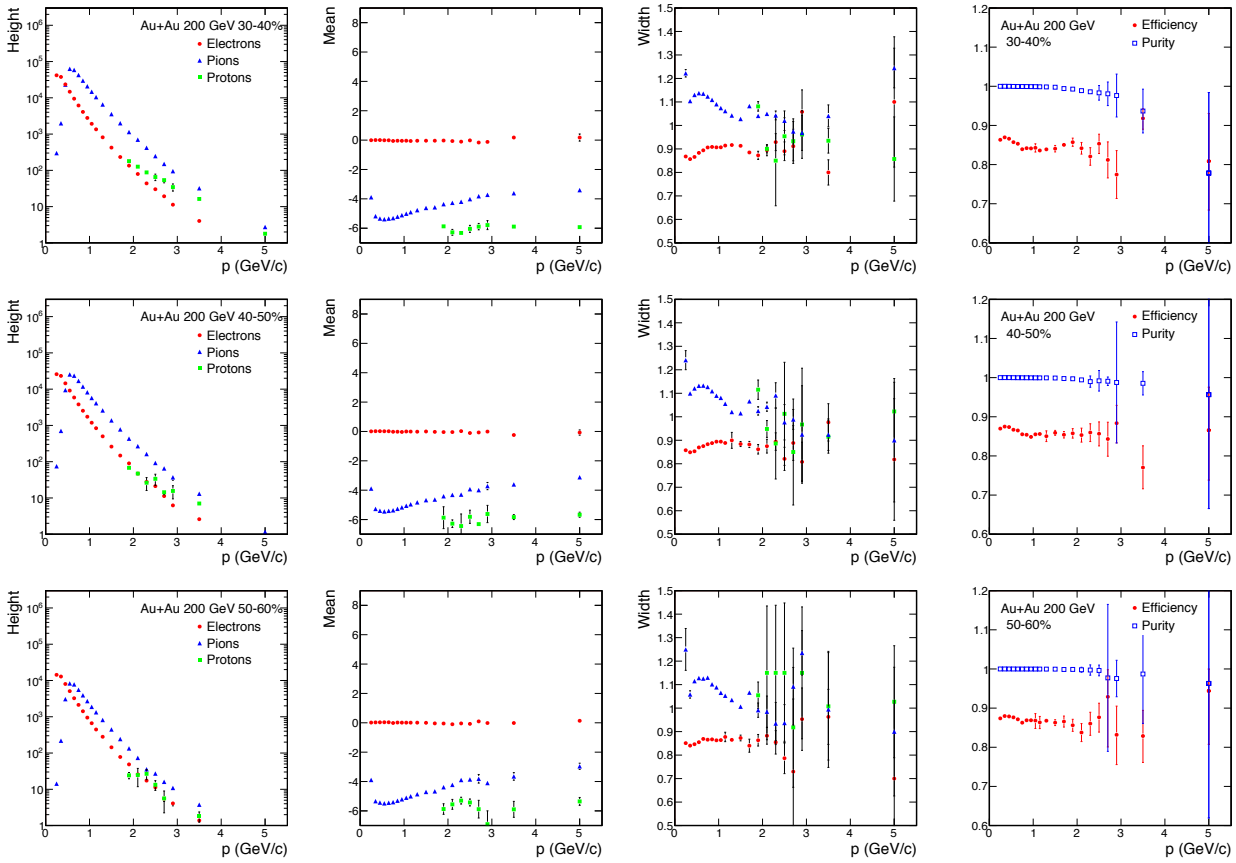

Figure B.6: From left to right: The height, mean, width, and efficiency (circles) and purity (squares) for $-1 < n\sigma_e < 2$, obtained from the Gaussian functions fitted to the electrons (circles), pions (triangles), and protons (squares), in Au+Au collisions in $30-40\%$ centrality (top) to $50-60\%$ centrality (bottom).

Appendix C

Efficiency Plots

C.1 TOF Plots in Au+Au

The TOF mtching efficiency and $1/\beta$ cut efficiency have been determined from data. Since a high purity electron sample cannot be obtained without the TOF for low p_T, the matching efficiency from hadrons has been calculated. The ratio of the matching efficiency between electrons and hadrons for $p > 1.2$ GeV/c has been used to scale the hadron matching efficiency, which has been used to correct the data. A comparison of the electron and hadron matching efficiency are shown in Fig. C.1 and Fig. C.2. The $1/\beta$ cut efficiency has been calculated using a pure sample of electrons, and this is shown in Fig. C.3.

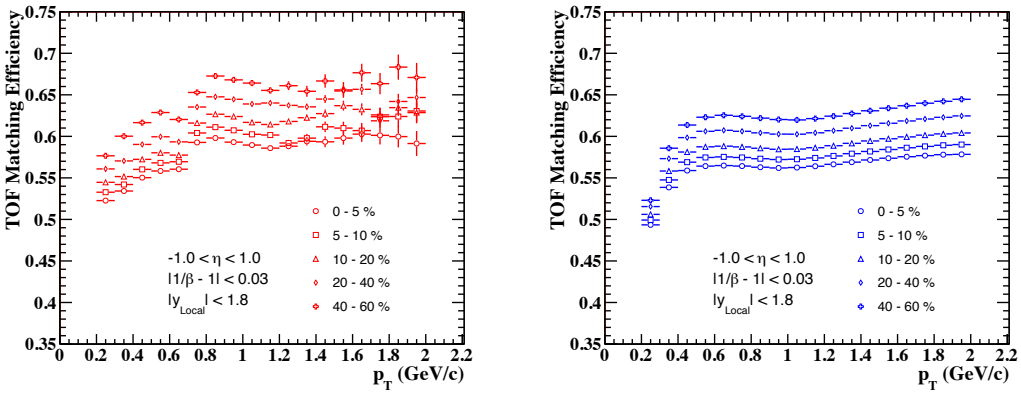

Figure C.1: The TOF matching efficiency for electrons (left) and hadrons (right) versus p_T in $|\eta| < 1$ for various centrality bins in Au+Au collisions.

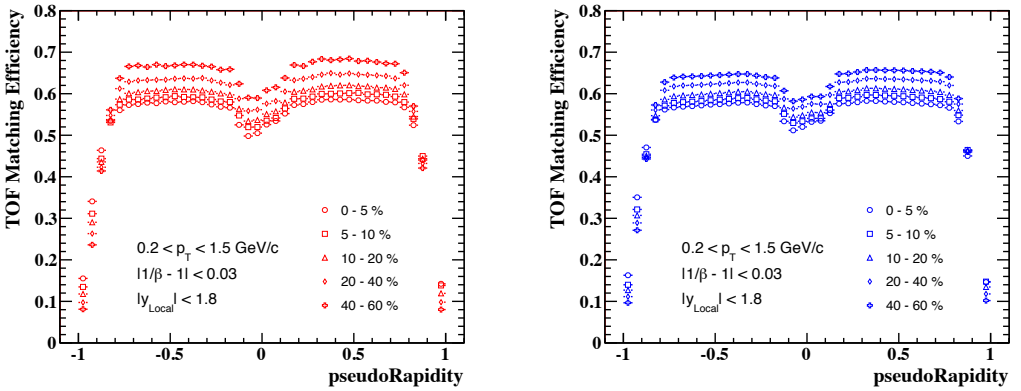

Figure C.2: The TOF matching efficiency for electrons (left) and hadrons (right) versus η in $0.2 < p < 1.5$ GeV/c for various centrality bins in Au+Au collisions.

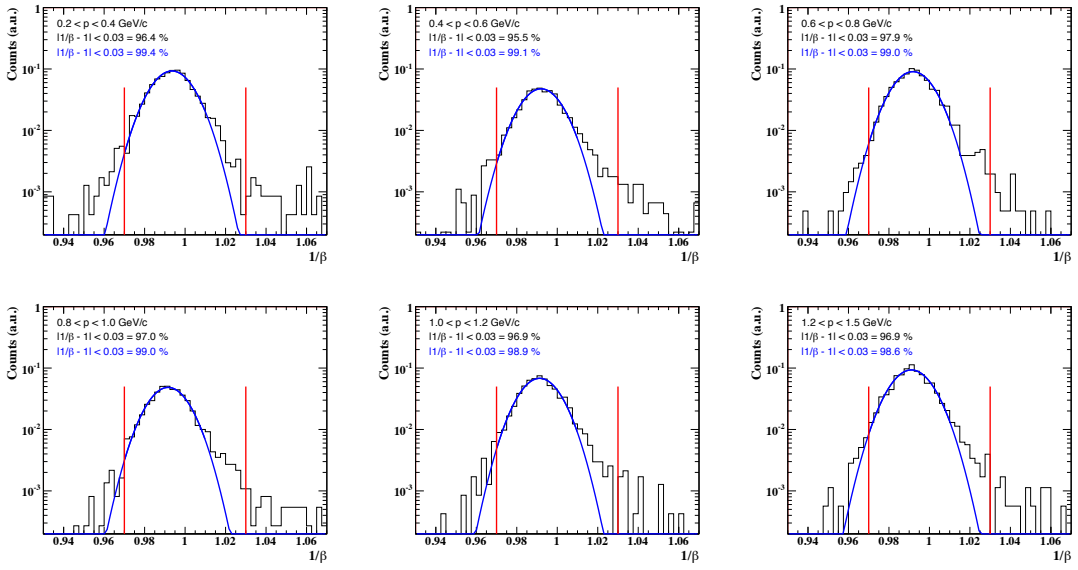

Figure C.3: The TOF $1/\beta$ distribution for electrons in various momentum bins (black histogram) in Au+Au collisions. The data are fitted with a Gaussian distribution (blue line).

C.2 BEMC Plots in Au+Au

The methods of matching electrons to the BEMC is described in Chapter 4. A pure sample of electrons is obtained by requiring $0 < n\sigma_e < 2$ and placing a pair-wise invariant mass cut $m_{\rm ee} < 10$ MeV/c^2 to select on photonic electrons. The TOF was not used to improve the electron identification as this creates a bias in the BEMC matching efficiency. The electron tracks are projected to the BEMC and matched to a maximum-energy tower within a cluster. The position of the cluster is determined from the BSMD η and ϕ strips. The same procedure is followed in simulation using Monte Carlo electrons embedded into real data events.

The distance between electrons and energy clusters in the BEMC for Au+Au collisions is shown for various momentum bins in Fig. C.4. The distribution from data (circles) is slightly wider than the simulation (triangles) when using the BSMD, and the agreement improves at higher momentum. Electrons with $R < 0.035$ are accepted, and their energy-to-momentum ratio is shown in Fig. C.5 for various momentum bins. A similar trend is observed, with the data (circles) exhibiting a slightly wider distribution than simulation (triangles). The agreement improvers at higher momentum.

The efficiency of matching an electron to the BEMC with $R < 0.035$ has been obtained from simulation, and the transverse momentum, centrality, and pseudorapidity dependence are shown in Fig. C.6.

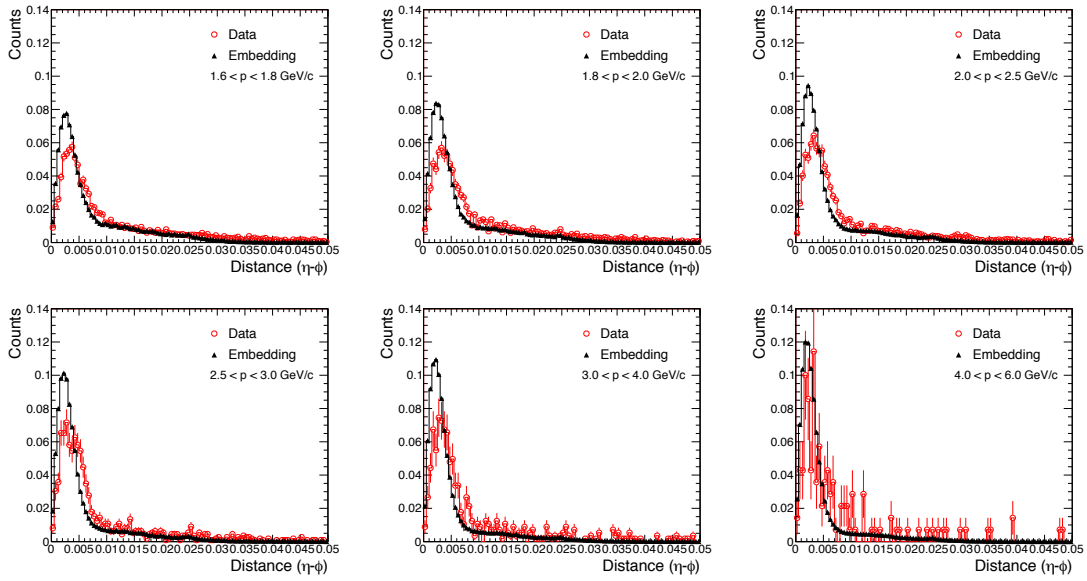

Figure C.4: The distance between electrons and clusters in the BEMC. The BEMC cluster position is determined using the BSMD.

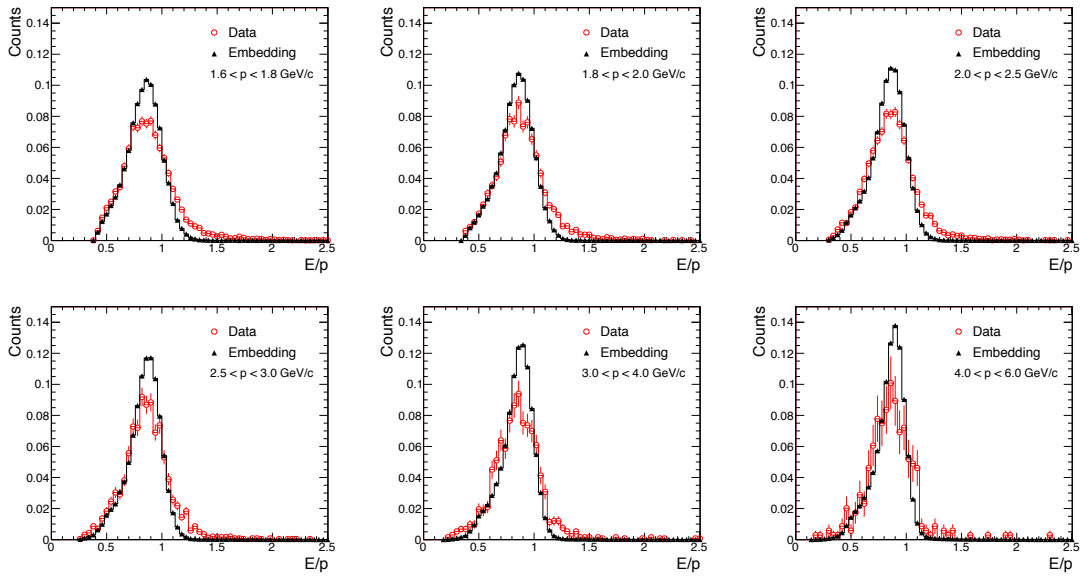

Figure C.5: The electron energy-to-momentum ratio E/p for $R < 0.035$. The BEMC cluster position is determined using the BSMD.

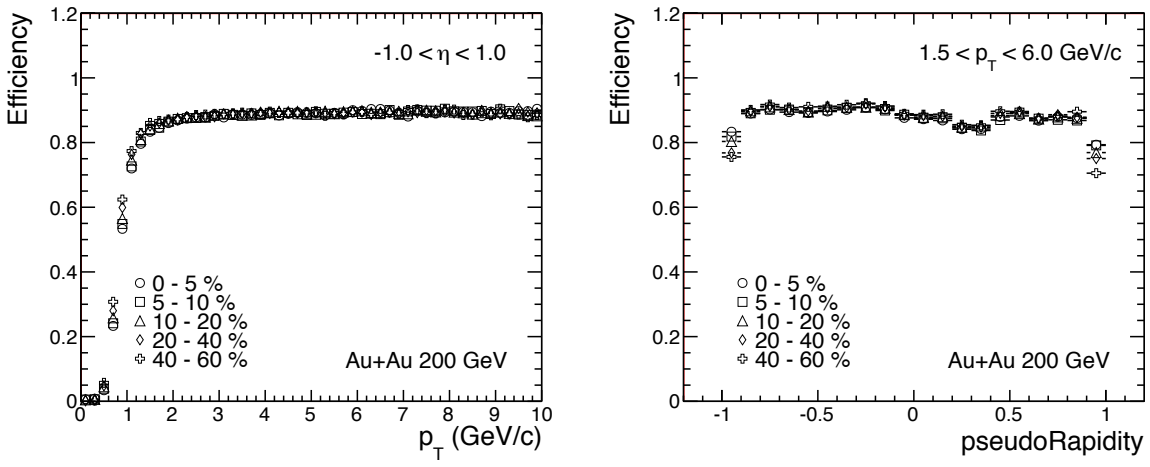

Figure C.6: The centrality dependence of the BEMC matching efficiency obtained from simulation versus p_T (left) and η (right) in Au+Au collisions. The efficiency is obtained using the BTOW+BSMD with $R < 0.035$.

Appendix D

Embedding Plots

The J/ψ tracking efficiency and acceptance, including track quality requirements on $nHitsFit$, DCA, etc., are determined from simulations. Monte Carlo J/ψs are embedded into real data events and decayed. Their daughter electrons are propagated through the detector and the detector responses are obtained. The track reconstruction is performed and the reconstructed tracks associated to the Monte Carlo electrons are subjected to the same requirements as the real data to determine the corresponding efficiencies.

D.1 Embedding Plots in d+Au

The vertex position and event multiplicity are shown in Fig. D.1 (left and right panel, respectively) for real data (circles) and simulation (triangles) in d+Au collisions. The $nHitsFit$ and DCA distributions of electrons from data and simulation are shown in Fig. D.2 and Fig. D.3, respectively, for various momentum bins in d+Au collisions. The distributions from data and simulation agree reasonably well, and the differences are included in the systematic uncertainties.

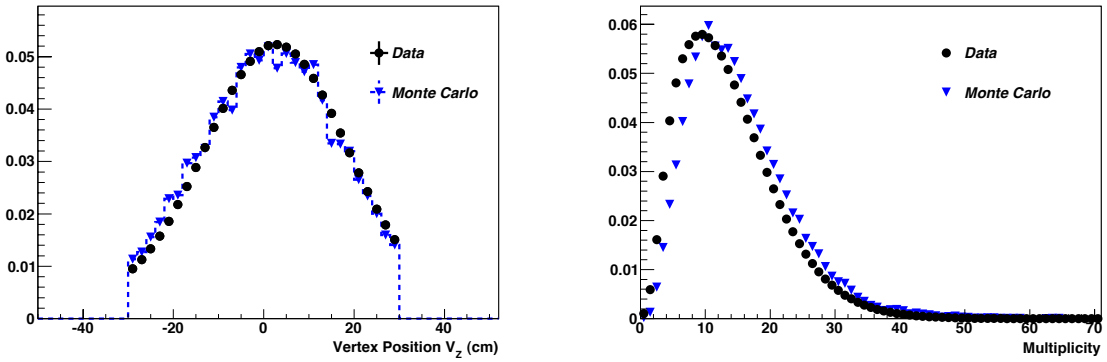

Figure D.1: The event vertex position (left) and charged particle multiplicity (right) in $|V_Z| < 30$ cm for data (circles) and embedding (triangles).

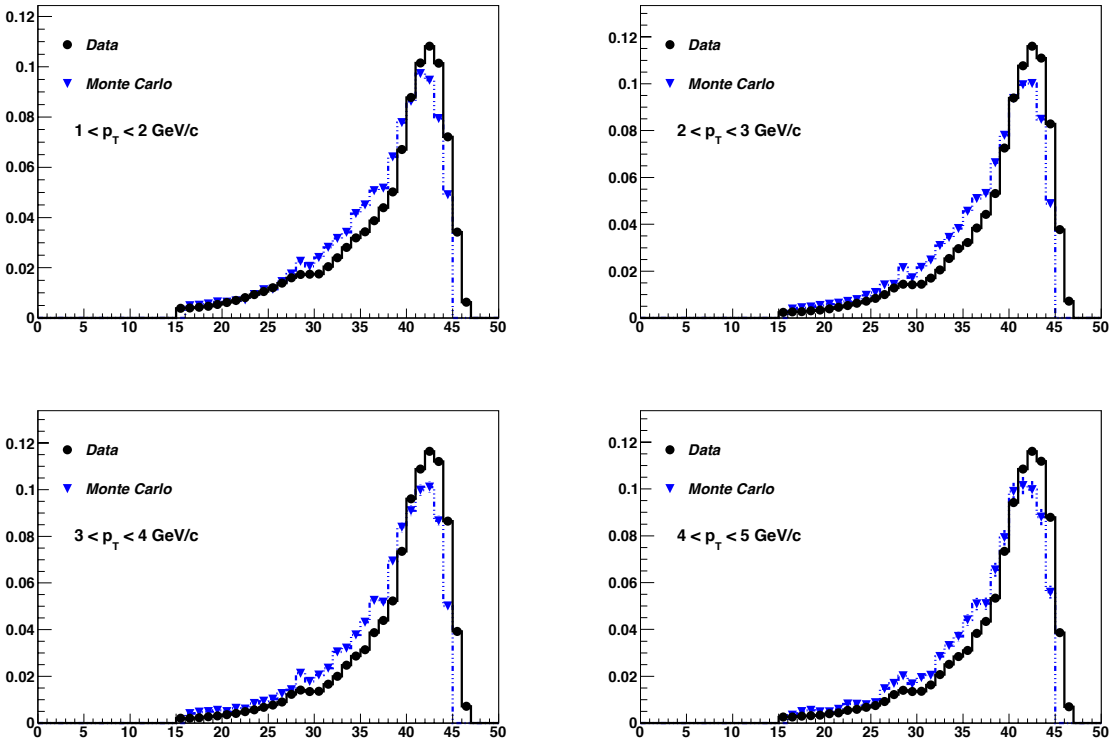

Figure D.2: The electron $nHitsFit$ distribution from data (circles) and simulation (triangles), for various momentum bins in d+Au collisions.

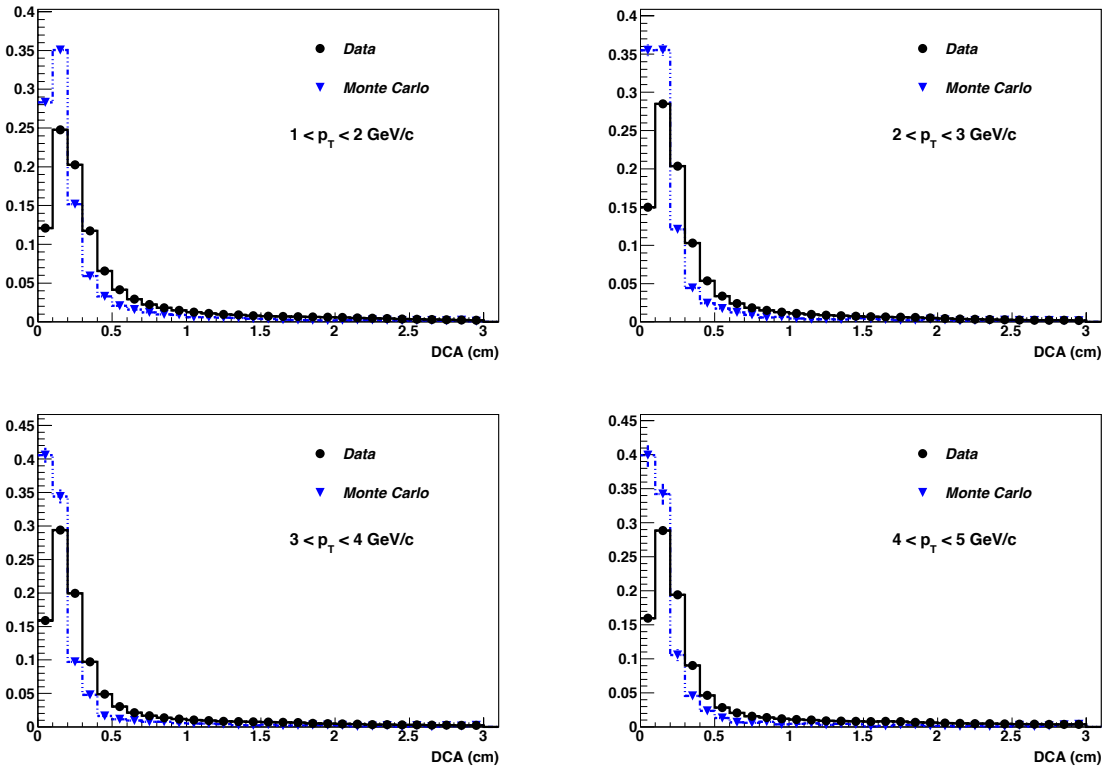

Figure D.3: The electron DCA distribution from data (circles) and simulation (triangles), for various momentum bins in d+Au collisions.

D.2 Embedding Plots in Au+Au

The input p_T and rapidity spectrum for the J/ψ are simulated by sampling a flat distribution. These are then weighted with distributions obtained from PYTHIA. The weighted input spectra are shown in Fig. D.4. To ensure the simulation is correctly calculating the tracking efficiency and acceptance, the distributions are compared to a pure electron sample from data. The $nHitsFit$, DCA, and ϕ distributions of electrons from data and simulation are shown in Fig. D.5, Fig. D.6, and Fig. D.7, respectively, for various momentum bins in $0-60\%$ central collisions. In general, the agreement is good. There is a slight offset in the $nHitsFit$ distribution at low-p_T, and this has a small impact on the efficiency ($\sim 2-4\%$). The ϕ distributions are shown for various momentum bins, and are only for negatively charged electrons from Au+Au collisions recorded in a reversed full-field magnetic field. This is done to emphasize the sector boundaries, as the curvature changes direction with a change of sign or magnetic field. The distributions agree well, and the dip corresponding to the masked sector 20 in the TPC can be seen.

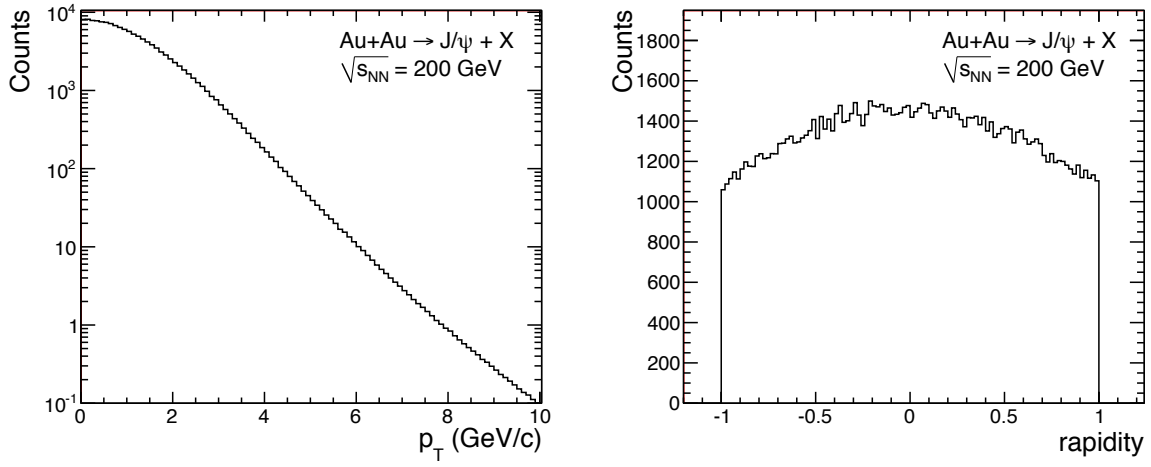

Figure D.4: The weighted input transverse momentum (left) and rapidity distribution (right) from embedding Monte Carlo J/ψ into real data events in Au+Au collisions.

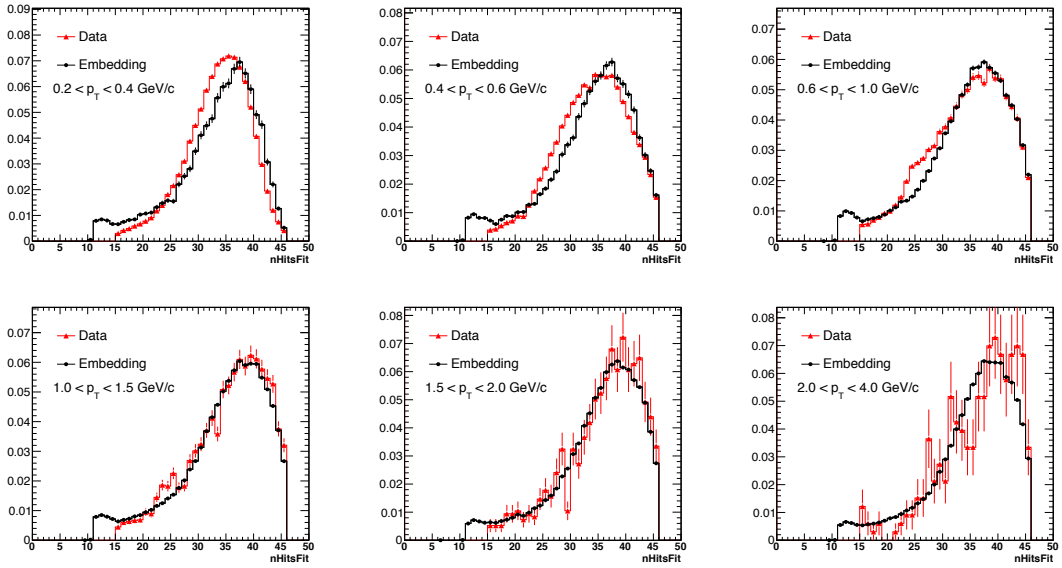

Figure D.5: The electron $nHitsFit$ distribution from data (triangles) and simulation (circles).

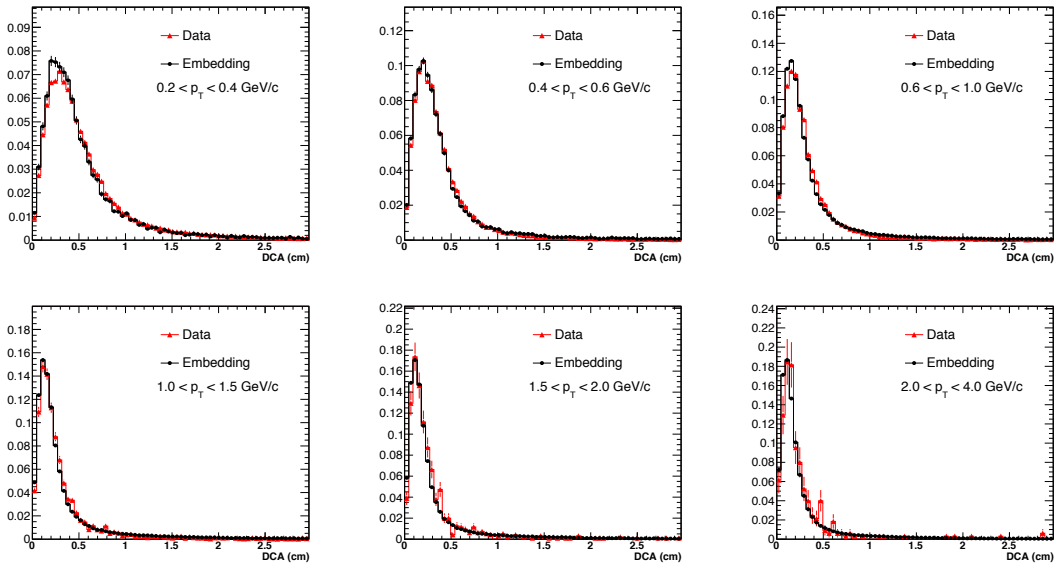

Figure D.6: The electron DCA distribution from data (triangles) and simulation (circles).

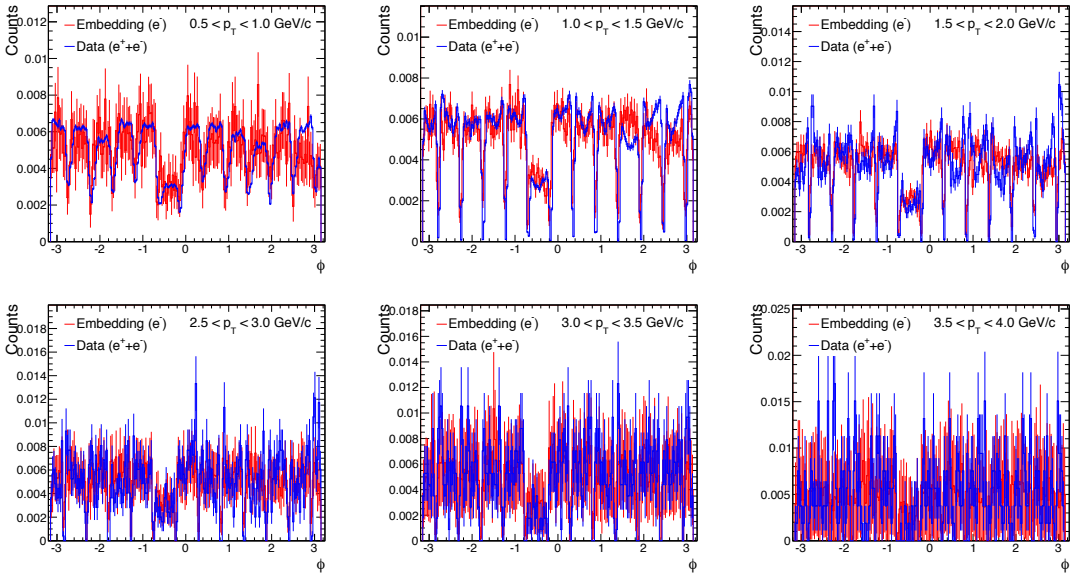

Figure D.7: The electron ϕ distribution from data (blue) and simulation (red).

Appendix E

Momentum Resolution

The J/ψ signal shape was determined from simulation by embedding Monte Carlo J/ψs into real data, and results from the momentum resolution of the TPC and the radiative energy loss of electrons (Bremsstrahlung) interacting with the material in the detector. The J/ψ signal shape from simulation has been fitted to the dielectron mass spectrum after background subtraction to determine the J/ψ yield, and this is shown in Fig. E.1 for $0-60\%$ central Au+Au collisions. The signal shape from simulation has been combined with a straight line (dot-dashed line) to account for residual background contributions from $c\bar{c}$ and Drell-Yan, and the total (solid line) is fitted to the data. The χ^2 of the fit in $2.9 < m < 3.2$ GeV/c^2 is 33/14, and the data suggests a slightly broader lineshape. The signal shape from simulation depends on the amount of material in the detector and the momentum resolution. To improve the agreement between the J/ψ signal shape in data and simulation, a data-driven correction was performed by smearing the momentum resolution in simulation.

The transverse momentum resolution in Au+Au was obtained from simulation by comparing the transverse momentum of simulated electrons and their associated reconstructed track in the detector. The momentum resolution is defined as $\Delta p_T = ({p_T}^{\rm MC} - {p_T}^{\rm Rec})/{p_T}^{\rm MC}$, where ${p_T}^{\rm MC}$ and ${p_T}^{\rm Rec}$ are the Monte Carlo and reconstructed transverse momentum, respectively. The transverse momentum resolution for electrons in Au+Au collisions is shown in Fig. E.2 versus p_T (left panel), and

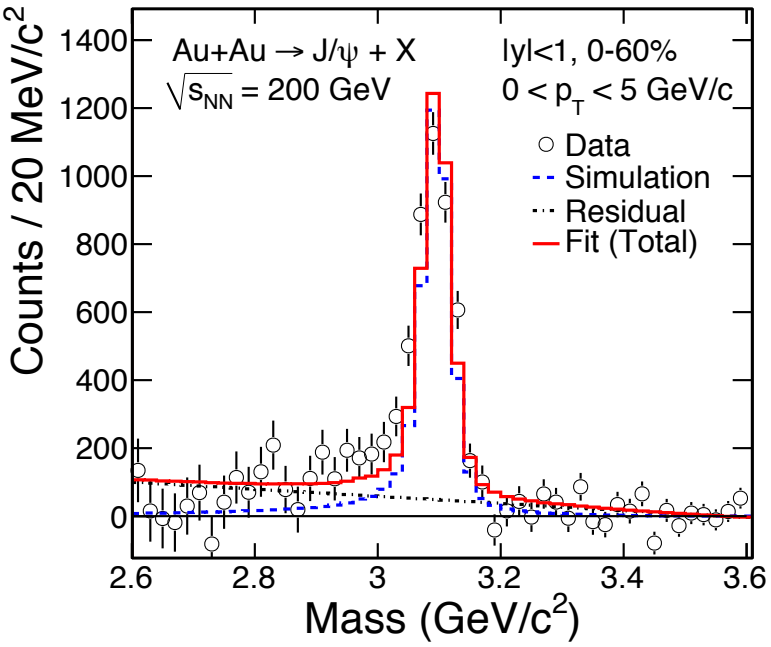

Figure E.1: The J/ψ signal (open circles) for $|y| < 1$ and $p_T < 5$ GeV/c in $0-60\%$ central Au+Au minimum bias collisions after mixed-event background subtraction.

integrated for $p_T < 10$ GeV/c (right panel). The asymmetry of the resolution is due to Bremsstrahlung of electrons in the detector material. Since the detector measures curvature and because $\Delta(1/p_T)$ is Gaussian, the distribution of Δp_T exhibits non-Gaussian tails for $|\Delta p_T| > 0.1$.

The momentum resolution was fitted with a Gaussian distribution as a function of p_T to determine the magnitude of the resolution. The Gaussian was fitted in the range $-0.1 < \Delta p_T < 0.1$ to remove the non-Gaussian tails in Δp_T. The width of the Gaussian fit is shown as a function of p_T in Fig. E.3. At higher momentum, the resolution increases linearly and is dominated by the TPC resolution $\sim 1/p_T$. For $p < 1$ GeV/c, the resolution is dominated by multi-Coulomb scattering, which increases towards low-p_T. The resolution is fitted with a straight line for $p_T > 1.5$ GeV/c to obtain a resolution of $\Delta p_T \approx 0.6\% + 0.2\% \times p_T$.

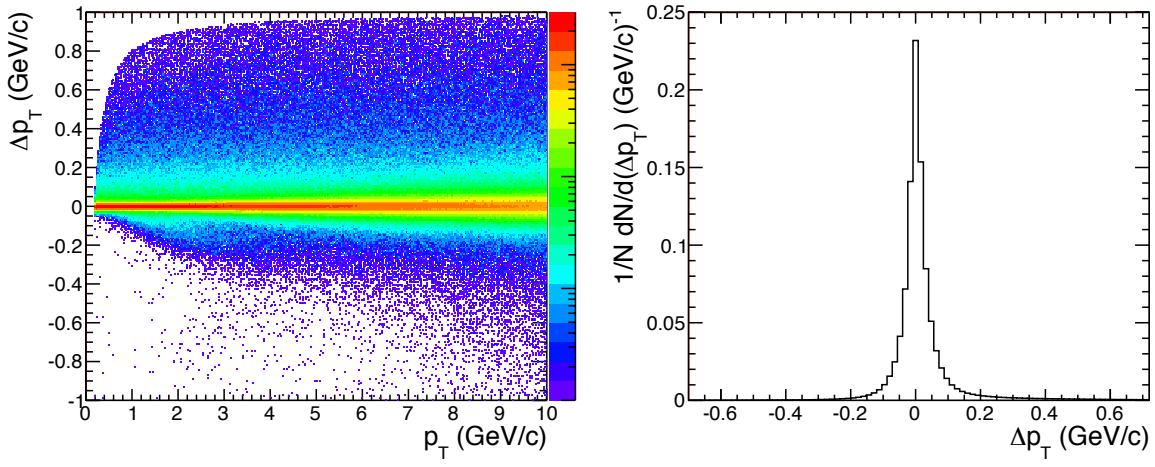

Figure E.2: The transverse momentum resolution for electrons in Au+Au collisions versus p_T (left panel), and for $p_T < 10$ GeV/c (right panel).

A data-driven correction has been performed to improve the agreement between the signal shape from data and simulation in Au+Au collisions. This is done by including an additional Gaussian smearing of the form $\sigma \cdot p_T$ to the electron p_T resolution and reconstructing the resulting J/ψ mass spectrum. The resulting signal shape was fitted to the minimum bias Au+Au data in $0-60\%$ centrality as a function of the smearing coefficient σ, and a χ^2 minimization has been performed to determine the most probable smearing coefficient. The χ^2 distribution is shown in Fig. E.4, and a value for the smearing coefficient of $\sigma = 0.61\% \pm 0.1\%$ has been obtained from the χ^2 minimization. This method has not been applied to the d+Au data, as the agreement between the simulation and data is consistent within errors and the statistical fluctuations in the data result in a large uncertainty on the smearing coefficient.

The transverse momentum resolution of electrons from simulation has been smeared according to a Gaussian with a width of $0.61\% \times p_T$, and the resulting J/ψ signal shape in Au+Au has been fitted to the J/ψ signal from data to determine the J/ψ yield. This is shown in Fig. E.5 for the minimum bias $0-60\%$ central collisions. The

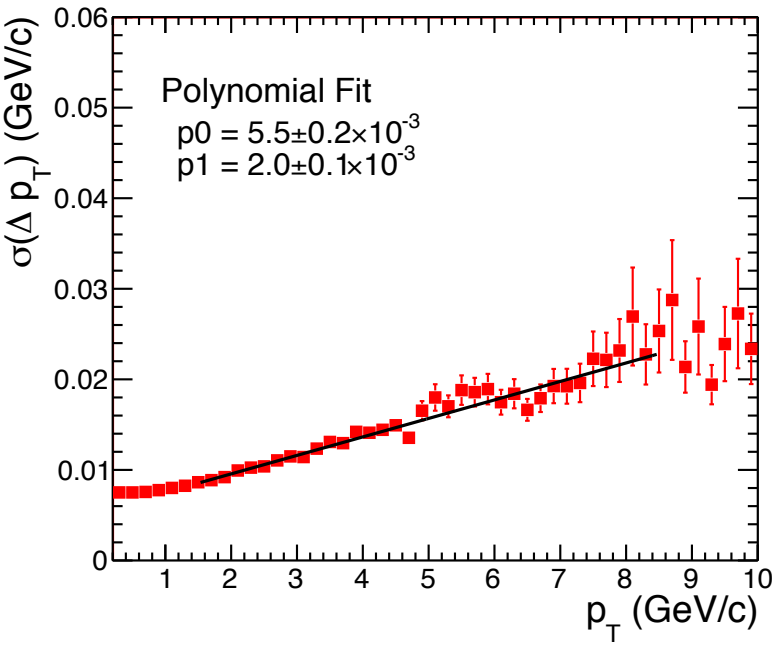

Figure E.3: The width of the transverse momentum resolution from simulation for electrons in Au+Au collisions. A straight line is fitted to the distribution for $p_T > 1.5$ GeV/c.

χ^2 of the fit to the J/ψ signal shape in Au+Au collisions has improved from 33/14 to 6/14 after applying the additional smearing to the momentum resolution.

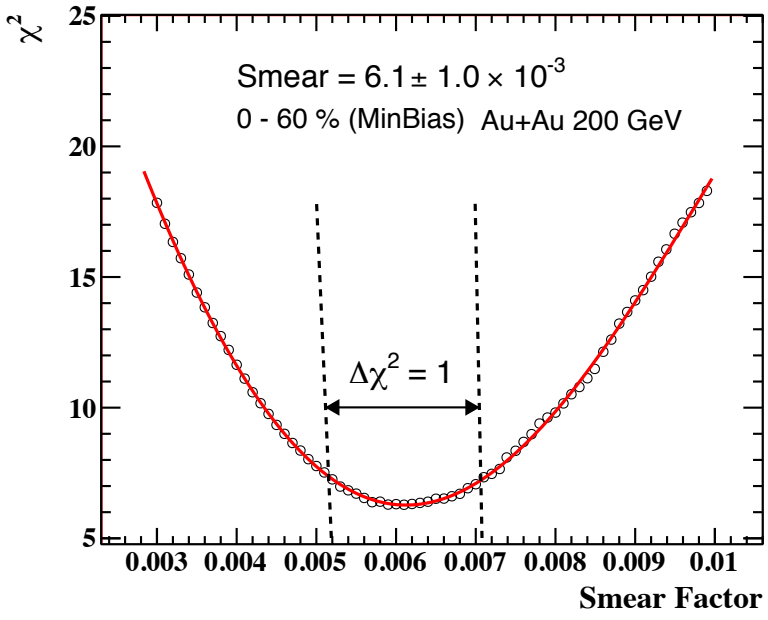

Figure E.4: The χ^2 between the J/ψ signal shape from data and simulation with an additional Gaussian smearing added to the electron momentum resolution.

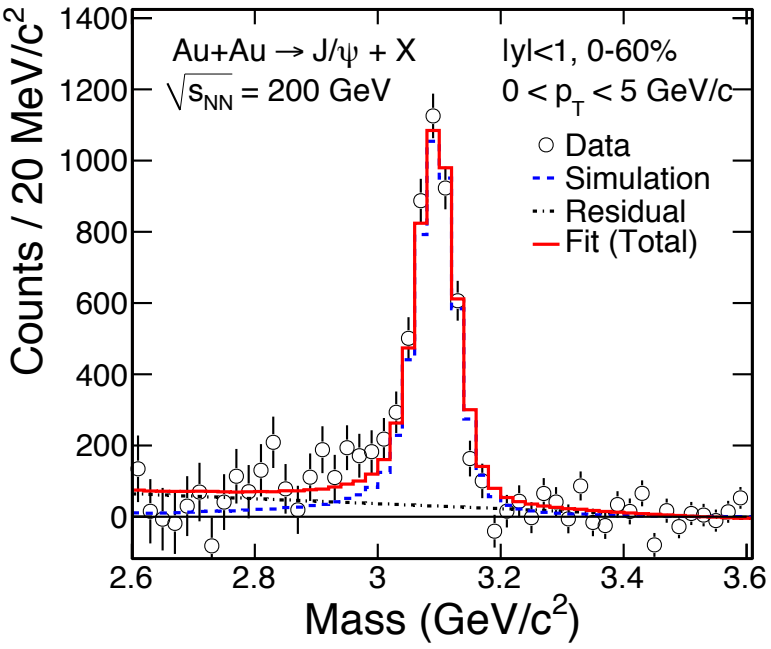

Figure E.5: The J/ψ signal for $|y| < 1$ and $p_T < 5$ GeV/c (open circles) in minimum bias $0-60\%$ central Au+Au collisions. An additional momentum resolution of $0.61\% \times p_T$ has been included in the J/ψ signal shape from simulation (dashed line).

Appendix F

Signal Plots

F.1 Signal Plots in d+Au

The dielectron invariant mass spectrum in d+Au collisions has been obtained using the electron identification requirements in Table 4.7. This is obtained for various momentum bins in $0-100\%$ central collisions, and for $p_T < 5$ GeV/c in various centrality bins, and the results have been obtained without and with the use of the BEMC, respectively. The combinatorial background from like-sign pairs (closed triangles) is subtracted from the opposite-sign dielectrons (open circles) to obtain the J/ψ signal.

The J/ψ signal obtained after like-sign background subtraction is shown for various momentum bins in $0-100\%$ central collisions, and for $p_T < 5$ GeV/c in various centrality bins, and the results have been obtained without and with the use of the BEMC, respectively. The J/ψ signal shape, determined from simulation (dashed line) has been combined with a straight line (dot-dashed line) to account for residual background contributions, and the total (solid line) is fitted to the data (open circles).

Figure F.1: The dielectron mass spectrum in d+Au collisions before background subtraction (no BEMC) for various p_T and centrality bins.

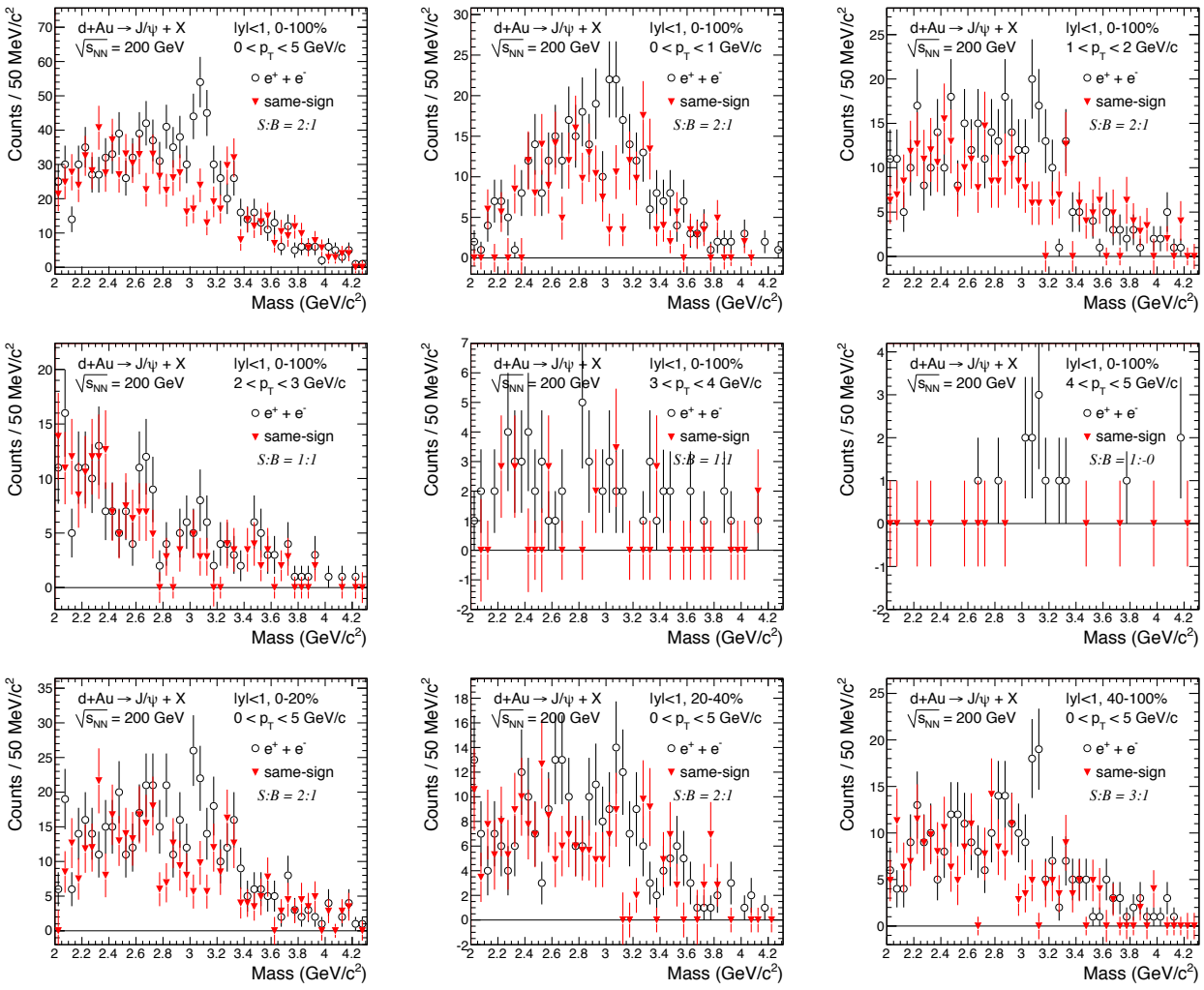

Figure F.2: The dielectron mass spectrum in d+Au collisions before background subtraction (with BEMC) for various p_T and centrality bins.

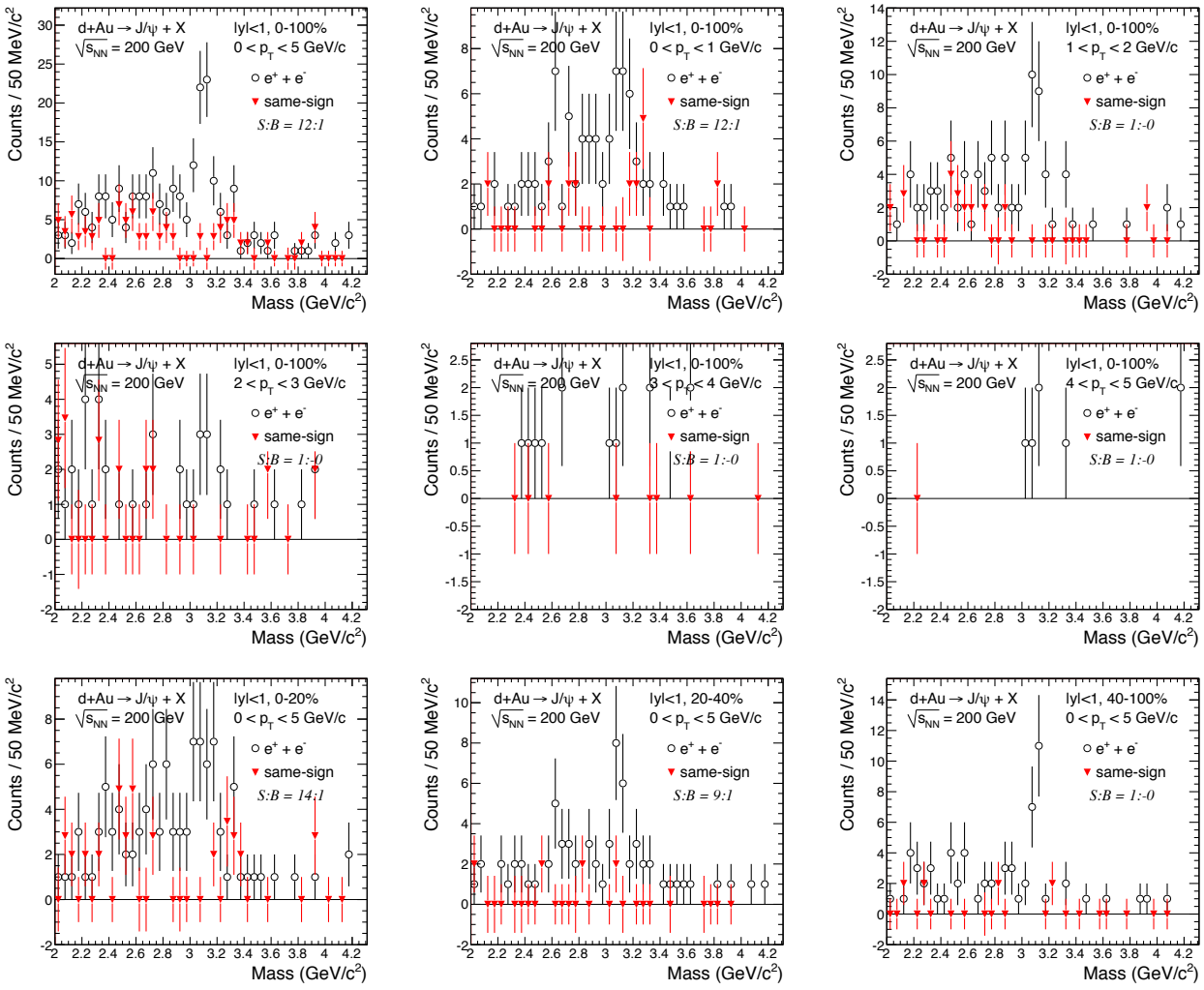

Figure F.3: The dielectron mass spectrum in d+Au collisions after background subtraction (no BEMC) for various p_T and centrality bins.

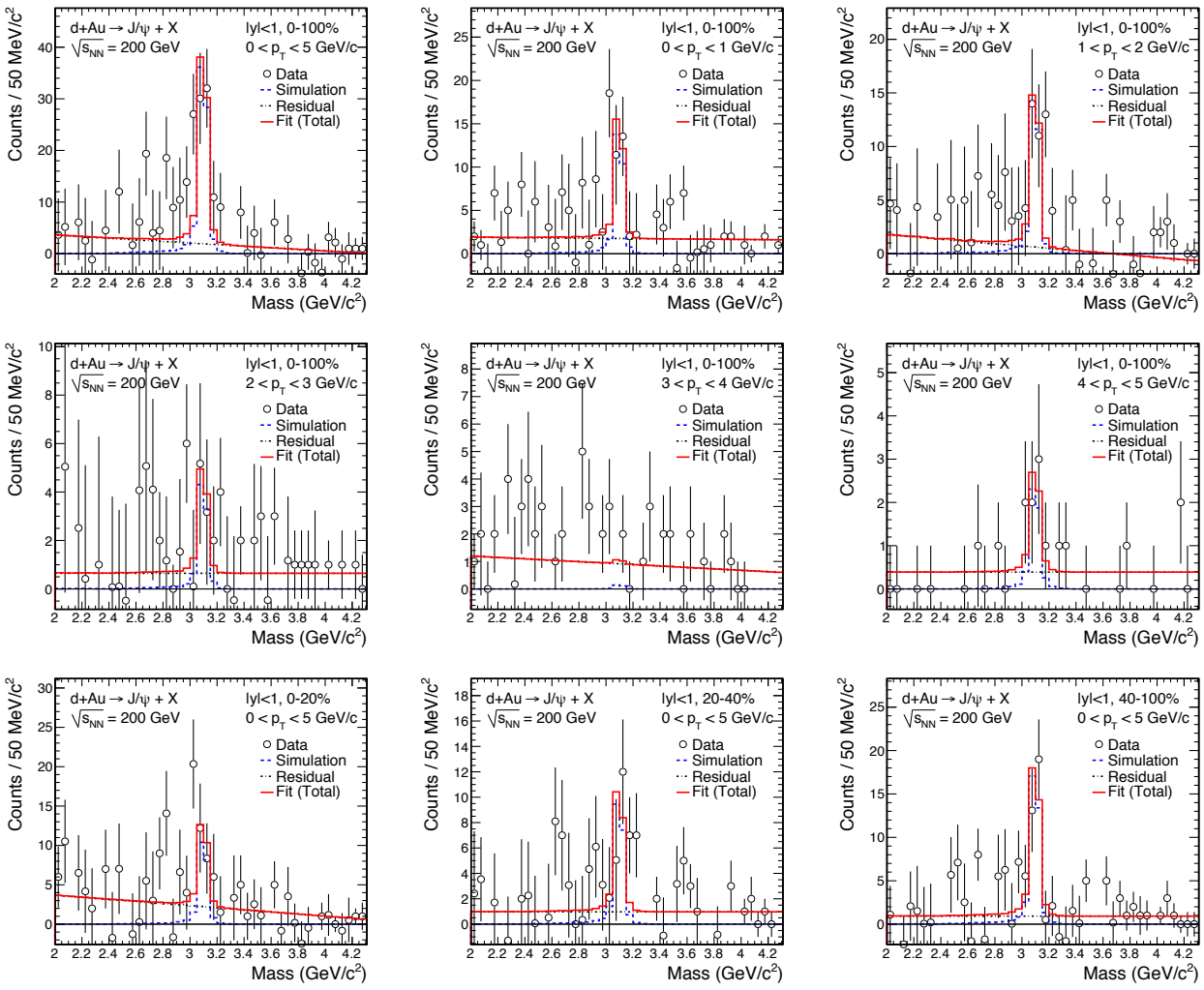

Figure F.4: The dielectron mass spectrum in d+Au collisions after background subtraction (with BEMC) for various p_T and centrality bins.

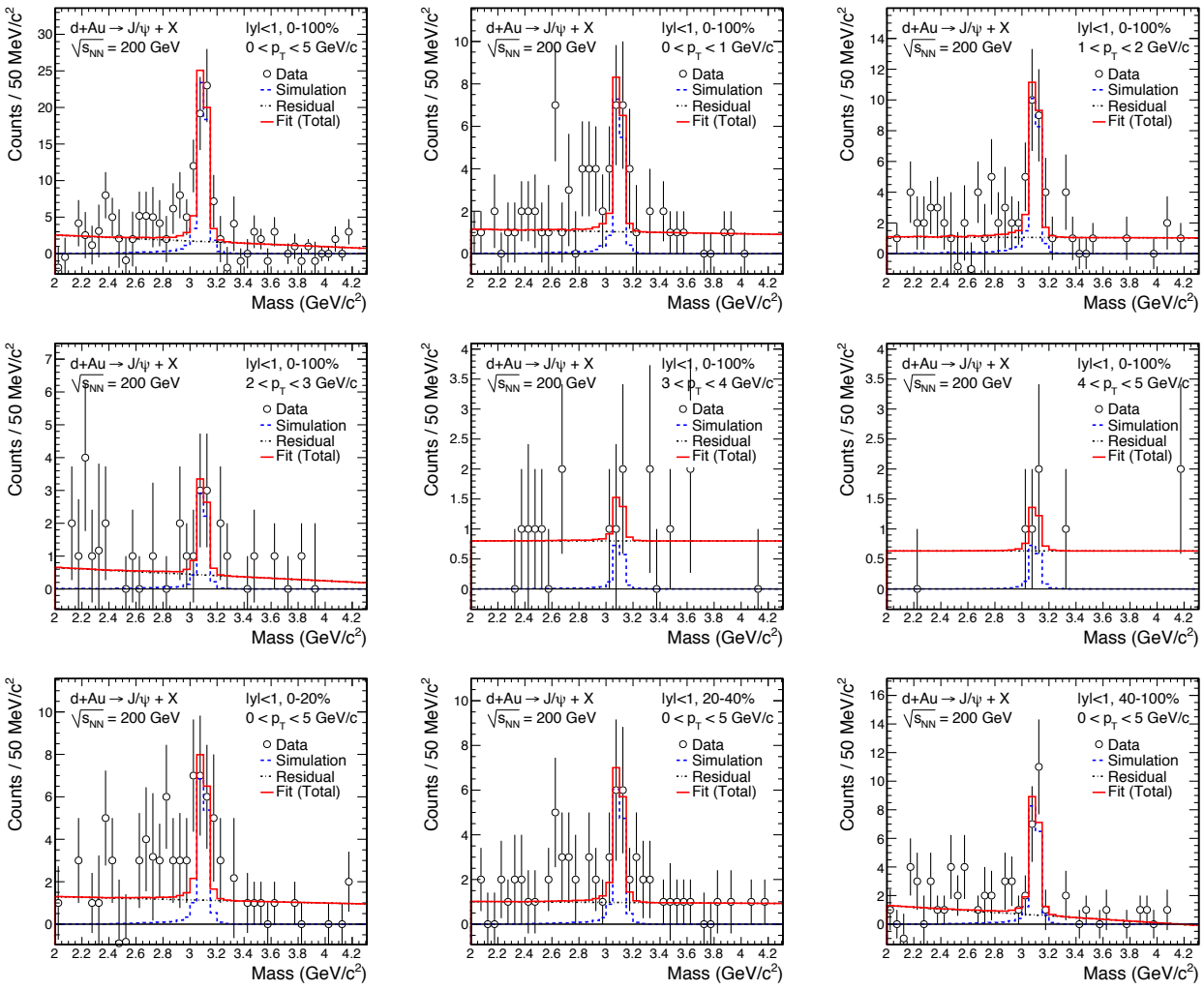

F.2 Signal Plots in Au+Au

The dielectron mass spectrum (open circles) in Au+Au collisions has been obtained using the electron identification requirements in Table 4.8. The mixed-event background (downward triangles) is fitted to the like-sign background (upward triangles) and subtracted from the opposite-sign mass spectrum to obtain the J/ψ signal.

The J/ψ signal has been obtained by subtracting the mixed-event background from the dielectron mass spectrum. The J/ψ signal shape, determined from simulation and combined with an additional Gaussian smearing of width $0.61\% \times p_T$ (dashed line), has been combined with a straight line (dot-dashed line) to account for residual background contributions, and the total (solid line) is fitted to the data (open circles).

Figure F.5: The dielectron mass spectrum in Au+Au collisions before background subtraction for various p_T and centrality bins.

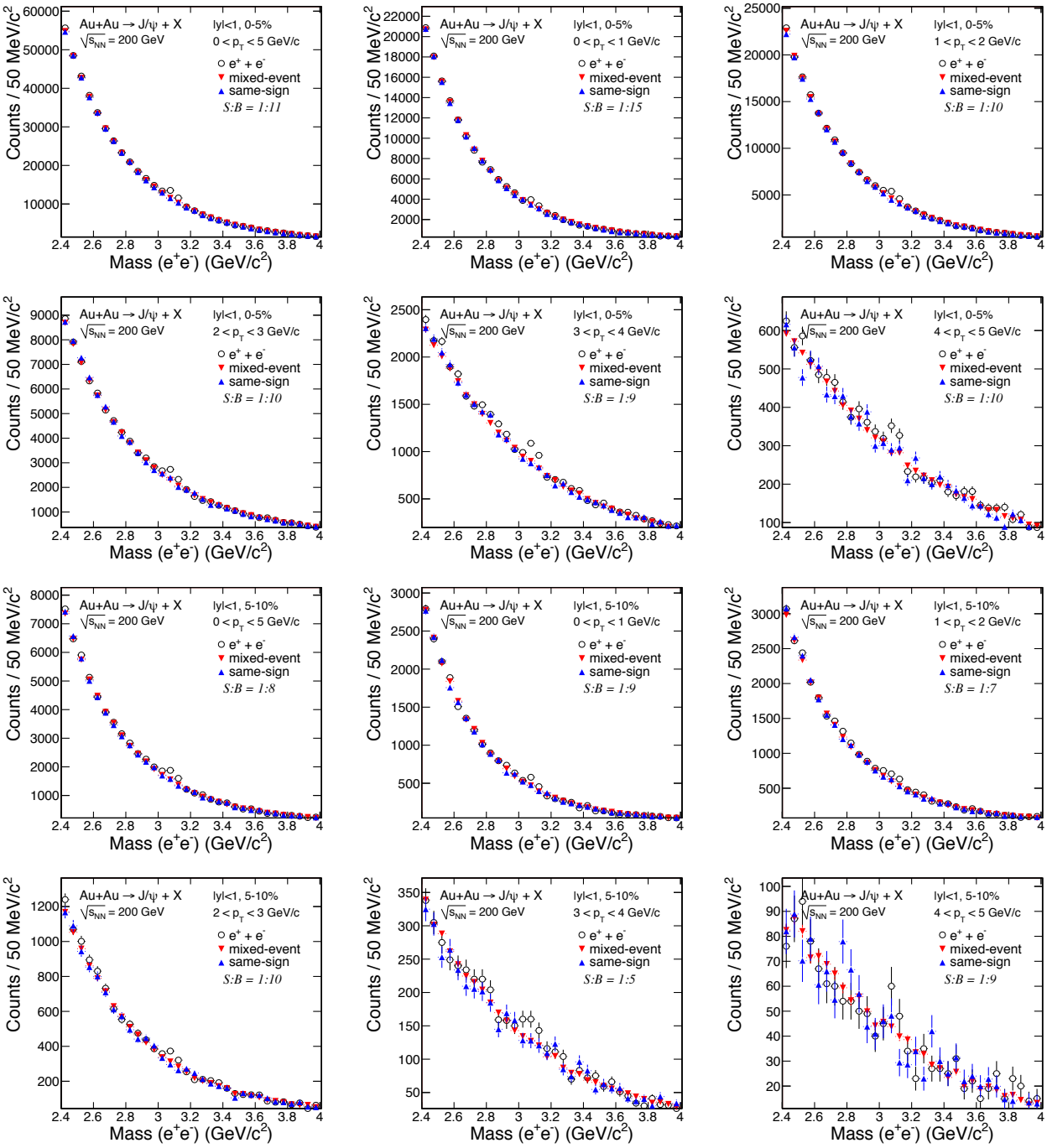

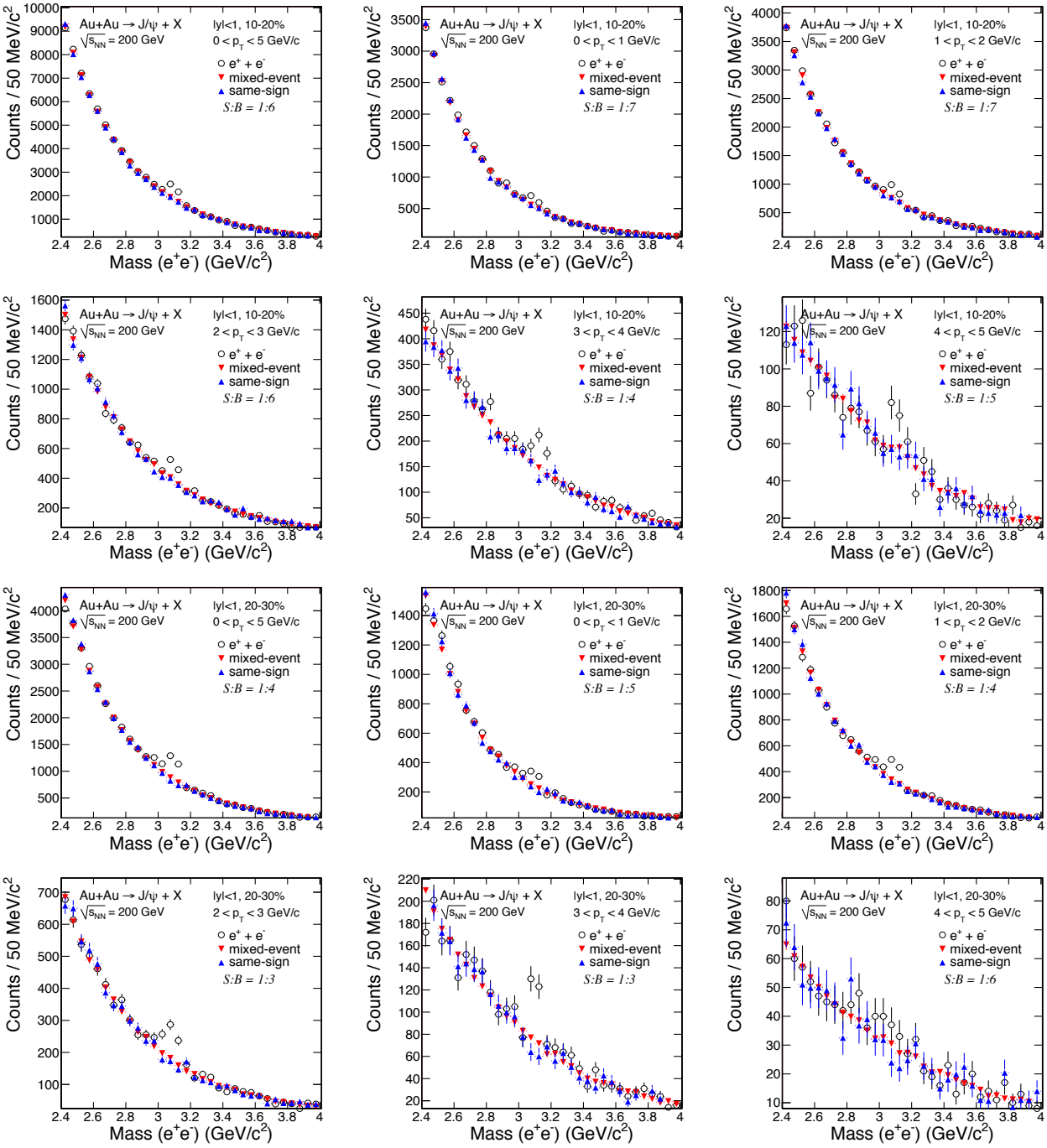
Au+Au → J/ψ + X
√sNN = 200 GeV
|y|<1, 10-20%
0 < pT < 5 GeV/c
e+ + e-
mixed-event
same-sign
S:B = 1:6
0 < pT < 1 GeV/c
S:B = 1:7
1 < pT < 2 GeV/c
S:B = 1:7
2 < pT < 3 GeV/c
S:B = 1:6
3 < pT < 4 GeV/c
S:B = 1:4
4 < pT < 5 GeV/c
S:B = 1:5
|y|<1, 20-30%
0 < pT < 5 GeV/c
S:B = 1:4
0 < pT < 1 GeV/c
S:B = 1:5
1 < pT < 2 GeV/c
S:B = 1:4
2 < pT < 3 GeV/c
S:B = 1:3
3 < pT < 4 GeV/c
S:B = 1:3
4 < pT < 5 GeV/c
S:B = 1:6
Counts / 50 MeV/c2
Mass (e+e-) (GeV/c2)

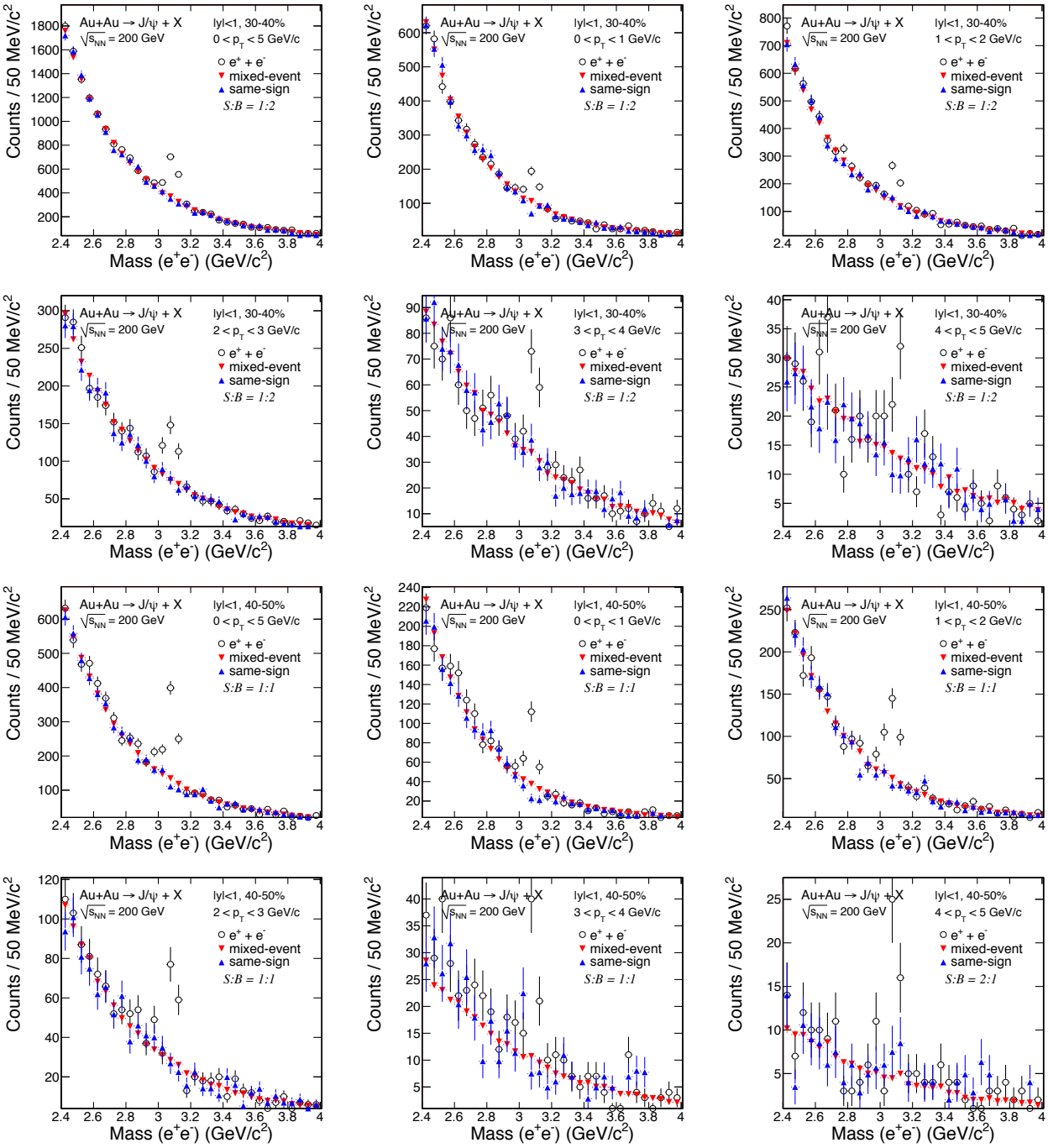
Au+Au → J/ψ + X
√s_NN = 200 GeV
|y|<1, 30-40%
0 < p_T < 5 GeV/c
e+ + e-
mixed-event
same-sign
S:B = 1:2
Counts / 50 MeV/c²
Mass (e+e-) (GeV/c²)
Au+Au → J/ψ + X
√s_NN = 200 GeV
|y|<1, 30-40%
0 < p_T < 1 GeV/c
e+ + e-
mixed-event
same-sign
S:B = 1:2
Counts / 50 MeV/c²
Mass (e+e-) (GeV/c²)
Au+Au → J/ψ + X
√s_NN = 200 GeV
|y|<1, 30-40%
1 < p_T < 2 GeV/c
e+ + e-
mixed-event
same-sign
S:B = 1:2
Counts / 50 MeV/c²
Mass (e+e-) (GeV/c²)
Au+Au → J/ψ + X
√s_NN = 200 GeV
|y|<1, 30-40%
2 < p_T < 3 GeV/c
e+ + e-
mixed-event
same-sign
S:B = 1:2
Counts / 50 MeV/c²
Mass (e+e-) (GeV/c²)
Au+Au → J/ψ + X
√s_NN = 200 GeV
|y|<1, 30-40%
3 < p_T < 4 GeV/c
e+ + e-
mixed-event
same-sign
S:B = 1:2
Counts / 50 MeV/c²
Mass (e+e-) (GeV/c²)
Au+Au → J/ψ + X
√s_NN = 200 GeV
|y|<1, 30-40%
4 < p_T < 5 GeV/c
e+ + e-
mixed-event
same-sign
S:B = 1:2
Counts / 50 MeV/c²
Mass (e+e-) (GeV/c²)
Au+Au → J/ψ + X
√s_NN = 200 GeV
|y|<1, 40-50%
0 < p_T < 5 GeV/c
e+ + e-
mixed-event
same-sign
S:B = 1:1
Counts / 50 MeV/c²
Mass (e+e-) (GeV/c²)
Au+Au → J/ψ + X
√s_NN = 200 GeV
|y|<1, 40-50%
0 < p_T < 1 GeV/c
e+ + e-
mixed-event
same-sign
S:B = 1:1
Counts / 50 MeV/c²
Mass (e+e-) (GeV/c²)
Au+Au → J/ψ + X
√s_NN = 200 GeV
|y|<1, 40-50%
1 < p_T < 2 GeV/c
e+ + e-
mixed-event
same-sign
S:B = 1:1
Counts / 50 MeV/c²
Mass (e+e-) (GeV/c²)
Au+Au → J/ψ + X
√s_NN = 200 GeV
|y|<1, 40-50%
2 < p_T < 3 GeV/c
e+ + e-
mixed-event
same-sign
S:B = 1:1
Counts / 50 MeV/c²
Mass (e+e-) (GeV/c²)
Au+Au → J/ψ + X
√s_NN = 200 GeV
|y|<1, 40-50%
3 < p_T < 4 GeV/c
e+ + e-
mixed-event
same-sign
S:B = 1:1
Counts / 50 MeV/c²
Mass (e+e-) (GeV/c²)
Au+Au → J/ψ + X
√s_NN = 200 GeV
|y|<1, 40-50%
4 < p_T < 5 GeV/c
e+ + e-
mixed-event
same-sign
S:B = 2:1
Counts / 50 MeV/c²
Mass (e+e-) (GeV/c²)

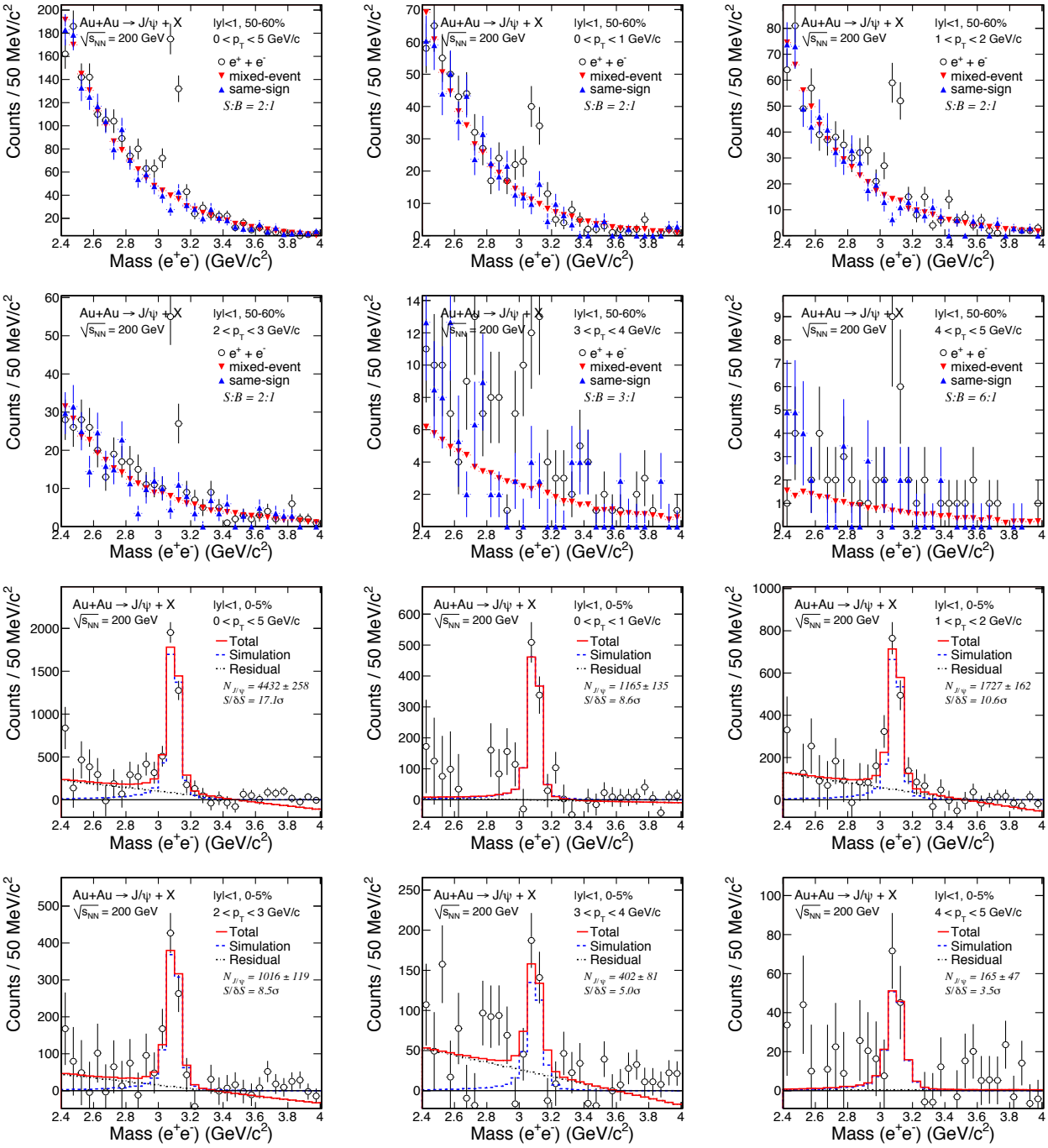
Au+Au → J/ψ + X
√sNN = 200 GeV
|y|<1, 50-60%
0 < pT < 5 GeV/c
e+ + e-
mixed-event
same-sign
S:B = 2:1
Counts / 50 MeV/c2
Mass (e+e-) (GeV/c2)
Au+Au → J/ψ + X
√sNN = 200 GeV
|y|<1, 50-60%
0 < pT < 1 GeV/c
e+ + e-
mixed-event
same-sign
S:B = 2:1
Counts / 50 MeV/c2
Mass (e+e-) (GeV/c2)
Au+Au → J/ψ + X
√sNN = 200 GeV
|y|<1, 50-60%
1 < pT < 2 GeV/c
e+ + e-
mixed-event
same-sign
S:B = 2:1
Counts / 50 MeV/c2
Mass (e+e-) (GeV/c2)
Au+Au → J/ψ + X
√sNN = 200 GeV
|y|<1, 50-60%
2 < pT < 3 GeV/c
e+ + e-
mixed-event
same-sign
S:B = 2:1
Counts / 50 MeV/c2
Mass (e+e-) (GeV/c2)
Au+Au → J/ψ + X
√sNN = 200 GeV
|y|<1, 50-60%
3 < pT < 4 GeV/c
e+ + e-
mixed-event
same-sign
S:B = 3:1
Counts / 50 MeV/c2
Mass (e+e-) (GeV/c2)
Au+Au → J/ψ + X
√sNN = 200 GeV
|y|<1, 50-60%
4 < pT < 5 GeV/c
e+ + e-
mixed-event
same-sign
S:B = 6:1
Counts / 50 MeV/c2
Mass (e+e-) (GeV/c2)
Au+Au → J/ψ + X
√sNN = 200 GeV
|y|<1, 0-5%
0 < pT < 5 GeV/c
Total
Simulation
Residual
NJ/ψ = 4432 ± 258
S/δS = 17.1σ
Counts / 50 MeV/c2
Mass (e+e-) (GeV/c2)
Au+Au → J/ψ + X
√sNN = 200 GeV
|y|<1, 0-5%
0 < pT < 1 GeV/c
Total
Simulation
Residual
NJ/ψ = 1165 ± 135
S/δS = 8.6σ
Counts / 50 MeV/c2
Mass (e+e-) (GeV/c2)
Au+Au → J/ψ + X
√sNN = 200 GeV
|y|<1, 0-5%
1 < pT < 2 GeV/c
Total
Simulation
Residual
NJ/ψ = 1727 ± 162
S/δS = 10.6σ
Counts / 50 MeV/c2
Mass (e+e-) (GeV/c2)
Au+Au → J/ψ + X
√sNN = 200 GeV
|y|<1, 0-5%
2 < pT < 3 GeV/c
Total
Simulation
Residual
NJ/ψ = 1016 ± 119
S/δS = 8.5σ
Counts / 50 MeV/c2
Mass (e+e-) (GeV/c2)
Au+Au → J/ψ + X
√sNN = 200 GeV
|y|<1, 0-5%
3 < pT < 4 GeV/c
Total
Simulation
Residual
NJ/ψ = 402 ± 81
S/δS = 5.0σ
Counts / 50 MeV/c2
Mass (e+e-) (GeV/c2)
Au+Au → J/ψ + X
√sNN = 200 GeV
|y|<1, 0-5%
4 < pT < 5 GeV/c
Total
Simulation
Residual
NJ/ψ = 165 ± 47
S/δS = 3.5σ
Counts / 50 MeV/c2
Mass (e+e-) (GeV/c2)

Figure F.6: The dielectron mass spectrum in Au+Au collisions after background subtraction for various p_T and centrality bins.

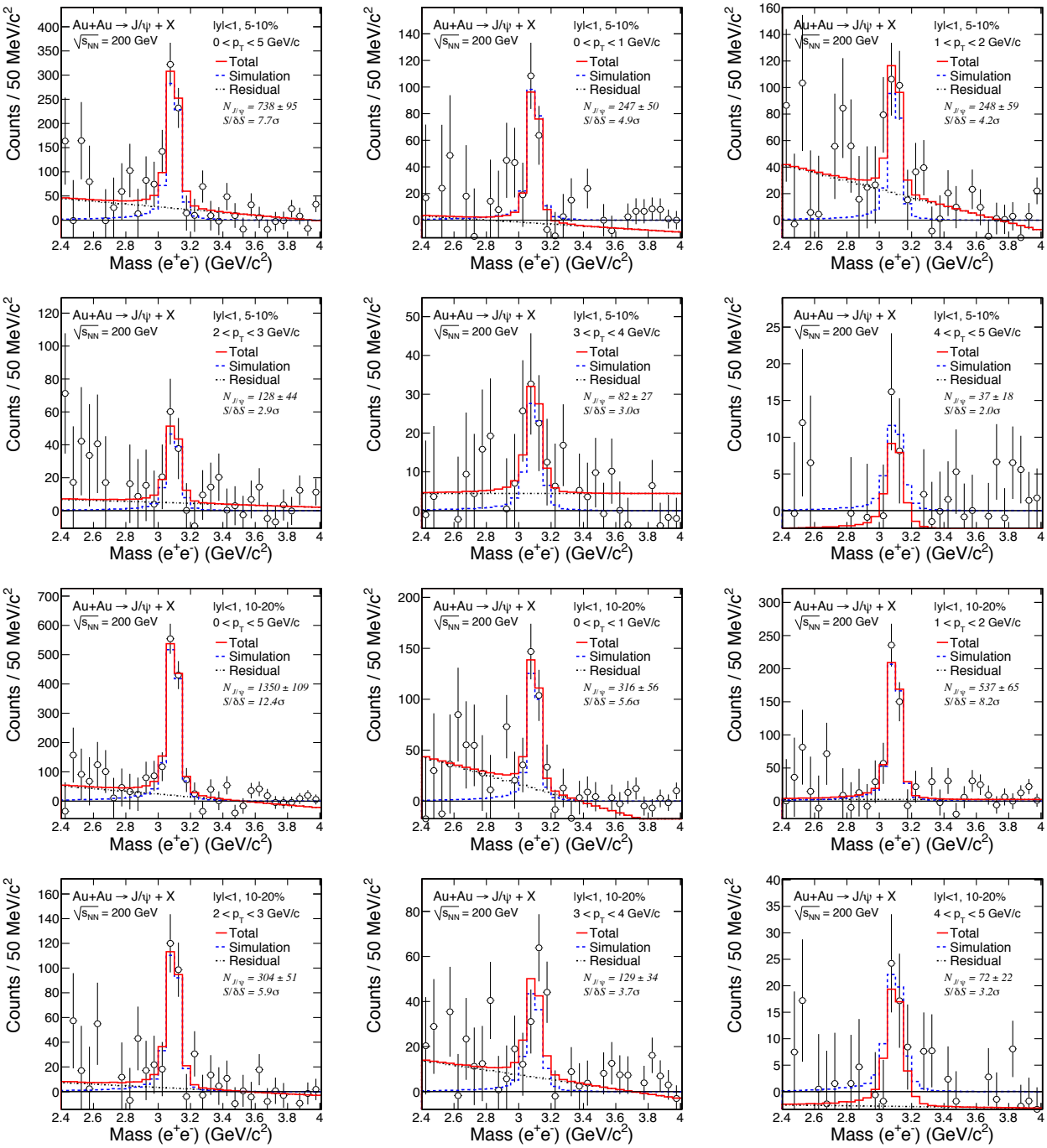

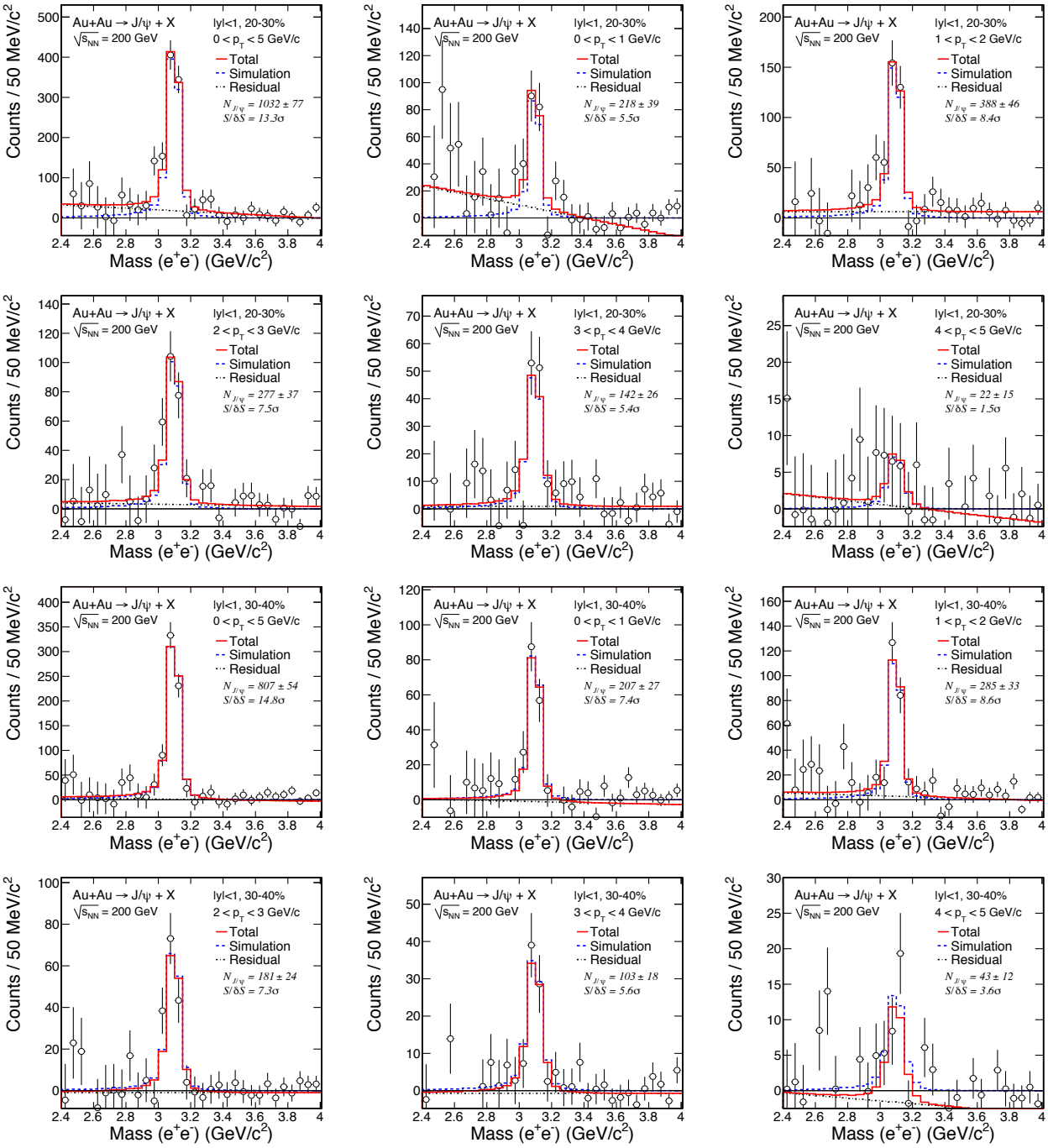
Au+Au → J/ψ + X
√sNN = 200 GeV
|y|<1, 20-30%
0 < pT < 5 GeV/c
Total
Simulation
Residual
NJ/ψ = 1032 ± 77
S/δS = 13.3σ
Au+Au → J/ψ + X
√sNN = 200 GeV
|y|<1, 20-30%
0 < pT < 1 GeV/c
Total
Simulation
Residual
NJ/ψ = 218 ± 39
S/δS = 5.5σ
Au+Au → J/ψ + X
√sNN = 200 GeV
|y|<1, 20-30%
1 < pT < 2 GeV/c
Total
Simulation
Residual
NJ/ψ = 388 ± 46
S/δS = 8.4σ
Au+Au → J/ψ + X
√sNN = 200 GeV
|y|<1, 20-30%
2 < pT < 3 GeV/c
Total
Simulation
Residual
NJ/ψ = 277 ± 37
S/δS = 7.5σ
Au+Au → J/ψ + X
√sNN = 200 GeV
|y|<1, 20-30%
3 < pT < 4 GeV/c
Total
Simulation
Residual
NJ/ψ = 142 ± 26
S/δS = 5.4σ
Au+Au → J/ψ + X
√sNN = 200 GeV
|y|<1, 20-30%
4 < pT < 5 GeV/c
Total
Simulation
Residual
NJ/ψ = 22 ± 15
S/δS = 1.5σ
Au+Au → J/ψ + X
√sNN = 200 GeV
|y|<1, 30-40%
0 < pT < 5 GeV/c
Total
Simulation
Residual
NJ/ψ = 807 ± 54
S/δS = 14.8σ
Au+Au → J/ψ + X
√sNN = 200 GeV
|y|<1, 30-40%
0 < pT < 1 GeV/c
Total
Simulation
Residual
NJ/ψ = 207 ± 27
S/δS = 7.4σ
Au+Au → J/ψ + X
√sNN = 200 GeV
|y|<1, 30-40%
1 < pT < 2 GeV/c
Total
Simulation
Residual
NJ/ψ = 285 ± 33
S/δS = 8.6σ
Au+Au → J/ψ + X
√sNN = 200 GeV
|y|<1, 30-40%
2 < pT < 3 GeV/c
Total
Simulation
Residual
NJ/ψ = 181 ± 24
S/δS = 7.3σ
Au+Au → J/ψ + X
√sNN = 200 GeV
|y|<1, 30-40%
3 < pT < 4 GeV/c
Total
Simulation
Residual
NJ/ψ = 103 ± 18
S/δS = 5.6σ
Au+Au → J/ψ + X
√sNN = 200 GeV
|y|<1, 30-40%
4 < pT < 5 GeV/c
Total
Simulation
Residual
NJ/ψ = 43 ± 12
S/δS = 3.6σ
Counts / 50 MeV/c2
Mass (e+e-) (GeV/c2)

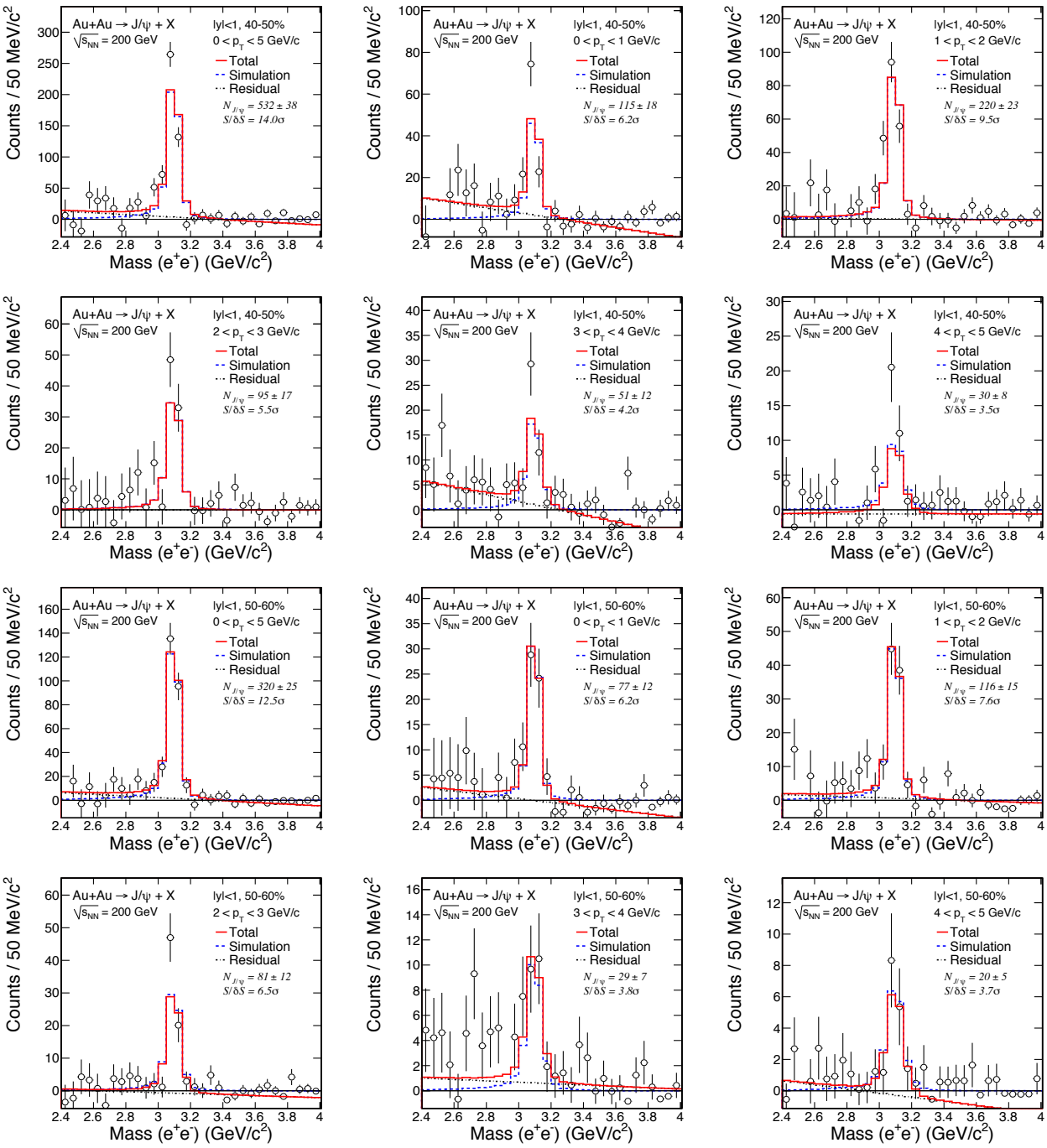
Au+Au → J/ψ + X
√s_NN = 200 GeV
|y|<1, 40-50%
0 < p_T < 5 GeV/c
Total
Simulation
Residual
N_J/ψ = 532 ± 38
S/δS = 14.0σ
Counts / 50 MeV/c²
Mass (e⁺e⁻) (GeV/c²)
Au+Au → J/ψ + X
√s_NN = 200 GeV
|y|<1, 40-50%
0 < p_T < 1 GeV/c
Total
Simulation
Residual
N_J/ψ = 115 ± 18
S/δS = 6.2σ
Counts / 50 MeV/c²
Mass (e⁺e⁻) (GeV/c²)
Au+Au → J/ψ + X
√s_NN = 200 GeV
|y|<1, 40-50%
1 < p_T < 2 GeV/c
Total
Simulation
Residual
N_J/ψ = 220 ± 23
S/δS = 9.5σ
Counts / 50 MeV/c²
Mass (e⁺e⁻) (GeV/c²)
Au+Au → J/ψ + X
√s_NN = 200 GeV
|y|<1, 40-50%
2 < p_T < 3 GeV/c
Total
Simulation
Residual
N_J/ψ = 95 ± 17
S/δS = 5.5σ
Counts / 50 MeV/c²
Mass (e⁺e⁻) (GeV/c²)
Au+Au → J/ψ + X
√s_NN = 200 GeV
|y|<1, 40-50%
3 < p_T < 4 GeV/c
Total
Simulation
Residual
N_J/ψ = 51 ± 12
S/δS = 4.2σ
Counts / 50 MeV/c²
Mass (e⁺e⁻) (GeV/c²)
Au+Au → J/ψ + X
√s_NN = 200 GeV
|y|<1, 40-50%
4 < p_T < 5 GeV/c
Total
Simulation
Residual
N_J/ψ = 30 ± 8
S/δS = 3.5σ
Counts / 50 MeV/c²
Mass (e⁺e⁻) (GeV/c²)
Au+Au → J/ψ + X
√s_NN = 200 GeV
|y|<1, 50-60%
0 < p_T < 5 GeV/c
Total
Simulation
Residual
N_J/ψ = 320 ± 25
S/δS = 12.5σ
Counts / 50 MeV/c²
Mass (e⁺e⁻) (GeV/c²)
Au+Au → J/ψ + X
√s_NN = 200 GeV
|y|<1, 50-60%
0 < p_T < 1 GeV/c
Total
Simulation
Residual
N_J/ψ = 77 ± 12
S/δS = 6.2σ
Counts / 50 MeV/c²
Mass (e⁺e⁻) (GeV/c²)
Au+Au → J/ψ + X
√s_NN = 200 GeV
|y|<1, 50-60%
1 < p_T < 2 GeV/c
Total
Simulation
Residual
N_J/ψ = 116 ± 15
S/δS = 7.6σ
Counts / 50 MeV/c²
Mass (e⁺e⁻) (GeV/c²)
Au+Au → J/ψ + X
√s_NN = 200 GeV
|y|<1, 50-60%
2 < p_T < 3 GeV/c
Total
Simulation
Residual
N_J/ψ = 81 ± 12
S/δS = 6.5σ
Counts / 50 MeV/c²
Mass (e⁺e⁻) (GeV/c²)
Au+Au → J/ψ + X
√s_NN = 200 GeV
|y|<1, 50-60%
3 < p_T < 4 GeV/c
Total
Simulation
Residual
N_J/ψ = 29 ± 7
S/δS = 3.8σ
Counts / 50 MeV/c²
Mass (e⁺e⁻) (GeV/c²)
Au+Au → J/ψ + X
√s_NN = 200 GeV
|y|<1, 50-60%
4 < p_T < 5 GeV/c
Total
Simulation
Residual
N_J/ψ = 20 ± 5
S/δS = 3.7σ
Counts / 50 MeV/c²
Mass (e⁺e⁻) (GeV/c²)